THÈSE DE DOCTORAT
DE L'UNIVERSITÉ DE LILLE

LABORATOIRE DE MÉCANIQUE, MULTIPHYSIQUE ET MULTIECHELLE (FRE 2016, CNRS)

Présentée par

Lunyang ZHAO

pour obtenir le grade de

DOCTEUR DE L'UNIVERSITÉ DE LILLE

Domaine

GÉNIE CIVIL

Sujet de la thèse

Contribution à la modélisation micro-mécanique de l'endommagement et du comportement plastique des géomatériaux (Contribution to micro-mechanical modeling of damage and plastic behavior of geomaterials)

Soutenue le 19 Mars 2019 devant le jury composé de :

H. DUMONTET, Professuer	Sorbonne Université	*Président*
A. GIRAUD, Professeur	Université de Lorraine,	*Rapporteur*
N. LAHELLEC, MCF HDR	Université Aix Marseille	*Rapporteur*
A. ABOU CHAKRA, MCF	INSA Toulouse	*Membre*
I. DOGHRI, Professeur	Université catholique de Louvain	*Membre*
Q.Z. ZHU, Professeur	HOHAI University	*Membre*
J.B. COLLIAT, Professeur	Université de Lille	*Co-directeur de thèse*
J.F. SHAO, Professeur	Université de Lille	*Directeur de thèse*

LAMCUBE - UNIVERSITÉ LILLE

Abstract

Damage due to micro-cracking and plastic deformation are two main dissipation processes in most rock-like materials. They are related to the evolution of micro-structure and influenced by mineralogical compositions. In this study, we present some new contributions on the micro-mechanical modeling of damage and plastic behavior of rock-like materials based on linear and non-linear homogenization techniques.

The first part is devoted to the estimation of macroscopic plastic behavior of a class of quasi-ductile materials, composed of a pressure-dependent plastic solid matrix in which various inclusions and (or) pores are embedded. We propose a new incremental variational model. Unlike most mean-field methods previously developed, the non-uniform local strain field in the solid matrix is taken into account. Moreover, in order to take into account the transition from volumetric compressibility to dilatancy of those materials, a non-associated plastic flow rule is adopted. The incremental variational model is formulated by using a bi-potential theory for the determination of the incremental potential of plastic matrix. The accuracy of the proposed model is assessed by a series of comparisons with reference solutions obtained from full-field finite element simulations. The proposed model is then applied to several rock-like materials with rigid inclusions or pores.

In the second part, we focus on the modeling of induced damage in brittle materials which are represented by an elastic solid matrix weakened by randomly distributed micro-cracks. The emphasis is put on the case of closed cracks under a large range of compressive stress. The damage evolution is due to the initiation and propagation of micro-cracks while the plastic deformation is directly related to the frictional sliding along micro-cracks. The two dissipation processes are physically coupled. A specific friction model is formulated. The efficiency of the proposed model is verified against experimental data on typical granites. Furthermore, the model is extended to study the transition from diffuse damage to localized cracking. The localized cracking is considered as a consequence of coalescence of diffuse micro-cracks. After the onset of a localized crack, the energy dissipation of material is entirely driven by the frictional sliding and propagation of the localized crack. And a specific frictional damage model is developed for the localized crack in consistence with the diffuse damage model. The proposed model is also verified against laboratory tests.

Résumé

L'endommagement induit par micro-fissuration et la déformation plastique sont deux principaux mécanismes de dissipation des matériaux rocheux. Ils sont liés à la modification de micro-structure et influencés par les compositions minéralogiques. Dans cette étude, nous présentons quelques nouvelles contributions à la modélisation micro-mécanique de l'endommagement et du comportement plastique.

La première partie est consacrée à la détermination du comportement élastique-plastique d'une classe de matériaux quasi-ductiles, composés d'une matrice plastique dépendant de la contrainte moyenne dans laquelle sont distribués des inclusions et des pores. Nous proposons un nouveau modèle micro-mécanique basée sur une approche variationnelle incrémentale. Comme différence majeure par rapport à la plupart des modèles en champs moyens, le champ local de déformation plastique non-uniforme est pris en compte. Par ailleurs, une loi d'écoulement plastique non-associée est utilisée pour la matrix solid afin de mieux décrire la transition de la compressibilité à la dilatance volumique des ces matériaux. Le modèle variationnel incrémental est formulé à l'aide de la théorie de bi-potentiel. La performance du modèle est vérifiée à travers des comparaisons avec des solutions numériques de références issues des calculs directs par les éléments finis. Le modèle proposé est ensuite utilisé à des matériaux argileux et poreux pour illustrer son efficacité.

Dans la deuxième partie, nous abordons la modélisation micro-mécanique de l'endommagement induit des matériaux fragiles caractérisés par une matrice solide élastique contenant une distribution aléatoire de micro-fissures. L'accent est mis sur des micro-fissures avec frottement fermées sous contraintes de compression. Le modèle est formulé à l'aide d'une technique d'homogénéisation linéaire et en proposant une loi de glissement frottant à l"échelle locale. Le modèle proposé est d'abord validé par rapport à des essais en laboratoire en supposant une distribution diffuse de micro-fissures. Ensuite, nous proposons une extension du modèle en considérant la transition de l'endommagement diffuse à la fissuration localisée. Celle-ci est décrite comme une conséquence de la coaléscence de micro-fussures. Après la localisation, la dissipation est entièrement pilotté par la fissure localisée. Un modèle de glissement avec frottement est alors développé pour la fissure localisée d'une manière consistante avec le modèle d'endommagement diffuse. Le modèle complet décrivant la transition de l'endommagement diffuse à la fissuration localisé est validé par rapport à des données expérimentales.

Acknowledgement

I would like to express my gratitude to all those who helped me during the writing of this thesis.

I gratefully acknowledge the help of my main supervisor, Pro. Jianfu SHAO, who has offered me valuable suggestions in the academic studies and whose useful suggestions, incisive comments as well as constructive criticism have contributed greatly to the completion of this thesis. I also do appreciate his precious guidances, patiences, confidences and courages during three years of my research and it is a great honor for me to be one of his students.

I would like also to acknowledge my secondary supervisor, Professor Jean-Baptiste COLLIAT, for his support, motivation and enthusiasm throughout the duration of my research.

I am deeply grateful to Professor Qizhi ZHU in Hohai University, as the supervisor of my master in China, for his helps and encouragement. I would never be in France without him.

I am deeply grateful for the comments from Professor A. GIRAUD and N. LAHELLEC as the reviewers of the manuscript of my dissertation. My sincerely gratitude goes to Professor H. DUMONTET as the president jury.

Great thanks also give to all the members of the research group in Lamcube, including Dr. Dr. Zhan YU, Dr. Yue SUN, Dr. Yue TONG, Dr. Jianjian ZHAO, Dr. Jueliang CHEN, Dr. Siyu LIU, Dr. Yajun CAO, Dr. Yulong ZHANG, Dr Jin ZHANG, Dr Bei HAN, Dr Hailing SHI.... They gave me not only many help in the research, but also provide much assistance, specially for French.

Last but not the least, I have to give a great appreciation to my parents and my girlfriend Wanlu for their unconditional support and encouragement during my academic career.

Lunyang Zhao

Contents

List of Figures

List of Tables

General Introduction

Rock-like materials, such as soils, rocks and concretes are largely used in civil engineering applications. It is essential and necessary to determine the mechanical behavior. To date, it has been done by developing various phenomenological models, for instances, plastic models (Shao and Henry, 1991; Xie and Shao, 2006; Zhang et al., 2013), damage models (Dragon et al., 2000; Shojaei et al., 2014) and coupled models (Chiarelli et al., 2003; Conil et al., 2004; Yuan et al., 2013; Zhou et al., 2013), just to mention a few. These models are generally fitted from macroscopic laboratory tests and can reasonably reproduce main features of mechanical responses of rock-like materials. However, most rock-like materials characterized by complex and multi-scale microstructures and textures. For example, some ductile rocks, such as hard clay rocks and sandstone, which composed of various mineral phases, pores in microscale (Figure 1(a)), and some brittle rocks (granite and diabase) can be considered as heterogeneous media composed of solid matrix weakened by randomly distributed microcracks, see Figure 1(b). The macroscopic properties of these rock-like materials are inherently related to local properties of constituent phases and affected by the mineralogical compositions and morphology at different scales. In order to predict macroscopic mechanical responses of these materials in relation with the spatial and temporal change of mineralogical compositions and microscopic structures, constitutive models issued from various homogenization techniques have been developed (Guéry et al., 2008; Jiang et al., 2009; Shen et al., 2012; Zhao et al., 2018; Zhu et al., 2008a, 2016).

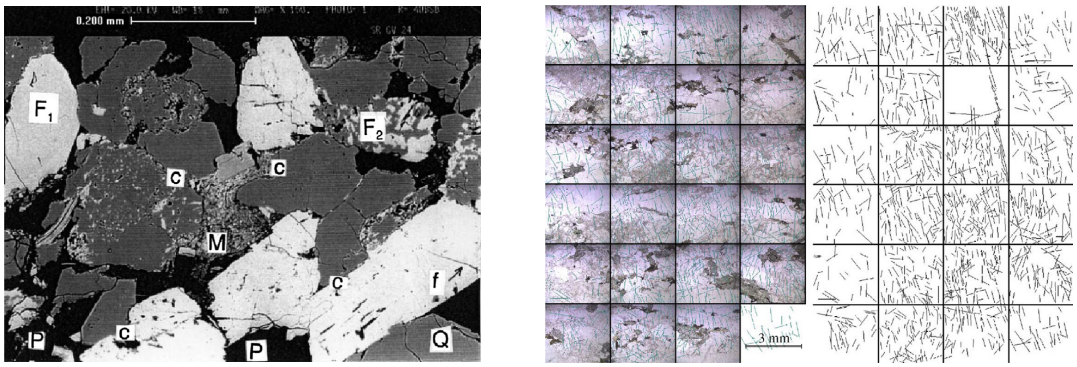

(a) Microstructure of a sandstone (b) Microstructure of a granite rock

Figure 1: Microstructure of two typical rock-like materials

Let considering a class of ductile rock-like materials which are regarded as heterogeneous composites composed of solid matrix and mineral inclusions as well as (or) pores. In literature, Guo et al. (2008a); Maghous et al. (2009b); Shen et al. (2017, 2015), who adopted a Drucker-Prager type criterion for the solid matrix and by using limit analysis techniques and variational approaches, established different analytical forms of the macroscopic strength criterion of porous materials. Moreover, with a two-step homogenization method, an analytical criterion has been proposed for clayey rocks containing a porous clay matrix at the microscopic scale and mineral grains at the mesoscopic scale (Shen et al., 2013). However, in these analytical models, only one family of pores or inclusions is taken into account. In real materials, several families of mineral grains of different mechanical properties and pores may exist at the same scale. In order to determine the effective behavior of such materials, semi-analytical models have been developed. Based on a simple extension of elastic materials, the Hill incremental method has first been developed for composite materials (Doghri and Tinel, 2005; Hill, 1965b). It has also been applied to rock-like materials (Guéry et al., 2008; Shen et al., 2012). In these models based on the Hill incremental method, it is assumed that the local strain field is uniform in each constituent phase. This is a strong assumption which is not verified by most experimental evidences showing strongly non-uniform strain fields in the plastic matrix (Robinet et al., 2012; Wang et al., 2015, 2014). As a consequence, this class of models generally leads to too stiffer macroscopic responses (Chaboche et al., 2005). Some numerical techniques, such as the isotropization of tangent stiffness operator, have been proposed to improve the performance of those models. However, those corrective techniques are not physically founded.

Recently, important efforts have been made in nonlinear homogenization methods in order to account for the effect of non-uniform strain fields in constituent phases. Starting from variational principles for linear composite materials, an effective incremental variational (EIV) method has been proposed for nonlinear composite materials in (Lahellec and Suquet, 2007b,c) in the framework of Generalized Standard Materials (Halphen and Nguyen, 1975). Non-uniform local strain fields are characterized by introducing effective incremental variables. By using an implicit time-discretization scheme, the local evolution problem is reduced to the minimization of an incremental potential function. This effective incremental variable model was first applied to linear and nonlinear viscoelastic composites (Lahellec and Suquet, 2007b,c). More recently, the incremental variational formulation has been used for the prediction of the effective behavior of elastic-plastic composites with local plastic threshold and isotropic and/or linear kinematic plastic hardening (Boudet

et al., 2016). On the other hand, based on the variational principle established by Ortiz and Stainier (1999), some authors have also proposed another incremental variational procedure for elasto-(visco)plastic composites with local isotropic hardening (Brassart et al., 2011, 2012). However, most previous studies were devoted to composite materials with pressure-independent plastic phases. Moreover, all these previous models have been developed in the scope of Generalized Standard Materials (GSM) (Halphen and Nguyen, 1975) with an associated plastic flow rule.

In fact, rock-like materials are known to be non-associated, which can be attributed to implicit standard materials (ISM) (Bodovillé, 2001b; Bodovillé and De Saxcé, 2001; De Saxcé, 1995; Hjiaj et al., 2003; Saxcé and Bousshine, 1998). In this context, the mechanical behaviors of rock-like can be well described by the bi-potential theory which is in the framework of Convex Analysis. The knowledge of a bi-potential function depends on dual variables, for instances, stress and plastic strain rate. This unique function allows simultaneously to define the yield locus and the flow rule, although they are not associated. In the last few decades, the bi-potential theory has been used to investigate a board of non-associated laws of ISMs, including, non-associated metal materials materials (Bodovillé, 2001a; Bousshine et al., 2003), frictional contact (Bousshine et al., 2002; De Saxcé and Bousshine, 1998; Joli and Feng, 2008), and non-associated geomaterials (Cheng et al., 2015; Hjiaj et al., 2003; Zouain et al., 2007). A complete survey of the bi-potential approach and numerical algorithm for non-associated Drucker-Prager plasticity can refer to Hjiaj et al. (2003). In this thesis we will extend the variational principle to pressure-dependent ductile rock-like materials and considering the non-associated issue by using the bi-potential theory. However, to the knowledge of the author, it is difficult to describe the overall behavior of the brittle rock-like materials with randomly distributed frictional closed micro-craks by Hill increment method or variational principle.

For the brittle rock-like materials, it is acknowledged that the complex behaviors can be reasonably related to two coupled physical process at a microscale: the micro-crack growth and frictional sliding along closed crack tips (Walsh, 1980). The growth of micro-cracks induces a material damage while the frictional sliding generates macroscopic irreversible strains which are often described by plasticity theory. The inherent coupling between this two dissipation processes is the main issue for modeling mechanical behaviors of such a class of materials. Indeed, the accumulation of frictional sliding enhances the damage evolution, which inversely effect the frictional sliding. Thus, they are two competing processes governing the inelastic behavior of such material.

By now, the most popular way to formulate constitutive models for quasi-brittle mate-

rials consists in describing the above two dissipative mechanisms separately. During more than three decades, various efforts have been made to develop appropriate elastoplastic damage coupling models essentially within the framework of irreversible thermodynamics. When focusing on application to rock-like materials, we can make the following gross classification:

- Theoretical contributions to the development of elastoplastic damage theories, Dragon and Mroz (1979); Frantziskonis and Desai (1987); Hansen and Schreyer (1994a); Lubarda and Krajcinovic (1995); Maugin (1992);

- Isotropic or anisotropic damage models coupled with plasticity for concrete. For instance, Abu-Lebdeh and Voyiadjis (1993); Cicekli et al. (2007); Grassl and Jirásek (2006b); Jason et al. (2006); Lubliner et al. (1989); Luccioni and Rougier (2005); Voyiadjis et al. (2008); Yazdani and Schreyer (1990);

- Plasticity-damage models for various rocks. We can cite as representatives Chiarelli et al. (2003); Conil et al. (2004); Khan et al. (1991);

- It is finally worth highlighting some discrete orientation-dependent plasticity-damage models. For example, the plasticity-damage coupling in the microplane theory (Carol and Bazant, 1997); the discrete anisotropic plasticity-damage formulations (Zhu et al., 2010); the micromechanical damage-friction coupling models (Gambarotta and Lagomarsino, 1993; Pensee et al., 2002; Zhu et al., 2008a; Zhu and Shao, 2015; Zhu et al., 2016).

Focus here are taken on the micro-mechanics based approaches. Recently, the coupling between crack propagation and frictional sliding has been properly investigated in micro-mechanics based approaches (Zhu and Shao, 2015; Zhu et al., 2016). A micro-mechanics based thermodynamics formulation has been proposed for isotropic damage with unilateral and friction effects (Zhu et al., 2011). Some analytical and numerical analyses of frictional damage have been performed for specific loading paths (Zhu et al., 2016). Some micro-mechanics based models have been extended to initially anisotropic materials (Qi et al., 2016), and to time-dependent behavior analysis related to sub-critical propagation of micro-cracks (Bikong et al., 2015; Zhao et al., 2016).

In spite of the significant progress made so far, there are still some open issues to be investigated. In most micro-mechanical models recently developed, the effect of confining pressure on propagation kinetics of micro-cracks was neglected. The corresponding macroscopic strength envelop is described by a linear function. These models are not able to

properly capture the transition from brittle to ductile behavior with the increase of confining pressure neither the nonlinear strength surface. On the other hand, the progressive degradation of surface asperity of micro-cracks has also not been considered. As a consequence, post-peak behavior and residual strength of materials are not correctly described. Besides, the crucial issue of the transition from the diffuse damage or plastic deformation to the localized cracking of brittle materials has not been systematically investigated. All these mentioned issues will be investigated here by using an micro-mechanics based friction-damage approach.

The main objective of this thesis is to develop homogenization methods for ductile and brittle rock-like materials via incremental variational and micro-mechanics based friction-damage approaches respectively. To this end, this thesis is organized as follows.

- In Chapter I , a bibliographic review will be given on basic principle of homogenization and general aspects of nonlinear homogenization methods for heterogeneous and linear homogenization approaches for crack materials. Some homogenization approaches will be adopted in the following section.

- In Chapter II , we present an incremental variational principle based homogenization method of ductile rock-like materials with an associated plastic matrix. This class of materials are characterized by a solid matrix with embedded mineral inclusions and(or) pores. The plastic behavior of solid matrix is described by a plastic model based on the pressure-dependent Drucker-Prager criterion. Unlike most mean-field methods previously developed, the non-uniform local strain field in the solid matrix is taken into account.

- Chapter III is devoted to establish a bi-potential based incremental variational homogenization of rock-like materials with with a non-associated and strain-hardening plastic matrix. Elastic inclusions or voids are embedded in the plastic matrix. This class of materials does not belong to generalized standard materials investigated in previous studies. The emphasis of this chapter is put on the treatment of non-associated plastic flow and strain hardening. This is done by using a bi-potential theory based method, allowing the determination of the incremental potential of plastic matrix. The effective incremental potential and macroscopic stress tensor are then estimated through an extension of the incremental variational principle established by (Lahellec and Suquet, 2007c).

- In Chapter IV , a new micro-mechanics based plastic damage model is proposed for quasi-brittle materials under a large range of compressive stress. The damage

is due to initiation and propagation of micro-cracks while the plastic deformation is directly related to frictional sliding along micro-cracks. The two dissipation processes are then physically coupled. With the Mori-Tanaka homogenization procedure and thermodynamics framework, the macroscopic state equations are deduced and the local driving forces of damage and plasticity are defined. New specific criteria are proposed for the description of damage evolution and plastic flow. These criteria take into account the variation of material resistance to damage with confining pressure and the degradation of surface asperity of micro-cracks during the frictional sliding.

- In Chapter V , based on the chapter IV , we devoted to the study of transition from diffuse damage to localized cracking in quasi-brittle materials. The localized cracking is considered as a consequence of coalescence of diffuse micro-cracks. The onset of localized crack is then defined by introducing a critical value of diffuse damage density parameter. The orientation of localized crack is determined from the Mohr's maximization postulate. After the onset of a localized crack, the energy dissipation of material is entirely related to the frictional sliding and propagation of the localized crack. In this context, a localized friction damage model is developed in the framework of thermodynamics to describe the frictional sliding of the localized crack which acts as the driving force for its propagation.

- Chapter VI concludes the research of these homogenization approaches and some recommendations for future research.

Throughout this thesis, the following notions of tensorial products of any second order tensors $\boldsymbol{A}$ and $\boldsymbol{B}$ will be used: $(\boldsymbol{A}\otimes\boldsymbol{B})_{ijkl} = A_{ij}B_{kl}$ and $\boldsymbol{A} : \boldsymbol{B} = A_{ij}B_{ij}$. Fourth order tensors are denoted by blackboard bold characters, and one can define $(\mathbb{C} : \boldsymbol{B})_{kl} = C_{ijkl}B_{kl}$. The symbol $\|\boldsymbol{A}\| = \sqrt{\boldsymbol{A} : \boldsymbol{A}}$ is used to denote the norm of any second order tensor $\boldsymbol{A}$. With the second order identity tensor $\boldsymbol{\delta}$, usually used fourth order isotropic identity tensor $\mathbb{I}$ and fourth order hydrostatic projects $\mathbb{J}$ are expressed in the components form as $I_{ijkl} = \frac{1}{2}(\delta_{ik}\delta_{jl} + \delta_{il}\delta_{jk})$ and $J_{ijkl} = \frac{1}{3}\delta_{ij}\delta_{kl}$, respectively. The fourth order deviatoric projects $\mathbb{K} = \mathbb{I} - \mathbb{J}$ is then obtained. Moreover, the fourth-order tensors $\mathbb{J}$ and , $\mathbb{K}$ have the properties: $\mathbb{J} : \mathbb{J} = \mathbb{J}$, $\mathbb{K} : \mathbb{K} = \mathbb{K}$, $\mathbb{J} : \mathbb{K} = \mathbb{K} : \mathbb{J} = \mathbf{0}$.

Supporting publications

- **Lun-Yang Zhao**, Jian-Fu Shao, Qi-Zhi Zhu: Analysis of localized cracking in quasi-brittle materials with a micro-mechanics based friction-damage approach. Journal of the Mechanics and Physics of Solids 06/2018; 119., DOI:10.1016/j.jmps.2018.06.017.

- **Lun-yang Zhao**, Qizhi Zhu, Jianfu Shao: A Micro-mechanics Based Plastic Damage Model for Quasi-Brittle Materials under a Large Range of Compressive Stress. International Journal of Plasticity 01/2018;, DOI:10.1016/j.ijplas.2017.10.004.
- **Lun-Yang Zhao**, Q.Z. Zhu, W.Y. Xu, F. Dai, J.F. Shao: A Unified Micromechanics-based Damage Model for Instantaneous and Time-Dependent Behaviors of Brittle Rocks. International Journal of Rock Mechanics and Mining Sciences 04/2016; 87:187-196., DOI:10.1016 /j.ijrmms. 2016.01.015
- **Lun-Yang Zhao**, Jian-Fu Shao, Qi-Zhi Zhu: Homogenization of rock-like materials with plastic matrix based on an incremental variational principle. Submitted to International Journal of Plasticity.
- **Lun-Yang Zhao**, Jian-Fu Shao, Qi-Zhi Zhu: Homogenization of rock-like materials with a non-associated and strainhardening plastic matrix by a bi-potential based incremental variational approach. Submitted to International Journal of Engineering Science.
- Qi-Zhi Zhu, **Lun-Yang Zhao,** Jian-Fu Shao: Analytical and Numerical Analysis of Frictional Damage in Quasi Brittle Materials. Journal of the Mechanics and Physics of Solids 04/2016; 92., DOI:10.1016/j.jmps.2016.04.002

Chapter I

Literature Review

In this chapter, we shall to propose a short review of main homogenization approaches developed for heterogeneous materials and cracked materials. Some of them will be used in the following chapters. The cracked materials can be regarded as a kind of special heterogeneous materials.

1 Basic principle of homogenization

1.1 Local problem

From the viewpoint of micro-mechanics, we consider the mechanical properties of macroscopic point regarded as a regular homogeneous medium, are equivalent to the overall properties of a Representative Volume Element (RVE) in microscale. A heterogeneous material in which the typical size of an heterogeneity (inclusion or pore) is much smaller than the size of RVE. The geometric domain the RVE is denoted by Ω, with the boundary being $\partial\Omega$. Generally, the RVE composed of N constituents. Each phase occupies a domain Ω_r $(r = 1, 2, ..., N)$ of the RVE with the volume fraction $c_r = V_r/V$. Each point in the RVE is denoted by its position vector $\underline{z}$. The characteristic function $\mathcal{H}^{(r)}$, with $\mathcal{H}^{(r)}(\underline{z}) = 1$ if $\underline{z}$ is in the phase r and $\mathcal{H}^{(r)}(\underline{z}) = 0$ otherwise. The volume fraction of each phase satisfies

$$c_r = \left\langle \mathcal{H}^{(r)}(\underline{z}) \right\rangle, \quad \text{with} \sum_{r=1}^{N} c_r = 1 \tag{I .1}$$

where $\langle\cdot\rangle$ denotes the volume average of the RVE. Similarly, $\langle\cdot\rangle_r$ is the volume average over the phase r, so that

$$\langle\cdot\rangle = \frac{1}{\Omega}\int_{\Omega}(\cdot)\,\mathrm{d}\Omega = \sum_{r=1}^{N} c_r \langle\cdot\rangle_r\,,\quad \langle\cdot\rangle_r = \frac{1}{\Omega_r}\int_{\Omega_r}(\cdot)\,\mathrm{d}\Omega_r \tag{I .2}$$

Note that $\boldsymbol{\sigma}(\underline{z})$ and $\boldsymbol{\varepsilon}(\underline{z})$ are microscopic stress and strain tensor at the point $\underline{z}$. The macroscopic stress and strain can be obtained by the volume averages of the microscopic ones

$$\boldsymbol{\Sigma} = \langle\boldsymbol{\sigma}\rangle\,,\qquad \boldsymbol{E} = \langle\boldsymbol{\varepsilon}\rangle \tag{I .3}$$

The effective behavior of the heterogeneous material is defined as the relation between average stress and strain over the RVE. Two steps are usually distinguished: (1) a localization step, in which local fields within the RVE are computed from the knowledge of the macroscopic strain or stress as an input; (2) a homogenization step, in which the macroscopic response is determined by averaging local fields. The scale transition problem is represented in Figure I .1 for the case of prescribed macroscopic stress.

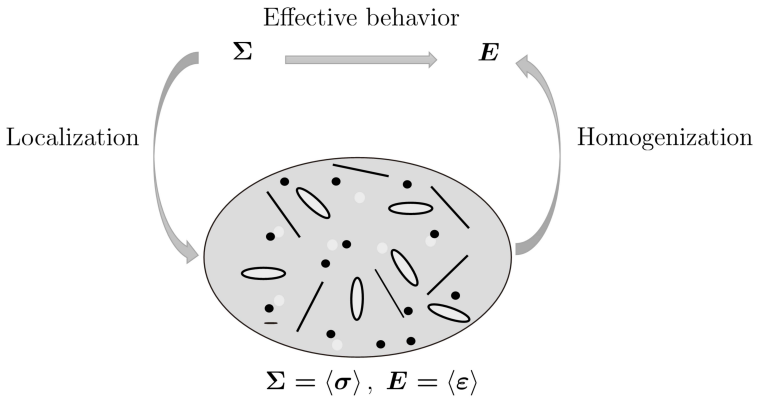

Figure I .1: The effective behavior of the composite is computed on a RVE of the microstructure

In fact, for estimating local stress and strain distribution inside the RVE, two kinds of boundary conditions, uniform stress condition and uniform strain condition are generally prescribed on $\partial\Omega$, see Figure I .2. This two conditions are expressed as:

- **The uniform stress boundary condition:** represents the case of a REV subjected to a constant stress tensor. Let $\boldsymbol{\Sigma}$ be a constant (static) uniform stress field prescribed on $\partial\Omega$, which generates a surface force $\underline{T}^d = \boldsymbol{\Sigma}\cdot\underline{n}(\underline{z})$,$\forall\underline{z}\in\partial\Omega$. At the microscopic scale, the local stress field $\boldsymbol{\sigma}$ satisfies the following condition:

$$\boldsymbol{\sigma}(\underline{z})\cdot\underline{n}(\underline{z}) = \boldsymbol{\Sigma}\cdot\underline{n}(\underline{z}) \qquad (\forall\underline{z}\in\partial\Omega) \tag{I .4}$$

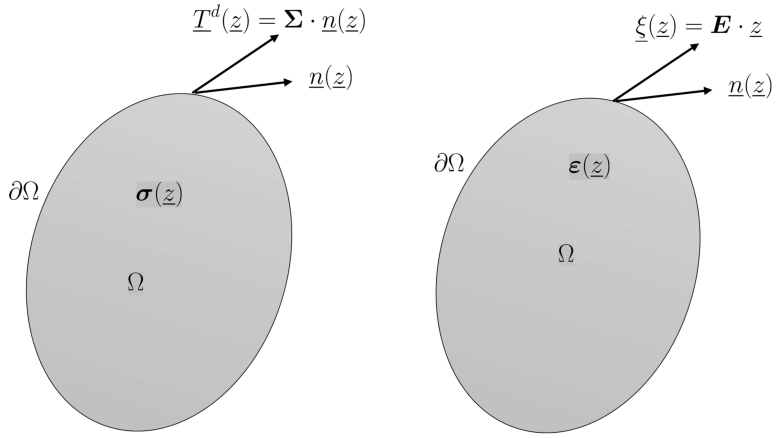

(a) Uniform stress boundary condition

(b) Uniform strain boundary condition

Figure I .2: Two types of boundary conditions applied to RVE

It can be proven that $\boldsymbol{\Sigma}$ is equivalent to the volume average of the local stress $\boldsymbol{\sigma}$ in the REV for any equilibrated, which obeys:

$$\langle \boldsymbol{\sigma} \rangle = \boldsymbol{\Sigma} \tag{I .5}$$

where $\langle \cdot \rangle_\Omega$ denotes the volumetric averaging over the domain Ω.

In this case, the average stress is given by:

$$\langle \boldsymbol{\sigma} \rangle := \frac{1}{\mid V \mid} \int_V \boldsymbol{\sigma}(\underline{z}) dz \tag{I .6}$$

- **The uniform strain boundary condition:** represents the case of a REV subjected to a regular displacement condition at its boundary. Let $\boldsymbol{E}$ be the macroscopic uniform strain field on the boundary $\partial\Omega$. Correspondingly, the displacement boundary condition reads:

$$\underline{\xi}(\underline{z}) = \boldsymbol{E} \cdot \underline{z} \qquad (\forall \underline{z} \in \partial\Omega) \tag{I .7}$$

whereas $\underline{z}$ and $\underline{\xi}$ are denoted the position vector in the REV and the microscopic displacement.

It also implies the relationship between the average of local strain field $\boldsymbol{\varepsilon}$ in the REV and the macroscopic strain $\boldsymbol{E}$ as:

$$\langle \boldsymbol{\varepsilon} \rangle = \boldsymbol{E} \tag{I .8}$$

In this case, the average strain is given by:

$$\langle \boldsymbol{\varepsilon} \rangle := \frac{1}{\mid V \mid} \int_V \boldsymbol{\varepsilon}(\underline{z}) dz \tag{I .9}$$

1.2 Hill-Mandel condition

The Hill-Mandel condition is a fundamental precondition for scale transition. It is first proposed by Hill (1967) , which reads as follows. Considering σ an equilibrated stress field ($\nabla \cdot \sigma = \mathbf{0}$) and $\boldsymbol{\varepsilon}$ a compatible strain field $\boldsymbol{\varepsilon} = \boldsymbol{\varepsilon}(\underline{u})$ which are not necessarily related by a constitutive relation. In this context, if $\boldsymbol{\sigma}$ satisfies uniform stress boundary condition or if $\boldsymbol{\varepsilon}$ is compatible with uniform strain boundary condition, the following equality holds

$$\langle \boldsymbol{\sigma} : \boldsymbol{\varepsilon} \rangle = \langle \boldsymbol{\sigma} \rangle : \langle \boldsymbol{\varepsilon} \rangle = \boldsymbol{\Sigma} : \boldsymbol{E} \tag{I .10}$$

This equality is called Hill's Lemma, which ensures the equality of macroscopic and microscopic work. Note that equality (I .10) can be established without specifying the boundary conditions, provided that the mechanical fields are macroscopically homogeneous (Hill, 1967).

2 Review of nonlinear homogenization approaches to heterogeneous materials

In many engineering applications, it is necessary to determine mechanical properties of so-called rock-like materials, such as rocks, hard soils and concretes. For a kind of rock-like materials composed of various mineral phases and pores, it is needed to adopt nonlinear homogenization approaches for describing the effective behavior. In this section, we will have a short review for these approaches.

2.1 Approaches based on a linearization of the local stress-strain relation

2.1.1 Hill's tangent incremental approach

Hill (1965a) proposed a method to transform the nonlinear homogenization problem to a multi linear one in an incremental form:

$$\dot{\boldsymbol{\sigma}}(\underline{z}) = \mathbb{C}^{tan}(\underline{z}) : \dot{\boldsymbol{\varepsilon}}(\underline{z}) \tag{I .11}$$

where $\mathbb{C}^{tan}(\underline{z})$ is the tangent operator at each microscopic point. With the assumption of the local tangent operator is uniform inside each phase, the increment form of local stress-strain relation reads

$$\dot{\boldsymbol{\sigma}}_r = \mathbb{C}_r^{tan} : \dot{\boldsymbol{\varepsilon}}_r \tag{I .12}$$

where the fourth order tensor $\mathbb{C}_r^{tan}$ is the local tangent operator r^{th} material phase. $\dot{\boldsymbol{\sigma}}_r$ and $\dot{\boldsymbol{\varepsilon}}_r$ are the average value of local stress and strain fields in this phase, respectively.

In this context, the macroscopic effective tangent operator to the reference homogeneous medium can be formulated

$$\mathbb{C}^{hom} = \langle \mathbb{C}^{\tan}(\underline{z}) : \mathbb{A}(\underline{z}) \rangle = \sum_r c_r \mathbb{C}_r^{\tan} : \mathbb{A}_r \tag{I .13}$$

where c_r is the volume fraction of the phase r, and $\mathbb{A}_r$ is the strain localization tensor, which should be determined at each time increment with an appropriate linear homogenization scheme, such as dilute scheme, Mori-Tanaka scheme and PC-W scheme, which will be reviewed in Section 3. After that, the macroscopic stress-strain behavior can be expressed as

$$\dot{\boldsymbol{\Sigma}} = \mathbb{C}^{hom} : \dot{\boldsymbol{E}}. \tag{I .14}$$

This incremental approach has been considered for a long time the standard for deriving nonlinear estimates of heterogeneous materials (Mareau et al., 2009). This method have been largely applied and two phase nonlinear composite materials, for instance, Chaboche et al. (2005) for metals with von-Mises type plasticity theory, Doghri and Ouaar (2003)for cyclic plasticity with non linear kinematical hardening. Guéry et al. (2008); Jiang and Shao (2009); Shen et al. (2012) have extended the method to geomaterials considering the pressure-dependent effects.

2.1.2 Secant approach

Following Hill's works, some researchers proposed other ways to linearization the local constitutive relation rather than the tangent form. One of them is secant method, which approximate the local behavior in a total deformation formalism using the secant operator $\mathbb{C}_r^{\sec}$ of the phase r, in this case, the local constitutive can be read

$$\boldsymbol{\sigma}_r = \mathbb{C}_r^{\sec} : \boldsymbol{\varepsilon}_r \tag{I .15}$$

After volumetric averaging, the macroscopic constitutive equation can be obtained and also written in secant form

$$\boldsymbol{\Sigma} = \mathbb{C}^{\sec} : \boldsymbol{E} \tag{I .16}$$

where $\mathbb{C}^{\sec}$ is the macroscopic secant modulus tensor of the equivalent homogenized medium.

2.1.3 Affine approach

Recently, Masson et al. (2000); Masson and Zaoui (1999) proposed an "affine" approximation using the tangent stiffness tensor but in a non-incremental form to linearize the

local constitutive equation:

$$\boldsymbol{\sigma}_r = \mathbb{C}_r : \boldsymbol{\varepsilon}_r + \boldsymbol{\sigma}_r^0 \tag{I .17}$$

Then the overall constitutive equation is obtained

$$\boldsymbol{\Sigma} = \mathbb{C}^{\tan} : \boldsymbol{E} + \boldsymbol{\Sigma}^0 \tag{I .18}$$

For more difference between the aforementioned three different mean field homogenization approaches, one can refer in Chaboche et al. (2001).

2.2 Variational approaches

The other fruitful research approaches is in the variational framework (Brassart et al., 2011, 2012; Castañeda, 1991, 1992, 2002b; Lahellec and Suquet, 2007b, 2013). We here will first review the general framework, and then will introduce several variational approaches.

2.2.1 Variational framework

In the variational framework, the local behavior is described by a single convex potential, i.e.,

$$\boldsymbol{\sigma} = \frac{\partial W}{\partial \boldsymbol{\varepsilon}}(\underline{z}, \boldsymbol{\varepsilon}), \quad \text{with} \quad W(\underline{z}, \boldsymbol{\varepsilon}) = \sum_{r=1}^{N} \mathcal{H}^r(\underline{z}) W^{(r)}(\boldsymbol{\varepsilon}) \tag{I .19}$$

where $W^{(r)}$ is the potential of phase r. Under the uniform strain boundary condition, the minimum energy principle states that the strain field $\boldsymbol{\varepsilon}(\underline{z})$ is the solution of the following variational problem

$$\bar{W} = \inf_{\boldsymbol{\varepsilon} \in \mathcal{R}(\boldsymbol{E})} \langle W(\boldsymbol{\varepsilon}) \rangle \tag{I .20}$$

where the set $\mathcal{R}(\boldsymbol{E})$ is the kinematically admissible strain field

$$\mathcal{R}(\boldsymbol{E}) = \left\{ \boldsymbol{E} = \frac{1}{2}\left(\nabla \underline{\xi} + \nabla^T \underline{\xi}\right) \right\} \tag{I .21}$$

with $\underline{\xi}(\underline{z})$ has been defined in. Note that the minimum average strain energy $\bar{W}$ is the effective potential of the composite, from which the effective stress-strain relation is obtained:

$$\boldsymbol{\Sigma} = \frac{\partial \bar{W}}{\partial \boldsymbol{E}} \tag{I .22}$$

This relation is derived by (Ponte-Castañeda and Suquet, 1998)

$$\frac{\partial \bar{W}}{\partial \boldsymbol{E}} = \left\langle \frac{\partial W(\boldsymbol{\varepsilon})}{\partial \boldsymbol{\varepsilon}} : \frac{\partial \boldsymbol{\varepsilon}}{\partial \boldsymbol{E}} \right\rangle = \left\langle \boldsymbol{\sigma} : \frac{\partial \boldsymbol{\varepsilon}}{\partial \boldsymbol{E}} \right\rangle = \langle \boldsymbol{\sigma} \rangle : \left\langle \frac{\partial \boldsymbol{\varepsilon}}{\partial \boldsymbol{E}} \right\rangle \tag{I .23}$$

where $\boldsymbol{\varepsilon}$ is the strain field solution of the variational problem. The last equality is obtained by applying the Hill's lemma. Eq. (I .23) is then proven noting that: $\left\langle \frac{\partial \boldsymbol{\varepsilon}}{\partial \boldsymbol{E}} \right\rangle = \frac{\langle \partial \boldsymbol{\varepsilon} \rangle}{\partial \boldsymbol{E}} = \boldsymbol{\delta}$.

By using Legendre transform, the function U which is convex dual of W is derived

$$U(\boldsymbol{\sigma}) = \sup_{\boldsymbol{\varepsilon}} \{\boldsymbol{\sigma} : \boldsymbol{\varepsilon} - W(\boldsymbol{\varepsilon})\} \tag{I .24}$$

and the local strain behavior can be expressed as

$$\boldsymbol{\varepsilon} = \frac{\partial U}{\partial \boldsymbol{\sigma}}(\underline{z}, \boldsymbol{\sigma}), \quad \text{with } U(\underline{z}, \boldsymbol{\sigma}) = \sum_{r=1}^{N} \mathcal{H}^{(r)}(\underline{z}) U^{(r)}(\boldsymbol{\sigma}) \tag{I .25}$$

Then the overall stress potential in the composites is given by the principle of minimum complementary energy

$$\bar{U}(\boldsymbol{\sigma}) = \inf_{\boldsymbol{\sigma} \in \mathcal{F}(\boldsymbol{\Sigma})} \langle U(\boldsymbol{\sigma}) \rangle \tag{I .26}$$

Finally a proof similar to (I .22) reads that

$$\boldsymbol{E} = \frac{\partial \bar{U}}{\partial \boldsymbol{\Sigma}} \tag{I .27}$$

It is noted that the macroscopic constitutive relations ((I .22) and (I .27)) are completely equivalent in the case of that the effective potential $\bar{W}$ and $\bar{U}$ are dual of each other, i.e., (Willis, 1989)

$$\bar{U}(\boldsymbol{\Sigma}) = \sup_{\boldsymbol{E}} \left[\boldsymbol{\Sigma} : \boldsymbol{E} - \bar{W}(\boldsymbol{E})\right] \tag{I .28}$$

2.2.2 Variational approach of Castañeda (1991)

Castañeda (1991) considered the composites composed of J2 isotropic plastic phase, and introduced the following quadratic potential

$$W^{(r)}(\boldsymbol{\varepsilon}) = \frac{9}{2} k^{(r)} \varepsilon_m^2 + f^{(r)}\left(\varepsilon_{eq}^2\right) \tag{I .29}$$

where

$$f\left(\varepsilon_{eq}^2\right) = \inf_{\mu_0^{(r)}} \left[\frac{3}{2} \mu_0^{(r)} \varepsilon_{eq}^2 - f_*\left(\mu_0^{(r)}\right)\right]$$

For a fictitious linear composite is introduced, the phase potential

$$W_0^{(r)}\left(\mu_0^{(r)}, \boldsymbol{\varepsilon}\right) = \frac{1}{2} \boldsymbol{\varepsilon} : \mathbb{C}_0^{(r)} : \boldsymbol{\varepsilon}, \quad \text{with } \mathbb{C}_0^{(r)} = 2\mu_0^{(r)} \mathbb{K} + 3k^{(r)} \mathbb{J} \tag{I .30}$$

Substituting (I .30) into (I .29) , the potential (I .29) can be rewritten as

$$W^{(r)}(\boldsymbol{\varepsilon}) = \inf_{\mu_0^{(r)}} \left[W_0^{(r)}\left(\mu_0^{(r)}, \boldsymbol{\varepsilon}\right) + V^{(r)}\left(\mu_0^{(r)}\right)\right] \tag{I .31}$$

where the $V^{(r)}\left(\mu_0^{(r)}\right)$ is given by

$$V^{(r)}\left(\mu_0^{(r)}\right) = -f_*\left(\mu_0^{(r)}\right) = \sup_{\varepsilon_{eq}^2}\left[f\left(\varepsilon_{eq}^2\right) - \frac{3}{2}\mu_0^{(r)}\varepsilon_{eq}^2\right] \tag{I .32}$$

$$= \sup_{\boldsymbol{\varepsilon}}\left[W^{(r)}\left(\boldsymbol{\varepsilon}\right) - W_0^{(r)}\left(\mu_0^{(r)}, \boldsymbol{\varepsilon}\right)\right] \tag{I .33}$$

Then the optimality condition in corresponds to a secant condition

$$\frac{\partial W^{(r)}}{\partial \boldsymbol{\varepsilon}}\left(\boldsymbol{\varepsilon}\right) = \mathbb{C}_0^{(r)} : \boldsymbol{\varepsilon} \tag{I .34}$$

Inserting Eq (I .31) into the variational formulation of the homogenization problem (I .20),the following equivalent variational principle is obtained

$$\bar{W}\left(\boldsymbol{E}\right) = \inf_{\mu_0}\left[\bar{W}_0\left(\mu_0, \boldsymbol{\varepsilon}\right) + \left\langle V^{(r)}\left(\mu_0^{(r)}\right)\right\rangle\right] \tag{I .35}$$

where $\bar{W}_0$ is the effective potential of the LCC with phase potential, which reads

$$\bar{W}_0 = \inf_{\boldsymbol{\varepsilon}\in\mathcal{R}(\boldsymbol{E})}\sum_{r=1}^{N} c_r\left\langle W_0^{(r)}\left(\mu_0^{(r)}, \boldsymbol{\varepsilon}\right)\right\rangle_r = \frac{1}{2}\boldsymbol{E} : \bar{\mathbb{C}}_0 : \boldsymbol{E} \tag{I .36}$$

2.2.3 Second order procedure of Castañeda (2002a)

For incorporating the fluctuations for the nonlinear composites, Castañeda (2002a) proposed an improved second order homogenization method. In the following, we will have a brief review of this approach.

Based on the second-order Taylor approximation of the nonlinear potential, one obtains

$$W_0^{(r)}\left(\boldsymbol{\varepsilon}\right) = W^{(r)}\left(\boldsymbol{\varepsilon}^{(r)}\right) + \frac{\partial W^{(r)}}{\partial \boldsymbol{\varepsilon}}\left(\boldsymbol{\varepsilon}^{(r)}\right) : \left(\boldsymbol{\varepsilon} - \boldsymbol{\varepsilon}^{(r)}\right) + \frac{1}{2}\left(\boldsymbol{\varepsilon} - \boldsymbol{\varepsilon}^{(r)}\right) : \mathbb{C}_0^{(r)} : \left(\boldsymbol{\varepsilon} - \boldsymbol{\varepsilon}^{(r)}\right) \tag{I .37}$$

where $\boldsymbol{\varepsilon}^{(r)}$ is a uniform reference strain and $\mathbb{C}_0^{(r)}$ is a symmetric, postive definite, constant tensor. The following upper bound for the overall potential of the nonlinear composite read

$$\bar{W}\left(\boldsymbol{E}\right) \leq \inf_{\mathbb{C}_0^{(r)}, \boldsymbol{\varepsilon}^{(r)}}\left[\bar{W}_0\left(\boldsymbol{E}, \mathbb{C}_0^{(r)}, \boldsymbol{\varepsilon}^{(r)}\right) + \sum_{r=1}^{N} c_r V^{(r)}\left(\mathbb{C}_0^{(r)}, \boldsymbol{\varepsilon}^{(r)}\right)\right] \tag{I .38}$$

where $\bar{W}_0$ is the effective potential of the LCC, and the error function

$$V^{(r)} = \sup_{\hat{\boldsymbol{\varepsilon}}^{(r)}}\left[W^{(r)}\left(\hat{\boldsymbol{\varepsilon}}^{(r)}\right) - W_0^{(r)}\left(\hat{\boldsymbol{\varepsilon}}^{(r)}, \mathbb{C}_0^{(r)}\right)\right] \tag{I .39}$$

have been introduced for convenience.

It is noted that (I .38) holds for any choice of reference moduli $\mathbb{C}_0^{(r)}$ and strains $\boldsymbol{\varepsilon}^{(r)}$. For the sake of more accuracy, the infimum in and the supremum in have been replaced by stationarity conditions

$$\bar{W}\left(\boldsymbol{E}\right) \simeq \text{stat}_{\mathbb{C}_0^{(r)},\boldsymbol{\varepsilon}^{(r)}} \left[\bar{W}_0\left(\boldsymbol{E},\mathbb{C}_0^{(r)},\boldsymbol{\varepsilon}^{(r)}\right) + \sum_{r=1}^{N} c_r V^{(r)}\left(\mathbb{C}_0^{(r)},\boldsymbol{\varepsilon}^{(r)}\right)\right] \tag{I .40}$$

with

$$V^{(r)} = \text{stat}_{\hat{\boldsymbol{\varepsilon}}^{(r)}} \left[W^{(r)}\left(\hat{\boldsymbol{\varepsilon}}^{(r)}\right) - W_0^{(r)}\left(\hat{\boldsymbol{\varepsilon}}^{(r)},\mathbb{C}_0^{(r)}\right)\right] \tag{I .41}$$

The stationary condition w.r.t $\hat{\boldsymbol{\varepsilon}}^{(r)}$ in (IV .18) reads

$$\frac{\partial W^{(r)}}{\partial \boldsymbol{\varepsilon}}\left(\hat{\boldsymbol{\varepsilon}}^{(r)}\right) - \frac{\partial W^{(r)}}{\partial \boldsymbol{\varepsilon}}\left(\boldsymbol{\varepsilon}^{(r)}\right) = \mathbb{C}_0^{(r)} : \left(\hat{\boldsymbol{\varepsilon}}^{(r)} - \boldsymbol{\varepsilon}^{(r)}\right) \tag{I .42}$$

which can be interpreted as a generalized secant condition. From the general formulation (I .40), the following three estimates can be obtained.

a) Case of $\boldsymbol{\varepsilon}^{(r)} = \mathbf{0}$

By setting the tensor $\boldsymbol{\varepsilon}^{(r)} = \mathbf{0}$ in Eq.(I .37), the optimality condition on $\hat{\boldsymbol{\varepsilon}}$ in the variational principle (Eq. (I .38)) is equal to the variational principle of Castañeda (1991). In this case, the stationary condition (I .42) yields

$$\frac{\partial W^{(r)}}{\partial \boldsymbol{\varepsilon}}\left(\hat{\boldsymbol{\varepsilon}}^{(r)}\right) = \mathbb{C}_0^{(r)} : \hat{\boldsymbol{\varepsilon}}^{(r)} \tag{I .43}$$

where $\mathbb{C}_0^{(r)}$ is the secant modulus computed in $\hat{\boldsymbol{\varepsilon}}$ as demonstrated in Section 2.2.2.

b) Case of $\boldsymbol{\varepsilon}^{(r)} = \hat{\boldsymbol{\varepsilon}}^{(r)}$

By taking $\boldsymbol{\varepsilon}^{(r)} = \hat{\boldsymbol{\varepsilon}}^{(r)}$ in Eq.(I .42), implying the function $V^{(r)}$ vanish. Then the stationarity condition w.r.t. $\boldsymbol{\varepsilon}^{(r)}$ in (I .40) yields

$$\left(\mathbb{C}_{tan}^{(r)} - \mathbb{C}_0^{(r)}\right) : \left(\langle\boldsymbol{\varepsilon}\rangle_r - \boldsymbol{\varepsilon}^{(r)}\right) = \mathbf{0} \tag{I .44}$$

This condition is satisfied for $\boldsymbol{\varepsilon}^{(r)} = \hat{\boldsymbol{\varepsilon}}^{(r)} = \langle\boldsymbol{\varepsilon}\rangle_r$. However, in general the stationary condition on $\mathbb{C}^{(r)_0}$ cannot be enforced. For this issue, (Castañeda, 1996) proposed an approach to set $\mathbb{C}_0^{(r)} = \mathbb{C}_{tan}^{(r)}$, which yields the so-called second-order estimate

$$\bar{W} = \sum_{r=1}^{N} c_r \left(W^{(r)}(\boldsymbol{E}) + \frac{1}{2}\frac{\partial W^{(r)}}{\partial \boldsymbol{\varepsilon}}\left(\langle\boldsymbol{\varepsilon}_r\rangle\right) : \left(\bar{\boldsymbol{\varepsilon}} - \langle\boldsymbol{\varepsilon}_r\rangle\right)\right) \tag{I .45}$$

c) Case of $\boldsymbol{\varepsilon}^{(r)} \neq \hat{\boldsymbol{\varepsilon}}^{(r)}$

Most general estimates were obtained in the framework with the choice of $\boldsymbol{\varepsilon}^{(r)} \neq \hat{\boldsymbol{\varepsilon}}^{(r)}$. In this case, the nonlinear response is approximated by a linear interpolation between the two reference strains. The stationary condition on $\mathbb{C}_0^{(r)}$ is regarded to involve field fluctuations about the reference strain $\boldsymbol{\varepsilon}^{(r)}$ via the covariance tensor (Ponte Castaneda, 2002)

$$\left(\hat{\boldsymbol{\varepsilon}}^{(r)} - \boldsymbol{\varepsilon}^{(r)}\right) \otimes \left(\hat{\boldsymbol{\varepsilon}}^{(r)} - \boldsymbol{\varepsilon}^{(r)}\right) = \frac{2}{c_r} \frac{\partial \bar{W}_0}{\partial \mathbb{C}_0^{(r)}} = \left\langle \left(\boldsymbol{\varepsilon} - \boldsymbol{\varepsilon}^{(r)}\right) \otimes \left(\boldsymbol{\varepsilon} - \boldsymbol{\varepsilon}^{(r)}\right) \right\rangle_r \tag{I .46}$$

It is noted that the estimate (IV .18) must still be optimized w.r.t. the reference strains $\boldsymbol{\varepsilon}^{(r)}$. However, as all stationarity conditions cannot be simultaneously satisfied, and additional approximations must be introduced (Castañeda, 2002b).

2.2.4 Incremental variational approach of Lahellec and Suquet (2007b)

In the framework of Generalized Standard Materials, the local behavior of the composites can be described by a free energy and a dissipation function

$$\psi^{(r)}\left(\underline{z}, \boldsymbol{\varepsilon}, \boldsymbol{\alpha}\right) = \sum_{r=1}^{N} \mathcal{H}^{(r)}\left(\underline{z}\right) \psi^{(r)}\left(\boldsymbol{\varepsilon}, \boldsymbol{\alpha}\right), \qquad \phi\left(\underline{z}, \dot{\boldsymbol{\alpha}}\right) = \sum_{r=1}^{N} \mathcal{H}^{(r)}\left(\underline{z}\right) \phi\left(\dot{\boldsymbol{\alpha}}\right) \tag{I .47}$$

with

$$\psi^{(r)}\left(\boldsymbol{\varepsilon}, \boldsymbol{\alpha}\right) = \frac{1}{2}\left(\boldsymbol{\varepsilon} - \boldsymbol{\alpha}\right) : \mathbb{C}^{(r)} : \left(\boldsymbol{\varepsilon} - \boldsymbol{\alpha}\right) \tag{I .48}$$

$$\phi\left(\dot{\boldsymbol{\alpha}}\right) = f^{(r)}\left(\dot{\alpha}_{eq}^2\right), \quad \text{with } \dot{\alpha}_{eq} = \sqrt{\frac{2}{3}\dot{\boldsymbol{\alpha}} : \dot{\boldsymbol{\alpha}}} \tag{I .49}$$

where the function $f^{(r)}$ is supposed to concave w.r.t. its argument.

By adopting an incremental variational framework, the local stress-strain relation is derived from a single potential

$$\boldsymbol{\sigma}_{n+1} = \frac{\partial W_\Delta}{\partial \boldsymbol{\varepsilon}}\left(\boldsymbol{\varepsilon}_{n+1}\right) \tag{I .50}$$

where the condensed incremental potential is the solving of the following the minimization problem

$$W_\Delta\left(\underline{z}, \boldsymbol{\varepsilon}_{n+1}\right) = \inf_{\boldsymbol{\alpha}} J_\Delta\left(\underline{z}, \boldsymbol{\varepsilon}_{n+1}, \boldsymbol{\alpha}_{n+1}\right) \tag{I .51}$$

with

$$J_\Delta\left(\underline{z}, \boldsymbol{\varepsilon}_{n+1}, \boldsymbol{\alpha}_{n+1}\right) = \psi^{(r)}\left(\underline{z}, \boldsymbol{\varepsilon}_{n+1}, \boldsymbol{\alpha}_{n+1}\right) - \psi^{(r)}\left(\underline{z}, \boldsymbol{\varepsilon}_n, \boldsymbol{\alpha}_n\right) + \Delta t \phi\left(\underline{z}, \frac{\boldsymbol{\alpha}_{n+1} - \boldsymbol{\alpha}_n}{\Delta t}\right) \tag{I .52}$$

The effective incremental potential of the composites

$$\bar{W}_\Delta\left(\boldsymbol{E}\right) = \inf_{\boldsymbol{\varepsilon} \in \mathcal{R}(\boldsymbol{E})} \left\langle W_\Delta\left(\underline{z}, \boldsymbol{\varepsilon}\right) \right\rangle = \inf_{\boldsymbol{\varepsilon} \in \mathcal{R}(\boldsymbol{E})} \left\langle \inf_{\boldsymbol{\alpha}} J_\Delta\left(\underline{z}, \boldsymbol{\varepsilon}, \boldsymbol{\alpha}\right) \right\rangle \tag{I .53}$$

Inspiring from the variational procedure of Castañeda (2002b) , Lahellec and Suquet (2007b) introduced an energy J_0 (that for the linear comparison composite) which is more amenable to homogenization. For viscoelastic comparison composite, the phase potentials J_0 yields

$$J_0^{(r)}(\boldsymbol{\varepsilon},\boldsymbol{\alpha}) = w^{(r)}(\boldsymbol{\varepsilon},\boldsymbol{\alpha}) - w_n^{(r)} + \frac{\eta_0^{(r)}}{\Delta t}\left(\boldsymbol{\alpha}-\boldsymbol{\alpha}_n^{(r)}\right) : \left(\boldsymbol{\alpha}-\boldsymbol{\alpha}_n^{(r)}\right) \tag{I .54}$$

where $\eta_0^{(r)}$ and $\boldsymbol{\alpha}_n^{(r)}$ are uniform in phase r. In this context, the difference $\Delta J = J - J_0$ can still beestimated.

Then, the homogenizaiton problem , can be rewritten as

$$\bar{W}_\Delta(\boldsymbol{E}) = \inf_{\boldsymbol{\varepsilon}\in\mathcal{R}(\boldsymbol{E})}\left\langle \inf_{\boldsymbol{\alpha}}\left[J_0(\underline{z},\boldsymbol{\varepsilon},\boldsymbol{\alpha}) + \Delta J(\underline{z},\boldsymbol{\varepsilon},\boldsymbol{\alpha})\right]\right\rangle \tag{I .55}$$

and satisfies

$$\bar{W}_\Delta(\boldsymbol{E}) \leq \inf_{\boldsymbol{\varepsilon}\in\mathcal{R}(\boldsymbol{E})}\left[\left\langle \inf_{\boldsymbol{\alpha}} J_0(\underline{z},\boldsymbol{\varepsilon},\boldsymbol{\alpha})\right\rangle + \left\langle \sup_{\boldsymbol{\alpha}} \Delta J(\underline{z},\boldsymbol{\varepsilon},\boldsymbol{\alpha})\right\rangle\right] \tag{I .56}$$

Following recommendations of Castañeda (1991, 1992) , Lahellec and Suquet (2007b) proposed the following estimate

$$\bar{W}_\Delta(\boldsymbol{E}) \simeq \inf_{\boldsymbol{\varepsilon}\in\mathcal{R}(\boldsymbol{E})}\left[\left\langle \inf_{\boldsymbol{\alpha}} J_0(\underline{z},\boldsymbol{\varepsilon},\boldsymbol{\alpha})\right\rangle + \langle \mathrm{stat}_{\boldsymbol{\alpha}}\Delta J(\underline{z},\boldsymbol{\varepsilon},\boldsymbol{\alpha})\rangle\right] \tag{I .57}$$

3 Review of homogenization of cracked materials

Most rock-like materials are subjected to oriented nucleation and propagation of micro-cracks. The induced damage of micro-cracks effects not only mechanical but also transport properties of rock-like materials. In the present work, we propose to develop a micro-mechanical approach for the description of induced damage in initially isotropic materials. This approach will be based on the reference solution of Eshelby for inclusion problems Eshelby (1957a). Induced micro-cracks will be seen as spheroidal inclusions embedded in a solid matrix. The effective elastic properties of cracked materials will be determined using linear homogenization procedures which is combined with a irreversible thermodynamics framework for the description of damage evolution.

The determination of effective properties of a heterogeneous material through a homogenization procedure is generally carried out on a representative element volume (REV), as shown in Figure I .3, which occupies the geometric domain Ω and is limited by its external boundary surface $\partial\Omega$. For the sake of simplicity but without loosing the generality, the cracked material will be represented by a crack-matrix system. An elastic solid matrix with elastic tensor $\mathbb{C}_s$ which is weakened by a family of parallel penny shaped micro-cracks

with elastic tensor $\mathbb{C}_{f,r}$. In such a representation, each family of micro-cracks is seen as a phase of inclusions embedded in the matrix phase. The cracked material is a two-phase composite with a crack-matrix system.

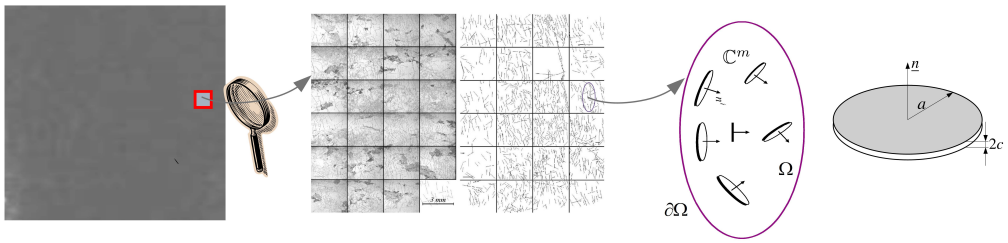

(a) Macroscale (b) Microscale (c) REV

Figure I .3: Representative elementary volume (REV) of microcracked solids

3.1 Effective elastic property of cracked materials

In order to determine the effective elastic property of the above described REV, suitable boundary conditions should be prescribed on the external boundary $\partial\Omega$. In conventional homogenization process Ponte-Castaneda and Willis (1995), we can adopt either the uniform stress boundary condition or the uniform strain boundary condition reviewed in Section II .11.

By adopting the uniform strain boundary condition, the crucial step of homogenization method consists in finding a fourth-order localization tensor $\mathbb{A}(\underline{z})$ which relates the microscopic strain field $\boldsymbol{\varepsilon}$ to the macroscopic strain $\boldsymbol{E}$.

$$\boldsymbol{\varepsilon} = \mathbb{A}(\underline{z}) : \boldsymbol{E} \qquad (\forall \underline{z} \in \Omega) \tag{I .58}$$

Note that the concentration tensor satisfies the condition $\langle \mathbb{A}(\underline{z}) \rangle = \mathbb{I}$, due to the fact that the average of microscopic strain is equal to the macroscopic strain, see I .8. $\mathbb{I}$ denotes the fourth order unit tensor: $\mathbb{I} = \frac{1}{2}(\boldsymbol{\delta}_{ik}\boldsymbol{\delta}_{jl} + \boldsymbol{\delta}_{il}\boldsymbol{\delta}_{jk})$ with $\boldsymbol{\delta}_{ij}$ the Kronecher's symbol.

By using the local elastic law and making the averaging of the local stress field, the following macroscopic elastic stress-strain relation is obtained

$$\boldsymbol{\Sigma} = \mathbb{C}^{\text{hom}} : \boldsymbol{E} \quad \text{with} \quad \mathbb{C}^{\text{hom}} = \langle \mathbb{C}_s : \mathbb{A} \rangle \tag{I .59}$$

where $\mathbb{C}^{\text{hom}}$ denotes the effective macroscopic elastic stiffness tensor of the homogenized material. Due to the fact that the local strain field is not uniform inside each inclusion phase, the volume averaging operation in the above relation is generally difficult to perform

and cannot be performed analytically. Therefore, for the sake of simplicity, it is generally assumed that the local strain field in each inclusion phase r can be represented by its constant average value. Accordingly, only the constant average of strain localization tensor $\mathbb{A}_r$ needs to be determined for each phase r. For a heterogeneous materials containing $\mathcal{N}$ phases of inclusions, the effective elastic stiffness is given by:

$$\mathbb{C}^{\text{hom}} = \sum_{r=1}^{N} \varphi_r \mathbb{C}_r : \mathbb{A}_r \tag{I .60}$$

where φ_r is the volume fraction of the phase r.

With the condition $\langle \mathbb{A}(\underline{x}) \rangle = \mathbb{I}$ and by denoting the elastic stiffness of the solid matrix by $\mathbb{C}_s$ and that of the inclusion phase r by $\mathbb{C}_{f,r}$, the effective elastic stiffness tensor can also be written in the following form:

$$\mathbb{C}^{\text{hom}} = \mathbb{C}_s + \sum_{r=1}^{N} \varphi_{f,r} (\mathbb{C}_{f,r} - \mathbb{C}_s) : \mathbb{A}_{f,r} \tag{I .61}$$

The determination of concentration tensor $\mathbb{A}_{f,r}$ for each phase r depends on the homogenization scheme used. Physically this is related to how the effects of crack interaction and spatial distribution are taken into into account. The well-known solutions to Eshelby's inclusion problem provide fundamentals for determination of such concentration tensors, Eshelby (1961, 1957a); Mori and Tanaka (1973b); Ponte Castañeda and Suquet (1997). The basic solution of $\mathbb{A}_{f,r}$ is written as

$$\mathbb{A}_{f,r} = [\mathbb{I} + \mathbb{P}^r_\epsilon : (\mathbb{C}_{f,r} - \mathbb{C}_s)]^{-1} = [\mathbb{I} - \mathbb{S}^r_\epsilon : (\mathbb{I} - \mathbb{S}_s : \mathbb{C}_{f,r})]^{-1} \tag{I .62}$$

which $\mathbb{S}^r_\epsilon$ is the Eshelby tensor corresponding to the rth family of micro-cracks and $\mathbb{S}^r_\epsilon$ is related to the Hill tensor $\mathbb{P}^r_\epsilon$ such as: $\mathbb{S}^r_\epsilon = \mathbb{P}^r_\epsilon : \mathbb{C}_s$. Therefore, the Hill tensor depends on the geometry of micro-cracks and the elastic properties of solid matrix. Here, it is worth to mention that for the case of initially isotropic matrix, the Eshelby tensor or Hill tensor has analytical solution for penny shaped micro-cracks Zhu (2006).

Here we will review three widely used schemes: Dilute scheme, Mori-Tanaka (MT) scheme and Ponte-Castaneda and Willis (PCW) scheme.

3.2 Dilute scheme

In the case of inclusions with low concentration, we consider simply that there is no interaction between different families of micro-cracks, which implies that all families of micro-cracks are independent from each other. The effective elastic stiffness tensor is then

reduced to:

$$\mathbb{C}^{\text{hom}} = \mathbb{C}_s + \sum_{r=1}^{N} \varphi_{f,r}(\mathbb{C}_{f,r} - \mathbb{C}_s) : [\mathbb{I} + \mathbb{P}_\epsilon^r : (\mathbb{C}_{f,r} - \mathbb{C}_s)]^{-1} \tag{I .63}$$

On the other hand, the effective elastic properties of cracked materials are also dependent on opening or closure state of micro-cracks. Three situations can be distinguished. For the case of open cracks, there is the cancellation of local stress on the crack faces. The elastic tensor of cracks then vanishes, $\mathbb{C}_{f,r} = 0$. For closed frictionless cracks, the idea introduced by (Deude et al. (2002)) consist in modelling the planar cracks as a fictitious elastic material with an elastic tensor $\mathbb{C}_{f,r} = 3k_s\mathbb{J}$, k_s being the bulk modulus of the isotropic solid matrix. This choice is justified by the need to take into account for the nullity of the tangential stress on the closed crack lips and the continuity of stress in the normal direction to cracks lips. In the last case of closed frictional cracks, we assume that the friction is large enough so that the crack lips are fully glued. Therefore, one gets $\mathbb{C}_{f,r} = \mathbb{C}_s$.

a) Case of open cracks:

By putting $\mathbb{C}_{f,r} = 0$ in (I .63), one obtains:

$$\mathbb{C}^{\text{hom}} = \mathbb{C}_s : [\mathbb{I} - \sum_{r=1}^{N} \varphi_{f,r}(\mathbb{I} - \mathbb{P}_\epsilon^r : \mathbb{C}_s)^{-1}] \tag{I .64}$$

The main difficulty for the calculation of $\mathbb{C}^{hom}$ lies in the fact that $(\mathbb{I} - \mathbb{P}_\epsilon^r : \mathbb{C}_s)^{-1}$ is singular when the aspect ratio ϵ tends to 0. In this context, the volume fraction of cracks $\varphi_{f,r}$ is expressed as:

$$\varphi_{f,r} = \frac{4}{3}\pi a^2 c\mathcal{N}_r = \frac{4}{3}\pi\epsilon d_r \tag{I .65}$$

where $\mathcal{N}_r$ denotes the number of cracks per unit volume of a family of cracks and $d_r = \mathcal{N}_r a^3$ is the crack density parameter. It is well known that when the aspect ratio ϵ tends to zero, the concentration tensor admits a limit value. The homogenized effective elasticity tensor can be also written as:

$$\mathbb{C}^{\text{hom}} = \mathbb{C}_s : [\mathbb{I} - \frac{4}{3}\pi \sum_{r=1}^{N} d_r\epsilon(\mathbb{I} - \mathbb{P}_\epsilon^r : \mathbb{C}_s)^{-1}] \tag{I .66}$$

where we denoted $\mathbb{T}^r = \epsilon(\mathbb{I} - \mathbb{P}_\epsilon^r : \mathbb{C}_s)^{-1}$. It follows that the homogenized elasticity tensor can be written as:

$$\mathbb{C}^{\text{hom}} = \mathbb{C}_s : [\mathbb{I} - \frac{4}{3}\pi \sum_{r=1}^{N} d_r\mathbb{T}^r] \ , \quad \text{with} \quad \mathbb{T}^r = \lim_{\epsilon\to 0} \epsilon(\mathbb{I} - \mathbb{P}_\epsilon^r : \mathbb{C}_s)^{-1} \tag{I .67}$$

Note that the expression (I .67) of the effective elastic stiffness tensor is valid not only for isotropic but also anisotropic solid matrix. The difference lies in the calculation of Hill's tensor.

b) Case of closed frictionless cracks:

As mentioned above, it is assumed that the tangential stiffness of cracks vanishes while the normal stiffness takes the value of solid matrix, that is $k_f = k_s$ and $\mu_f = 0$. Thus, one takes for the elastic tensor of cracks $\mathbb{C}_{f,r} = 3k_s\mathbb{J}$. As a consequence, the effective elastic stiffness tensor with an initially isotropic matrix is given by:

$$\mathbb{C}^{\text{hom}} = \mathbb{C}_s : [\mathbb{I} - \frac{4}{3}\pi \sum_{r=1}^{N} d_r \epsilon \mathbb{K} : (\mathbb{I} - \mathbb{P}^r_\epsilon : \mathbb{C}_s : \mathbb{K})^{-1}] \tag{I .68}$$

where: $\mathbb{C}_{f,r} - \mathbb{C}_s = -2\mu_s\mathbb{K} = -\mathbb{C}_s : \mathbb{K}$.

For low cracks aspect ratio $\epsilon \to 0$, the tensor $\mathbb{T}'^r = \epsilon\mathbb{K} : (\mathbb{I} - \mathbb{P}^r_\epsilon : \mathbb{C}_s : \mathbb{K})^{-1}$ tends to its limit. It follows that:

$$\mathbb{C}^{\text{hom}} = \mathbb{C}_s : [\mathbb{I} - \frac{4}{3}\pi \sum_{r=1}^{N} d_r \mathbb{T}'^r] \ , \quad \text{with} \quad \mathbb{T}'^r = \lim_{\epsilon \to 0} \epsilon\mathbb{K} : (\mathbb{I} - \mathbb{P}^r_\epsilon : \mathbb{C}_s : \mathbb{K})^{-1} \tag{I .69}$$

3.3 Mori-Tanaka scheme estimations

To overcome the limitations of the dilute scheme, Mori and Tanaka Mori and Tanaka (1973a) proposed a homogenization method to deal with interactions between inclusions in composite materials. It has been applied to micro-cracked materials in Benveniste (1986).

The idea in Mori-Tanaka scheme to take into account interactions between cracks consists in considering an intermediate prescribed macroscopic strain $\boldsymbol{E}^0$ on the external boundary of the RVE, instead of the remote macroscopic strain $\boldsymbol{E}$. For this new problem, the relation (I .62) is written:

$$\boldsymbol{\varepsilon}_r = [\mathbb{I} + \mathbb{P}^r_\epsilon : (\mathbb{C}_{f,r} - \mathbb{C}_s)]^{-1} : \boldsymbol{E}^0 \tag{I .70}$$

The use of the relation $\langle \boldsymbol{\varepsilon} \rangle_\Omega = \boldsymbol{E}$ leads to:

$$\boldsymbol{E}^0 = [\varphi_s \mathbb{I} + \sum_{j=1}^{N} \varphi_{f,j} [\mathbb{I} + \mathbb{P}^j_\epsilon : (\mathbb{C}_{r,j} - \mathbb{C}_s)]^{-1}]^{-1} : \boldsymbol{E} \tag{I .71}$$

from where it deduces the strain concentration rule (I .58) for the Mori-Tanaka scheme with:

$$\mathbb{A}_{f,r} = [\mathbb{I} + \mathbb{P}^r_\epsilon : (\mathbb{C}_{f,r} - \mathbb{C}_s)]^{-1} : [\varphi_s \mathbb{I} + \sum_{j=1}^{N} \varphi_{f,j} [\mathbb{I} + \mathbb{P}^j_\epsilon : (\mathbb{C}_{f,j} - \mathbb{C}_s)]^{-1}]^{-1} \tag{I .72}$$

The substitution of equation (I .72) into (I .61) allows to deduce the expression of the effective elasticity tensor corresponding to the MT scheme:

$$\begin{aligned}\mathbb{C}^{\mathrm{MT}} &= \mathbb{C}_s + \sum_{r=1}^{N} \varphi_{f,r}(\mathbb{C}_{f,r} - \mathbb{C}_s) \\ &: [\mathbb{I} + \mathbb{P}_\epsilon^r : (\mathbb{C}_{f,r} - \mathbb{C}_s)]^{-1} : [\varphi_s \mathbb{I} + \sum_{j=1}^{N} \varphi_{f,j}[\mathbb{I} + \mathbb{P}_\epsilon^j : (\mathbb{C}_{f,j} - \mathbb{C}_s)]^{-1}]^{-1}\end{aligned} \tag{I .73}$$

This general result can be applied to open and closed micro-cracks.

a) Case of open cracks: $(\mathbb{C}_{f,r} = 0)$

$$\mathbb{C}^{\mathrm{hom}} = \mathbb{C}_s - \sum_{r=1}^{N} \varphi_{f,r}\mathbb{C}_s : (\mathbb{I} - \mathbb{S}_\epsilon^r)^{-1} : [\varphi_s \mathbb{I} + \sum_{j=1}^{N} \varphi_{f,j}(\mathbb{I} - \mathbb{S}_\epsilon^j)]^{-1} \tag{I .74}$$

We recall that $\mathbb{S}_\epsilon = \mathbb{P}_\epsilon : \mathbb{C}_s$ is the Eshelby's tensor corresponding to one family of crack. Also, (I .74) can be written as:

$$\mathbb{C}^{\mathrm{hom}} = \varphi_s \mathbb{C}_s : [\varphi_s \mathbb{I} + \sum_{j=1}^{N} \varphi_{f,j}(\mathbb{I} - \mathbb{S}_\epsilon^j)^{-1}]^{-1} = \mathbb{C}_s : [\mathbb{I} + \frac{4}{3}\pi \sum_{j=1}^{N} d_j \mathbb{T}^r]^{-1} \tag{I .75}$$

with $\mathbb{T}^r = \lim_{\epsilon \to 0} \epsilon(\mathbb{I} - \mathbb{S}_\epsilon^j)^{-1}$, the quantity φ_s is sensibly equal to 1 as the volume of the cracks being almost zero. The inversion of (I .75) gives the effective elastic compliance tensor $\mathbb{S}^{hom}$ of cracked media:

$$\mathbb{S}^{\mathrm{hom}} = [\mathbb{I} + \frac{4}{3}\pi \sum_{j=1}^{N} d_j \mathbb{T}^r] : \mathbb{S}_s \tag{I .76}$$

b) Case of closed frictionless cracks: $(\mathbb{C}_{f,r} = 3k_s\mathbb{J})$

Considering $\mathbb{C}_{f,r} = 3k_s\mathbb{J}$, one gets for the MT scheme:

$$\mathbb{C}^{\mathrm{hom}} = \mathbb{C}_s - \sum_{r=1}^{N} \varphi_{f,r}\mathbb{C}_s : \mathbb{K} : (\mathbb{I} - \mathbb{S}_\epsilon^j : \mathbb{K})^{-1} : [\varphi_s \mathbb{I} + \sum_{j=1}^{N} \varphi_{f,j}(\mathbb{I} - \mathbb{S}_\epsilon^j : \mathbb{K})^{-1}]^{-1} \tag{I .77}$$

After arrangement of the results, one obtains:

$$\mathbb{C}^{\mathrm{hom}} = \mathbb{C}_s : [\mathbb{I} + \frac{4}{3}\pi \sum_{j=1}^{N} d_j \epsilon(\mathbb{I} - \mathbb{S}_\epsilon^j : \mathbb{K})^{-1}]^{-1} = \mathbb{C}_s : [\mathbb{I} + \frac{4}{3}\pi \sum_{j=1}^{N} d_j \mathbb{T}'^r]^{-1} \tag{I .78}$$

With $\mathbb{T}'^r = \lim_{\epsilon \to 0} \epsilon(\mathbb{I} - \mathbb{S}_\epsilon^j : \mathbb{K})^{-1}$. For the inversion of the above equation, the macroscopic compliance tensor is given by:

$$\mathbb{S}^{\mathrm{hom}} = [\mathbb{I} + \frac{4}{3}\pi \sum_{j=1}^{N} d_j \mathbb{T}'^r]^{-1} : \mathbb{S}_s \tag{I .79}$$

3.4 PCW scheme estimations

For taking into account both interactions between cracks and effects of spatial distribution of micro-cracks, the idea in the Ponte-Castaneda and Willis scheme (Ponte-Castañeda and Willis, 1995) is to consider two independent functions, one associated with the shape of inclusions, the other one associated with the spatial distribution form of inclusions. In the case of considering the same spatial distribution for all of inclusions, the strain concentration tensor can be taken into the form:

$$\begin{aligned}\mathbb{A}^{f,r} &= [\mathbb{I}+\mathbb{P}_\epsilon^r:(\mathbb{C}_{f,r}-\mathbb{C}_s)]^{-1}: \\ &\quad [\mathbb{I}+\textstyle\sum_{j=1}^N \varphi_{f,j}[\mathbb{I}+(\mathbb{P}_\epsilon^j-\mathbb{P}_d):(\mathbb{C}_{f,j}-\mathbb{C}_s)]:[\mathbb{I}+\mathbb{P}_\epsilon^j:(\mathbb{C}_{f,j}-\mathbb{C}_s)]^{-1}]^{-1}\end{aligned} \tag{I .80}$$

where the tensor $\mathbb{P}_\epsilon^r$ is related to the shape of the r^{th} family of cracks while $\mathbb{P}_d$ is the function associated with the spatial distribution of cracks. According to PCW scheme, the general expression of macroscopic elasticity tensor can be written as:

$$\mathbb{C}^{\mathrm{PCW}} = \mathbb{C}^s + (\mathbb{I}-\sum_{r=1}^N \varphi_{f,r}[(\mathbb{C}_{f,r}-\mathbb{C}_s)^{-1}+\mathbb{P}_\epsilon^r]^{-1}:\mathbb{P}_d)^{-1}:\sum_{r=1}^N \varphi_{f,r}[(\mathbb{C}_{f,r}-\mathbb{C}_s)^{-1}+\mathbb{P}_\epsilon^r]^{-1} \tag{I .81}$$

This result can be applied to open and closed micro-cracks by considering different elastic tensor of inclusion phase, as that already discussed for the Dilute and MT schemes.

Chapter II

Homogenization of rock-like materials with plastic matrix based on an incremental variational principle*

A large class of rock-like materials are composed of a plastic solid matrix in which various inclusions and pores are embedded. This paper is devoted to determine macroscopic inelastic responses of such materials by a nonlinear homogenization procedure. The plastic behavior of solid matrix is described by a plastic model based on the pressure-dependent Drucker-Prager criterion. The plastic strain field of solid matrix is divided into a volumetric part and a shear part. Unlike most mean-field methods previously developed, the strain field in the solid matrix is non-uniform and this non-uniform field is taken into account by using an incremental variational model. The whole loading history is divided into a limit number of increment. For the sake of simplicity, the behavior of solid matrix is first assumed to be elastic-perfectly plastic at each loading increment. With the help of a time derivative approximation, the local incremental potential of the solid matrix is deduced. By considering the effect of inclusions and pores, the effective incremental potential of the heterogeneous composite is determined and estimated with the help of a linear comparison material. The macroscopic stress of the composite is finally estimated from the effective incremental potential. The accuracy of the proposed model is assessed by a series of comparisons with reference results obtained from direct finite element simulations respectively

*Submitted to International journal of plasticity

for inclusion-reinforced and porous materials. Finally, by assuming that the general form of incremental variational model remains valid when the solid matrix exhibits isotropic plastic hardening, the proposed model is extended simply by updating the value of frictional coefficient of solid matrix at each loading increment. The proposed model in this case is also well validated by comparisons with finite element reference results. Moreover, as examples of application, the model is used to simulate laboratory tests performed on a cement mortar and a typical porous sandstone.

1 Introduction

In many engineering applications, it is necessary to determine mechanical properties of so-called rock-like materials, such as rocks, hard soils and concretes. This is so far essentially done by developing various phenomenological models including plastic models (Shao and Henry, 1991; Xie and Shao, 2006; Zhang et al., 2013), damage models (Dragon et al., 2000; Shojaei et al., 2014) and coupled models (Chiarelli et al., 2003; Conil et al., 2004; Yuan et al., 2013; Zhou et al., 2013), just to mention a few. These models are generally fitted from macroscopic laboratory tests and can reasonably reproduce main features of mechanical responses of rock-like materials. However, most rock-like materials are heterogeneous materials composed of various mineral phases and pores. Their macroscopic properties are inherently related to local properties of constituent phases and affected by the mineralogical compositions and morphology at different scales. In order to predict macroscopic mechanical responses of these materials in relation with the spatial and temporal change of mineralogical compositions and microscopic structures, constitutive models issued from various homogenization techniques have been developed. Representative examples include (Shen et al., 2012; Zhu et al., 2016).

Let considering a class of materials which are characterized by a solid matrix with embedded mineral inclusions and pores. By adopting a Drucker-Prager type criterion for the solid matrix and by using limit analysis techniques and variational approaches, different analytical criteria have been established for the macroscopic strength of porous materials, for instance (Guo et al., 2008a; Maghous et al., 2009b; Shen et al., 2017, 2015). With a two-step homogenization method, an analytical criterion has been proposed for clayey rocks containing a porous clay matrix at the microscopic scale and mineral grains at the mesoscopic scale (Shen et al., 2013). However, in these analytical models, only one family of pores or inclusions is taken into account. In real materials, several families of mineral grains of different mechanical properties and pores may exist at the same scale. In order

to determine the effective behavior of such materials, semi-analytical models have been developed. Based on a simple extension of elastic materials, the Hill incremental method has first been developed for composite materials (Doghri and Tinel, 2005; Hill, 1965b) and was recently enriched with second-order moments to take into account intra-phase field fluctuations (Doghri et al., 2011). It has also been applied to rock-like materials (Guéry et al., 2008; Shen et al., 2012). In those models based on the Hill incremental method, it relies on a direct linearization of the local stress-strain relation using instantaneous (anisotropic) tangent operator. However, this class of models generally leads to too stiffer macroscopic responses (Chaboche et al., 2005). Some numerical techniques, such as the isotropization of tangent stiffness operator, have been proposed to improve the performance of those models. Nevertheless, those corrective techniques are not physically founded.

Important efforts have been made in nonlinear homogenization methods in order to account for the effect of non-uniform strain fields in constituent phases on effective properties of composite materials. In the models based the Transformation Field Analysis (TFA) originally proposed by Dvorak and Benveniste (1992) for elastic-plastic composites, the local plastic strain field is assumed to be piecewise uniform. The class of models have been applied to various materials but their accuracy is strongly dependent on the number and the arrangement of the piecewise uniform sub-domains. For highly heterogeneous nonlinear materials, a high number of sub-domains is needed to obtain relative satisfactory results, implying a high computational cost. In order to overcome the shortcoming of the TFA based models, the Non-uniform Transformation Field Analysis (NTFA) has been proposed (Michel and Suquet, 2003, 2004). The local plastic strain field is decomposed into a linear combination of a limited number of non-uniform plastic strain modes. This method has been applied to rock-like materials (Jiang et al., 2013). However, it is not an easy task to identify the necessary plastic modes by preliminary full-field simulations.

Starting from variational principles for linear composite materials, an incremental variational method has been proposed for nonlinear composite materials in (Lahellec and Suquet, 2007b,c) in the framework of Generalized Standard Materials (Halphen and Nguyen, 1975). Non-uniform local strain fields are characterized by introducing effective incremental variables (EIV). By using an implicit time-discretization scheme, the local evolution problem is reduced to the minimization of an incremental potential function. This effective incremental variable model was first applied to linear and nonlinear viscoelastic composites (Lahellec and Suquet, 2007b,c) without plastic hardening. The same authors (Lahellec and Suquet, 2013) proposed a rate variational model (RVP) considering the elastic-viscoplastic composites with local threshold, isotropic and linear kinematic hardening.More recently,

the incremental variational formulation has been used for the prediction of the effective behavior of elastic-plastic composites with local plastic threshold and isotropic and/or linear kinematic plastic hardening (Boudet et al., 2016). On the other hand, based on the variational principle established by Ortiz and Stainier (1999), some authors have also proposed another incremental variational procedure for elasto-(visco)plastic composites with local isotropic hardening (Brassart et al., 2011, 2012). However, most previous studies were devoted to composite materials with pressure-independent plastic phases.

In the present study, we shall propose a new incremental variational model for rock-like materials constituted by a plastic matrix in which are embedded elastic inclusions and (or) pores. As the main difference with previous studies for metal materials, the plastic matrix is described by a pressure-dependent Drucker-Prager criterion. As a consequence, the local plastic strain field is decomposed into a volumetric part and a shear part. Further, most rock-like materials generally exhibit plastic hardening. In the case of an isotropic plastic hardening is considered, the hardening of rock-like materials is generally represented by the variation of internal frictional coefficient rather than the evolution of cohesion. However, this kind of plastic hardening renders the analytical formulation of incremental variational model very complex. We propose here a simplified approach. As the whole loading history is divided into a limit number of increments, the behavior of solid matrix is first assumed to be elastic-perfectly plastic for each loading increment. The general formulation of incremental variational model is obtained for this particular case. The proposed model is validated through comparisons with reference results obtained from direct finite element simulations for materials without plastic hardening. Then, we assume that the obtained formulation remains valid when the solid matrix exhibit an isotropic plastic hardening. The model is extended simply by updating the value of frictional coefficient of solid matrix at each loading increment with a specific law. The proposed extended model is verified through comparisons with reference results obtained from direct finite element simulations for materials with an isotropic plastic hardening law. Finally, the proposed extended model is validated against experimental data in some laboratory tests for cement mortar and porous sandstone.

2 Incremental variational principle for matrix-inclusion materials

We consider here a class of rock-like materials which are characterized at the mesoscopic scale by a continuous solid matrix in which mineral grains and pores are randomly

embedded. The Representative Volume Element (RVE) is shown in Figure II .1. The RVE occupies the geometrical domain $\Omega \subset \mathbb{R}^{n_{\text{dim}}}$ ($n_{\text{dim}} = 1, 2, 3$) and has an external boundary $\partial\Omega \subset \mathbb{R}^{n_{\text{dim}}-1}$. The solid matrix occupies the domain $\Omega^m \subset \mathbb{R}^{n_{\text{dim}}}$ and each of N inclusions phases the domain $\Omega^{i,r} \subset \mathbb{R}^{n_{\text{dim}}}$), $r = 1, ..., N$. Pores are here regarded as a special elastic inclusion phase with vanishing stiffness. For the convenience, the total volume of the RVE is denoted by V_Ω, the volume of matrix is V_{Ω^m}, the volume occupied by the inclusion phase r is $V_{\Omega^{i,r}}$. Therefore, the volume fractions of the matrix and the inclusion phase r are respectively defined as

$$f^m = \frac{V_{\Omega^m}}{V_\Omega}; \quad f^{i,r} = \frac{V_{\Omega^{i,r}}}{V_\Omega}, \quad r = 1, ..., N; \tag{II .1}$$

For the sake of clarity, $\langle\cdot\rangle$ denotes a volume average over the whole RVE, $\langle\cdot\rangle_m$ is a volume average over the matrix, and $\langle\cdot\rangle_{i,r}$ is a volume average over the inclusion phase r,:

$$\langle\cdot\rangle = \frac{1}{V_\Omega}\int_{V_\Omega}(\cdot)\,\mathrm{d}V_\Omega = f^m\langle\cdot\rangle_m + \sum_{r=1}^{N} f^{i,r}\langle\cdot\rangle_{i,r} \tag{II .2}$$

with

$$\langle\cdot\rangle_m = \frac{1}{V_{\Omega^m}}\int_{V_{\Omega^m}}(\cdot)\,\mathrm{d}V_{\Omega^m}; \quad \langle\cdot\rangle_{i,r} = \frac{1}{V_{\Omega^{i,r}}}\int_{V_{\Omega^{i,r}}}(\cdot)\,\mathrm{d}V_{\Omega^{i,r}} \tag{II .3}$$

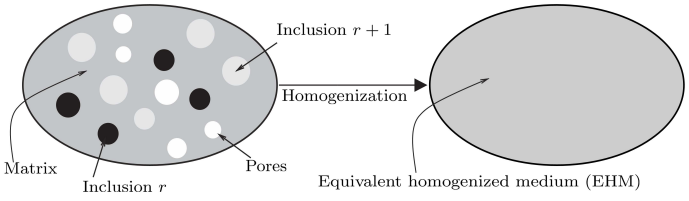

Figure II .1: Representative volume element of general rock-like materials

2.1 Local behavior of solid matrix

The solid matrix exhibits an elastic-plastic behavior. Its elastic stiffness tensor at any point $\underline{x} \in \Omega^m$ is defined by the fourth order tensor $\mathbb{C}^m$. Its elastic-plastic behavior at $\underline{x} \in \Omega^m$ is described by two local potentials, the free energy w^m and the dissipation potential φ^m. Both potentials are convex of the strain tensor $\boldsymbol{\varepsilon}(\underline{x})$, the internal state variables $\boldsymbol{\xi}(\underline{x})$ and their time-derivatives. The thermodynamics conjugate force variables associated with the state variables $\boldsymbol{\varepsilon}$ and $\boldsymbol{\xi}$ are defined by:

$$\boldsymbol{\sigma} = \frac{\partial w^m}{\partial \boldsymbol{\varepsilon}}(\boldsymbol{\varepsilon}, \boldsymbol{\xi}) \tag{II .4a}$$

$$\boldsymbol{F} = -\frac{\partial w^m}{\partial \boldsymbol{\xi}}(\boldsymbol{\varepsilon}, \boldsymbol{\xi}) = \frac{\partial \varphi^m}{\partial \dot{\boldsymbol{\xi}}}\left(\dot{\boldsymbol{\xi}}\right) \tag{II .4b}$$

$\boldsymbol{\sigma}(\underline{x})$ is the local Cauchy stress tensor and $\boldsymbol{F}$ is the conjugate force for plastic hardening.

Based on the previous studies in (Lahellec and Suquet, 2007b; Ortiz and Stainier, 1999), the time derivative $\dot{\boldsymbol{\xi}}$ is here approximated by a difference quotient after use of an implicit Euler-Scheme. The time interval (loading history) of study $[0, T]$ is thus divided into the time (loading) steps $t_0 = 0, t_1, ..., t_n, t_{n+1}, ..., t_N = T$. The time (loading) increment between t_n and t_{n+1} is denoted by Δt. By using this time-discretization procedure, the transformation of Eq. (III .13) leads to the following discretized equations:

$$\boldsymbol{\sigma}_{n+1} = \frac{\partial w^m}{\partial \boldsymbol{\varepsilon}} \left(\boldsymbol{\varepsilon}_{n+1}, \boldsymbol{\xi}_{n+1}\right), \quad \frac{\partial w^m}{\partial \boldsymbol{\xi}} \left(\boldsymbol{\varepsilon}_{n+1}, \boldsymbol{\xi}_{n+1}\right) + \frac{\partial \varphi^m}{\partial \dot{\boldsymbol{\xi}}} \left(\frac{\boldsymbol{\xi}_{n+1} - \boldsymbol{\xi}_n}{\Delta t}\right) = 0 \tag{II .5}$$

It is assumed that all local fields at time t_n are known and they have to be determined at time t_{n+1}. Inspired by Lahellec and Suquet (2007b), we introduce the following local incremental potential J^m, function of local variables $\boldsymbol{\varepsilon}$ and $\boldsymbol{\xi}$ (for the sake of simplicity the subscripts $n+1$ are omitted):

$$J^m \left(\boldsymbol{\varepsilon}, \boldsymbol{\xi}\right) = w^m(\boldsymbol{\varepsilon}, \boldsymbol{\xi}) + \Delta t \varphi^m \left(\frac{\boldsymbol{\xi} - \boldsymbol{\xi}_n}{\Delta t}\right) \tag{II .6}$$

It is found that the second relation in Eq. (II .5) is the Euler-Lagrange equation of the variational problem for the minimization of the local incremental potential with respect to $\boldsymbol{\xi}$. This leads to the following condensed local incremental potential:

$$\pi_\Delta^m \left(\boldsymbol{\varepsilon}\right) = \inf_{\boldsymbol{\xi}} J^m \left(\boldsymbol{\varepsilon}, \boldsymbol{\xi}\right) \tag{II .7}$$

As demonstrated in Lahellec and Suquet (2007b), the local stress field $\boldsymbol{\sigma}$ in the solid matrix can be derived from this sole potential:

$$\boldsymbol{\sigma} = \frac{\partial \pi_\Delta^m}{\partial \boldsymbol{\varepsilon}} \left(\boldsymbol{\varepsilon}\right) \tag{II .8}$$

2.2 Local behavior of mineral inclusions

It is here assumed that all mineral inclusions have a linear elastic behavior. The elastic properties are constant for each inclusion phase r, and defined by the elastic stiffness tensor $\mathbb{C}^{i,r}$. Therefore, the local mechanical behavior of inclusion phase r is entirely defined by the free energy function $w^{i,r}$, which is the sole convex potential of the strain tensor $\boldsymbol{\varepsilon}$. Accordingly, the local incremental potential $\pi_\Delta^{i,r}$ of the inclusion phase r is identical to its free energy function:

$$\pi_\Delta^{i,r} = w^{i,r} \left(\boldsymbol{\varepsilon}\right) = \frac{1}{2} \boldsymbol{\varepsilon} : \mathbb{C}^{i,r} : \boldsymbol{\varepsilon} \tag{II .9}$$

The local stress field $\boldsymbol{\sigma}$ in the inclusion phase r is given by:

$$\boldsymbol{\sigma} = \frac{\partial \pi_\Delta^{i,r}}{\partial \boldsymbol{\varepsilon}} \left(\boldsymbol{\varepsilon}\right) = \mathbb{C}^{i,r} : \boldsymbol{\varepsilon} \tag{II .10}$$

2.3 Effective behavior of matrix-inclusion composite

We assume that the RVE is subjected to a macroscopic strain tensor $\overline{\boldsymbol{\varepsilon}}(t)$. The problem to be solved here is the determination of local strain field $\boldsymbol{\varepsilon}$ or displacement field $\underline{u}$ and stress field $\boldsymbol{\sigma}$ by using the local constitutive models of constituents. By means of the time-discretization procedure, the governing equations of the local problem are given as follows:

$$\left\{\begin{array}{l} \operatorname{div}\boldsymbol{\sigma}_{n+1}=0 \\ \\ \boldsymbol{\sigma}_{n+1}=\frac{\partial\pi_{\Delta}}{\partial\boldsymbol{\varepsilon}_{n+1}}\left(\boldsymbol{\varepsilon}_{n+1}\right) \\ \\ \boldsymbol{\varepsilon}(\underline{x},t)=\left(\nabla\underline{u}(\underline{x},t)+\nabla^{T}\underline{u}(\underline{x},t)\right)/2 \end{array}\right\} \quad \text{for } (\underline{x},t)\in\Omega\times[0,T] \tag{II .11}$$

Further the local displacement field verifies the boundary conditions, i.e. $\underline{u}(\underline{x},t)=\overline{\boldsymbol{\varepsilon}}(t)\cdot\underline{x}$. It can be shown that due to these boundary conditions, the average local strain verifies the following requirement $\langle\boldsymbol{\varepsilon}(\underline{x},t)\rangle=\overline{\boldsymbol{\varepsilon}}\,(t)$.

The incremental potential in the composite $\pi_{\Delta}\left(\underline{x},\boldsymbol{\varepsilon}\right)$ is defined as:

$$\pi_{\Delta}=\left\{\begin{array}{ll} \pi_{\Delta}^{m} & \text{if } \underline{x}\in\Omega^{m} \\ \\ \pi_{\Delta}^{i,r} & \text{if } \underline{x}\in\Omega^{i,r} \end{array}\right. \tag{II .12}$$

By introducing the effective incremental potential Π_{Δ}, the macroscopic stress $\bar{\boldsymbol{\sigma}}$ can be derived as:

$$\bar{\boldsymbol{\sigma}}_{n+1}=\frac{\partial\Pi_{\Delta}}{\partial\overline{\boldsymbol{\varepsilon}}}\left(\overline{\boldsymbol{\varepsilon}}_{n+1}\right) \tag{II .13}$$

The key issue here is the estimation of the effective incremental potential Π_{Δ}. This is done by an optimization operation of the averaging process of local incremental potential with respect to the macroscopic strain:

$$\Pi_{\Delta}\left(\overline{\boldsymbol{\varepsilon}}_{n+1}\right)=\inf_{\langle\boldsymbol{\varepsilon}\rangle=\overline{\boldsymbol{\varepsilon}}_{n+1}}\left\langle\pi_{\Delta}\left(\underline{x},\boldsymbol{\varepsilon}\right)\right\rangle=\inf_{\langle\boldsymbol{\varepsilon}\rangle=\overline{\boldsymbol{\varepsilon}}_{n+1}}\left[f^{m}\left\langle\inf_{\boldsymbol{\xi}}J^{m}\left(\boldsymbol{\varepsilon},\boldsymbol{\xi}\right)\right\rangle_{m}+\sum_{r=1}^{N}f^{i,r}\left\langle w^{i,r}\left(\boldsymbol{\varepsilon}\right)\right\rangle_{i,r}\right] \tag{II .14}$$

The effective incremental potential $\Pi_{\Delta}\left(\overline{\boldsymbol{\varepsilon}}\right)$ is a function of the macroscopic strain $\overline{\boldsymbol{\varepsilon}}$ only. The macroscopic stress given in Eq.(II .13) is thus the conjugate thermodynamic force associated with the macroscopic strain. Further, the macroscopic stress defined here also coincides with the volumetric average of the local stress field over the RVE. However, the determination of the macroscopic stress comes to solving the variational problem (II .14) at each time step, which itself involves a local optimization problem (II .7) with respect

to the internal variables $\boldsymbol{\xi}$ at every position $\underline{x} \in \Omega^m$. Instead of using a computationally-costly numerical full-field solution, an approximate mean-field approach based on Lahellec and Suquet (2007b) will be developed in Section 4 .

3 Determination of local incremental potential for Drucker-Prager matrix

3.1 Determination of dissipation potential φ^m

As mentioned above, the local mechanical behavior of solid matrix is described by an elastic-perfectly plastic model at each loading increment. The plastic deformation is described by an associated plastic model based on the linear Drucker-Prager type criterion. The related constitutive relations are expressed as follows:

$$\left.\begin{array}{l} \dot{\boldsymbol{\varepsilon}} = \mathbb{S}^m : \dot{\boldsymbol{\sigma}} + \dot{\boldsymbol{\varepsilon}}^p, \quad f(\boldsymbol{\sigma}) = \sigma_{eq} + 3\kappa(\sigma_m - c) \leq 0 \\ \dot{\boldsymbol{\varepsilon}}^p = \dot{\gamma}^p \boldsymbol{N}, \quad \boldsymbol{N} = \frac{3}{2}\frac{\boldsymbol{s}}{\sigma_{eq}} + \kappa\boldsymbol{\delta} \\ \boldsymbol{\varepsilon}^p = \boldsymbol{\alpha} + \boldsymbol{\beta}, \quad \boldsymbol{\alpha} = \boldsymbol{\varepsilon}^p : \mathbb{K}, \quad \boldsymbol{\beta} = \boldsymbol{\varepsilon}^p : \mathbb{J} = \beta\boldsymbol{\delta} \end{array}\right\} \tag{II .15}$$

where $\boldsymbol{\sigma}$ and $\boldsymbol{\varepsilon}$ denote the local stress and strain fields in the matrix, with $\sigma_{eq} = \sqrt{\frac{3}{2}\boldsymbol{s} : \boldsymbol{s}}$ being the equivalent shear stress (with $\boldsymbol{s} = \boldsymbol{\sigma} : \mathbb{K}$), and $\sigma_m = \frac{1}{3}\boldsymbol{\sigma} : \boldsymbol{\delta}$ the mean stress. $\boldsymbol{\varepsilon}^p$ is the local plastic strain tensor. The fourth order tensor $\mathbb{S}^m = (\mathbb{C}^m)^{-1}$ is the elastic compliance tensor. The parameter c and κ represent the hydrostatic tensile strength and friction coefficient of the matrix respectively.

The equivalent plastic shear strain γ^p and plastic volumetric strain β are both related to the deviatoric plastic strain tensor by:

$$\dot{\gamma}^p = \sqrt{\frac{2}{3}\dot{\boldsymbol{\alpha}} : \dot{\boldsymbol{\alpha}}} = \dot{\alpha}_{eq}, \ \dot{\beta} = \kappa\dot{\alpha}_{eq}, \quad \text{with} \quad \dot{\boldsymbol{\alpha}} = \mathbb{K} : \dot{\boldsymbol{\varepsilon}}^{\boldsymbol{p}} \tag{II .16}$$

As it is mentioned in Section 2.1, the constitutive relations (II .15) can be formulated with the free-energy density $w^m(\boldsymbol{\varepsilon}, \boldsymbol{\xi})$ and the dissipation potential $\varphi^m\left(\dot{\boldsymbol{\xi}}\right)$. It is noticed that for the perfectly plastic model presented in Eq.(II .15), one gets $\boldsymbol{\xi} = (\boldsymbol{\alpha}, \boldsymbol{\beta})$. The free-energy density $w^m(\boldsymbol{\varepsilon}, \boldsymbol{\xi})$ is expressed as the elastic strain energy density. Assuming that the elastic behavior is independent of irreversible plastic deformation, then $w^m(\boldsymbol{\varepsilon}, \boldsymbol{\xi})$ is written by:

$$w^m(\boldsymbol{\varepsilon}, \boldsymbol{\xi}) = \frac{1}{2}(\boldsymbol{\varepsilon} - \boldsymbol{\alpha} - \boldsymbol{\beta}) : \mathbb{C}^m : (\boldsymbol{\varepsilon} - \boldsymbol{\alpha} - \boldsymbol{\beta}) \tag{II .17}$$

Within the framework of thermodynamics, the local stress tensor is given by:

$$\boldsymbol{\sigma} = \frac{\partial w^m}{\partial \boldsymbol{\varepsilon}}(\boldsymbol{\varepsilon}, \boldsymbol{\alpha}, \boldsymbol{\beta}) = \mathbb{C}^m : (\boldsymbol{\varepsilon} - \boldsymbol{\varepsilon}^p) \tag{II .18}$$

Accordingly, the conjugate thermodynamic forces respectively associated with $\boldsymbol{\alpha}$ and $\boldsymbol{\beta}$ are also reduced:

$$-\frac{\partial w^m}{\partial \boldsymbol{\alpha}}(\boldsymbol{\varepsilon}, \boldsymbol{\alpha}, \boldsymbol{\beta}) = -\frac{\partial w^m}{\partial \boldsymbol{\beta}}(\boldsymbol{\varepsilon}, \boldsymbol{\alpha}, \boldsymbol{\beta}) = \boldsymbol{\sigma} \tag{II .19}$$

On the other hand, the mechanical dissipation $\mathcal{D}$ in this case can be expressed in terms of the conjugate thermodynamic forces as follows (Lemaitre et al., 1993):

$$\mathcal{D}\left(\dot{\boldsymbol{\alpha}}, \dot{\boldsymbol{\beta}}\right) = \boldsymbol{\sigma} : \left(\dot{\boldsymbol{\alpha}} + \dot{\boldsymbol{\beta}}\right) \tag{II .20}$$

Furthermore, $\mathcal{D}$ can conveniently be rewritten in a condensed form which accounts for the constitutive relations: (II .15) and (II .16)

$$\mathcal{D}\left(\dot{\boldsymbol{\alpha}}, \dot{\boldsymbol{\beta}}\right) = \mathcal{D}\left(\dot{\alpha}_{eq}\right) = Y\left(\boldsymbol{N}\right)\dot{\alpha}_{eq} \tag{II .21}$$

where the function Y is defined as

$$Y = \boldsymbol{\sigma} : \boldsymbol{N} = \sigma_{eq} + 3\kappa\sigma_m \tag{II .22}$$

One notices that the expression (II .21) of the mechanical dissipation indicates that the new scalar quantity Y is the conjugate thermodynamic force associated with α_{eq}. Then the evolution law for α_{eq} can be expressed as a kinetic relation between Y and $\dot{\alpha}_{eq}$. Therefore, it can be derived from a dissipation potential $\phi\left(\dot{\alpha}_{eq}\right)$:

$$Y = \frac{\partial \phi}{\partial \dot{\alpha}_{eq}}\left(\dot{\alpha}_{eq}\right) \quad \text{or equivalently} \quad \dot{\alpha}_{eq} = \frac{\partial \phi^*}{\partial Y}\left(Y\right) \tag{II .23}$$

where ϕ^* is the convex dual of ϕ by Legendre transform

$$\phi^*\left(Y\right) = \sup_{\dot{\alpha}_{eq}} \left\{\mathcal{D} - \phi\left(\dot{\alpha}_{eq}\right)\right\} \tag{II .24}$$

By choosing $\phi\left(\dot{\alpha}_{eq}\right)$ non-negative, convex and such that $\phi\left(0\right) = 0$, the mechanical dissipation (II .21) is necessarily positive.

For the constitutive equations given in (II .15), by introducing $\sigma_y = 3c\kappa$, the kinetic relation (II .23) yields

$$\begin{aligned} Y &= \sigma_y \Leftrightarrow \dot{\alpha}_{eq} \geq 0 \\ Y &< \sigma_y \Leftrightarrow \dot{\alpha}_{eq} = 0 \end{aligned} \tag{II .25}$$

In this context, one can write the dissipation potential of the pressure-dependent perfectly plastic matrix $\varphi^m\left(\dot{\boldsymbol{\xi}}\right)$ as follows:

$$\varphi^m\left(\dot{\boldsymbol{\xi}}\right) = \phi\left(\dot{\alpha}_{eq}\right) + \omega_c\left(\dot{\alpha}_{eq}, \dot{\beta}\right) = \sigma_y \dot{\alpha}_{eq} + \omega_c\left(\dot{\alpha}_{eq}, \dot{\beta}\right) \tag{II .26}$$

where $\omega_c\left(\dot{\alpha}_{eq}, \dot{\beta}\right)$ is the indicative function of a convex set C_1

$$\omega_c\left(\dot{\alpha}_{eq}, \dot{\beta}\right) = \begin{cases} 0 & \text{if } \left(\dot{\alpha}_{eq}, \dot{\beta}\right) \in C_1 = \left\{\left(\dot{\alpha}_{eq}, \dot{\beta}\right) | h\left(\dot{\alpha}_{eq}, \dot{\beta}\right) = \kappa\dot{\alpha}_{eq} - \dot{\beta} \leq 0\right\} \\ +\infty & \text{otherwise} \end{cases} \tag{II .27}$$

Since φ^m is not differentiable at $\dot{\alpha}_{eq} = 0$, the partial derivative in (II .23) must be understood in the sense of sub-differential.

Remark 1

The corresponding variation of the free energy is then

$$\delta w^m = \left(\frac{\partial w^m}{\partial \boldsymbol{\varepsilon}^e} : \frac{\partial \boldsymbol{\varepsilon}^e}{\partial\ \boldsymbol{\varepsilon}^p} : \delta\boldsymbol{\varepsilon}^p\right) = -Y\left(\boldsymbol{N}\right)\delta\alpha_{eq} \tag{II .28}$$

Thus, the quantity $Y\left(\boldsymbol{N}\right)\delta\alpha_{eq}$ measures the variation of free energy at constant total deformation for a given variation of α_{eq}.

3.2 Local incremental potential J^m

After introducing the free energy (II .17) and dissipation potential (II .26), the local incremental potential J^m defined in (II .6) for the pressure-dependent plastic matrix can be now written as follows:

$$J^m\left(\boldsymbol{\varepsilon}, \boldsymbol{\alpha}, \boldsymbol{\beta}\right) = w^m(\boldsymbol{\varepsilon}, \boldsymbol{\alpha}, \boldsymbol{\beta}) + \Delta t \varphi^m\left(\frac{\boldsymbol{\alpha} - \boldsymbol{\alpha}_n}{\Delta t}, \frac{\boldsymbol{\beta} - \boldsymbol{\beta}_n}{\Delta t}\right). \tag{II .29}$$

Accordingly, the condensed local incremental potential defined in (II .7) is determined from the optimization of J^m, with respect to $\boldsymbol{\alpha}$ and $\boldsymbol{\beta}$:

$$\pi_\Delta^m\left(\boldsymbol{\varepsilon}\right) = \inf_{\boldsymbol{\alpha}, \boldsymbol{\beta}} J^m\left(\boldsymbol{\varepsilon}, \boldsymbol{\alpha}, \boldsymbol{\beta}\right) \tag{II .30}$$

3.3 Linearization of local incremental potential

In order to extend the EIV model proposed by Lahellec and Suquet (2007b) to rock-like materials with a pressure-dependent perfectly plastic solid matrix, we should linearize the

local incremental potential J^m given in (II .29). On the other hand, compared with the free energy given in Lahellec and Suquet (2007b) for composite materials, the free energy for the materials considered here (II .17) relates to the volumetric plastic strain field $\boldsymbol{\beta}$. In order to take advantage of the main results of Lahellec and Suquet (2007b), the following linearization method is adopted respectively for the free energy density and dissipation potential:

- Linearization of the free energy density $w^m(\boldsymbol{\varepsilon}, \boldsymbol{\alpha}, \boldsymbol{\beta})$ (see the detailed process in Appendix A.)

$$\begin{aligned} w^m(\boldsymbol{\varepsilon}, \boldsymbol{\alpha}, \boldsymbol{\beta}) &\simeq w^m_{lin}(\boldsymbol{\varepsilon},\ \boldsymbol{\alpha}) \\ &= \frac{1}{2}\left(\boldsymbol{\varepsilon} - \boldsymbol{\alpha} - \langle \boldsymbol{\beta}_n \rangle_m - \overline{\overline{\boldsymbol{\alpha} - \boldsymbol{\alpha}_n}}\kappa\boldsymbol{\delta}\right) : \mathbb{C}^m : \left(\boldsymbol{\varepsilon} - \boldsymbol{\alpha} - \langle \boldsymbol{\beta}_n \rangle_m - \overline{\overline{\boldsymbol{\alpha} - \boldsymbol{\alpha}_n}}\kappa\boldsymbol{\delta}\right) \end{aligned} \tag{II .31}$$

- Linearization of the dissipation potential $\varphi^m\left(\dot{\boldsymbol{\alpha}}, \dot{\boldsymbol{\beta}}\right)$. Here we adopt the same quadratic form as that used in Lahellec and Suquet (2007b) and Boudet et al. (2016) related to a linear comparison material, i.e. $\frac{\eta_0}{\Delta t}\left(\boldsymbol{\alpha} - \tilde{\boldsymbol{\alpha}}_n\right) : \left(\boldsymbol{\alpha} - \tilde{\boldsymbol{\alpha}}_n\right)$. In this expression, the scale coefficient η_0 and second-order tensor $\tilde{\boldsymbol{\alpha}}_n$ are both uniform in the matrix.

We here take advantage of the key idea of the variational procedure proposed by Castañeda (1992) and rewrite the local incremental potential as the sum of two terms:

$$\begin{cases} J^m\left(\boldsymbol{\varepsilon}, \boldsymbol{\alpha}, \boldsymbol{\beta}\right) \simeq J_0^m\left(\boldsymbol{\varepsilon}, \boldsymbol{\alpha}\right) + \Delta J^m\left(\boldsymbol{\alpha}, \boldsymbol{\beta}\right) \\ J_0^m\left(\boldsymbol{\varepsilon}, \boldsymbol{\alpha}\right) = \frac{1}{2}\left(\boldsymbol{\varepsilon} - \boldsymbol{\alpha} - \langle \boldsymbol{\beta}_n \rangle_m - \overline{\overline{\boldsymbol{\alpha} - \boldsymbol{\alpha}_n}}\kappa\boldsymbol{\delta}\right) : \mathbb{C}^m : \left(\boldsymbol{\varepsilon} - \boldsymbol{\alpha} - \langle \boldsymbol{\beta}_n \rangle_m - \overline{\overline{\boldsymbol{\alpha} - \boldsymbol{\alpha}_n}}\kappa\boldsymbol{\delta}\right) \\ \qquad\qquad + \frac{\eta_0}{\Delta t}\left(\boldsymbol{\alpha} - \tilde{\boldsymbol{\alpha}}_n\right) : \left(\boldsymbol{\alpha} - \tilde{\boldsymbol{\alpha}}_n\right) \\ \Delta J^m\left(\boldsymbol{\alpha}, \boldsymbol{\beta}\right) = \sigma_y\left(\alpha - \alpha_n\right)_{eq} - \frac{\eta_0}{\Delta t}\left(\boldsymbol{\alpha} - \tilde{\boldsymbol{\alpha}}_n\right) : \left(\boldsymbol{\alpha} - \tilde{\boldsymbol{\alpha}}_n\right) + \Delta t \omega_c\left(\frac{(\alpha - \alpha_n)_{eq}}{\Delta t}, \frac{\beta - \beta_n}{\Delta t}\right) \end{cases} \tag{II .32}$$

4 Optimization of the effective incremental potential

4.1 Estimation of the effective incremental potential $\Pi_\Delta(\bar{\varepsilon})$

Based on the local incremental potential given in the previous section and making the volumetric averaging, the effective incremental potential is expressed as:

$$\Pi_\Delta(\bar{\boldsymbol{\varepsilon}}_{n+1}) = \inf_{\langle\boldsymbol{\varepsilon}\rangle=\bar{\boldsymbol{\varepsilon}}_{n+1}} \left[f^m \left\langle \inf_{\boldsymbol{\alpha},\boldsymbol{\beta},\gamma^p} \left(J_0^m(\boldsymbol{\varepsilon},\boldsymbol{\alpha}) + \Delta J^m(\boldsymbol{\alpha},\boldsymbol{\beta}) \right) \right\rangle_m + \sum_{r=1}^{N} f^{i,r} \left\langle w^{i,r}(\boldsymbol{\varepsilon}) \right\rangle_{i,r} \right] \tag{II .33}$$

One notices that the minimum over $(\boldsymbol{\alpha},\boldsymbol{\beta})$ of (II .33) is attained with the condition of $\omega_c = 0$. Accordingly, the secant function $\eta_{sct}(\dot{\alpha}_{eq})$ of the matrix is defined as

$$\eta_{sct}(\dot{\alpha}_{eq}) = \frac{\phi'(\dot{\alpha}_{eq})}{3\dot{\alpha}_{eq}} = \frac{\sigma_y}{3\dot{\alpha}_{eq}} \tag{II .34}$$

and Eq.(II .33) can be rewritten as

$$\begin{aligned} \Pi_\Delta(\bar{\boldsymbol{\varepsilon}}) &= \inf_{\langle\boldsymbol{\varepsilon}\rangle=\bar{\boldsymbol{\varepsilon}}} \left[f^m \left\langle \inf_{\boldsymbol{\alpha}} \left(J_0^m(\boldsymbol{\varepsilon},\boldsymbol{\alpha}) + \Delta J^m(\boldsymbol{\alpha}) \right) \right\rangle_m + \sum_{r=1}^{N} f^{i,r} \left\langle w^{i,r}(\boldsymbol{\varepsilon}) \right\rangle_{i,r} \right] \qquad \text{(II .35)} \\ &\leq \inf_{\langle\boldsymbol{\varepsilon}\rangle=\bar{\boldsymbol{\varepsilon}}} \left\{ f^m \left[\left\langle \inf_{\boldsymbol{\alpha}} J_0^m(\boldsymbol{\varepsilon},\boldsymbol{\alpha}) \right\rangle_m + \left\langle \sup_{\boldsymbol{\alpha}} \Delta J^m(\boldsymbol{\alpha}) \right\rangle_m \right] + \sum_{r=1}^{N} f^{i,r} \left\langle w^{i,r}(\boldsymbol{\varepsilon}) \right\rangle_{i,r} \right\} \end{aligned}$$

where

$$\Delta J^m(\boldsymbol{\alpha}) = \left[\sigma_y (\boldsymbol{\alpha} - \boldsymbol{\alpha}_n)_{eq} - \frac{\eta_0}{\Delta t} (\boldsymbol{\alpha} - \tilde{\boldsymbol{\alpha}}_n) : (\boldsymbol{\alpha} - \tilde{\boldsymbol{\alpha}}_n) \right] \tag{II .36}$$

The local optimization problem in Eq. (II .35) is now to be performed with respect to the internal variable $\boldsymbol{\alpha}$ only rather than to $(\boldsymbol{\alpha},\boldsymbol{\beta})$ in Eq.(II .30) at every position $\underline{x} \subset \Omega_m$. This largely deduces the complexity of the local optimization problem. The estimates (II .35) of the effective potential $\Pi_\Delta(\bar{\boldsymbol{\varepsilon}})$ for the rock-like materials with the pressure-dependent perfectly plastic matrix without hardening have the same form as that related to nonlinear viscoleastic composites without hardening in Lahellec and Suquet (2007b) .

4.2 Stationarity of the effective incremental potential $\Pi_\Delta(\bar{\varepsilon})$

In order to further simplify the prediction of (II .35) (Lahellec and Suquet, 2007b; Ponte Castaneda, 2002; Ponte Castaneda and Willis, 1999), the estimate of $\Pi_\Delta(\bar{\boldsymbol{\varepsilon}})$ can be obtained by requiring only the stationarity of ΔJ^m with respect to $\boldsymbol{\alpha}$, i.e.,

$$\Pi_\Delta(\bar{\boldsymbol{\varepsilon}}) \simeq \inf_{\langle\boldsymbol{\varepsilon}\rangle=\bar{\boldsymbol{\varepsilon}}} \left\{ f^m \left[\left\langle \inf_{\boldsymbol{\alpha}} J_0^m(\boldsymbol{\varepsilon},\boldsymbol{\alpha}) \right\rangle_m + \left\langle \operatorname*{stat}_{\boldsymbol{\alpha}} \Delta J^m(\boldsymbol{\alpha}) \right\rangle_m \right] + \sum_{r=1}^{N} f^{i,r} \left\langle w^{i,r}(\boldsymbol{\varepsilon}) \right\rangle_{i,r} \right\} \tag{II .37}$$

It is worth noting that ΔJ is here non-quadratic. In order to express the stationarity of ΔJ with respect to $\boldsymbol{\alpha}$, we here consider that the concavity of F yields (Suquet, 1995)

$$\left\langle \Delta J^m(\boldsymbol{\alpha}) \right\rangle_m \leq \left\langle \Delta J'(\boldsymbol{\alpha}) \right\rangle_m = \Delta t F\left(\left\langle \frac{(\boldsymbol{\alpha}-\boldsymbol{\alpha}_n)^2_{eq}}{\Delta t} \right\rangle_m \right) - \left\langle \frac{\eta_0}{\Delta t}(\boldsymbol{\alpha}-\tilde{\boldsymbol{\alpha}}_n) : (\boldsymbol{\alpha}-\tilde{\boldsymbol{\alpha}}_n) \right\rangle_m \tag{II .38}$$

The order relations (II .38) are deduced from the concavity of F which ensures $\left\langle F(\boldsymbol{a}) \right\rangle_m \leq F\left\langle (\boldsymbol{a}) \right\rangle_m$ for any field $\boldsymbol{a}(\underline{x})$. Further, the sationarity of $\left\langle \Delta J'(\boldsymbol{\alpha}) \right\rangle_m$ with respect to $\boldsymbol{\alpha}$ leads to

$$2\eta_p \frac{(\boldsymbol{\alpha}-\boldsymbol{\alpha}_n)}{\Delta t} = 2\eta_0 \frac{(\boldsymbol{\alpha}-\tilde{\boldsymbol{\alpha}}_n)}{\Delta t} \tag{II .39}$$

where η_p is the secant viscosity associated with the perfectly plastic matrix, which is given by:

$$\eta_p = \eta_{sct}\left(\overline{\overline{\dot{\boldsymbol{\alpha}}}}\right) = \frac{\sigma_y}{3\overline{\overline{\dot{\boldsymbol{\alpha}}}}}, \quad \text{with } \overline{\overline{\dot{\boldsymbol{\alpha}}}} = \sqrt{\frac{2}{3}\left\langle \dot{\boldsymbol{\alpha}} : \dot{\boldsymbol{\alpha}} \right\rangle_m} \tag{II .40}$$

The solution of (II .39) gives:

$$\boldsymbol{\alpha} = \frac{\boldsymbol{\alpha}_n - \theta\tilde{\boldsymbol{\alpha}}_n}{1-\theta} \qquad \text{with } \theta = \frac{\eta_0}{\eta_p} \tag{II .41}$$

With this relation, the expression of $\Pi_\Delta(\bar{\boldsymbol{\varepsilon}})$ becomes:

$$\Pi_\Delta(\bar{\boldsymbol{\varepsilon}}) \simeq \Pi_0(\bar{\boldsymbol{\varepsilon}}) + f^m \left\langle \frac{\eta_p \theta}{\Delta t(\theta-1)}(\boldsymbol{\alpha}_n - \tilde{\boldsymbol{\alpha}}_n) : (\boldsymbol{\alpha}_n - \tilde{\boldsymbol{\alpha}}_n) \right\rangle_m \tag{II .42}$$

with

$$\Pi_0(\bar{\boldsymbol{\varepsilon}}) = \inf_{\langle \boldsymbol{\varepsilon} \rangle = \bar{\boldsymbol{\varepsilon}}} \left[f^m \left\langle \inf_{\boldsymbol{\alpha}} J_0^m(\boldsymbol{\varepsilon}, \boldsymbol{\alpha}) \right\rangle_m + \sum_{r=1}^{N} f^{i,r} \left\langle w^{i,r}(\boldsymbol{\varepsilon}) \right\rangle_{i,r} \right] \tag{II .43}$$

By using the stationarity condition over $\tilde{\boldsymbol{\alpha}}_n$ and θ of (II .42), one gets

$$\theta = 1 \pm \sqrt{\frac{\left\langle (\boldsymbol{\alpha}_n - \tilde{\boldsymbol{\alpha}}_n) : (\boldsymbol{\alpha}_n - \tilde{\boldsymbol{\alpha}}_n) \right\rangle_m}{\left\langle (\boldsymbol{\alpha} - \tilde{\boldsymbol{\alpha}}_n) : (\boldsymbol{\alpha} - \tilde{\boldsymbol{\alpha}}_n) \right\rangle_m}} \tag{II .44}$$

$$\tilde{\boldsymbol{\alpha}}_n = \frac{\left\langle \boldsymbol{\alpha}_n \right\rangle_m + (\theta - 1)\left\langle \boldsymbol{\alpha} \right\rangle_m}{\theta} \tag{II .45}$$

By making use of minimization of $J_0^m(\boldsymbol{\varepsilon}, \boldsymbol{\alpha})$ with respect to $\boldsymbol{\alpha}$, one obtains

$$\frac{\partial J_0^m}{\partial \boldsymbol{\alpha}} = -\mathbb{K} : \mathbb{C}^m : (\boldsymbol{\varepsilon}_m - \boldsymbol{\alpha} - \left\langle \boldsymbol{\beta} \right\rangle_m) - \mathbb{C}^m : (\boldsymbol{\varepsilon} - \boldsymbol{\alpha} - \left\langle \boldsymbol{\beta} \right\rangle_m) \frac{\partial \left\langle \boldsymbol{\beta} \right\rangle_m}{\partial \boldsymbol{\alpha}} + 2\frac{\eta_p \theta}{\Delta t}(\boldsymbol{\alpha} - \tilde{\boldsymbol{\alpha}}_n) = 0 \tag{II .46}$$

It is noted that Eq.(II .41) in its field form can be rewritten as

$$\theta(\boldsymbol{\alpha} - \tilde{\boldsymbol{\alpha}}_n) = (\boldsymbol{\alpha} - \boldsymbol{\alpha}_n) \quad \forall \underline{x} \in \Omega_m \tag{II .47}$$

Considering the expressions (II .69) and (II .47), one obtains

$$\frac{\partial \langle \boldsymbol{\beta} \rangle_m}{\partial \boldsymbol{\alpha}} = \frac{2\kappa\theta}{3\Delta t \bar{\bar{\dot{\boldsymbol{\alpha}}}}} \boldsymbol{\delta} \otimes (\boldsymbol{\alpha} - \tilde{\boldsymbol{\alpha}}_n) \tag{II .48}$$

then

$$-\mathbb{C}^m : (\boldsymbol{\varepsilon} - \boldsymbol{\alpha} - \langle \boldsymbol{\beta} \rangle_m) : \frac{\partial \langle \boldsymbol{\beta} \rangle_m}{\partial \boldsymbol{\alpha}} = 2\frac{\eta_{cp}\theta}{\Delta t} (\boldsymbol{\alpha} - \tilde{\boldsymbol{\alpha}}_n) \tag{II .49}$$

with

$$\eta_{cp} = \frac{-3\kappa\sigma_m}{3\bar{\bar{\dot{\boldsymbol{\alpha}}}}}, \quad \sigma_m = \frac{1}{3}\mathbb{C}^m : (\boldsymbol{\varepsilon} - \boldsymbol{\alpha} - \langle \boldsymbol{\beta} \rangle_m) : \boldsymbol{\delta} \tag{II .50}$$

Substituting Eqs. (II .47) and (II .49) for (II .46) leads to

$$\frac{\partial J_0^m}{\partial \boldsymbol{\alpha}} = -\mathbb{K} : \mathbb{C}^m : (\boldsymbol{\varepsilon} - \boldsymbol{\alpha} - \langle \boldsymbol{\beta} \rangle_m) + 2\frac{\eta\theta}{\Delta t} (\boldsymbol{\alpha} - \tilde{\boldsymbol{\alpha}}_n) = 0 \tag{II .51}$$

with

$$\eta = \eta_p + \eta_{cp} = \frac{1}{3\bar{\bar{\dot{\boldsymbol{\alpha}}}}} [\sigma_y - 3\kappa\sigma_m] = -\frac{\kappa (\sigma_m - c)}{\bar{\bar{\dot{\boldsymbol{\alpha}}}}} \tag{II .52}$$

or equivalently, the volume average of the deviatoric stress of the matrix phase

$$\boldsymbol{s}\mathbb{K} : \mathbb{C}^m : (\boldsymbol{\varepsilon} - \boldsymbol{\alpha} - \langle \boldsymbol{\beta} \rangle_m) = 2\frac{\eta}{\Delta t} (\boldsymbol{\alpha} - \boldsymbol{\alpha}_n) = 2\frac{\eta\theta}{\Delta t} (\boldsymbol{\alpha} - \tilde{\boldsymbol{\alpha}}_n) \tag{II .53}$$

Finally, from (II .51), one gets

$$\boldsymbol{\alpha} = \left(\mathbb{C}^m + \frac{2\theta\eta}{\Delta t}\mathbb{K} \right)^{-1} : \left[\mathbb{K} : \mathbb{C}^m : \boldsymbol{\varepsilon} + \frac{2\theta\eta}{\Delta t}\tilde{\boldsymbol{\alpha}}_n \right] = d\mathbb{K} : \boldsymbol{\varepsilon} + e\tilde{\boldsymbol{\alpha}}_n$$

where $d = \frac{\mu}{\frac{\eta\theta}{\Delta t}+\mu}$, $e = \frac{\frac{\eta\theta}{\Delta t}}{\frac{\eta\theta}{\Delta t}+\mu}$.

One notices that η expressed in (II .52) is not uniformed in the matrix due to the non-uniform mean stress field σ_m. For ease of calculation, the average value of η in the matrix phase is here adopted

$$\eta = \langle \eta \rangle_m = -\frac{\kappa (\langle \sigma_m \rangle_m - c)}{\bar{\bar{\dot{\boldsymbol{\alpha}}}}} \tag{II .54}$$

4.3 Choice of a thermoelastic linear comparison composite (LCC)

Substituting the results (II .54) for the expression of $J_0^m(\boldsymbol{\varepsilon}, \boldsymbol{\alpha})$ in (II .32), the local increment potential of the linear comparison composite $\pi_0^m(\boldsymbol{\varepsilon})$ is expressed as:

$$\pi_0^m(\boldsymbol{\varepsilon}) = \inf_{\boldsymbol{\alpha}} J_0^m(\boldsymbol{\varepsilon}, \boldsymbol{\alpha}) = \frac{1}{2}\boldsymbol{\varepsilon} : \mathbb{C}_0^m : \boldsymbol{\varepsilon} + \boldsymbol{\rho}_0^m : \boldsymbol{\varepsilon} + \zeta_0^m \tag{II .55}$$

The tensors $\mathbb{C}_0^m$, $\boldsymbol{\rho}_0^m$ and scale ζ_0^m are all uniform in the matrix phase respectively given by:

$$\begin{cases} \mathbb{C}_0^m = \mathbb{C}^m - \mathbb{C}^m : \mathbb{K} : \left(\mathbb{C}^m + \frac{2\theta\eta}{\triangle t}\mathbb{K}\right)^{-1} : \mathbb{K} : \mathbb{C}^m \\ \boldsymbol{\rho}_0^m = -\frac{2\theta\eta}{\triangle t}\mathbb{C}^m : \left(\mathbb{C}^m + \frac{2\theta\eta}{\triangle t}\mathbb{K}\right)^{-1} : \tilde{\boldsymbol{\alpha}}_n - \mathbb{C}^m : \left(\langle\boldsymbol{\beta}_n\rangle_m + \overline{\overline{\boldsymbol{\alpha} - \boldsymbol{\alpha}_n}}\kappa\boldsymbol{\delta}\right) \\ \zeta_0^m = \frac{\theta\eta}{\triangle t}\tilde{\boldsymbol{\alpha}}_n : \mathbb{C}^m : \left(\mathbb{C}^m + \frac{2\theta\eta}{\triangle t}\mathbb{K}\right)^{-1} : \tilde{\boldsymbol{\alpha}}_n + \frac{1}{2}\left(\langle\boldsymbol{\beta}_n\rangle_m + \overline{\overline{\boldsymbol{\alpha} - \boldsymbol{\alpha}_n}}\kappa\boldsymbol{\delta}\right) : \mathbb{C}^m : \left(\langle\boldsymbol{\beta}_n\rangle_m + \overline{\overline{\boldsymbol{\alpha} - \boldsymbol{\alpha}_n}}\kappa\boldsymbol{\delta}\right) \end{cases} \tag{II .56}$$

In these relations, θ, $\tilde{\boldsymbol{\alpha}}_n$and η are defined in Eqs.(II .44), (II .45) and (II .54), respectively. The effective free energy $\Pi_0(\bar{\boldsymbol{\varepsilon}})$ defined in Eq. (II .43) can be now written as

$$\Pi_0(\bar{\boldsymbol{\varepsilon}}) = \frac{1}{2}\bar{\boldsymbol{\varepsilon}} : \bar{\mathbb{C}} : \bar{\boldsymbol{\varepsilon}} + \bar{\boldsymbol{\rho}} : \bar{\boldsymbol{\varepsilon}} + \bar{\zeta} \tag{II .57}$$

The effective tensors of $\bar{\mathbb{C}}$, $\bar{\boldsymbol{\rho}}$ and scale $\bar{\zeta}$ are expressed in Appendix B.

Substituting the expression of $\Pi_0(\bar{\boldsymbol{\varepsilon}})$ (Eq. (II .57)) for (II .42), one gets the macroscopic stress $\bar{\boldsymbol{\sigma}}$ of the rock composite from the effective incremental potential:

$$\bar{\boldsymbol{\sigma}} = \frac{\partial\Pi_\Delta}{\mathrm{d}\bar{\boldsymbol{\varepsilon}}}(\bar{\boldsymbol{\varepsilon}}) = \frac{\mathrm{d}\Pi_0}{\partial\bar{\boldsymbol{\varepsilon}}}(\bar{\boldsymbol{\varepsilon}}) = f^m\langle\boldsymbol{\sigma}\rangle_m + \sum_{r=1}^{N} f^{i,r}\langle\boldsymbol{\sigma}\rangle_{i,r} = \bar{\mathbb{C}} : \bar{\boldsymbol{\varepsilon}} + \bar{\boldsymbol{\rho}} \tag{II .58}$$

where

$$\langle\boldsymbol{\sigma}\rangle_m = \mathbb{C}_0^m : \langle\boldsymbol{\varepsilon}\rangle_m + \boldsymbol{\rho}_0 \tag{II .59a}$$

$$\langle\boldsymbol{\sigma}\rangle_{i,r} = \mathbb{C}^{i,r} : \langle\boldsymbol{\varepsilon}\rangle_{i,r} \tag{II .59b}$$

One notices that the macroscopic stress obtained above coincides with the volumetric average of local stress field.

5 Computational aspects

5.1 Computation of the first- and second-order moment of $l\alpha$

To calculate the constants θ and $\tilde{\boldsymbol{\alpha}}_n$ defined in Eqs.(II .44) and (II .45), it is needed to calculate the first- and second-order moment of $\boldsymbol{\alpha}$ for the matrix. The first moment is expressed as follows:

$$\langle\boldsymbol{\alpha}\rangle_m = \langle d\mathbb{K} : \boldsymbol{\varepsilon} + e\tilde{\boldsymbol{\alpha}}_n\rangle_m \tag{II .60}$$

Since d, e and $\tilde{\boldsymbol{\alpha}}_n$ are uniform in the matrix phase, one obtains

$$\langle\boldsymbol{\alpha}\rangle_m = d\mathbb{K} : \langle\boldsymbol{\varepsilon}\rangle_m + e : \tilde{\boldsymbol{\alpha}}_n \tag{II .61}$$

On the other hand, the second-order moment of $\boldsymbol{\alpha}$ is expressed by:

$$\langle \boldsymbol{\alpha} : \boldsymbol{\alpha} \rangle_m = d^2 \mathbb{K} :: \langle \boldsymbol{\varepsilon} \otimes \boldsymbol{\varepsilon} \rangle_m + 2de \tilde{\boldsymbol{\alpha}}_n : \langle \boldsymbol{\varepsilon} \rangle_m + e^2 \tilde{\boldsymbol{\alpha}}_n : \tilde{\boldsymbol{\alpha}}_n \tag{II .62}$$

The first and second terms at the right hand side of Eq.(II .62) are related to the second- and first moments of $\boldsymbol{\varepsilon}$ in the matrix. The calculation of these terms is respectively detailed in Eqs.(II .78) and (II .75) in Appendix B.

5.2 Computation of the second-order moment of $\dot{\alpha}$

In order to calculate η by Eq.(II .54), the denominator $\overline{\overline{\dot{\boldsymbol{\alpha}}}}$ related to the second-order moment of $\dot{\boldsymbol{\alpha}}$ should be first determined:

$$\overline{\overline{\dot{\boldsymbol{\alpha}}}} = \sqrt{\frac{2}{3} \langle \dot{\boldsymbol{\alpha}} : \dot{\boldsymbol{\alpha}} \rangle_m} = \frac{1}{\Delta t} \sqrt{\frac{2}{3} \langle (\boldsymbol{\alpha} - \boldsymbol{\alpha}_n) : (\boldsymbol{\alpha} - \boldsymbol{\alpha}_n) \rangle_m} \tag{II .63}$$

However, it is difficult to evaluate the product $\langle (\boldsymbol{\alpha} - \boldsymbol{\alpha}_n) : (\boldsymbol{\alpha} - \boldsymbol{\alpha}_n) \rangle_m$ due to the fact that the term $\langle \boldsymbol{\alpha} : \boldsymbol{\alpha}_n \rangle_m$ cannot be calculated. With the help of Eq.(II .45), $\overline{\overline{\dot{\boldsymbol{\alpha}}}}$ can be calculated through the following relation when $\theta \neq 1$

$$\begin{aligned} \overline{\overline{\dot{\boldsymbol{\alpha}}}} &= \left[\frac{\theta}{\Delta t \, (1-\theta)} \right] \sqrt{\frac{2}{3} \langle (\boldsymbol{\alpha}_n - \tilde{\boldsymbol{\alpha}}_n) : (\boldsymbol{\alpha}_n - \tilde{\boldsymbol{\alpha}}_n) \rangle_m} \\ &= \left[\frac{\theta}{\Delta t \, (1-\theta)} \right] \sqrt{\frac{2}{3} \left(\langle \boldsymbol{\alpha}_n : \boldsymbol{\alpha}_n \rangle_m - 2 \langle \boldsymbol{\alpha}_n \rangle_m : \tilde{\boldsymbol{\alpha}}_n + \tilde{\boldsymbol{\alpha}}_n : \tilde{\boldsymbol{\alpha}}_n \right)} \end{aligned} \tag{II .64}$$

where the first- and second-order moment of $\boldsymbol{\alpha}$ are determined by (II .61)and (II .62), respectively.

5.3 Local implementation algorithm

The local numerical algorithm for determining the macroscopic stress ($\bar{\boldsymbol{\sigma}}_{n+1}$) of the composite is now given. The algorithm is based on a classical elastic predictor/plastic corrector return-mapping scheme. The difference here is that the average values of trial elastic stress in the plastic matrix are used in the yield function. This algorithm is then implemented as an UMAT subroutine in the framework of a the standard finite element code (Abaqus). The RVE of the composite at each Gauss point at the macroscopic scale is subjected to a macroscopic strain $\bar{\boldsymbol{\varepsilon}}_{n+1} = \bar{\boldsymbol{\varepsilon}}_n + \Delta\bar{\boldsymbol{\varepsilon}}$ at t_{n+1} with the prescribed strain increment $\Delta\bar{\boldsymbol{\varepsilon}}$ ($\Delta\bar{\boldsymbol{\varepsilon}} = \dot{\bar{\boldsymbol{\varepsilon}}}\Delta t$). The purpose here is the determination of corresponding macroscopic stress verifying the local constitutive relations. The computational procedure is summarized in Algorithm 3.

Algorithm 1: Flowchart of the local implantation algorithm

Input: $\dot{\bar{\boldsymbol{\varepsilon}}}, \Delta t, \bar{\boldsymbol{\sigma}}_n, \bar{\boldsymbol{\varepsilon}}_n, \langle \boldsymbol{\alpha}_n \rangle_m, \langle \boldsymbol{\beta}_n \rangle_m, \langle \gamma_n^p \rangle_m, \langle \boldsymbol{\alpha}_n : \boldsymbol{\alpha}_n \rangle_m, \theta_n, \eta_n$

Output: $\bar{\boldsymbol{\sigma}}_{n+1}, \bar{\boldsymbol{\varepsilon}}_{n+1}, \langle \boldsymbol{\alpha}_{n+1} \rangle_m, \langle \boldsymbol{\beta}_{n+1} \rangle_m, \langle \gamma_{n+1}^p \rangle_m \langle, \boldsymbol{\alpha}_{n+1} : \boldsymbol{\alpha}_{n+1} \rangle_m, \theta_{n+1}, \eta_{n+1}$

$\bar{\boldsymbol{\varepsilon}}_{n+1} = \bar{\boldsymbol{\varepsilon}}_n + \dot{\bar{\boldsymbol{\varepsilon}}} \Delta t$,

Initialize $\eta_{n+1} = \eta_n, \theta_{n+1} = \theta_n$

Calculate $\mathbb{A}_{n+1}^m$, $\mathbb{A}_{n+1}^{i,r}$, $\boldsymbol{a}_{n+1}^m$, $\boldsymbol{a}_{n+1}^{i,r}$, $\mathbb{C}_{0,n+1}^m$, $\boldsymbol{\rho}_{0n+1}^m$,

Calculate first order moment of strain field $\langle \boldsymbol{\varepsilon}_{n+1} \rangle_m^{trial} = \mathbb{A}_{n+1}^m : \bar{\boldsymbol{\varepsilon}}_{n+1} + \boldsymbol{a}_{n+1}^m$, $\langle \boldsymbol{\varepsilon}_{n+1} \rangle_{i,r}^{trial} = \mathbb{A}_{n+1}^{i,r} : \bar{\boldsymbol{\varepsilon}}_{n+1} + \boldsymbol{a}_{n+1}^{i,r}$,

Elastic prediction: $\langle \boldsymbol{\sigma}_{n+1} \rangle_m^{trial} = \mathbb{C}^m : (\langle \boldsymbol{\varepsilon}_{n+1} \rangle_m^{trial} - \langle \boldsymbol{\alpha}_n \rangle_m - \langle \boldsymbol{\beta}_n \rangle_m)$, substituting $\langle \boldsymbol{\sigma}_{n+1} \rangle_m^{trial}$ into the yield function f in Eq.(II .15).

if $f\left(\langle \boldsymbol{\sigma}_{n+1} \rangle_m^{trial}\right) < 0$ **then**

  $\langle \boldsymbol{\varepsilon}_{n+1} \rangle_m = \langle \boldsymbol{\varepsilon}_{n+1} \rangle_m^{trial}$; $\langle \boldsymbol{\varepsilon}_{n+1} \rangle_{i,r} = \langle \boldsymbol{\varepsilon}_{n+1} \rangle_{i,r}^{trial}$ $\langle \boldsymbol{\alpha}_{n+1} \rangle_m = \mathbf{0}$; $\langle \boldsymbol{\beta}_{n+1} \rangle_m = \mathbf{0}$; $\langle \gamma_{n+1}^p \rangle_m = 0$; $\langle \boldsymbol{\alpha}_{n+1} : \boldsymbol{\alpha}_{n+1} \rangle_m = 0$

else

  (For clarity, the subscript n+1 will be omitted in the *for* loop)

  for $j = 1 \ldots m_{iter}$, **do**

    Calculate $\mathbb{C}_{0,j}^m$, $\boldsymbol{\rho}_{0,j}^m$, $\varsigma_{0,j}^m$ and $\bar{\mathbb{C}}_j$ with Eqs. (II .56) and (II .74a)

    Calculate $\mathbb{A}_j^m$, $\mathbb{A}_j^{i,r}$, $\boldsymbol{a}_j^m$, $\boldsymbol{a}_j^{i,r}$ (with Eq.(II .79) for two-phases composite).

    Calculate first moment of strain field $\langle \boldsymbol{\varepsilon} \rangle_{m,j} = \mathbb{A}_j^m : \bar{\boldsymbol{\varepsilon}} + \boldsymbol{a}_j^m$ and $\langle \boldsymbol{\varepsilon} \rangle_{i,r,j} = \mathbb{A}_j^{i,r} : \bar{\boldsymbol{\varepsilon}} + \boldsymbol{a}_j^{i,r}$ with Eqs.(II .75) and (II .76) ;

    Calculate effective internal variable $\tilde{\boldsymbol{\alpha}}_{n,j}$ and $\langle \boldsymbol{\alpha} \rangle_{m,j}$ with Eqs.(II .45) and (II .61);

    Calculate second moment of strain field $\mathbb{K} :: \langle \boldsymbol{\varepsilon} \otimes \boldsymbol{\varepsilon} \rangle_{m,j}$ and $\langle \boldsymbol{\alpha} : \boldsymbol{\alpha} \rangle_{m,j}$ with Eqs.(II .78) and (II .62);

    Calculate $\overline{\overline{\dot{\boldsymbol{\alpha}}}}_j$, $\langle \boldsymbol{\beta} \rangle_{m,j}$ and $\langle \gamma^p \rangle_{m,j}$ with Eqs.(II .64), (II .69) and (II .70).

    Calculate θ_j and η_j with Eqs.(II .44) and (II .54);

    if $\frac{|\delta\theta_j|}{\theta_j} < \epsilon$ *and* $\frac{|\delta\eta_j|}{\eta_j} < \epsilon$, **then**

      Return;

    else

      $j = j + 1$

    end

  end

  Calculate $\langle \boldsymbol{\sigma}_{n+1} \rangle_m$ and $\langle \boldsymbol{\sigma}_{n+1} \rangle_{i,r}$ by using Eq.(II .59)

  $\bar{\boldsymbol{\sigma}}_{n+1} = \langle \boldsymbol{\sigma}_{n+1} \rangle = f^m \langle \boldsymbol{\sigma}_{n+1} \rangle_m + \sum_{r=1}^N f^{i,r} \langle \boldsymbol{\sigma}_{n+1} \rangle_{i,r}$;

end

6 Numerical assessment

The purpose of this section is to verify the accuracy of the proposed model by comparing its predictions with reference solutions. Two kinds of materials are considered. The

first one is composed of a pressure sensitive Drucker-Prager perfectly plastic matrix in which elastic mineral grains are embedded (Figure II .2(b)). The second one is a porous material with a Drucker-Prager matrix and pores (Figure II .2(c)). In this section and section 7, the effective properties of the LCC as well as the field statistics are evaluated by using the Hashinand Shtrikman bounds, i.e., the HS lower bound for inclusion-reinforced material and upper bound for porous material, more details are given in Appendix C. The reference solutions are obtained by direct simulations on unit cells using the finite element method (FEM). The micro-structure of studied materials is represented by an periodic assembly of 3D unit cells containing spherical inclusions or pores. Taking advantage of axial symmetry, the actual hexagonal cell is approximated by a cylinder one and only half an axial symmetry plain is considered in the FEM calculations, as illustrated in Figure II .2. The macroscopic responses of unit cells are calculated by volumetric averaging (Sun and Vaidya, 1996).

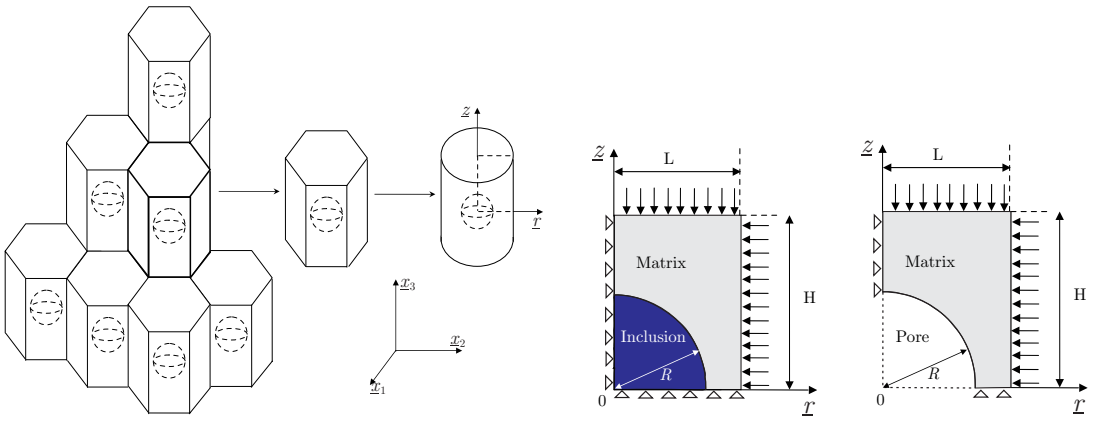

(a) Approximation of 3D hexagonal periodic array material

(b) Inclusion-reinforced material

(c) porous material

Figure II .2: Approximation from 3D hexagonal periodic array with spherical inclusion/pore to axi-symmetric cylinder unit cell

Uniaxial compression tests and conventional triaxial compression tests are here considered for the two types of materials selected here. In each case, the composite material is first subjected to a hydrostatic stress or a confining stress and then to a differential stress by increasing the axial strain in the z direction. During the differential stress stage, the vertical displacement on the top side of the unit cell $\bar{U}_3$ is prescribed with a constant rate. The lateral displacement $\bar{U}_2$ is also kept uniform along the boundary to satisfy the uniform strain boundary condition.

For the inclusion-reinforced material, the material parameters for each phase under

consideration are listed in Tables II .1 and II .2. The volume fraction of inclusion is $f^i = 15\%$. The boundary conditions are illustrated on Figure II .2(b) and summarized as follows:

$$\begin{cases} U_3(r,H) = \bar{U}_3, & 0 < r < L \\ U_2(L,z) = \bar{U}_2, & 0 < z < H \\ U_3(r,0) = 0, & 0 < r < L \\ U_2(0,z) = 0, & 0 < z < H \end{cases} \tag{II .65}$$

Table II .1: Parameters of solid matrix for composite

E^m (MPa)	ν^m	κ	c(MPa)
3000	0.3	0.227	30

Table II .2: Parameters of elastic inclusion

E^i (MPa)	ν^i
98000	0.15

For the porous material, the parameters for the solid matrix are the same as those used for the inclusion-reinforced material and listed in Table II .1. The selected porosity is $f^i = 15\%$. The prescribed boundary conditions on the unit cell are presented below and illustrated in Figure II .2(c):

$$\begin{cases} U_3(r,H) = \bar{U}_3, & 0 < r < L \\ U_2(L,z) = \bar{U}_2, & 0 < z < H \\ U_3(r,0) = 0, & R < r < L \\ U_2(0,z) = 0, & R < z < H \end{cases} \tag{II .66}$$

In Figure II .3, we present the macroscopic stress-strain curves for both the inclusion-reinforced material and porous material under uniaxial and triaxial compression tests with

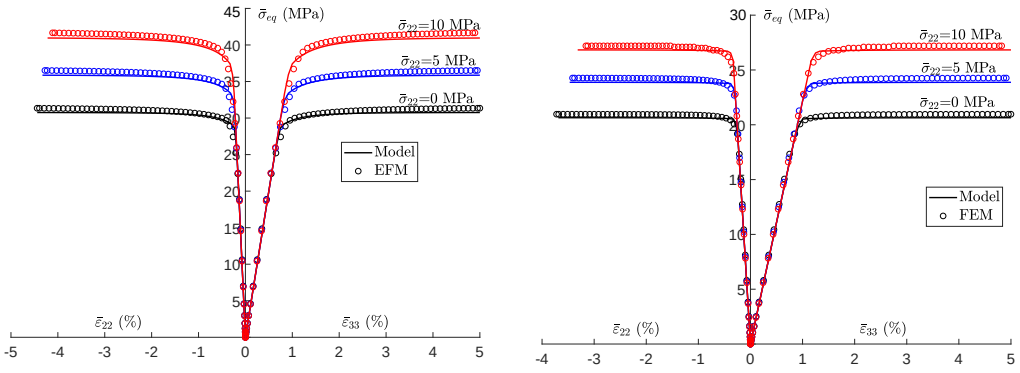

(a) Inclusion-reinforced material (b) Porous material

Figure II .3: Macroscopic predictions for two kinds of composite material with Drucker-Prager perfectly plastic matrix and inclusion/pores ($f^i = 15\%$) under triiaxial compressions with different confining stress

different confining stresses, respectively obtained by the proposed incremental variational model and direct finite element simulations. One can observe that the model's predictions coincide very well with the FEM solutions both for the all cases considered.

7 Extension to plastic matrix with isotropic hardening

It is known that the isotropic plastic hardening of rock-like materials is usually described by the evolution of internal frictional coefficient κ. In this study, we consider the following specific hardening law:

$$\kappa(\gamma^p) = \kappa_m - (\kappa_m - \kappa_0)\, e^{-b_1 \gamma^p} \tag{II .67}$$

where κ_0 and κ_m denote the initial threshold and the asymptotic value of the frictional coefficient respectively, while b_1 is a parameter controlling the plastic hardening rate.

In order to account for this kind of plastic hardening in the incremental variational model and avoid complex mathematical treatment, we shall here propose a heuristic extension of the model formulated for materials without plastic hardening. According to the theoretical formulation presented in Sections 3 and 4, when the values κ and c are constant, the average secant viscosity function of solid matrix η is given in Eq.(II .54). We here assume that this result remains applicable for the solid matrix where the value of κ is updated at each loading increment. Therefore, the average secant viscosity function is written as:

$$\eta = -\frac{\kappa\left(\langle\gamma_n^p\rangle_m\right)\left(\langle\sigma_m\rangle_m - c\right)}{\overline{\overline{\dot{\boldsymbol{\alpha}}}}} \tag{II .68}$$

In this expression, $\langle \gamma_n^p \rangle_m$ is the average value of equivalent plastic shear strain field in the solid matrix γ^p at step n, which is denoted in Eq.(II .70). It is noted that when the isotropic hardening is considered, the value of frictional coefficient $\kappa\left(\langle \gamma_n^p \rangle_m\right)$ is also updated in the yield function at each loading increment.

Remark 2

The framework proposed in Sections 3 and 4 can also be easily extended to an alternative form of Drucker-Prager criterion written as$(\sigma_{eq} + 3\kappa\sigma_m - c = 0)$ *with a plastic hardening law on hydrostatic tensile yield stress c. In this context, if we choose* $\kappa = 0$*, the present model will coincide with that proposed by Boudet et al. (2016), who extended the work of Lahellec and Suquet (2007b) to composites with J2 plastic matrix including an isotropic hardening.*

7.1 Comparisons with FEM simulations

In this subsection, we shall verify the accuracy of the heuristic extended incremental variational model for materials with an isotropic hardening also by comparing the model's predictions with numerical results provided by finite element simulations. As for the validation presented in Section 6.2, we here also consider two kinds of rock-like materials: inclusion-reinforced material and porous material. Conventional triaxial compression tests are studied. The boundary conditions for the inclusion-reinforced material and porous material are the same as those given in (2) and (II .66), respectively. For the isotropic hardening law, we here choose $\kappa_0 = 0.00001$, $\kappa_m = 0.227$ and $b_1 = 140$ for all numerical calculations.

7.1.1 Inclusion-reinforced material

Two volume fractions of mineral inclusions are considered, respectively equal to $f^i = 5\%$ and $f^i = 15\%$. In Figure II .4, the macroscopic stress-strain curves for the uniaxial compression test are presented. There is a good agreement between the model's predictions and FEM solutions.

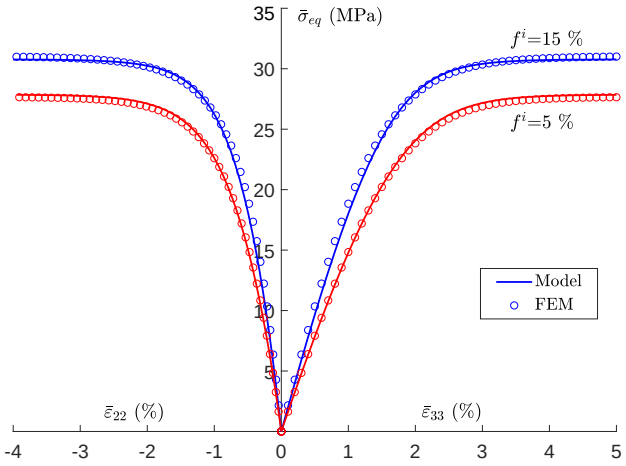

Figure II .4: Macroscopic predictions for a peridic inclusion-reinforced material with Drucker-Prager matrix and elastic inclusions for two volume fractions of inclusions: $f^i = 5\%$ and $f^i = 15\%$ under uniaxial compression

To further access the accuracy of the proposed model, a sensitivity analysis on the parameters κ_m and b_1 is performed and the obtained stress-strain curves are presented in Figure II .5. One can see again a good agreement between the model's predictions and FEM solutions. In Figure II .5(b), a sharp elastic-plastic transition is clearly seen with $\kappa_0 = 0.1$. In order to assess the effect of confining stress on macroscopic mechanical behavior of rock-like materials, two values of confining stress are here considered, namely 5MPa and 10MPa for $f^i = 15\%$. The obtained stress-strain curves are presented in Figure II .6. It is clear that the model's predictions coincide with the FEM solutions very well.

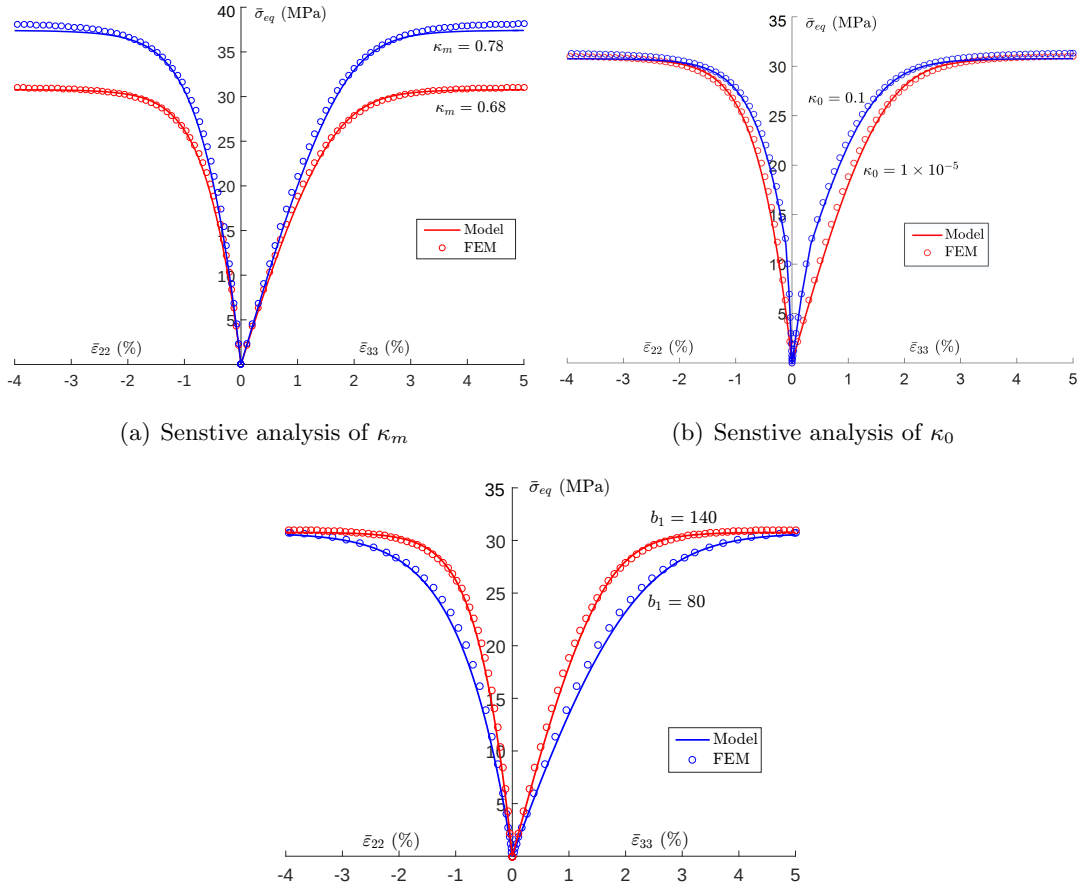

(a) Senstive analysis of κ_m

(b) Senstive analysis of κ_0

(c) Senstive analysis of b_1

Figure II .5: Macroscopic predictions for a peridic inclusion-reinforced material with Drucker-Prager matrix and elastic inclusions ($f^i = 15\%$) under uniaxial compression for (a) different κ_m and (b)different κ_0 and (c) different b_1

7.1.2 Porous material

Two values of porosity are here considered, namely $f^i = 15\%$ and 5%. The obtained macroscopic stress-strain curves are shown in Figure II .7 for the uniaxial compression test. One can see that there is a good agreement between the model's predictions and FEM results. Furthermore, the influence of confining pressure on macroscopic responses of porous material is also investigated. The obtained results are presented in Figure II .8 for two different values of confining pressure, 5MPa and 10MPa. Once again, the model's predictions are in good concordance with FEM solutions.

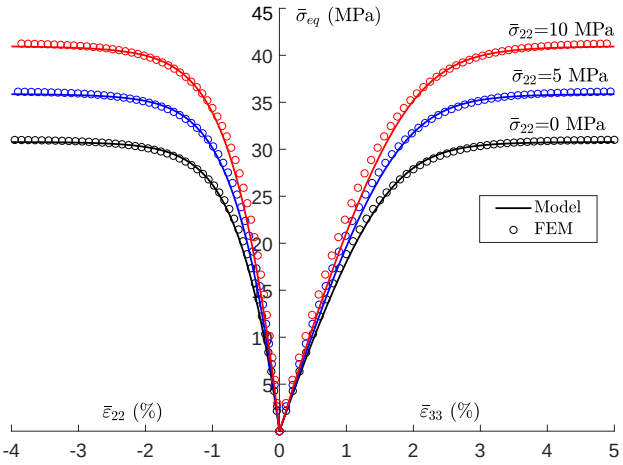

Figure II .6: Macroscopic predictions for a periodic inclusion-reinforced material with Drucker-Prager matrix and elastic inclusions ($f^i = 15\%$) in triaxial compressions with different confining pressures

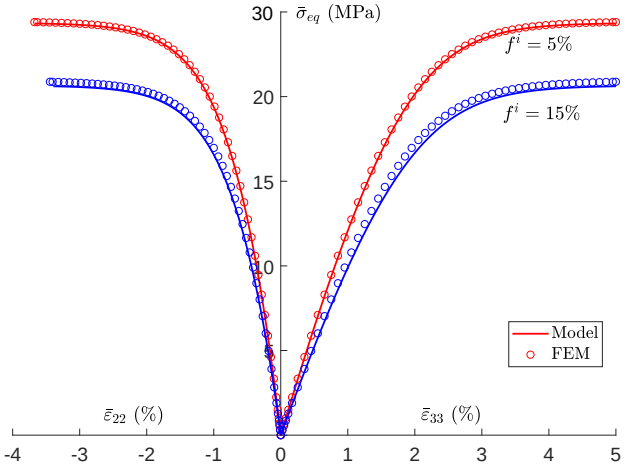

Figure II .7: Macroscopic predictions for a peridic porous material with different porosity in uniaxial compressions test

7.2 Application examples

In this section, we present two examples of application of the proposed incremental variational model for rock-like materials. The first example is about a Portland cement mortar and the second one is on a typical sandstone.

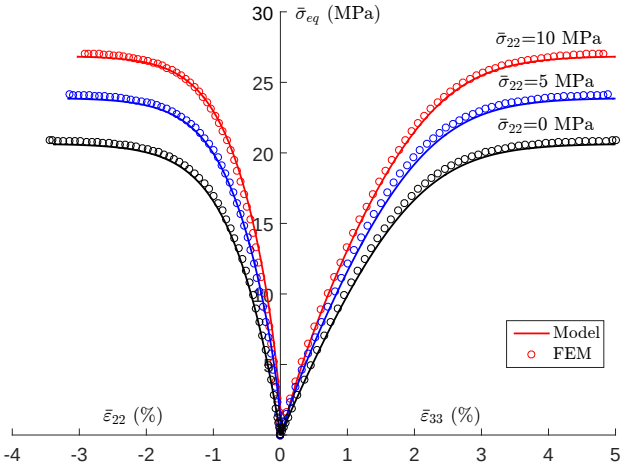

Figure II .8: Macroscopic predictions for a peridic porous material with Drucker-Prager matrix and porosity $f^i = 15\%$ in triaxial compressions with different confining pressures

7.2.1 Application to mortar

The mechanical behavior of a normalized mortar (European norm EN 196-1) with a water to cement ratio equal to 0.5 was investigated in Yurtdas et al. (2004). At the mesoscopic scale, this material can be approximated by a continuous cement paste in which sand grains are randomly embedded. The volume fractions of the cement paste and sand are respectively equal to $f^m = 40\%$ and $f^i = 60\%$. The cement paste is regarded as a Drucker-Prager plastic matrix, and the sand grains as elastic inclusions phase. For numerical simulations, 2 elastic coefficients should be determined respectively for the cement paste and sand. Further, 3 plastic parameters are involved in the cement paste.

The elastic coefficients of quartz sand have been chosen from literature, namely $E^i = 95$ GPa, and $\nu^i = 0.15$. The elastic coefficients of the cement paste are not directly measured. They are identified from an inverse homogenization procedure. The macroscopic elastic coefficients of the mortar are first expressed as functions of the elastic properties of cement paste and sand as well as of volume fraction of sand. Then their values are determined from triaxial compression tests. Now knowing the elastic coefficients of sand and its volume fraction, it is possible to extract the elastic coefficients of cement paste from the macroscopic elastic properties. For the mortar studied here, one gets the following values of $E^m = 12$ GPa for the elastic modulus and of $\nu^m = 0.2$ for the Poisson's ratio. The values of plastic parameters of cement paste by iterative numerical fitting of experimental stress-strain curves in a triaxial compression test. The calibration procedure is similar to

that used in (Guéry et al., 2008; Shen et al., 2012). The obtained parameter values are given in Table II .3.

Table II .3: Typical values of model parameters for each phase of cement mortar

	Phase 1:cement paste matrix	Phase 2:sand
Elastic parameters	$E^m = 12\text{GPa}$	$E^i = 95\text{GPa}$
	$\nu^m = 0.2$	$\nu^i = 0.15$
Plastic parameters	$\kappa_0 = 0.167$	
	$\kappa_m = 0.25$	
	$c = 32\text{MPa}$	

One uniaxial compression test and one triaxial compression test with a 15MPa confining stress are considered here. It was found that the plastic hardening behavior of the studied mortar was strongly sensitive to confining pressure Yurtdas et al. (2004). As shown in Figure II .5(c), the plastic hardening rate is controlled by the parameter b_1. Therefore, two distinct values of the parameter b_1 are used in numerical calculations, namely $b_1 = 2000$ for the uniaxial compression and $b_1 = 70$ for triaxial compression test with a confining stress of 15MPa. With additional experimental data, it will be needed to identify a continuous evolution law of this parameter with confining stress.

Using the above parameters, numerical simulations are performed using the proposed incremental variational model. The obtained macroscopic stress-strain curves are compared with experimental data in Figures II .9. One can find a good agreement between the model's predictions and experimental data. Especially, the axial strain is well reproduced for two values of confining stress. However, as shown in the comparisons, the proposed model overestimates the lateral strain or volumetric dilatancy. That is due to the fact that the present incremental variational model is based on the framework of Generalized Standard Materials (GSM), implying an associated plastic flow rule for the cement paste matrix. In order to improve the prediction of volumetric strain in future, an extension of the present model is needed by considering a non-associated plastic flow rule for the matrix phase.

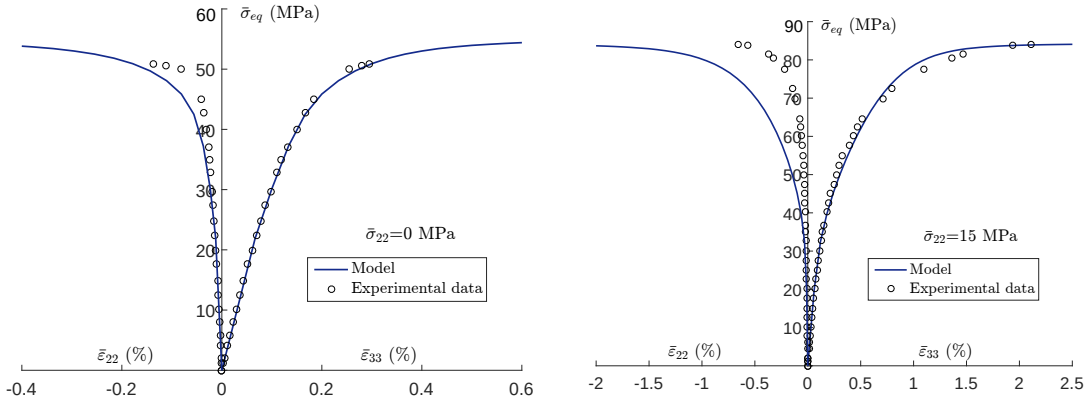

(a) Confining pressure $\bar{\sigma}_{22} = 0$MPa (b) Confining pressure $\bar{\sigma}_{22} = 15$MPa

Figure II .9: Comparisons between experimental data and numerical model results for triaxial compression tests on Mortar

7.2.2 Application to Vosges sandstone

The Vosges sandstone has been investigated in previous studies for various engineering applications (Bésuelle et al., 2000; Khazraei, 1996). As a first approximation, the sandstone can be represented an isotropic porous material. The average porosity is about 20%. The solid matrix is composed of nearly 93% quartz grains and a small quantity of feldspar and white mica. The mechanical behavior of the solid matrix is here described by an pressure sensitive plastic model based on the Drucker-Prager criterion.

As input data to the incremental variational model, both elastic and plastic parameters of the solid matrix should be identified. Unfortunately, direct measurements of those parameters are not available. We have then used an indirect calibration method. As for the mortar studied above, the elastic coefficients of the solid matrix are obtained from the inverse Mori-Tanaka homogenization scheme. The plastic parameters are obtained from an iterative numerical fitting of experimental stress-strain curves. The obtained values of parameters are listed in Table II .4.

Table II .4: Parameters of solid matrix for porous Vosges sandstone

E^m (GPa)	ν^m	κ_0	κ_m	c(MPa)	b_1
40	0.25	10^{-5}	0.467	45	800

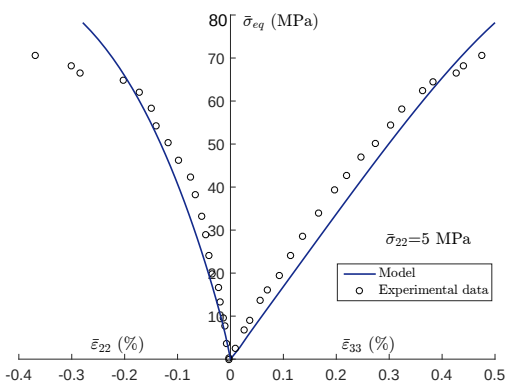

(a) Confining pressure $\bar{\sigma}_{22} = 5$MPa

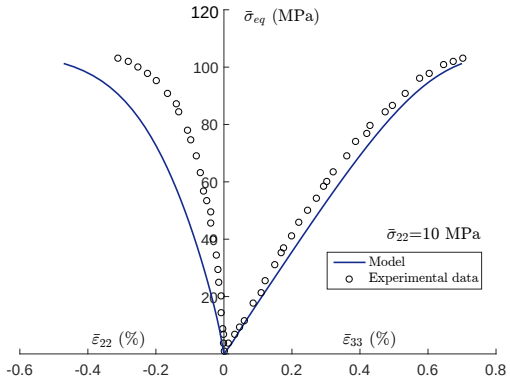

(b) Confining pressure $\bar{\sigma}_{22} = 10$MPa

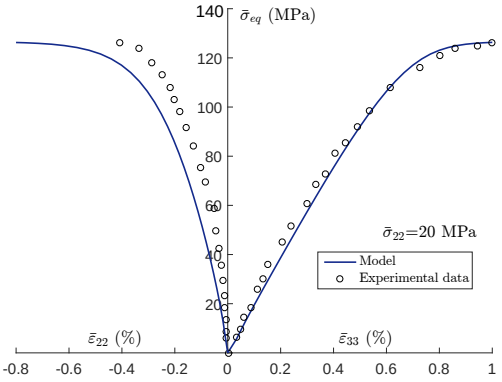

(c) Confining pressure $\bar{\sigma}_{22} = 20$MPa

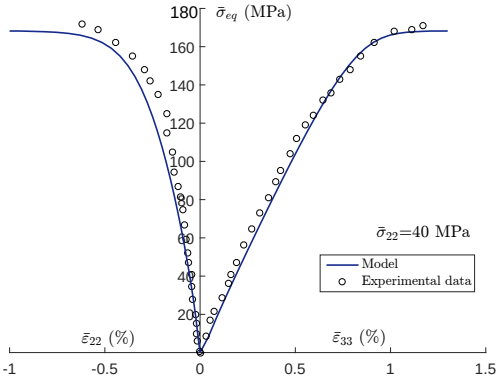

(d) Confining pressure $\bar{\sigma}_{22} = 40$MPa

Figure II .10: Comparisons between experimental data and model numerical results for triaxial compression tests on Vosges sandstone

In Figure II .10, one shows the comparisons of macroscopic stress-strain curves between the incremental variational model and experimental data, for four values of confining stress. Generally, there is a good agreement. The main features of the mechanical behavior of sandstone are well reproduced, for instances, the influence of confining stress, plastic strain hardening and peak strength. However, as for the mortar, some scatters are obtained. The lateral strain is still overestimated by the micro-mechanical model. The use of a non-associated flow rule for the solid matrix would improve these results. Furthermore, the peak strength of sandstone is also overestimated for the test with low confining stress, i.e., 5MPa. This is due to the fact that the linear Drucker-Prager criterion used for the solid matrix is maybe not well adapted in the zones of low mean stress and tensile stress. The use of a curved yield surface, for example the Mises-Schleicher yield criterion, for the solid matrix would improve numerical results.

8 Concluding remarks

In this paper, we have proposed a new micro-mechanical model based on the incremental variational principle for describing the elastic-plastic behavior of rock-like materials. The microstructure of materials is composed of a pressure sensitive Drucker-Prager solid matrix in which elastic inclusions or pores are embedded. The effective incremental variational (EIV) principle proposed by Lahellec and Suquet (2007b) has been extended in order to account for the volumetric plastic strain and pressure-dependency of plastic deformation in the solid matrix. The proposed model is able to account for the non-uniform local plastic strain field in the solid matrix.

The proposed model has been formulated in two steps. At the first step, by assuming an elastic-perfectly plastic behavior for the solid matrix, the incremental variational model has been properly formulated. The local dissipation potential and incremental potential have been constructed for the pressure sensitive plastic matrix. An appropriate linearization procedure has been introduced for the local incremental potential and for reducing the complexity of local variation procedure. The accuracy of the proposed micro-mechanical model has well been demonstrated through the comparisons with direct field finite element simulations for both inclusion-reinforced and porous materials without plastic hardening.

At the second step, a heuristic extension of the micro-mechanical model has been proposed in view of estimating effective behaviors of rock-like materials with an isotropic plastic hardening law. This has been done by assuming that the general incremental variational formulation obtained from perfectly plastic solid matrix remains applicable for materials with isotropic hardening. The plastic hardening has been simply taken into account by updating the value of international frictional coefficient at each loading increment. The accuracy of the heuristic extended model has been well verified by comparing the model's predictions with finite element results also for both inclusion-reinforced and porous materials. Furthermore, the proposed model has been applied to describe the mechanical behaviors of cement mortar and sandstone under triaxial compression tests. The numerical results obtained were generally in good agreement with experimental data. The main features of their responses have been correctly reproduced. Due to the fact that an associated plastic flow rule was adopted for the solid matrix, the volumetric strain was not well reproduced. This aspect will be improved in our ongoing work by considering a non-associated plastic flow rule for the plastic matrix. This will be done by using the concept of bi-potential theory proposed by Saxcé and Bousshine (1998) to deal with the non-associated plastic potential function.

Appendix A: Linearization of local free energy function (II .17)

Inspired by Boudet et al. (2016), the volumetric plastic strain field $\boldsymbol{\beta}$ and the internal variable field γ^p are taken as uniform in the solid matrix, by using their average values respectively denoted as $\langle\boldsymbol{\beta}\rangle_m$ and $\langle\gamma^p\rangle_m$. By taking into account Eq.(II .16), their evolutions are determined as follows:

$$\langle\boldsymbol{\beta}\rangle_m = \langle\boldsymbol{\beta}_n\rangle_m + \overline{\overline{\dot{\boldsymbol{\alpha}}}}\Delta t\kappa\boldsymbol{\delta} \tag{II .69}$$

$$\langle\gamma^p\rangle_m = \langle\gamma^p_n\rangle_m + \overline{\overline{\dot{\boldsymbol{\alpha}}}}\Delta t \tag{II .70}$$

where $\langle\boldsymbol{\beta}_n\rangle_m$ and $\langle\gamma^p_n\rangle_m$ are the volume average values of fields $\boldsymbol{\beta}$ and γ over matrix at step n, and

$$\overline{\overline{\dot{\boldsymbol{\alpha}}}} = \frac{1}{\Delta t}\sqrt{\frac{2}{3}\left\langle(\boldsymbol{\alpha}-\boldsymbol{\alpha}_n):(\boldsymbol{\alpha}-\boldsymbol{\alpha}_n)\right\rangle_m} = \frac{1}{\Delta t}\overline{\overline{\boldsymbol{\alpha}-\boldsymbol{\alpha}_n}} \tag{II .71}$$

Accordingly, the free energy denstiy is approximated by

$$w^m(\boldsymbol{\varepsilon},\boldsymbol{\alpha},\boldsymbol{\beta}) \simeq w_{lin}(\boldsymbol{\varepsilon},\boldsymbol{\alpha}) = \frac{1}{2}\left(\boldsymbol{\varepsilon}-\boldsymbol{\alpha}-\langle\boldsymbol{\beta}_n\rangle_m - \overline{\overline{\boldsymbol{\alpha}-\boldsymbol{\alpha}_n}}\kappa\boldsymbol{\delta}\right):\mathbb{C}^m:\left(\boldsymbol{\varepsilon}-\boldsymbol{\alpha}-\langle\boldsymbol{\beta}_n\rangle_m - \overline{\overline{\boldsymbol{\alpha}-\boldsymbol{\alpha}_n}}\kappa\boldsymbol{\delta}\right) \tag{II .72}$$

Appendix B: Effective behavior and field statistics for RVE

The effective energy $\Pi_0(\bar{\boldsymbol{\varepsilon}})$ is written as

$$\Pi_0(\bar{\boldsymbol{\varepsilon}}) = \frac{1}{2}\bar{\boldsymbol{\varepsilon}}:\bar{\mathbb{C}}:\bar{\boldsymbol{\varepsilon}} + \bar{\boldsymbol{\rho}}:\bar{\boldsymbol{\varepsilon}} + \bar{\zeta} \tag{II .73}$$

where

$$\bar{\mathbb{C}} = f^m\mathbb{C}_0^m:\mathbb{A}^m + \sum_{r=1}^{N} f^{i,r}\mathbb{C}^{i,r}:\mathbb{A}^{i,r} \tag{II .74a}$$

$$\bar{\boldsymbol{\rho}} = f^m\boldsymbol{\rho}_0^m:\mathbb{A}^m \tag{II .74b}$$

$$\bar{\zeta} = f^m\left(\zeta_0^m + \boldsymbol{\rho}_0^m:\boldsymbol{a}^m\right) \tag{II .74c}$$

The average of the local strain filed in the matrix can be related to the macroscopic strain by two strain concentration tensors $\mathbb{A}^m, \boldsymbol{a}^m$, i.e., (Willis, 1981)

$$\langle\boldsymbol{\varepsilon}\rangle_m = \mathbb{A}^m:\bar{\boldsymbol{\varepsilon}} + \boldsymbol{a}^m \tag{II .75}$$

Similarly, the average of the local strain filed in the inclusion phase r can also be expressed as

$$\langle\boldsymbol{\varepsilon}\rangle_{i,r} = \mathbb{A}^{i,r}:\bar{\boldsymbol{\varepsilon}} + \boldsymbol{a}^{i,r} \tag{II .76}$$

One notices that the fourth-order tensors $\mathbb{A}^m$ and $\mathbb{A}^{i,r}$ can be identified to those computed for composites in the purely elastic case. However, the expressions of second-order tensor $\boldsymbol{a}^m$ and $\boldsymbol{a}^{i,r}$ are necessary to compute the phase averages of stress and strain.

The second-order moment of the strain filed $\boldsymbol{\varepsilon}$ in the matrix phase can be obtained from the effective free energy $\Pi_0\left(\bar{\boldsymbol{\varepsilon}}\right)$ by the relations given in (Lahellec and Suquet, 2007b; Ponte Castaneda, 2002)

$$\left\langle \boldsymbol{\varepsilon} \otimes \boldsymbol{\varepsilon} \right\rangle_m = \frac{2}{f^m} \frac{\partial \Pi_0}{\partial \mathbb{C}_0^m} \tag{II .77}$$

Note that $\mathbb{C}_0^m$ can be expressed by two effective moduli as $\mathbb{C}_0^m = 3k^m\ \mathbb{J} + 2\mu_0^m\ \mathbb{K}$. Then the deviatoric part of the second-order moment leads to(Huang et al., 2015; Lahellec and Suquet, 2007a)

$$\mathbb{K} : \left\langle \boldsymbol{\varepsilon} \otimes \boldsymbol{\varepsilon} \right\rangle_m = \frac{1}{f^m} \frac{\partial \Pi_0}{\partial \mu_0^m} \tag{II .78}$$

In order to take advantage of the explicit expressions of the tensors $\mathbb{A}^m$, $\mathbb{A}^{i,r}$, $\boldsymbol{a}^m$ and $\boldsymbol{a}^{i,r}$, a two-phase material, one phase of elastic inclusion ($r = N = 1$) and one phase of elastic-plastic matrix, is considered for the validation and application. In this case, the fourth order concentration tensors associated to the Hashin and Shtrikman (HS) estimates are adopted (Hashin, 1962)

$$\mathbb{A}^m = \mathbb{I} + \frac{1}{f^m} \left(\mathbb{C}_0^m - \mathbb{C}^{i,r} \right)^{-T} : \left(\bar{\mathbb{C}} - \langle \mathbb{C} \rangle \right)^T \tag{II .79a}$$

$$\mathbb{A}^{i,r} = \mathbb{I} + \frac{1}{f^{i,r}} \left(\mathbb{C}^{i,r} - \mathbb{C}_0^m \right)^{-T} : \left(\bar{\mathbb{C}} - \langle \mathbb{C} \rangle \right)^T \tag{II .79b}$$

$$\boldsymbol{a}^m = \left(\mathbb{C}_0^m - \mathbb{C}^{i,r} \right)^{-1} : \left(\mathbb{I} - \mathbb{A}_m \right)^T : \boldsymbol{\rho}_0^m \tag{II .79c}$$

$$\boldsymbol{a}^{i,r} = -\left(\mathbb{C}^{i,r} - \mathbb{C}_0^m \right)^{-1} : \left(\mathbb{I} - \mathbb{A}_{i,r} \right)^T : \boldsymbol{\rho}_0^m \tag{II .79d}$$

where $\langle \mathbb{C} \rangle = f^m \mathbb{C}_0^m + f^{i,r}\ \mathbb{C}^{i,r}$.

Chapter III

Homogenization of rock-like materials with a non-associated and strain-hardening plastic matrix by a bi-potential based incremental variational approach*

In this paper, we shall develop a new bi-potential based incremental variational (BIV) approach for estimation of elastic-plastic behavior of rock-like materials. The studied materials are assumed composed of a non-associated plastic matrix. Elastic inclusions or voids are embedded in the plastic matrix. This class of materials does not belong to generalized standard materials investigated in previous studies. For simplicity, the behavior of solid matrix is first assumed to be elastic-perfectly plastic at each loading increment. The emphasis of the present study is firstly put on the treatment of non-associated plastic flow. This is done by using a bi-potential theory based method, allowing the determination of the incremental potential of plastic matrix. The effective incremental potential and macroscopic stress tensor are then estimated through an extension of the incremental variational principle established by Lahellec and Suquet (2007b). The accuracy of the BIV model is verified by comparing the model simulations with with reference results obtained from direct finite element simulations. In order to consider the solid matrix exhibits isotropic hardening, we assume that the general form of BIV model remains valid, and the model

*Submitted to International Journal of Engineering Science

is extended simply by updating the value of frictional coefficient and dilatancy coefficient of solid matrix at each loading increment. The accuracy of BIV model in this case is validated by a series of comparisons with reference solutions obtained from full-field finite element simulations respectively for inclusion-reinforced materials and porous materials. Both local and macroscopic responses are compared. As an example of application, the heuristic extended BIV model is used to estimate mechanical responses of typical claystone and sandstone under different loading paths, showing the BIV approach could well reproduce the specific properties of rock-like materials such as the influence of mean stress, strain hardening and volumetric compressibility-dilatancy transition.

1 Introduction

Soils, rocks and concretes are largely used in civil engineering. These materials contain different kinds of heterogeneities at different scales. Pores and inclusions are two main families of heterogeneities. Furthermore, these materials are composed of several mineral phases of different properties. The mineral compositions may significantly vary in space, for instance with geological depth. Laboratory studies have shown that macroscopic physical and mechanical properties of these materials are affected by heterogeneities and mineral compositions. So far, different kinds of macroscopic models, mainly elastic-plastic and damage models have been developed for modeling mechanical properties of rock-like materials. Fitted from a large number of laboratory tests, these models are able to correctly reproduce main features of mechanical behavior of studied materials. However, they are not able to properly consider the effect of heterogeneities and mineralogical compositions on macroscopic mechanical responses.

Based on linear homogenization techniques, micro-mechanical models have first been developed during the last decades for modeling of induced damage in brittle rock-like materials (Zhao et al., 2018; Zhu et al., 2008a, 2016). Important advances have also been obtained on micro-mechanical modeling of plastic deformation in rock-like materials using nonlinear homogenization methods. For instance, clayey rocks have been characterized as a matrix-inclusion composite material at the mesoscopic scale, constituted of a plastic clay matrix in which calcite and quartz grains are embedded (Guéry et al., 2008; Jiang et al., 2009). The microstructure of clayey rocks has further been enriched by considering the clay matrix as a porous material with pores at the microscopic scale (Shen et al., 2012). The nonlinear behavior of the plastic clay matrix has been handled by using the Hill incremental method (Hill, 1965b). This method has also been largely used in various

composite materials. It is found that the use of simple Hill's incremental method generally leads to a too stiff mechanical strength of heterogeneous materials (Chaboche et al., 2005; Suquet, 1996). The main reason of such results is the fact that uniform strain fields are assumed in constituents in the Hill's model. In order to improve the numerical performance of this model, artificial techniques, such as isotropization of tangent elastic-plastic stiffness tensor, have been proposed. This correction technique has been applied to clayey rocks (Guéry et al., 2008; Jiang and Shao, 2009; Shen et al., 2012). However, the isotropization procedure is not based on any physical background.

Meanwhile, advanced nonlinear homogenization techniques have been developed for composite materials considering non-uniform local fields in constituents(Boudet et al., 2016; Brassart et al., 2011, 2012; Castañeda, 1991, 1992, 2002b; Danas and Castañeda, 2012; Lahellec and Suquet, 2007a,b, 2013), just to mention a few. Variational principles based on the use of a "linear comparison composite" (LCC) were proposed for the mean field homogenization of nonlinear elastic composites (Castañeda, 1991, 1992, 2002b), and used to generate improved bounds and more generate estimates for the nonlinear elasto-plastic composites (Castañeda and Suquet, 1997; Danas and Castañeda, 2012). Motivated by the previous work (Castañeda, 1991), Lahellec and Suquet (2007a,b) proposed their new incremental variational method for nonlinear viscoelasticity composites without local threshold or hardening. In this method, equivalent interval variables (EIV) are defined to capture the non-uniform local plastic strain field. Recently, the same authors (Lahellec and Suquet, 2013) proposed a rate variational model (RVP)considering a non-uniform field of plastic strain rate. The RVP model is able to deal with elastic-viscoplastic composites with local threshold, isotropic and linear kinematic hardening. More recently, the work of Lahellec and Suquet (2007b) has been extended in Boudet et al. (2016) for elastic-(visco)plastic composites with local threshold and isotropic and/or linear kinematic hardening. On the other hand, based on the variational principle established by Ortiz and Stainier (1999), alternative incremental variational models have been proposed in (Brassart et al., 2011, 2012) for elastic-(visco)plastic composites with local isotropic hardening. However, all these previous models have been developed in the scope of Generalized Standard Materials (GSM) (Halphen and Nguyen, 1975) with an associated plastic flow rule.

The contribution of the present work is to develop a new incremental variational model for rock-like materials which do not verify the assumptions of generalized standard materials. Indeed, for most rock-like materials, the transition from volumetric compressibility to dilatancy is an essential issue. It is generally related to a non-associated plastic flow rule. The plastic behavior is described by two distinct functions, the plastic yield criterion and

the plastic potential. However, according to innovative studies on the bi-potential theory (De Saxcé, 1995; De Saxcé and Feng, 1991; Saxcé and Bousshine, 1998), rock-like materials can be attributed to a class of implicit standard materials (ISM). This concept has been successfully used for various soil and rock-like materials (Bodovillé, 2001b; Bodovillé and De Saxcé, 2001; Hjiaj et al., 2003). The use of a bi-potential function allows simultaneously to define the yield locus and the flow rule, although they are not associated.

In this study, we shall consider a class of rock-like materials composed of a non-associated Drucker-Prager type plastic matrix, elastic mineral inclusions and(or) pores. A new bi-potential based incremental variational model (BIV) is proposed to consider non-uniform stress and plastic strain fields in the matrix. It is worth pointing out that most rock-like materials generally exhibit plastic hardening. In the case of an isotropic plastic hardening is considered, the hardening of rock-like materials is generally represented by the variation of internal frictional coefficient rather than the evolution of cohesion. However, this kind of plastic hardening renders the analytical formulation of BIV model very complex. To this end, we propose here a simplified approach. As the whole loading history is divided into a limit number of increments, the behavior of solid matrix is first assumed to be elastic-perfectly plastic for each loading increment. The general formulation of BIV model is obtained for this particular case. The proposed model is validated through comparisons with reference results obtained from direct finite element simulations for materials without plastic hardening. Then, we assume that the obtained formulation remains valid when the solid matrix exhibit an isotropic plastic hardening. The model is extended simply by updating the value of frictional coefficient of solid matrix at each loading increment with a specific law. The proposed extended model is validated against FEM results both for local and macroscopic responses. Finally, the proposed extended model is applied to to study mechanical behaviors of a typical clayey rock and porous sandstone in various loading paths.

2 Bi-potential of non-associated Drucker-Prager plasticity model

We consider here a class of rock-like materials with a perfectly plastic matrix described by a non-associated plastic model. As those materials are not generalized standard materials (GSM), we shall here propose an extension of the incremental variational method previously developed for GSM by using a bi-potential theory.

2.1 The non-associated model for plastic matrix

We adopt here a non-associated plastic model without strain hardening for the matrix phase with the assumption of small strain. The model is based on a Drucker-Prager criterion and the local yield function is written as:

$$f(\boldsymbol{\sigma}) = \sigma_{eq} + 3\kappa\left(\sigma_m - c\right) \leq 0 \tag{III .1}$$

where $\sigma_{eq} = \sqrt{\frac{3}{2}\boldsymbol{s} : \boldsymbol{s}}$ is the equivalent stress (with $\boldsymbol{s} = \boldsymbol{\sigma} : \mathbb{K}$), and $\sigma_m = \frac{1}{3}\boldsymbol{\sigma} : \boldsymbol{\delta}$ the mean stress. The parameter c and κ respectively represent the hydrostatic tensile strength and friction coefficient of the matrix.

The non-associated plastic flow rule is defined by the following plastic potential:

$$g(\boldsymbol{\sigma}, \chi) = \sigma_{eq} + 3\chi\sigma_m \tag{III .2}$$

Further, for any stress state situated on the regular part of the yield surface, it is assumed that the plastic dilatancy coefficient χ is equal or less than the friction coefficient, i.e., $\chi \leq \kappa$ (Hjiaj et al., 2003). The corresponding rate form of plastic strain $\boldsymbol{\varepsilon}^p$ is expressed as follows:

$$\dot{\boldsymbol{\varepsilon}}^p = \dot{\gamma}^p \frac{\partial g}{\partial \boldsymbol{\sigma}} = \dot{\gamma}^p \left(\frac{3}{2}\frac{\boldsymbol{s}}{\sigma_{eq}} + \chi\boldsymbol{\delta}\right) \tag{III .3}$$

where γ^p is an internal variable. For convenience, the plastic strain tensor is decomposed into a spherical part and a deviatoric part:

$$\boldsymbol{\varepsilon}^p = \boldsymbol{\alpha} + \boldsymbol{\beta},\ \boldsymbol{\alpha} = \boldsymbol{\varepsilon}^p : \mathbb{K},\quad \boldsymbol{\beta} = \boldsymbol{\varepsilon}^p : \mathbb{J} = \frac{1}{3}\mathrm{tr}\boldsymbol{\varepsilon}^p\boldsymbol{\delta} = \beta\boldsymbol{\delta} \tag{III .4}$$

One thus obtains:

$$\dot{\gamma}^p = \sqrt{\frac{2}{3}\dot{\boldsymbol{\alpha}} : \dot{\boldsymbol{\alpha}}} = \dot{\alpha}_{eq},\quad \dot{\boldsymbol{\alpha}} = \mathbb{K} : \dot{\boldsymbol{\varepsilon}}^{\boldsymbol{p}},\quad \dot{\beta} = \frac{1}{3}\mathrm{tr}\dot{\boldsymbol{\varepsilon}}^p = \chi\dot{\alpha}_{eq} \tag{III .5}$$

It is noted that the apex point on the Drucker-Prager yield surface is not taken into account here. More discussions about this issue are given in the previous work by Hjiaj et al. (2003).

2.2 Bi-potential function for the non-associated plastic model

According to Hjiaj et al. (2003), the bi-potential formulation of a non-associated Drucker-Prager model without strain hardening takes the form

$$b_p\left(\boldsymbol{\sigma}, \dot{\boldsymbol{\varepsilon}}^p\right) = \begin{cases} 3c\dot{\beta} + 3\left(\chi - \kappa\right)\left(\sigma_m - c\right)\dot{\alpha}_{eq} & \text{if } \ f(\boldsymbol{\sigma}) \leq 0 \\ +\infty & \text{otherwise} \end{cases} \tag{III .6}$$

The proof that the function (III .6) is a bi-potential has been given is given in Hjiaj et al. (2003).With the help of Eq.(III .5), the function (III .6) can be rewritten as

$$b_p\left(\boldsymbol{\sigma},\dot{\boldsymbol{\alpha}}\right)=\begin{cases}\underbrace{\left[3\sigma_m\left(\chi-\kappa\right)+3c\kappa\right]}_{\sigma_y}\dot{\alpha}_{eq}=\sigma_y\dot{\alpha}_{eq} & \text{if } \ f(\boldsymbol{\sigma})\leq 0\\ +\infty & \text{otherwise}\end{cases} \tag{III .7}$$

Remark 3

The second part of the first line in the right hand side of Eq. (III .7) contains a mixed term of stress and plastic strain rate. When $\chi=\kappa$, the mixed term disappears and the bi-potential reduces to the plastic dissipation potential for GSM.

$$b_p\left(\boldsymbol{\sigma},\dot{\boldsymbol{\alpha}}\right)=\varphi\left(\dot{\boldsymbol{\alpha}}\right)=\begin{cases}3c\kappa\dot{\alpha}_{eq} & \textit{if } \ f(\boldsymbol{\sigma})\leq 0\\ +\infty & \textit{otherwise}\end{cases} \tag{III .8}$$

3 Bi-potential based incremental variational principle for rock-like materials with a non-associated plastic matrix

In this section, we shall propose a bi-potential theory based incremental variational model (BIV). The incremental variational principle proposed by (Lahellec and Suquet, 2007b) for GSM is extended to rock-like materials with a non-associated plastic matrix.

3.1 Representative Volume Element (RVE) and constituents properties

At the microscopic scale, rock-like materials are characterized by an isotropic solid matrix in which mineral grains and pores are randomly embedded. The Representative Volume Element (RVE) is shown in Figure II .1, occupying the domain $\Omega\subset\mathbb{R}^{n_{\text{dim}}}$ ($n_{\text{dim}}=1,2,3$) and having a boundary $\Omega\subset\mathbb{R}^{n_{\text{dim}}-1}$. The solid matrix occupies the sub-domain $\Omega^m\subset\mathbb{R}^{n_{\text{dim}}}$. It is characterized by an isotropic elastic tensor $\mathbb{C}^m$ and the non-associated plastic model presented above. The r^{th} phase of inclusion (solid grains or pores) occupies the sub-domain $\Omega^{i,r}\subset\mathbb{R}^{n_{\text{dim}}}$, $r=1,...,N$, and characterized by the elastic stiffness tensor $\mathbb{C}^{i,r}$. The phase of pores is here treated as a special inclusion phase with a vanished elastic stiffness.

For the convenience of the subsequent formulation, the total volume of the RVE is denoted as V_Ω, the volume of matrix as V_{Ω^m}, the volume occupied by the r^{th} inclusion

phase as $V_{\Omega^{i,r}}$. Accordingly, the volume fractions of the constituents are defined as

$$f^m = \frac{V_{\Omega^m}}{V_\Omega}; \quad f^{i,r} = \frac{V_{\Omega^{i,r}}}{V_\Omega}, \quad r = 1, ..., N; \tag{III .9}$$

Further, the operator $\langle\cdot\rangle$ denotes a volume average over the whole RVE, $\langle\cdot\rangle_m$ is a volume average over the matrix, and $\langle\cdot\rangle_{i,r}$ is a volume average over the r^{th} inclusion phase. That is

$$\langle\cdot\rangle = \frac{1}{V_\Omega}\int_{V_\Omega}(\cdot)\,\mathrm{d}V_\Omega = f^m\langle\cdot\rangle_m + \sum_{r=1}^{N} f^{i,r}\langle\cdot\rangle_{i,r} \tag{III .10}$$

with

$$\langle\cdot\rangle_m = \frac{1}{V_{\Omega^m}}\int_{V_{\Omega^m}}(\cdot)\,\mathrm{d}V_{\Omega^m}; \quad \langle\cdot\rangle_{i,r} = \frac{1}{V_{\Omega^{i,r}}}\int_{V_{\Omega^{i,r}}}(\cdot)\,\mathrm{d}V_{\Omega^{i,r}} \tag{III .11}$$

3.1.1 Incremental potential of the elastic-plastic matrix

From the viewpoint of bi-potential theory, the non-associated perfectly plastic matrix can be seen as an implicit standard material (ISM) (De Saxcé and Bousshine, 2002; Hjiaj et al., 2003). In this context, at any point $\underline{x} \in \Omega^m$, the local mechanical behavior can be described by two thermodynamic potentials. The first one is the free energy w^m, which is convex of strain field $\boldsymbol{\varepsilon}$ and plastic strain fields $\boldsymbol{\varepsilon}^p$. The second one is the aforementioned bi-potential $b_p\left(\boldsymbol{\sigma}, \dot{\boldsymbol{\varepsilon}}^p\right)$ instead of the dissipation potential for GSM. In fact, a GSM can be seen as a special case of ISM. In this context, the bi-potential is equivalent to the dissipation potential as it is noted in *Remark 3*. Consequently, the classical EIV principle for GSM is here treated as a special case of the BIV principle for ISM that is developed in this study. By assuming that the elastic behavior is independent of irreversible process, the free energy function $w^m(\boldsymbol{\varepsilon}, \boldsymbol{\varepsilon}^p)$ yields

$$w^m(\boldsymbol{\varepsilon}, \boldsymbol{\varepsilon}^p) = \frac{1}{2}(\boldsymbol{\varepsilon} - \boldsymbol{\alpha} - \boldsymbol{\beta}) : \mathbb{C}^m : (\boldsymbol{\varepsilon} - \boldsymbol{\alpha} - \boldsymbol{\beta}) \tag{III .12}$$

where the isotropic elastic stiffness tensor is expressed as $\mathbb{C}^m = 3k^m\mathbb{J} + 2\mu^m\mathbb{K}$, with k^m and μ^m being the bulk modulus and shear modulus of the matrix respectively.

By making the standard derivation of free energy function, the conjugated thermodynamic forces associated with $\boldsymbol{\varepsilon}$ and $\boldsymbol{\varepsilon}^p$ are determined:

$$\boldsymbol{\sigma} = \frac{\partial w^m}{\partial \boldsymbol{\varepsilon}}(\boldsymbol{\varepsilon}, \boldsymbol{\xi}) = \mathbb{C}^m : (\boldsymbol{\varepsilon} - \boldsymbol{\alpha} - \boldsymbol{\beta}) \tag{III .13a}$$

$$\boldsymbol{\sigma} = -\frac{\partial w^m}{\partial \boldsymbol{\varepsilon}^p}(\boldsymbol{\varepsilon}, \boldsymbol{\varepsilon}^p) = \frac{\partial b_p}{\partial \dot{\boldsymbol{\varepsilon}}^{\boldsymbol{p}}}(\boldsymbol{\sigma},\ \dot{\boldsymbol{\varepsilon}}^p) \tag{III .13b}$$

As in the incremental variational method developed for GSM Lahellec and Suquet (2007b) and based on the work by Ortiz and Stainier (1999), the time derivative $\dot{\boldsymbol{\varepsilon}}^{\boldsymbol{p}}$ is

approximated by a difference quotient after use of an implicit Eular-Scheme. The time interval (loading history) of study $[0,T]$ is accordingly discretized into the time (loading) steps $t_0=0,t_1,...,t_n,t_{n+1},...,t_N=T$. The time increment between t_n and t_{n+1} (loading step) is denoted by Δt. For the sake of simplicity, its dependence on n is omitted. By using this time-discretization scheme, the system of differential equations (III .13) is transformed to the following discretized system:

$$\boldsymbol{\sigma}_{n+1}=\frac{\partial w^m}{\partial\ \boldsymbol{\varepsilon}}\left(\boldsymbol{\varepsilon}_{n+1},\boldsymbol{\varepsilon}^p_{n+1}\right),\quad \frac{\partial w^m}{\partial\boldsymbol{\varepsilon}^p}\left(\boldsymbol{\varepsilon}_{n+1},\boldsymbol{\varepsilon}^p_{n+1}\right)+\frac{\partial b^p}{\partial\dot{\boldsymbol{\varepsilon}}^p}\left(\boldsymbol{\sigma}_{n+1},\frac{\boldsymbol{\varepsilon}^p_{n+1}-\boldsymbol{\varepsilon}^p_n}{\Delta t}\right)\ =0 \tag{III .14}$$

The values of local fields at time t_{n+1} $(\boldsymbol{\varepsilon}_{n+1},\boldsymbol{\sigma}_{n+1},\boldsymbol{\varepsilon}^p_{n+1})$ are unknown, while their values at time t_n $(\boldsymbol{\varepsilon}_n,\boldsymbol{\sigma}_n,\boldsymbol{\varepsilon}^p_n)$ are assumed to be all known. We introduce here the following incremental potential J^m, function of local variables $\boldsymbol{\varepsilon}$, $\boldsymbol{\sigma}$ and $\boldsymbol{\varepsilon}^p$:

$$J^m\left(\boldsymbol{\varepsilon},\boldsymbol{\sigma},\boldsymbol{\varepsilon}^p\right)=w^m(\boldsymbol{\varepsilon},\boldsymbol{\varepsilon}^p)+\Delta t b^p\left(\boldsymbol{\sigma},\frac{\boldsymbol{\varepsilon}^p-\boldsymbol{\varepsilon}^p_n}{\Delta t}\right) \tag{III .15}$$

For the sake of clarity, the subscripts $n+1$ are omitted. Notice that the second relation in (III .14) is the Euler-Lagrange equation of the variational problem for the minimization of the local incremental potential with respect to $\boldsymbol{\varepsilon}^p$. This leads to the following condensed local incremental potential:

$$\pi^m_\Delta\left(\boldsymbol{\varepsilon},\boldsymbol{\sigma}\right)=\inf_{\boldsymbol{\varepsilon}^p}J^m\left(\boldsymbol{\varepsilon},\boldsymbol{\sigma},\boldsymbol{\varepsilon}^p\right) \tag{III .16}$$

After that, the local stress field $\boldsymbol{\sigma}$ in the solid matrix can be derived from this sole potential

$$\boldsymbol{\sigma}=\frac{\partial\pi^m_\Delta}{\partial\ \boldsymbol{\varepsilon}}\left(\boldsymbol{\varepsilon},\boldsymbol{\sigma}\right) \tag{III .17}$$

3.1.2 Behavior of elastic inclusion

At any point inside the elastic inclusion phase, i.e., $\underline{x}\in\Omega^{i,r}$, the free energy function $w^{i,r}$ is the sole convex potential of inclusion strain field $\boldsymbol{\varepsilon}$. Accordingly, the local incremental potential $\pi^{i,r}_\Delta$ of the elastic inclusion phase r reads

$$\pi^{i,r}_\Delta=w^{i,r}\left(\boldsymbol{\varepsilon}\right)=\frac{1}{2}\boldsymbol{\varepsilon}:\mathbb{C}^{i,r}:\boldsymbol{\varepsilon} \tag{III .18}$$

The local stress field $\boldsymbol{\sigma}$ in the inclusion phase r is determined by:

$$\boldsymbol{\sigma}=\frac{\partial\pi^{i,r}_\Delta}{\partial\ \boldsymbol{\varepsilon}}\left(\boldsymbol{\varepsilon}\right)=\mathbb{C}^{i,r}:\boldsymbol{\varepsilon} \tag{III .19}$$

3.2 Effective behavior of heterogeneous rock-like materials

We consider that the RVE of heterogeneous rock-like materials is subjected to a macroscopic strain $\overline{\boldsymbol{\varepsilon}}(t)$, and for definiteness, periodic boundary conditions are prescribed on its boundary $\partial\Omega$ at time t_{n+1}. Due to the time-discretization scheme adopted, the local problem to be solved is formulated as follows:

$$\left\{\begin{array}{l} \operatorname{div}\boldsymbol{\sigma}_{n+1}=0 \\ \boldsymbol{\sigma}_{n+1}=\frac{\partial\pi_{\Delta}}{\partial\boldsymbol{\varepsilon}_{n+1}}\left(\boldsymbol{\varepsilon}_{n+1},\boldsymbol{\sigma}_{n+1}\right) \\ \langle\boldsymbol{\varepsilon}(t)\rangle=\overline{\boldsymbol{\varepsilon}}(t)+BC \quad \text{on } \partial\Omega \end{array}\right\} \quad \text{for } (\underline{x},t)\in\Omega\times[0,T] \tag{III .20}$$

The condensed incremental potential $\pi_{\Delta}\left(\underline{x},\boldsymbol{\varepsilon},\boldsymbol{\sigma}\right)$ is here defined as

$$\pi_{\Delta}=\left\{\begin{array}{ll} \pi_{\Delta}^{m} & \text{if } \underline{x}\in\Omega^{m} \\ \pi_{\Delta}^{i,r} & \text{if } \underline{x}\in\Omega^{i,r} \end{array}\right. \tag{III .21}$$

Finally, the macroscopic stress $\bar{\boldsymbol{\sigma}}$ can be derived from the effective incremental potential of the RVE:

$$\bar{\boldsymbol{\sigma}}_{n+1}=\frac{\partial\Pi_{\Delta}}{\partial\bar{\boldsymbol{\varepsilon}}}\left(\bar{\boldsymbol{\varepsilon}}_{n+1},\langle\boldsymbol{\sigma}_{n+1}\rangle_{m}\right) \tag{III .22}$$

The effective incremental potential Π_{Δ} can be determined by using the variational principle

$$\Pi_{\Delta}\left(\bar{\boldsymbol{\varepsilon}}_{n+1},\langle\boldsymbol{\sigma}_{n+1}\rangle_{m}\right)=\inf_{\langle\boldsymbol{\varepsilon}\rangle=\bar{\boldsymbol{\varepsilon}}_{n+1}}\langle\pi_{\Delta}\rangle=\inf_{\langle\boldsymbol{\varepsilon}\rangle=\bar{\boldsymbol{\varepsilon}}_{n+1}}\left[f^{m}\left\langle\inf_{\boldsymbol{\varepsilon}^{p}}J^{m}\left(\boldsymbol{\varepsilon},\boldsymbol{\varepsilon}^{p},\boldsymbol{\sigma}\right)\right\rangle_{m}+\sum_{r=1}^{N}f^{i,r}\left\langle w^{i,r}\left(\boldsymbol{\varepsilon}\right)\right\rangle_{i,r}\right] \tag{III .23}$$

The effective incremental potential of the RVE is not only related to the macroscopic strain $\bar{\boldsymbol{\varepsilon}}$, but also to the average value of local stress filed $\boldsymbol{\sigma}$ in the matrix. With this single effective potential in hand, according to Eq.(III .22), the macroscopic stress is the conjugated force associated with the macroscopic strain, which is consistent with the classical thermodynamic framework. Moreover, the macroscopic stress defined here also coincides with the average of the local stress field over the RVE. Accordingly, the problem of computing the overall response of the rock-like composite comes to solving the variational problem (III .23) at each time step, which itself involves a local optimization problem (III .16) with respect to the internal variables (plastic strain) $\boldsymbol{\varepsilon}^{p}$ at every position $\underline{x}\in\Omega^{m}$. Instead of searching a computationally-costly full-field numerical solution, an approximate variational procedure based on the previous study in Lahellec and Suquet (2007b) will be developed in Section 4 .

4 Optimization of the effective incremental potential

The main steps for the estimation of the effective incremental potential through a variational procedure are presented in this section.

4.1 Linearization of local incremental potential of plastic matrix

The first step is to linearize the local incremental potential J^m given in (III .15). Compared with the free energy used in Lahellec and Suquet (2007b), the free energy function for the perfectly plastic matrix given in (III .12) includes the plastic volumetric strain $\boldsymbol{\beta}$. However, in order to take advantage of the main results obtained in Lahellec and Suquet (2007b), both the free energy function (III .12) and bi-potential (III .7) are linearized as follows.

- Linearization of local free energy $w^m(\boldsymbol{\varepsilon}, \boldsymbol{\varepsilon}^p)$ (see detailed process in Appendix A)

$$w^m(\boldsymbol{\varepsilon}, \boldsymbol{\varepsilon}^p) \simeq w^m_{lin}(\boldsymbol{\varepsilon}, \boldsymbol{\alpha}) = \frac{1}{2}\left(\boldsymbol{\varepsilon} - \boldsymbol{\alpha} - \langle \boldsymbol{\beta}_n \rangle_m - \overline{\overline{\boldsymbol{\alpha} - \boldsymbol{\alpha}_n}}\chi\boldsymbol{\delta}\right) : \mathbb{C}^m : \left(\boldsymbol{\varepsilon} - \boldsymbol{\alpha} - \langle \boldsymbol{\beta}_n \rangle_m - \overline{\overline{\boldsymbol{\alpha} - \boldsymbol{\alpha}_n}}\chi\boldsymbol{\delta}\right) \tag{III .24}$$

- The bi-potential $b^p\left(\boldsymbol{\sigma}, \dot{\boldsymbol{\alpha}}\right)$ Here we use the same variational linearization procedure and take the same quadratic form as those used by Lahellec and Suquet (2007b) and Boudet et al. (2016), i.e. $\frac{\eta_0}{\Delta t}\left(\boldsymbol{\alpha} - \tilde{\boldsymbol{\alpha}}_n\right) : \left(\boldsymbol{\alpha} - \tilde{\boldsymbol{\alpha}}_n\right)$. In this expression, the scalar variable η_0 and second-order tensor $\tilde{\boldsymbol{\alpha}}_n$ are uniform in the elastic-plastic matrix.

With these two linearization procedures in hand, the local incremental potential J^m in (III .15) can be approximated as

$$\begin{cases} J^m\left(\boldsymbol{\varepsilon}, \boldsymbol{\sigma}, \boldsymbol{\xi}\right) \simeq J_0^m\left(\boldsymbol{\varepsilon}, \boldsymbol{\alpha}\right) + \Delta J^m\left(\boldsymbol{\sigma}, \boldsymbol{\alpha}\right) \\ J_0^m\left(\boldsymbol{\varepsilon}, \boldsymbol{\alpha}\right) = \frac{1}{2}\left(\boldsymbol{\varepsilon} - \boldsymbol{\alpha} - \langle \boldsymbol{\beta}_n \rangle_m - \overline{\overline{\boldsymbol{\alpha} - \boldsymbol{\alpha}_n}}\chi\boldsymbol{\delta}\right) : \mathbb{C}^m : \left(\boldsymbol{\varepsilon} - \boldsymbol{\alpha} - \langle \boldsymbol{\beta}_n \rangle_m - \overline{\overline{\boldsymbol{\alpha} - \boldsymbol{\alpha}_n}}\chi\boldsymbol{\delta}\right) \\ \qquad\qquad + \frac{\eta_0}{\Delta t}\left(\boldsymbol{\alpha} - \tilde{\boldsymbol{\alpha}}_n\right) : \left(\boldsymbol{\alpha} - \tilde{\boldsymbol{\alpha}}_n\right) \\ \Delta J^m\left(\boldsymbol{\sigma}, \boldsymbol{\alpha}\right) = \sigma_y\left(\alpha - \alpha_n\right)_{eq} - \frac{\eta_0}{\Delta t}\left(\boldsymbol{\alpha} - \tilde{\boldsymbol{\alpha}}_n\right) : \left(\boldsymbol{\alpha} - \tilde{\boldsymbol{\alpha}}_n\right) \end{cases} \tag{III .25}$$

where J_0^m is the linearized local incremental potential in the matrix phase.

4.2 Estimation of the effective incremental potential $\Pi_\Delta\left(\bar{\varepsilon}, \langle\, \sigma\rangle_m\right)$

Now as the local incremental potential is expressed as the sum of two terms (Eq.(III .25)), the effective incremental potential of matrix is determined by calculating the volumetric

average:

$$\Pi_{\Delta}\left(\bar{\boldsymbol{\varepsilon}}, \langle \boldsymbol{\sigma} \rangle_m\right) = \inf_{\langle \boldsymbol{\varepsilon} \rangle = \bar{\boldsymbol{\varepsilon}}} \left[f^m \left\langle \inf_{\boldsymbol{\alpha}} \left(J_0^m \left(\boldsymbol{\varepsilon}, \boldsymbol{\alpha} \right) + \Delta J^m \left(\boldsymbol{\sigma}, \boldsymbol{\alpha} \right) \right) \right\rangle_m + \sum_{r=1}^{N} f^{i,r} \left\langle w^{i,r} \left(\boldsymbol{\varepsilon} \right) \right\rangle_{i,r} \right] \tag{III .26}$$

The secant function $\eta_{sct}\left(\dot{\alpha}_{eq}, \boldsymbol{\sigma}\right)$ of the matrix phase is defined as (Lahellec and Suquet, 2007b)

$$\eta_{sct}\left(\dot{\alpha}_{eq}, \boldsymbol{\sigma}\right) = \frac{1}{3\dot{\alpha}_{eq}} \frac{\partial b^p}{\partial \dot{\alpha}_{eq}} \left(\boldsymbol{\sigma}, \boldsymbol{\alpha} \right) = \frac{\sigma_y}{3\dot{\alpha}_{eq}} \tag{III .27}$$

and Eq.(III .26) satisfies

$$\Pi_{\Delta}^m\left(\bar{\boldsymbol{\varepsilon}}, \langle \boldsymbol{\sigma} \rangle_m\right) \leq \inf_{\langle \boldsymbol{\varepsilon} \rangle = \bar{\boldsymbol{\varepsilon}}} \left\{ f^m \left[\left\langle \inf_{\boldsymbol{\alpha}} J_0^m \left(\boldsymbol{\varepsilon}, \boldsymbol{\alpha} \right) \right\rangle_m + \left\langle \sup_{\boldsymbol{\alpha}} \Delta J^m \left(\boldsymbol{\sigma}, \boldsymbol{\alpha} \right) \right\rangle_m \right] + \sum_{r=1}^{N} f^{i,r} \left\langle w^{i,r} \left(\boldsymbol{\varepsilon} \right) \right\rangle_{i,r} \right\} \tag{III .28}$$

Note that the local optimization problem in Eq. (III .28) is proceeded with respect to the internal variable $\boldsymbol{\alpha}$ only instead of the set of variables $(\boldsymbol{\alpha}, \boldsymbol{\beta})$ as defined in Eq.(II .7) at every position $\underline{x} \subset \Omega_m$. This procedure largely deduces the complexity of the local optimization problem. The estimate (III .28) of the effective potential $\Pi_{\Delta}\left(\bar{\boldsymbol{\varepsilon}}\right)$ with the non-associated perfectly plastic matrix had the similar form as that pertained to nonlinear viscoleastic composites without hardening in Lahellec and Suquet (2007b).

According to previous studies (Lahellec and Suquet, 2007b; Ponte Castaneda, 2002; Ponte Castaneda and Willis, 1999), sharper estimates of $\Pi_{\Delta}\left(\bar{\boldsymbol{\varepsilon}}, \langle \boldsymbol{\sigma} \rangle_m\right)$ can be obtained by requiring only the stationarity of ΔJ^m instead of its supremum with respect to $\boldsymbol{\alpha}$. Therefore, one gets:

$$\Pi_{\Delta}\left(\bar{\boldsymbol{\varepsilon}}, \langle \boldsymbol{\sigma} \rangle_m\right) \simeq \inf_{\langle \boldsymbol{\varepsilon} \rangle = \bar{\boldsymbol{\varepsilon}}} \left\{ f^m \left[\left\langle \inf_{\boldsymbol{\alpha}} J_0^m \left(\boldsymbol{\varepsilon}, \boldsymbol{\alpha} \right) \right\rangle_m + \left\langle \operatorname*{stat}_{\boldsymbol{\alpha}} \Delta J^m \left(\boldsymbol{\sigma}, \boldsymbol{\alpha} \right) \right\rangle_m \right] + \sum_{r=1}^{N} f^{i,r} \left\langle w^{i,r} \left(\boldsymbol{\varepsilon} \right) \right\rangle_{i,r} \right\} \tag{III .29}$$

It is worth noting that the difference function of increment potential ΔJ^m is generally non-quadratic. In order to determine the stationarity of ΔJ^m with respect to $\boldsymbol{\alpha}$, we rewrite the bi-potential in the following form:

$$b^p\left(\boldsymbol{\sigma}, \dot{\boldsymbol{\alpha}}\right) = Y(\boldsymbol{\sigma}, \frac{\left(\boldsymbol{\alpha} - \boldsymbol{\alpha}_n\right)_{eq}^2}{\Delta t^2}) \tag{III .30}$$

The concavity of Y ensures that $\left\langle Y\left(\boldsymbol{\sigma}, \boldsymbol{a}\right) \right\rangle_m \leq Y\left\langle \left(\boldsymbol{\sigma}, \boldsymbol{a}\right) \right\rangle_m$ for any field $\boldsymbol{a}\left(\underline{x}\right)$. One then obtains the following order relation:

$$\left\langle \Delta J^m\left(\boldsymbol{\sigma}, \boldsymbol{\alpha}\right) \right\rangle_m \leq \left\langle \Delta \tilde{J}^m\left(\boldsymbol{\sigma}, \boldsymbol{\alpha}\right) \right\rangle_m = \Delta t Y \left(\left\langle \boldsymbol{\sigma}, \frac{\left(\boldsymbol{\alpha} - \boldsymbol{\alpha}_n\right)_{eq}^2}{\Delta t^2} \right\rangle_m \right) - \left\langle \frac{\eta_0}{\Delta t} \left(\boldsymbol{\alpha} - \tilde{\boldsymbol{\alpha}}_n\right) : \left(\boldsymbol{\alpha} - \tilde{\boldsymbol{\alpha}}_n\right) \right\rangle_m \tag{III .31}$$

The stationarity of $\left\langle \Delta\tilde{J}^m\left(\boldsymbol{\sigma},\boldsymbol{\alpha}\right)\right\rangle_m$ with respect to $\boldsymbol{\alpha}$ yields

$$2\eta_p\frac{\left(\boldsymbol{\alpha}-\boldsymbol{\alpha}_n\right)}{\Delta t}=2\eta_0\frac{\left(\boldsymbol{\alpha}-\tilde{\boldsymbol{\alpha}}_n\right)}{\Delta t} \tag{III .32}$$

The coefficient η_p is the secant viscosity associated with the plastic material without hardening and reads

$$\eta_p=\eta_{sct}\left(\overline{\overline{\dot{\boldsymbol{\alpha}}}},\left\langle\boldsymbol{\sigma}\right\rangle_m\right)=\frac{\left\langle\sigma_y\right\rangle_m}{3\overline{\overline{\dot{\boldsymbol{\alpha}}}}},\quad\text{with }\overline{\overline{\dot{\boldsymbol{\alpha}}}}=\sqrt{\frac{2}{3}\left\langle\dot{\boldsymbol{\alpha}}:\dot{\boldsymbol{\alpha}}\right\rangle_m} \tag{III .33}$$

Notice that (II .39) can be rewritten in the following form

$$\boldsymbol{\alpha}=\frac{\boldsymbol{\alpha}_n-\theta\tilde{\boldsymbol{\alpha}}_n}{1-\theta},\quad\text{with }\theta=\frac{\eta_0}{\eta_p} \tag{III .34}$$

With this relation, the last term in (III .29) can be evaluated and $\Pi_\Delta\left(\bar{\boldsymbol{\varepsilon}}\right)$ can be further estimated as follows

$$\Pi_\Delta\left(\bar{\boldsymbol{\varepsilon}},\left\langle\boldsymbol{\sigma}\right\rangle_m\right)\simeq\Pi_0\left(\bar{\boldsymbol{\varepsilon}}\right)+f^m\Delta\Pi^m\left(\left\langle\boldsymbol{\sigma}\right\rangle_m\right) \tag{III .35}$$

with

$$\Pi_0\left(\bar{\boldsymbol{\varepsilon}}\right)=\inf_{\langle\boldsymbol{\varepsilon}\rangle=\bar{\boldsymbol{\varepsilon}}}\left[f^m\left\langle\inf_{\boldsymbol{\alpha}}J_0^m\left(\boldsymbol{\varepsilon},\boldsymbol{\alpha}\right)\right\rangle_m+\sum_{r=1}^{N}f^{i,r}\left\langle w^{i,r}\left(\boldsymbol{\varepsilon}\right)\right\rangle_{i,r}\right] \tag{III .36a}$$

$$\Delta\Pi^m\left(\left\langle\boldsymbol{\sigma}\right\rangle_m\right)=\left\langle\frac{\eta_p\theta}{\Delta t\left(\theta-1\right)}\left(\boldsymbol{\alpha}_n-\tilde{\boldsymbol{\alpha}}_n\right):\left(\boldsymbol{\alpha}_n-\tilde{\boldsymbol{\alpha}}_n\right)\right\rangle_m \tag{III .36b}$$

By using the stationarity condition of (III .35) over $\tilde{\boldsymbol{\alpha}}_n$ and θ, one obtains:

$$\theta=1\pm\sqrt{\frac{\left\langle\left(\boldsymbol{\alpha}_n-\tilde{\boldsymbol{\alpha}}_n\right):\left(\boldsymbol{\alpha}_n-\tilde{\boldsymbol{\alpha}}_n\right)\right\rangle_m}{\left\langle\left(\boldsymbol{\alpha}-\tilde{\boldsymbol{\alpha}}_n\right):\left(\boldsymbol{\alpha}-\tilde{\boldsymbol{\alpha}}_n\right)\right\rangle_m}} \tag{III .37}$$

$$\tilde{\boldsymbol{\alpha}}_n=\frac{\left\langle\boldsymbol{\alpha}_n\right\rangle_m+\left(\ \theta-1\right)\left\langle\boldsymbol{\alpha}\right\rangle_m}{\theta} \tag{III .38}$$

With the help of minimization of $J_0^m\left(\boldsymbol{\varepsilon},\boldsymbol{\alpha}\right)$ with respect to $\boldsymbol{\alpha}$, one finally obtains (the detailed calculation given in Appendix B):

$$\boldsymbol{\alpha}=\left(\mathbb{C}^m+\frac{2\theta\eta}{\Delta t}\mathbb{K}\right)^{-1}:\left[\mathbb{K}:\mathbb{C}^m:\boldsymbol{\varepsilon}+\frac{2\theta\eta}{\Delta t}\tilde{\boldsymbol{\alpha}}_n\right]=d\mathbb{K}:\boldsymbol{\varepsilon}+e\tilde{\boldsymbol{\alpha}}_n \tag{III .39a}$$

where $d=\frac{\mu}{\frac{\eta\theta}{\Delta t}+\mu}$, $e=\frac{\frac{\eta\theta}{\Delta t}}{\frac{\eta\theta}{\Delta t}+\mu}$. η denotes the uniform total secant viscosity taken at $\overline{\overline{\dot{\boldsymbol{\alpha}}}}$ of the non-associated plastic matrix with isotropic hardening

$$\eta\left(\overline{\overline{\dot{\boldsymbol{\alpha}}}},\left\langle\boldsymbol{\sigma}\right\rangle_m\right)=-\frac{\kappa\left(\left\langle\sigma_m\right\rangle_m-c\right)}{\overline{\overline{\dot{\boldsymbol{\alpha}}}}} \tag{III .40}$$

4.3 Estimation of the effective potential of homogenized material

The estimation of the effective potential of heterogeneous rock-like materials is based on the choice of a thermoelastic linear comparison composite (LCC). Substituting the result found in (III .39a) into the expression of $J_0^m(\boldsymbol{\varepsilon}, \boldsymbol{\alpha})$ in (III .25) and combining with Eq.(III .34), one defines the local increment potential $\pi_0^m(\boldsymbol{\varepsilon})$ of the thermoelastic LCC as follows:

$$\pi_0^m(\boldsymbol{\varepsilon}) = \inf_{\boldsymbol{\alpha}} J_0^m(\boldsymbol{\varepsilon}, \boldsymbol{\alpha}) = \frac{1}{2}\boldsymbol{\varepsilon} : \mathbb{C}_0^m : \boldsymbol{\varepsilon} + \boldsymbol{\rho}_0^m : \boldsymbol{\varepsilon} + \zeta_0^m \tag{III .41}$$

The tensors $\mathbb{C}_0^m$ and $\boldsymbol{\rho}_0^m$ as well as the scalar coefficient ζ_0^m are all uniform in the matrix phase and given by:

$$\begin{cases} \mathbb{C}_0^m = 3k^m\mathbb{J} + 2\mu_0^m\mathbb{K}, \quad \text{with} \;\; \mu_0^m = (1-d)^2\mu^m + \frac{\theta\eta_p}{\Delta t}d^2 \\ \boldsymbol{\rho}_0^m = 2\left[\frac{\theta\eta_p}{\Delta t}d\,(e-1) - \mu^m\,(1-d)\right]\tilde{\boldsymbol{\alpha}}_n - 3k^m\left(\langle\boldsymbol{\beta}_n\rangle_m + \overline{\overline{\boldsymbol{\alpha}-\boldsymbol{\alpha}_n}}\chi\boldsymbol{\delta}\right) \\ \zeta_0^m = \left[e^2\mu^m + \frac{\theta\eta_p}{\Delta t}(e-1)^2\right]\tilde{\boldsymbol{\alpha}}_n : \tilde{\boldsymbol{\alpha}}_n + \frac{9}{2}k^m\left(\langle\beta_n\rangle_m + \overline{\overline{\boldsymbol{\alpha}-\boldsymbol{\alpha}_n}}\chi\right)^2 \end{cases} \tag{III .42}$$

The quantities θ, $\tilde{\boldsymbol{\alpha}}_n$ and η are defined in Eqs.(III .37), (III .38) and (III .40), respectively. Further, the effective free energy $\Pi_0(\bar{\boldsymbol{\varepsilon}})$ defined in Eq. (III .36a) can be written as

$$\Pi_0(\bar{\boldsymbol{\varepsilon}}) = \frac{1}{2}\bar{\boldsymbol{\varepsilon}} : \bar{\mathbb{C}} : \bar{\boldsymbol{\varepsilon}} + \bar{\boldsymbol{\rho}} : \bar{\boldsymbol{\varepsilon}} + \bar{\zeta} \tag{III .43}$$

The effective tensors of $\bar{\mathbb{C}}$, $\bar{\boldsymbol{\rho}}$ and scale $\bar{\zeta}$ are expressed in Appendix C.

By using the expression of $\Pi_0(\bar{\boldsymbol{\varepsilon}})$ (Eq. (III .43)) in (III .36a), the the macroscopic stress $\bar{\boldsymbol{\sigma}}$ of the RVE as that defined in Eq. (III .22) can be approximated by the following differentiation procedure:

$$\bar{\boldsymbol{\sigma}} = \frac{\partial\Pi_\Delta}{\partial\bar{\boldsymbol{\varepsilon}}}(\bar{\boldsymbol{\varepsilon}}, \langle\boldsymbol{\sigma}\rangle_m) = \frac{\mathrm{d}\Pi_0}{\mathrm{d}\bar{\boldsymbol{\varepsilon}}}(\bar{\boldsymbol{\varepsilon}}) = f^m\langle\boldsymbol{\sigma}\rangle_m + \sum_{r=1}^{N} f^{i,r}\langle\boldsymbol{\sigma}\rangle_{i,r} \tag{III .44}$$

with

$$\langle\boldsymbol{\sigma}\rangle_m = \mathbb{C}_0^m : \langle\boldsymbol{\varepsilon}\rangle_m + \boldsymbol{\rho}_0 \tag{III .45a}$$

$$\langle\boldsymbol{\sigma}\rangle_{i,r} = \mathbb{C}^{i,r} : \langle\boldsymbol{\varepsilon}\rangle_{i,r} \tag{III .45b}$$

5 Fluctuations of local fields and computational aspects

5.1 Fluctuations of local fields in matrix

In order to assess the accuracy of the BIV model, not only macroscopic responses of the RVE but also representative fluctuations of local fields are generally investigated. In

this study, we shall evaluate fluctuations of local stress and plastic strain fields in the elastic-plastic matrix. The fluctuations of interest correspond to the first- and second-order moments of the these fields. Following Idiart and Castañeda (2007) the quadratic fluctuation of the local stress in the matrix is defined as

$$\mathbb{F}^m_{\boldsymbol{\sigma}} \equiv \langle \boldsymbol{\sigma} - \langle \boldsymbol{\sigma} \rangle_m \rangle_m \otimes \langle \boldsymbol{\sigma} - \langle\, \boldsymbol{\sigma} \rangle_m \rangle_m = \langle \boldsymbol{\sigma} \otimes \boldsymbol{\sigma} \rangle_m - \langle\, \boldsymbol{\sigma} \rangle_m \otimes \langle \boldsymbol{\sigma} \rangle_m \tag{III .46}$$

where $\langle \boldsymbol{\sigma} \rangle_m$ and $\langle \boldsymbol{\sigma} \otimes \boldsymbol{\sigma} \rangle_m$ represent the first and second-order moment of local stress field over the matrix. $\langle \boldsymbol{\sigma} \rangle_m$ can be obtained from the relation (III .45a). However it is generally difficult to calculate $\langle \boldsymbol{\sigma} \otimes \boldsymbol{\sigma} \rangle_m$. In order to amend this issue, here we adopt the following expression proposed in (Agoras et al., 2016)

$$\sqrt{\mathbb{F}^m_{\boldsymbol{\sigma}} :: \mathbb{K}} = \sqrt{\langle \boldsymbol{s} : \boldsymbol{s} \rangle_m - \langle \boldsymbol{s} \rangle_m : \langle \boldsymbol{s} \rangle_m} = \sqrt{\frac{2}{3}\left(\overline{\overline{\boldsymbol{\sigma}}}^2 - \left(\bar{\sigma}^m_{eq}\right)^2\right)} \tag{III .47}$$

with $\bar{\sigma}^{(m)}_{eq} = \sqrt{\frac{3}{2}\langle \boldsymbol{s} \rangle_m : \langle \boldsymbol{s} \rangle_m}$ and $\overline{\overline{\boldsymbol{\sigma}}} = \sqrt{\frac{3}{2}\langle \boldsymbol{s} : \boldsymbol{s} \rangle_m}$ for the evaluation of $\langle \boldsymbol{s} \rangle_m$ and $\langle \boldsymbol{s} : \boldsymbol{s} \rangle_m$. Together with Eq.(III .73), one further obtains

$$\overline{\overline{\boldsymbol{\sigma}}} = 3\eta \overline{\overline{\dot{\boldsymbol{\alpha}}}} \tag{III .48}$$

The calculation of the denominator $\overline{\overline{\dot{\boldsymbol{\alpha}}}}$ is given in Section 5.3. One can notice that it is easy to obtain the fluctuation of local stress field (III .47) with the help of Eqs. (III .45a) and (III .48).

Similarly, the fluctuation of the local plastic strain field in the matrix is defined as

$$\mathbb{F}^m_{\boldsymbol{\varepsilon}^p} \equiv \langle \boldsymbol{\varepsilon}^p - \langle \boldsymbol{\varepsilon}^p \rangle_m \rangle_m \otimes \langle\, \boldsymbol{\varepsilon}^p - \langle \boldsymbol{\varepsilon}^p \rangle_m \rangle_m = \langle \boldsymbol{\varepsilon}^p \otimes \boldsymbol{\varepsilon}^p \rangle_m - \langle\, \boldsymbol{\varepsilon}^p \rangle_m \otimes \langle\, \boldsymbol{\varepsilon}^p \rangle_m \tag{III .49}$$

where $\langle \boldsymbol{\varepsilon}^p \rangle_m$ and $\langle \boldsymbol{\varepsilon}^p \otimes \boldsymbol{\varepsilon}^p \rangle_m$ represent the first and second-order moment of local plastic strain field over the matrix. For the ease of calculation, we provide the result for the standard derivation of the plastic strain filed in the matrix phase, which reads

$$\sqrt{\mathbb{F}^m_{\boldsymbol{\varepsilon}^p} :: \mathbb{K}} = \sqrt{\langle \boldsymbol{\alpha} : \boldsymbol{\alpha} \rangle_m - \langle \boldsymbol{\alpha} \rangle_m : \langle \boldsymbol{\alpha} \rangle_m} = \sqrt{\frac{3}{2}\left(\overline{\overline{\boldsymbol{\alpha}}}^2 - \left(\bar{\alpha}^m_{eq}\right)^2\right)} \tag{III .50}$$

with $\bar{\alpha}^m_{eq} = \sqrt{\frac{2}{3}\langle \boldsymbol{\alpha} \rangle_m : \langle \boldsymbol{\alpha} \rangle_m}$ and $\overline{\overline{\boldsymbol{\alpha}}} = \sqrt{\frac{2}{3}\langle \boldsymbol{\alpha} : \boldsymbol{\alpha} \rangle_m}$, being the first- and second-order moment of $\boldsymbol{\alpha}$.

5.2 Computation of the first and second-order moment of α

The calculation of θ, $\tilde{\boldsymbol{\alpha}}_n$ and $\sqrt{\mathbb{F}^m_{\boldsymbol{\varepsilon}^p} :: \mathbb{K}}$ from Eqs.(III .37), (III .38) and (III .50) needs the determination of the first- and second-order moment of $\boldsymbol{\alpha}$ in the plastic matrix. The first moment is given by:

$$\langle \boldsymbol{\alpha} \rangle_m = \langle d\mathbb{K} : \boldsymbol{\varepsilon} + e\tilde{\boldsymbol{\alpha}}_n \rangle_m \tag{III .51}$$

Since the quantities d, e and $\tilde{\boldsymbol{\alpha}}_n$ are uniform in the matrix phase, one thus obtains

$$\langle \boldsymbol{\alpha} \rangle_m = d\mathbb{K} : \langle \boldsymbol{\varepsilon} \rangle_m + e : \tilde{\boldsymbol{\alpha}}_n \tag{III .52}$$

Similarly, the second-order moment of $\boldsymbol{\alpha}$ is calculated by:

$$\langle \boldsymbol{\alpha} : \boldsymbol{\alpha} \rangle_m = d^2\mathbb{K} :: \langle \boldsymbol{\varepsilon} \otimes \boldsymbol{\varepsilon} \rangle_m + 2de\tilde{\boldsymbol{\alpha}}_n : \langle \boldsymbol{\varepsilon} \rangle_m + e^2\tilde{\boldsymbol{\alpha}}_n : \tilde{\boldsymbol{\alpha}}_n \tag{III .53}$$

The first term and the second term at the right hand side of Eq.(III .53) are related to the second- and first-order moment of $\boldsymbol{\varepsilon}$ in the matrix phase and can be obtained from Eqs.(II .78) and (II .75), respectively.

5.3 Computation of the second-order moment of $\dot{\alpha}$

To calculate η from Eq.(III .40), the denominator $\overline{\overline{\dot{\boldsymbol{\alpha}}}}$ related to the second-order moment of $\dot{\boldsymbol{\alpha}}$ should be first determined by

$$\overline{\overline{\dot{\boldsymbol{\alpha}}}} = \sqrt{\frac{2}{3}\left\langle \dot{\boldsymbol{\alpha}} : \dot{\boldsymbol{\alpha}} \right\rangle_m} = \frac{1}{\Delta t}\sqrt{\frac{2}{3}\left\langle (\boldsymbol{\alpha} - \boldsymbol{\alpha}_n) : (\boldsymbol{\alpha} - \boldsymbol{\alpha}_n) \right\rangle_m} \tag{III .54}$$

It is noted that it is generally difficult to calculate $\langle (\boldsymbol{\alpha} - \boldsymbol{\alpha}_n) : (\boldsymbol{\alpha} - \boldsymbol{\alpha}_n) \rangle_m$ due to inaccessibility of the term $\langle \boldsymbol{\alpha} : \boldsymbol{\alpha}_n \rangle_m$. However, thanks to Eq.(III .38), $\overline{\overline{\dot{\boldsymbol{\alpha}}}}$ can be alternatively calculated by the following relation when $\theta \neq 1$

$$\begin{aligned} \overline{\overline{\dot{\boldsymbol{\alpha}}}} &= \left[\frac{\theta}{\Delta t\,(1-\theta)}\right]\sqrt{\frac{2}{3}\left\langle (\boldsymbol{\alpha_n} - \tilde{\boldsymbol{\alpha}}_n) : (\boldsymbol{\alpha_n} - \tilde{\boldsymbol{\alpha}}_n) \right\rangle_m} \\ &= \left[\frac{\theta}{\Delta t\,(1-\theta)}\right]\sqrt{\frac{2}{3}\left(\langle \boldsymbol{\alpha_n} : \boldsymbol{\alpha_n} \rangle_m - 2\left\langle \boldsymbol{\alpha}_n \right\rangle_m : \tilde{\boldsymbol{\alpha}}_n + \tilde{\boldsymbol{\alpha}}_n : \ \tilde{\boldsymbol{\alpha}}_n\right)} \end{aligned} \tag{III .55}$$

where the first- and second-order moment of $\boldsymbol{\alpha}$ are already determined from (III .52) and (III .53) respectively.

6 Implementation and numerical validation of the model

6.1 Numerical implementation algorithm

The numerical implantation algorithm of the proposed BIV model is now presented. This algorithm is developed as a user-defined subroutine for the determination of mechanical behavior of a macroscopic material point in a standard computation code. The material point is subjected to a macroscopic strain increment $\Delta\bar{\boldsymbol{\varepsilon}}$ ($\Delta\bar{\boldsymbol{\varepsilon}} = \dot{\bar{\boldsymbol{\varepsilon}}}\Delta t$) such that $\bar{\boldsymbol{\varepsilon}}_{n+1} = \bar{\boldsymbol{\varepsilon}}_n + \Delta\bar{\boldsymbol{\varepsilon}}$ at t_{n+1}. The numerical algorithm is here used to calculate the macroscopic stress increment using the proposed BIV model. The flowchart of the computational procedure is summarized in Algorithm 2:

Algorithm 2: Flowchart of the local implementation algorithm of BIV

Input: $\dot{\bar{\boldsymbol{\varepsilon}}}, \Delta t, \bar{\boldsymbol{\sigma}}_n, \bar{\boldsymbol{\varepsilon}}_n, \langle\boldsymbol{\alpha}_n\rangle_m, \langle\boldsymbol{\beta}_n\rangle_m, \langle\boldsymbol{\alpha}_n : \boldsymbol{\alpha}_n\rangle_m, \theta_n, \eta_n$

Output: $\bar{\boldsymbol{\sigma}}_{n+1}, \bar{\boldsymbol{\varepsilon}}_{n+1}, \langle\boldsymbol{\alpha}_{n+1}\rangle_m, \langle\boldsymbol{\beta}_{n+1}\rangle_m, \langle\boldsymbol{\alpha}_{n+1} : \boldsymbol{\alpha}_{n+1}\rangle_m, \theta_{n+1}, \eta_{n+1}$

$\bar{\boldsymbol{\varepsilon}}_{n+1} = \bar{\boldsymbol{\varepsilon}}_n + \dot{\bar{\boldsymbol{\varepsilon}}}\Delta t$,

Initialize $\eta_{n+1} = \eta_n, \theta_{n+1} = \theta_n$

Calculate $\mathbb{A}^m_{n+1}$, $\mathbb{A}^{i,r}_{n+1}$, $\boldsymbol{a}^m_{n+1}$, $\boldsymbol{a}^{i,r}_{n+1}$, $\mathbb{C}^m_{0,n+1}$, $\boldsymbol{\rho}^m_{0n+1}$,

Calculate first order moment of strain field $\langle\boldsymbol{\varepsilon}_{n+1}\rangle^{trial}_m = \mathbb{A}^m_{n+1} : \bar{\boldsymbol{\varepsilon}} + \boldsymbol{a}^m_{n+1}$, $\langle\boldsymbol{\varepsilon}_{n+1}\rangle^{trial}_{i,r} = \mathbb{A}^{i,r}_{n+1} : \bar{\boldsymbol{\varepsilon}} + \boldsymbol{a}^{i,r}_{n+1}$,

Elastic prediction: $\langle\boldsymbol{\sigma}_{n+1}\rangle^{trial}_m = \mathbb{C}^m : (\langle\boldsymbol{\varepsilon}_{n+1}\rangle^{trial}_m - \langle\boldsymbol{\alpha}_n\rangle_m - \langle\boldsymbol{\beta}_n\rangle_m)$

if $f(\langle\boldsymbol{\sigma}_{n+1}\rangle^{trial}_m) < 0$ **then**

  $\langle\boldsymbol{\varepsilon}_{n+1}\rangle_m = \langle\boldsymbol{\varepsilon}_{n+1}\rangle^{trial}_m ; \langle\boldsymbol{\varepsilon}_{n+1}\rangle_{i,r} = \langle\boldsymbol{\varepsilon}_{n+1}\rangle^{trial}_{i,r}$ $\langle\boldsymbol{\alpha}_{n+1}\rangle_m = \mathbf{0}; \langle\boldsymbol{\beta}_{n+1}\rangle_m = \mathbf{0}; \langle\boldsymbol{\alpha}_{n+1} : \boldsymbol{\alpha}_{n+1}\rangle_m = 0$

else

  (For clarity, the subscript n+1 will be omitted in the *for* loop)

  for $j = 1 \ldots m_{iter}$, **do**

    Calculate $\mathbb{C}^m_{0,j}$, $\boldsymbol{\rho}^m_{0,j}$, $\varsigma^m_{0,j}$ and $\bar{\mathbb{C}}_j$ with Eqs. (III .42) and (II .74a)

    Calculate $\mathbb{A}^m_j$, $\mathbb{A}^{i,r}_j$, $\boldsymbol{a}^m_j$, $\boldsymbol{a}^{i,r}_j$ (with Eq.(II .79) for two-phases composite).

    Calculate first moment of strain field $\langle\boldsymbol{\varepsilon}\rangle_{m,j} = \mathbb{A}^m_j : \bar{\boldsymbol{\varepsilon}} + \boldsymbol{a}^m_j$ and $\langle\boldsymbol{\varepsilon}\rangle_{i,r,j} = \mathbb{A}^{i,r}_j : \bar{\boldsymbol{\varepsilon}} + \boldsymbol{a}^{i,r}_j$ with Eqs.(II .75) and (II .76) ;

    Calculate $\langle\boldsymbol{\sigma}\rangle_{m,j}$ and $\langle\boldsymbol{\sigma}\rangle_{i,r,j}$ by using Eq.(III .45);

    Calculate effective internal variable $\tilde{\boldsymbol{\alpha}}_{n,j}$ and $\langle\boldsymbol{\alpha}\rangle_{m,j}$ with Eqs.(III .38) and (III .52);

    Calculate second moment of strain field $\mathbb{K} :: \langle\boldsymbol{\varepsilon}\otimes\boldsymbol{\varepsilon}\rangle_{m,j}$ and $\langle\boldsymbol{\alpha} : \boldsymbol{\alpha}\rangle_{m,j}$ with Eqs.(II .78) and (III .53);

    Calculate $\bar{\bar{\boldsymbol{\alpha}}}_j$ and $\langle\boldsymbol{\beta}\rangle_j$ with Eqs.(III .55) and (III .61)

    Calculate θ_j and η_j with Eqs.(III .37) and (III .40);

    if $\frac{|\delta\theta_j|}{\theta_j} < \epsilon$ *and* $\frac{|\delta\eta_j|}{\eta_j} < \epsilon$, **then**

      Return;

    else

      $j = j + 1$

    end

  end

  $\bar{\boldsymbol{\sigma}}_{n+1} = \langle\boldsymbol{\sigma}_{n+1}\rangle = f^m \langle\boldsymbol{\sigma}_{n+1}\rangle_m + \sum_{r=1}^N f^{i,r} \langle\boldsymbol{\sigma}_{n+1}\rangle_{i,r}$;

end

6.2 Comparisons with direct FEM simulations

The purpose of this section is to verify the accuracy of the BIV model by comparing its prediction with the reference solutions obtained by direct finite element simulations on the unit cell for two kinds of materials. The first one is a composite material with a non-associated Drucker-Prager plastic matrix and elastic inclusions (Figure II .2(b)), while the

second one is a porous material with non-associated Drucker-Prager matrix and pores . In this section and section 7, the effective properties of the LCC as well as the field statistics are evaluated by using the Hashinand Shtrikman bounds, i.e., the HS lower bound for inclusion-reinforced material and upper bound for porous material, more details are given in Appendix C in Chapter II. The microstructure of studied materials is represented by a periodic assembly of 3D unit cells with spherical inclusion or pore. Taking advantage of axial symmetry, the actual hexagonal unit cell is approximated by a cylinder one and only half an axial symmetry plain is considered in the finite element calculations, as illustrated in Figure II .2. The first- and second-order moments of the local fields under study are computed from direct volume averaging of the local fields in the unit cell (Yan et al., 2007).

For the inclusion-reinforced material, the solid matrix obeys non-associated Drucker-Prager perfect plasticity. The model's parameters for each constituent phase are listed in Tables III .1 and III .2. Uniaxial and triaxial compression tests are investigated. The unit cell is first subjected to a confining stress or hydrostatic stress and then a differential stress by increasing the axial strain in the z direction. During the differential stress stage, the lateral displacement $\bar{U}_2$ is kept uniform along the boundary to satisfy the uniform strain boundary condition. The boundary conditions are illustrated in Figure II .2(b) and summarized as follows

$$\begin{cases} U_3(r,H) = \bar{U}_3, & 0 < r < L \\ U_2(L,z) = \bar{U}_2, & 0 < z < H \\ U_3(r,0) = 0, & 0 < r < L \\ U_2(0,z) = 0, & 0 < z < H \end{cases} \tag{III .56}$$

Table III .1: Parameters of solid matrix for composite

E^m (MPa)	ν^m	κ	c(MPa)	χ_m
3000	0.3	0.227	30	0.083

Similarly, the solid phase of porous material is described by a non-associated Drucker-Prager type plastic matrix. The parameters for the matrix are listed in Table III .1. The boundary conditions on the unit cell are given below and illustrated in Figure II .2(c).

Table III .2: Parameters of elastic inclusion

E^i (MPa)	ν^i
98000	0.15

$$\begin{cases} U_3(r,H) = \bar{U}_3, & 0 < r < L \\ U_2(L,z) = \bar{U}_2, & 0 < z < H \\ U_3(r,0) = 0, & R < r < L \\ U_2(0,z) = 0, & R < z < H \end{cases} \tag{III .57}$$

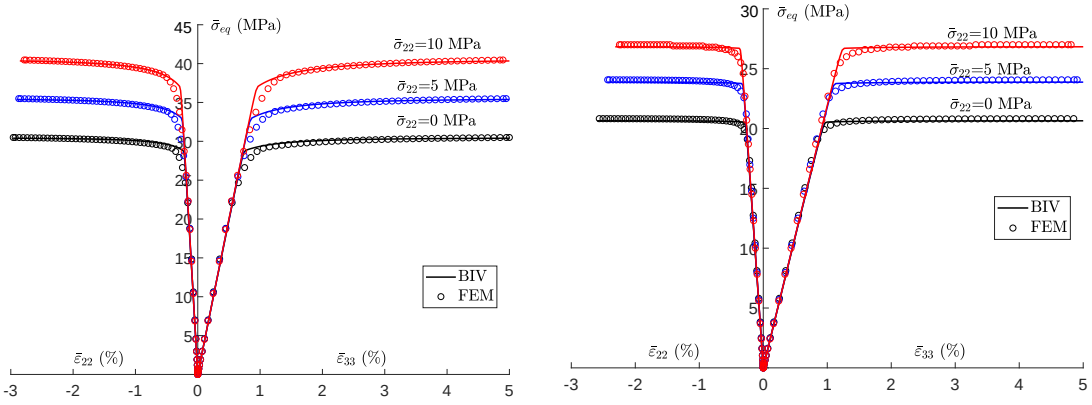

(a) Inclusion-reinforced material (b) Porous material

Figure III .1: Macroscopic predictions for two kinds of composite material with non-associated Drucker-Prager perfectly plastic matrix and inclusion/pores ($f^i = 15\%$) under triiaxial compressions with different confining stress

Figure III .1 shows the macroscopic stress-strain curves for both the inclusion-reinforced material and porous material under uniaxial and triaxial compression tests with different confining stresses, respectively obtained by the proposed BIV model and direct finite element simulations. One can observe that the model's predictions coincide very well with the FEM solutions both for the all cases considered.

7 Extension to non-associated plastic matrix with isotropic hardening

It is acknowledged that the isotropic plastic hardening of rock-like materials is usually described by the evolution of internal frictional coefficient κ. In this study, we consider the following specific hardening law:

$$\kappa(\gamma^p) = \kappa_m - (\kappa_m - \kappa_0)\, e^{-b_1 \gamma^p} \tag{III .58}$$

where κ_0 and κ_m denote the initial threshold and the asymptotic value of the frictional coefficient respectively, while b_1 is a parameter controlling the plastic hardening rate.

Without loss of generality, we assume that χ is also a function of γ^p

$$\chi(\gamma^p) = \chi_m(1 - e^{-b_2 \gamma^p}) \tag{III .59}$$

where χ_m is the asymptotic value of the plastic dilatancy coefficient.

In order to account for this kind of plastic hardening in the BIV model and avoid complex mathematical treatment, we shall here propose a heuristic extension of the model formulated for materials without plastic hardening. According to the theoretical formulation presented in Sections 3 and 4, when the values κ and c are constant, the average secant viscosity function of solid matrix η is given in Eq.(III .40). We here assume that this result remains applicable for the solid matrix where the value of κ is updated at each loading increment. Therefore, the average secant viscosity function is written as:

$$\eta = -\frac{\kappa\left(\langle \gamma_n^p \rangle_m\right)\left(\langle \sigma_m \rangle_m - c\right)}{\bar{\bar{\boldsymbol{\alpha}}}} \tag{III .60}$$

In this expression, $\langle \gamma_n^p \rangle_m$ is the average value of equivalent plastic shear strain field in the solid matrix γ^p at step n, which is shown in Eq.(III .62). It is noted that when the isotropic hardening is considered, the values of frictional coefficient $\kappa\left(\langle \gamma_n^p \rangle_m\right)$ and plastic dilatancy coefficient $\chi\left(\langle \gamma_n^p \rangle_m\right)$ are updated and keep constant at each loading increment, implying an explicit calculation for $\kappa\left(\langle \gamma_n^p \rangle_m\right)$ and $\chi\left(\langle \gamma_n^p \rangle_m\right)$ are taken.

7.1 Comparisons with direct FEM simulations

Here the validations of the heuristic extended BIV model for rock-like materials with an isotropic hardening are conducted by comparing the BIV predictions with direct FEM simulations both for local and macroscopic scale responses. We here also consider two kinds of rock-like materials: inclusion-reinforced material and porous material. Conventional triaxial compression tests are studied. The boundary conditions for these two materials

are same as those presented in Section 6.2. We here choose $\kappa_0 = 1 \times 10^{-5}$, $\kappa_m = 0.227$, $b_1 = 140$, $\chi_m = 0.083$ and $b_2 = 70$ for the following numerical simulations.

7.1.1 Inclusion-reinforced material

Two volume fractions of elastic inclusion are considered: $f^i = 5\%$ and $f^i = 15\%$. In Figure III .2, we show the macroscopic stress-strain curves for the uniaxial compression test obtained by BIV and FEM. It can be seen that there is a good agreement between these two results. In Figure III .3, we emphasize the volume strain evolution $\bar{\varepsilon}_v$ as a function of axial strain $\bar{\varepsilon}_{33}$ with different values of dilatancy coefficient χ_m and for $f^i = 15\%$. It is noticed that the proposed BIV model is able to well reproduce the volume compressibility-dilatancy transition which is controlled by the parameter χ_m. More precisely, the volumetric dilatancy is enhanced when the value of χ_m increases. The results due to the BIV model well coincident with the FEM simulations.

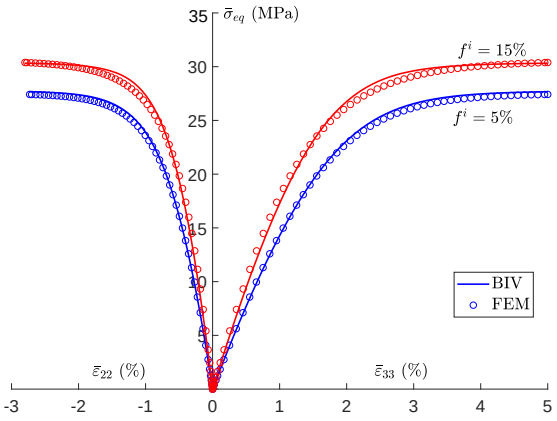

Figure III .2: Macroscopic stress-strain curves under uniaxial compression for an inclusion-reinforced material with two volume fractions of inclusions ($f^i = 5\%$ and $f^i = 15\%$)

Moreover, the proposed BIV model is also able to account for the influence of confining stress on the macroscopic response of composite material. This is illustrated in Figure III .4. The stress-strain curves are presented for two triaxial compression tests respectively with a different confining stress of 10MPa and 20MPa. Again, the BIV predictions coincide with the FEM solutions very well.

In order to further assess the accuracy of the BIV model, the evolution of local stresses during the loading history is also investigated for the case of uniaxial compression and taking $f^i = 15\%$. For instance, the evolution of average stress respectively in the inclusion

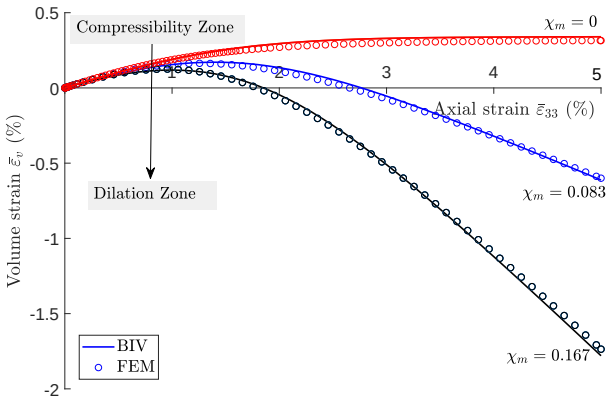

Figure III .3: Evolution of macroscopic volumetric strain for different values of plastic dilatancy coefficient χ in uniaxial compression for an inclusion-reinforced material with a volume fraction of inclusions of $f^i = 15\%$

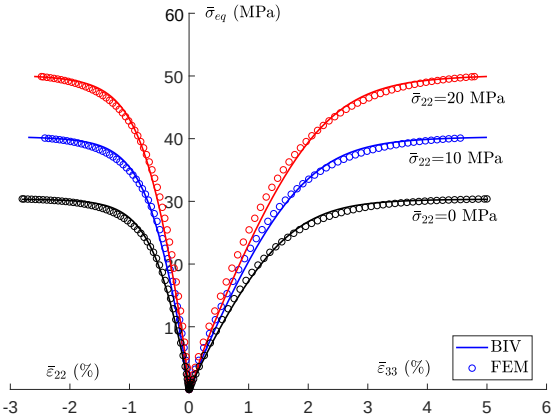

Figure III .4: Macroscopic stress-strain curves under triaxial compression with two different confining stresses two for an inclusion-reinforced material with $c^{(2)} = 15\%$

and matrix is presented in Figure III .5(a). In Figure III .5(b), one finds the evolution with respect to the macroscopic axial strain of the different denominators $\bar{\sigma}^m_{eq}$ and $\overline{\overline{\boldsymbol{\sigma}}}$, respectively related to first-order and second-order moment of the stress over the matrix. Lastly, in Figure III .5(c), the evolution of the stress fluctuations $\sqrt{\mathbb{F}^m_{\boldsymbol{\sigma}} :: \mathbb{K}}$ in the matrix is presented. It is observed that the BIV model provides an accurate prediction for the evolution of average stress within the matrix, while a less accurate prediction regarding the average inclusion response (Figure III .5(a)). The BIV results are also in good agreement with the FEM solutions for the stress moments $\bar{\sigma}^m_{eq}$ and $\overline{\overline{\boldsymbol{\sigma}}}$ (Figure III .5(b)). Lastly, although the BIV model overestimates the stress fluctuation within the matrix, it is still able to reproduce the good evolution trend of FEM solutions (Figure III .5(c)).

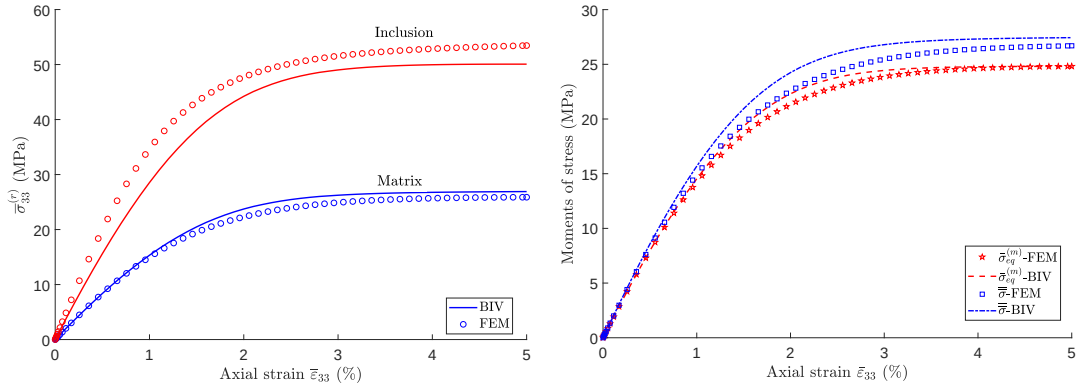

(a) Evolution of phase average stress versus macroscopic strain

(b) First and second moments of stress over matrix

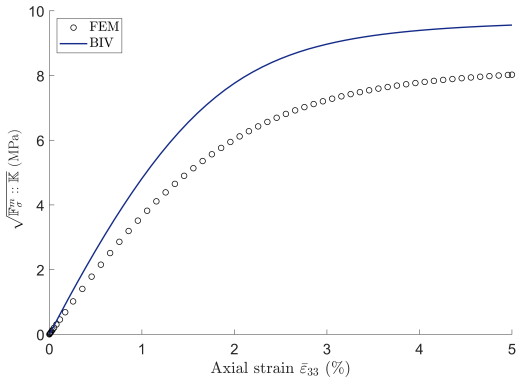

(c) Fluctuations of stress over matrix

Figure III .5: Local stress responses under uniaxial compression in an inclusion-reinforced material with $f^{(i} = 15\%$

On the other hand, the evolution of the local plastic strain is also studied. In Figure III .6(a), one can find a quite good agreement between the BIV result and FEM solution for the first-order moment of plastic strain over the matrix $\bar{\alpha}_{eq}^{m}$. However, it seems that the BIV model underestimates the second-order moment of plastic strain in the matrix $\overline{\overline{\boldsymbol{\alpha}}}$. The fluctuation of plastic strain field is shown in Figure III .6(b). The BIV model is able to capture the trend of the FEM solution although there exist some scatters between them.

7.1.2 Porous material with non-associated plastic matrix

The macroscopic stress-strain curves uniaxial compression with two values of porosity $f^i = 15\%$ and 5% are presented in Figure III .7. There is a good agreement between the

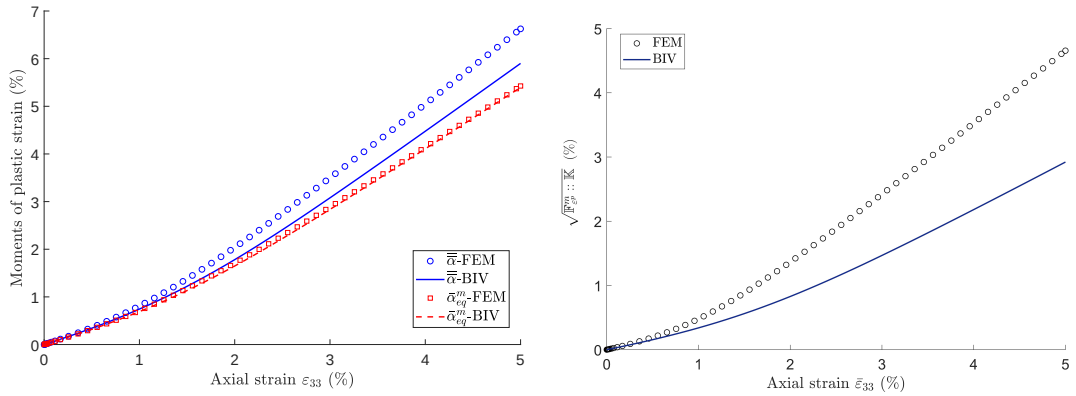

(a) First and second moments of plastic strain over matrix

(b) Fluctuation of plastic strain over matrix

Figure III .6: Local plastic strain responses under uniaxial compression of an inclusion-reinforced material with $f^{(i} = 15\%$

BIV predictions and FEM results. Furthermore, the stress-strain curves under triaxial compression with three different confining stresses are presented in Figure III .8 for a porosity of $f^i = 15\%$. Once again, the BIV model correctly captures the effect of confining stress and well reproduces the FEM solutions.

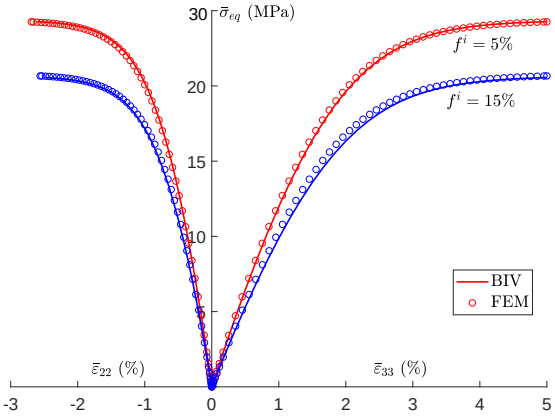

Figure III .7: Macroscopic stress-strain curves in uniaxial compression for a porous material with two different porosity ($f^i = 5\%$ and $f^i = 15\%$)

As for the inclusion-reinforced composite materials, the local stress and strain responses of porous material are investigated for the case of uniaxial compression and with a porosity of $f^i = 15\%$. In Figure III .9(a), the evolution of the first and second-order moment of local stress over the matrix, $\bar{\sigma}_{eq}^{m}$ and $\overline{\overline{\boldsymbol{\sigma}}}$, is depicted. The evolution of the stress fluctuations is given in Figure III .9(b). One can find a similar trend as that already obtained in Figure

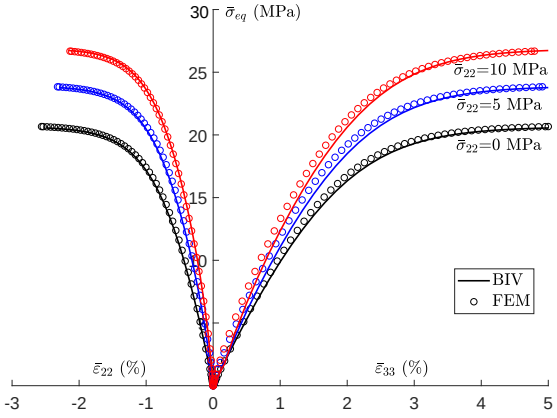

Figure III .8: Macroscopic stress-strain curves in triaxial compression with three different confining stresses for a porous material with a porosity of $f^i = 15\%$

III .5 for the inclusion-reinforced material. The evolution of the moments and fluctuations of local plastic strain field over the matrix is shown in Figure III .10. As shown in Figure III .10(a), although the BIV model qualitatively reproduces the trend of the FEM solution, it slightly underestimates the denominators $\bar{\alpha}^m_{eq}$ and $\overline{\overline{\boldsymbol{\alpha}}}$. Compared with Figures III .10(b) and III .6(b), the fluctuations of the plastic strain field are now better captured by the BIV model for the porous material than for the inclusion-reinforced material.

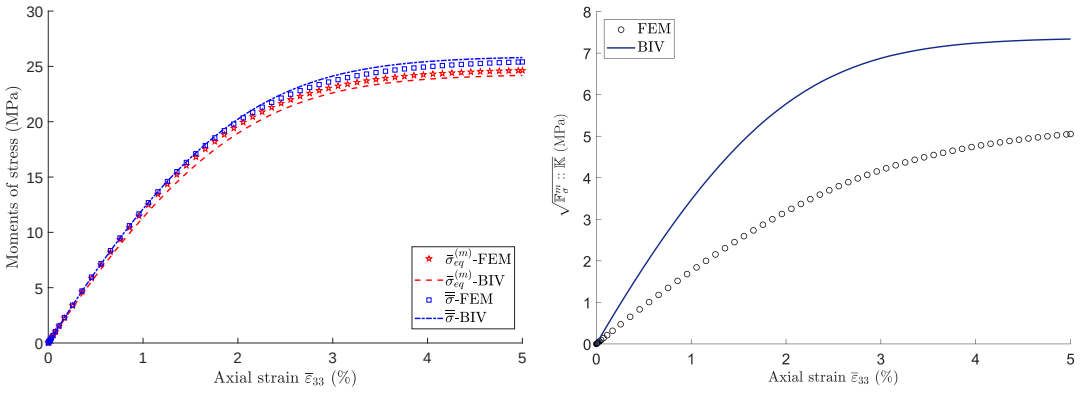

(a) First- and second-order moments of stress over matrix

(b) Fluctuations of stress over matrix

Figure III .9: Local stress responses under uniaxial compression of a porous material with a porosity $f^i = 15\%$

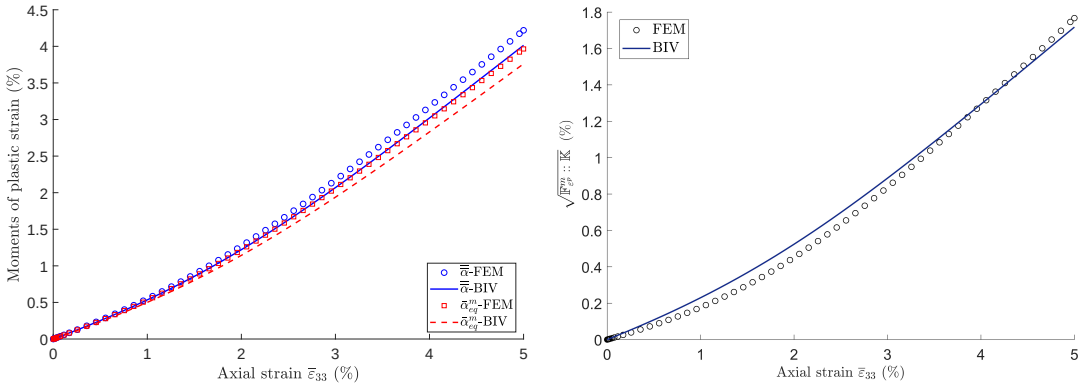

(a) First and second-order moments of plastic strain over matrix

(b) Fluctuations of plastic strain over matrix

Figure III .10: Local plastic strain responses under uniaxial compression of a porous material with a porosity of $f^i = 15\%$

7.2 Application examples

In this section, two application examples are presented to show the ability of the proposed bi-potential based incremental variational model to reproduce experimental responses of two typical rock-like materials: Callovo-Oxfordian claystone and Vosges sandstone.

7.2.1 Application to Callovo-Oxfordian claystone

The Callovo-Oxfordian claystone is extensively investigated in France as a potential geological barrier for the underground disposal of nuclear waste storage (Armand et al., 2016). It is a sedimentary rock with complex multi-scale structures (Robinet, 2008). At the mesoscopic scale (hundreds of micrometers), this clayey rock is composed of a quasi-continuous clay matrix containing elastic inclusions, mainly quartz and calcite grains. As a first approximation, the clay matrix can be characterized by an isotropic elastic-plastic model. The plastic behavior is here described by a non-associated Drucker-Prager type model (Guéry et al., 2008, 2010). On the other hand, for the range of stress considered in the application, the mechanical behavior of the quartz and calcite grains can be reasonably captured by a linear elastic model. Furthermore, as the elastic properties of calcite and quartz are quite similar, for the sake of simplicity, they are seen a single phase of elastic inclusions.

The BIV model contains 4 elastic coefficients and 6 plastic parameters for the clay matrix. The elastic coefficients of the elastic inclusion phase are taken as the volumetric

average values of the quartz and calcite grains (Jiang et al., 2009). The Young's modulus and Poisson's ratio are equal to $E^i = 98\text{GPa}$ and $\nu^i = 0.15$. The elastic coefficients of the clay matrix are not available from direct experimental measurement. They are calibrated by an inverse homogenization procedure (Guéry et al., 2008), from the macroscopic elastic coefficients obtained in triaxial compression tests on the samples with known mineralogical compositions (Chiarelli, 2000). We obtain the typical values of Young's modulus $E^m = 3\text{GPa}$ and Poisson's ratio $\nu^m = 0.3$. On the other hand, the values of plastic parameters of clay matrix are fitted by a numerical optimization of macroscopic stress-strain curves for a chosen mineralogical composition similar to that proposed in (Guéry et al., 2008; Shen et al., 2012). The obtained values are then fixed and applied to samples with different mineralogical compositions. The obtained values are given below:

- Matrix(clay): $E^m = 3\text{GPa}$, $\nu^m = 0.3$, $\kappa_0 = 10^{-5}$, $\kappa_m = 0.283$, $b_1 = 250$, $\chi_m = 0.05$, $b_2 = 50$, $c = 20\text{MPa}$
- Elastic inclusion(quartz + calcite): $E^i = 98\text{GPa}$, $\nu^i = 0.15$.

The mechanical responde of the claystone is now studied using the proposed BIV model under triaxial compression tests, proportional compression tests and lateral extension tests. It is noteworthy that these tests were performed on samples coming from different geological depths ranging from 415.4m to 482.4m, with different mineral compositions. However, a sole set of parameters is used for the modeling of different tests on different samples.

In Figure III .11, the stress-strain curves of claystone are presented for triaxial compression tests. One obtains a good agreement between model's predictions and experimental data. The BIV model is able to well reproduce main features of the claystone mechanical behavior in this loading path, such as the volume dilatancy and confining stress sensitivity. The impact of mineralogical compositions is also correctly taken into account. Further, in Figure III .11(a), the numerical results respectively provided by the associated and non-associated plastic model are compared. It is clear that the non-associated model gives a better description than the associated one.

For providing a complementary validation of the BIV model, proportional compression and lateral extension tests are also studied. In a proportional compression test, the axial stress $\bar{\sigma}_{33}$ and confining pressure $\bar{\sigma}_{11}$ are simultaneously increased with a constant ratio $k = \frac{\bar{\sigma}_{33}}{\bar{\sigma}_{11}}$. In a lateral extension test, the sample is first subjected to a hydrostatic stress state to a given value, and then the lateral stress $\bar{\sigma}_{11}$ is progressively decreased while the axial stress $\bar{\sigma}_{33}$ is kept constant. The comparison of claystone mechanical response

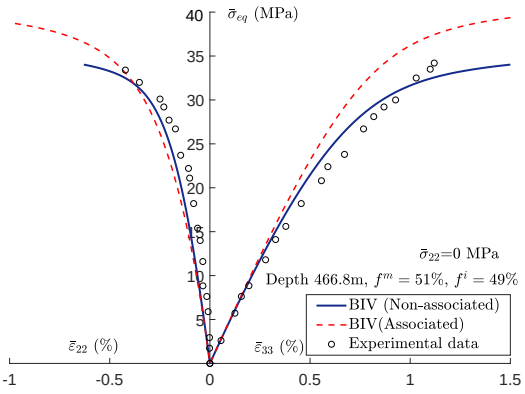

(a) Depth 466.8m, $f^m = 51\%$, $f^i = 49\%$,$\bar{\sigma}_{22} = 0$ MPa

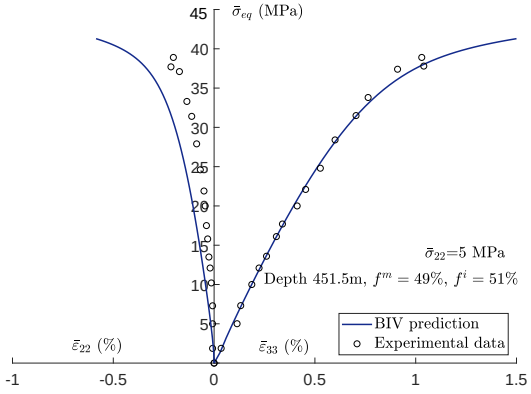

(b) Depth 451.5m, $f^m = 49\%$, $f^i = 51\%$,$\bar{\sigma}_{22} = 5$ MPa

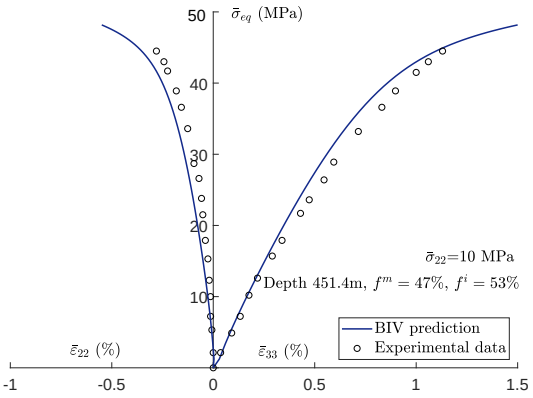

(c) Depth 451.4m, $f^m = 47\%$, $f^i = 53\%$,$\bar{\sigma}_{22} = 10$ MPa

Figure III .11: Comparison of stress-strain curves between experimental data and numerical results for triaxial compression tests on Callovo-Oxfordian claystone samples with different mineralogical compositions

between numerical predictions and experimental data for these two kinds of tests are shown in Figure III .12 and III .13, respectively. Again, one gets a good general agreement and the BIV model correctly describes the main characteristics of mechanical response of the claystone in these two loading paths.

7.2.2 Application to Vosges sandstone

The Vosges sandstone is here studied as a typical porous rock. Its microstructure and macroscopic behaviors have been investigated in a number of previous studies, for instance by (Bésuelle et al., 2000; Khazraei, 1996). The average porosity is about 20% and the solid

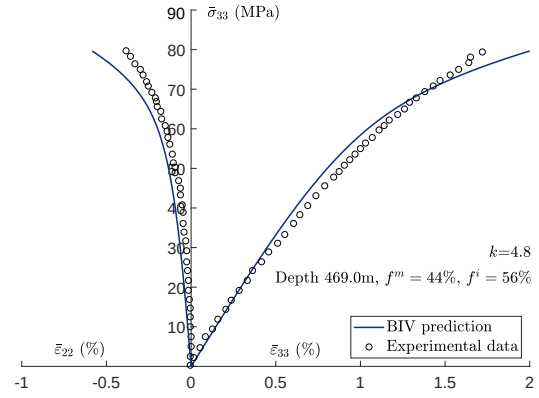

(a) Depth 469.0m, $f^m = 44\%$, $f^i = 56\%$, $k = 4.8$

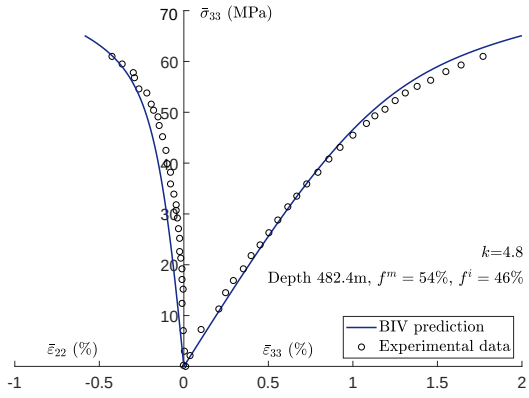

(b) Depth 482.4m, $f^m = 54\%$, $f^i = 46\%$, $k = 4.8$

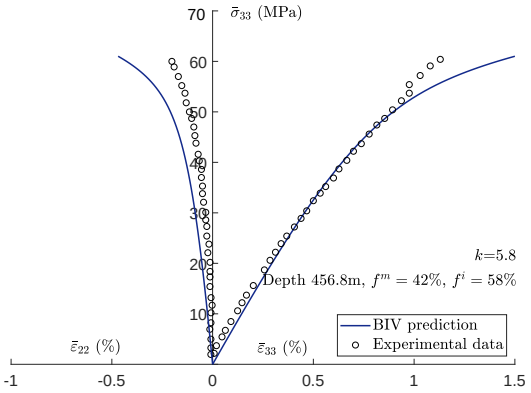

(c) Depth 456.8m, $f^m = 42\%$, $f^i = 58\%$, $k = 5.8$

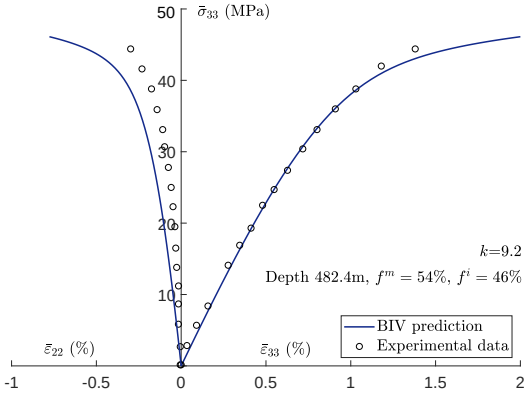

(d) Depth 482.4m, $f^m = 54\%$, $f^i = 46\%$, $k = 9.2$

Figure III .12: Comparisons of mechanical response between experimental data and numerical results for proportional compression tests on Callovo-Oxfordian claystone with different mineralogical compositions

matrix is composed of nearly 93% quartz grains with a few percent of feldspar and white mica. As a first approximation, the sandstone can be considered as an isotropic material. The mechanical strength of the sandstone strongly depends on confining pressure. In this study, the solid matrix is described by a non-associated Drucker-Prager type plastic model. The elastic and plastic parameters of solid matrix are not directly measured but indirectly estimated. The elastic coefficients can be easily identified by an inverse homogenization procedure from measured macroscopic data and porosity of sample. The plastic parameters are again fitted from a numerical optimization of macroscopic stress-strain curves for a given porosity. The obtained values of parameters are given in Table III .3.

In Figure III .14, we first present the stress-strain curves under conventional triaxial compression tests with four different confining stresses from 5MPa to 40MPa. Like the

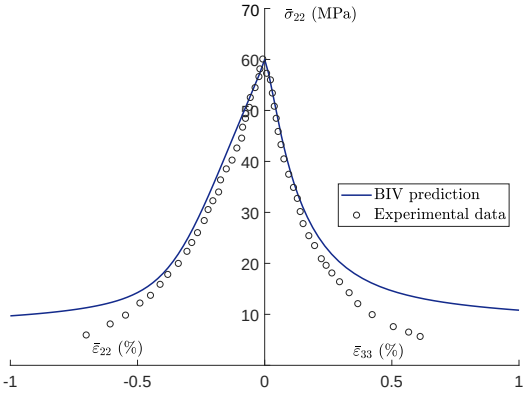

(a) Depth 469.0m, $f^m = 44\%$, $f^i = 56\%$

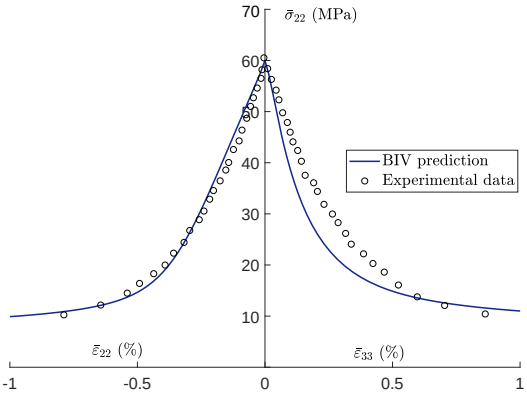

(b) Depth 482.3m, $f^m = 45\%$, $f^i = 55\%$

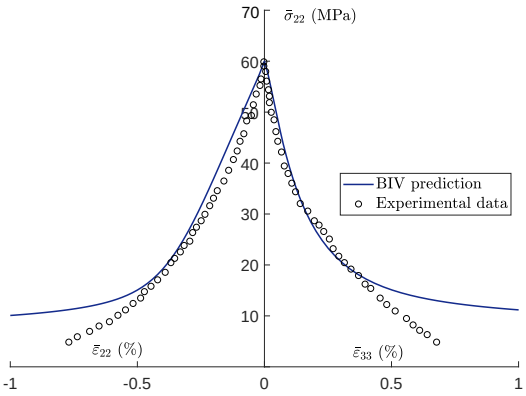

(c) Depth 456.6m, $f^m = 46\%$, $f^i = 54\%$

Figure III .13: Comparisons of mechanical response between experimental data and numerical results in lateral extension tests with initial confining pressure of 60MPa on Callovo-Oxfordian claystone with different mineralogical compositions

Table III .3: Parameters of solid matrix for porous Vosges sandstone

E^m (GPa)	ν^m	κ_0	κ_m	c(MPa)	b_1	χ_m	b_2
40	0.25	10^{-5}	0.433	40	900	0.333	500

claystone, there is a good agreement between model's predictions and experimental data. The effect of confining stress on macroscopic response is well captured. However, the mechanical strength of sandstone is slightly overestimated by the model for the test with a low confining stress if 5MPa. This is due to the fact that a linear Drucker-Prager

criterion used for the solid matrix is not well adopted in the zone of low mean stress and tensile stress. The use of a curved yield surface for the solid matrix, for example the Mises-Schleicher criterion, would improve numerical results. In Figure III .14(b), one can see that the non-associated model provides a better description of lateral strain that the associated model. However, unlike the result of claystone shown in Figure III .11(a), the non-associated flow rule coefficient has no influence on the peak strength of porous sandstone.

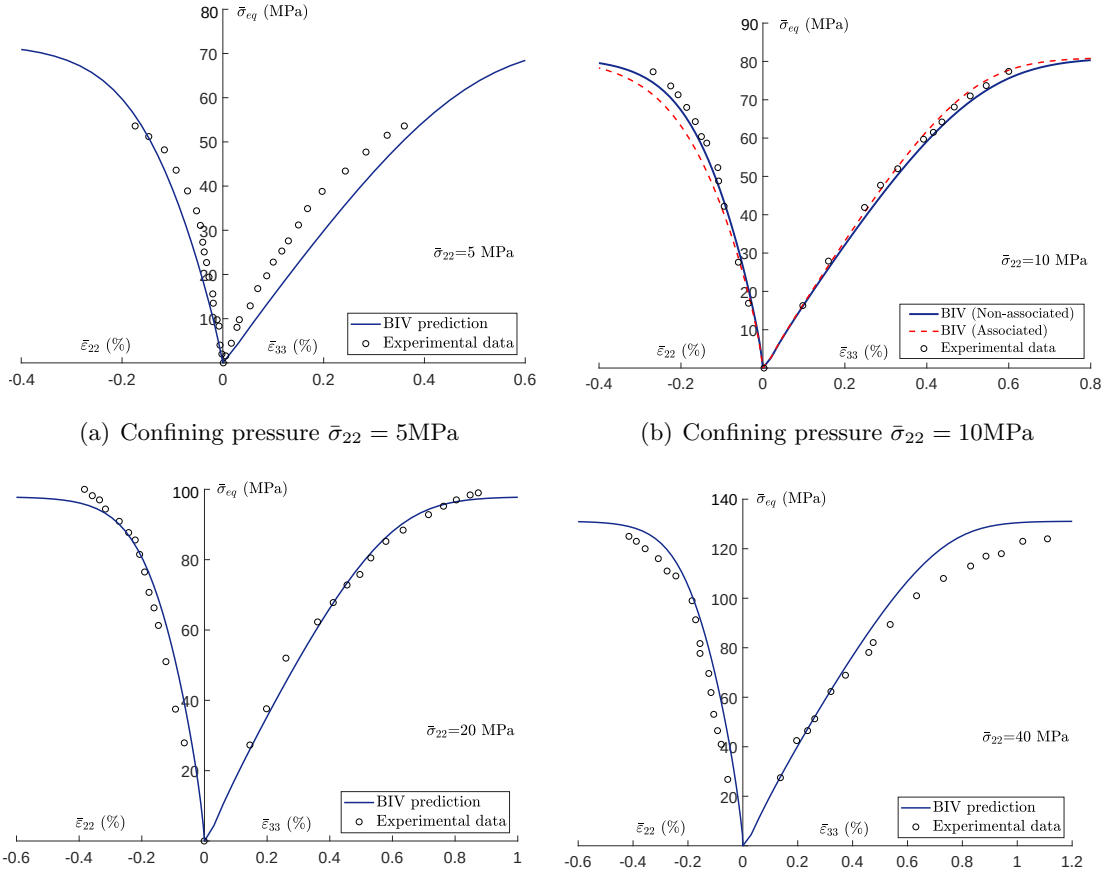

(a) Confining pressure $\bar{\sigma}_{22} = 5$MPa

(b) Confining pressure $\bar{\sigma}_{22} = 10$MPa

(c) Confining pressure $\bar{\sigma}_{22} = 20$MPa

(d) Confining pressure $\bar{\sigma}_{22} = 40$MPa

Figure III .14: Comparisons of mechanical response between experimental data and numerical results for triaxial compression tests on Vosges sandstone

The mechanical response of Vosges sandstone under proportional compression and lateral extension are presented respectively in Figures III .15 and III .16. Once again, it is found that the proposed BIV model well reproduce experimental data for these loading paths. In particular, as shown in Figure III .15, the transition from volumetric compressibility to dilatancy is well captured by the BIV model due to the non-associated plastic

flow rule in the solid matrix.

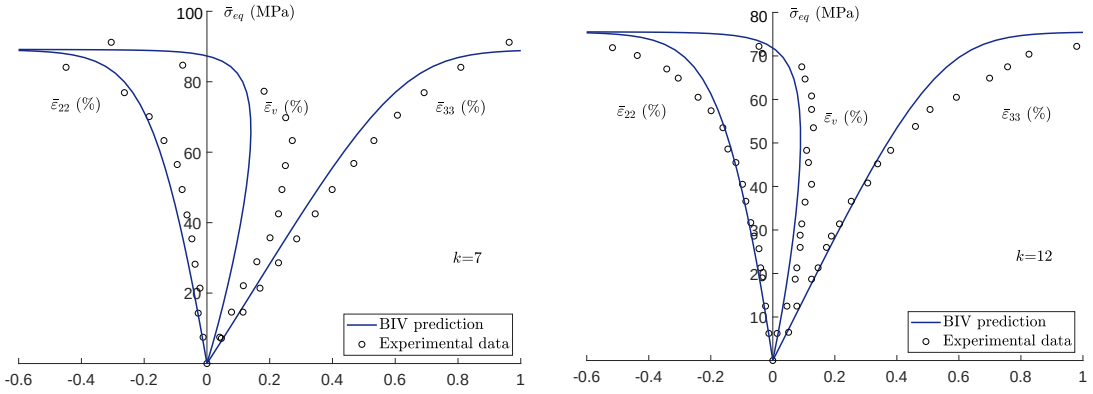

(a) $k = 7$ (b) $k = 12$

Figure III .15: Comparison of stress-strain curves between experimental data and numerical results for proportional compression tests on Vosges sandstone

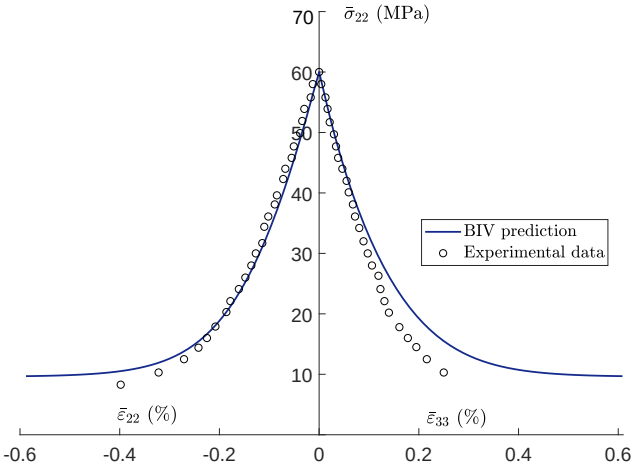

Figure III .16: Comparison of mechanical response between experimental data and numerical results for lateral extension test on Vosges sandstone with an initial confining pressure of 60MPa and axial stress of 90MPa

8 Concluding remarks

In this paper, we have proposed a new bi-potential based incremental variational (BIV) model for rock-like materials by making the extension of increment variational principle proposed for generalized standard materials. The BIV model has been formulated for a

class of rock-like materials with a non-associated plastic matrix described by a Drucker-Prager type yield function and an isotropic hardening law in two steps.

At the first step, we assume an non-associated perfectly plastic behavior for the solid matrix. With the help of the bi-potential theory, we have developed a new methodology for the determination of the incremental potential of plastic matrix. By introducing appropriate effective internal variables, the BIV model is able to account for non-uniform local stress and plastic strain fields in the plastic matrix. We have also introduced an appropriate optimization method for the estimation of the effective incremental potential and macroscopic stress. The accuracy of BIV model has well been demonstrated through the comparisons with direct field finite element simulations for both inclusion-reinforced and porous materials without plastic hardening.

At the second step, a heuristic extension of the micro-mechanical model has been proposed in view of estimating effective behaviors of rock-like materials with an isotropic plastic hardening law. This has been done by assuming that the general incremental variational formulation obtained from perfectly plastic solid matrix remains applicable for materials with isotropic hardening. The plastic hardening has been simply taken into account by updating the value of international frictional coefficient at each loading increment. The efficiency of the heuristic extended BIV model has been well evaluated by the comparison with a set of reference solutions provided by direct finite element simulation. Two classes of materials, inclusion-reinforced composites and porous materials, have been considered. It has been found that the BIV model was able to provide a good estimation of both local and overall responses of these heterogeneous materials. However, the average stress in the inclusion phase is underestimated for inclusion-reinforced composites, and the stress fluctuation in the matrix is overestimated for both materials. Therefore, some improvement remains needed, for example, by using a second-order comparison composite for the estimation of incremental potential of the plastic matrix.

Finally, the BIV model has been used to study the mechanical behavior of two typical rock-like materials, the Callovo-Oxifordian claystone and Vosges sandstone, under different loading paths. In a general way, the numerical results are in good agreement with experimental data. The main features of mechanical behavior of two materials are correctly reproduced by the BIV model, such as plastic hardening, influence of confining stress as well as volume compressibility/dilatancy transition.

In this work, we have focused on the short-term mechanical behavior of dry rock-like materials. In future, the BIV model is expected to be extended to the time-dependent behavior and to saturated and unsaturated conditions.

Appendix A: Linearization of the local free energy function (III .12)

Inspired by Boudet et al. (2016), we assume that the volumetric plastic strain field $\boldsymbol{\beta}$ and the internal variable field γ^p are constant values in the solid matrix, denoted by $\langle\boldsymbol{\beta}\rangle_m$ and $\langle\gamma^p\rangle_m$, respectively, evolving as follows by taking into account Eq.(III .5)

$$\langle\boldsymbol{\beta}\rangle_m = \langle\boldsymbol{\beta}_n\rangle_m + \overline{\overline{\dot{\boldsymbol{\alpha}}}}\Delta t\chi\boldsymbol{\delta} \tag{III .61}$$

$$\langle\gamma^p\rangle_m = \langle\gamma^p_n\rangle_m + \overline{\overline{\dot{\boldsymbol{\alpha}}}}\Delta t \tag{III .62}$$

where $\langle\boldsymbol{\beta}_n\rangle_m$ and $\langle\gamma^p_n\rangle_m$ are the volume average values of fields $\boldsymbol{\beta}$ and γ over matrix at step n, and

$$\overline{\overline{\dot{\boldsymbol{\alpha}}}} = \frac{1}{\Delta t}\sqrt{\frac{2}{3}\langle(\boldsymbol{\alpha}-\boldsymbol{\alpha}_n):(\boldsymbol{\alpha}-\boldsymbol{\alpha}_n)\rangle_m} = \frac{1}{\Delta t}\overline{\overline{\boldsymbol{\alpha}-\boldsymbol{\alpha}_n}} \tag{III .63}$$

Accordingly

$$w^m(\boldsymbol{\varepsilon},\boldsymbol{\alpha},\boldsymbol{\beta}) \simeq w_{lin}(\boldsymbol{\varepsilon},\boldsymbol{\alpha}) = \frac{1}{2}\left(\boldsymbol{\varepsilon}-\boldsymbol{\alpha}-\langle\boldsymbol{\beta}_n\rangle_m - \overline{\overline{\boldsymbol{\alpha}-\boldsymbol{\alpha}_n}}\chi\boldsymbol{\delta}\right):\mathbb{C}^m:\left(\boldsymbol{\varepsilon}-\boldsymbol{\alpha}-\langle\boldsymbol{\beta}_n\rangle_m - \overline{\overline{\boldsymbol{\alpha}-\boldsymbol{\alpha}_n}}\chi\boldsymbol{\delta}\right) \tag{III .64}$$

Appendix B: Minimization of $J_0^m(\varepsilon,\alpha)$

By making use of the minimization of $J_0^m(\boldsymbol{\varepsilon},\boldsymbol{\alpha})$ w.r.t. $\boldsymbol{\alpha}$, and after taking into account the form (II .32) of J_0^m, one gets,

$$\frac{\partial J_0^m}{\partial\boldsymbol{\alpha}} = -\mathbb{K}:\ \mathbb{C}^m:(\boldsymbol{\varepsilon}-\boldsymbol{\alpha}-\langle\boldsymbol{\beta}\rangle_m) - \mathbb{C}^m:(\boldsymbol{\varepsilon}-\boldsymbol{\alpha}-\langle\boldsymbol{\beta}\rangle_m)\frac{\partial\langle\boldsymbol{\beta}\rangle_m}{\partial\boldsymbol{\alpha}} + 2\frac{\eta_p\theta}{\Delta t}(\boldsymbol{\alpha}-\tilde{\boldsymbol{\alpha}}_n) = 0 \tag{III .65}$$

It is noted that Eq.(III .34) in its field form can be rewritten as

$$\theta(\boldsymbol{\alpha}-\tilde{\boldsymbol{\alpha}}_n) = (\boldsymbol{\alpha}-\boldsymbol{\alpha}_n) \quad \forall\underline{x}\in\Omega_m \tag{III .66}$$

Considering the expression (III .61) and (II .47), one obtains

$$\frac{\partial\langle\boldsymbol{\beta}\rangle_m}{\partial\boldsymbol{\alpha}} = \frac{2\chi\theta}{3\Delta t\overline{\overline{\dot{\boldsymbol{\alpha}}}}}\boldsymbol{\delta}\otimes(\boldsymbol{\alpha}-\tilde{\boldsymbol{\alpha}}_n) \tag{III .67}$$

then

$$-\mathbb{C}^m:(\boldsymbol{\varepsilon}-\boldsymbol{\alpha}-\langle\boldsymbol{\beta}\rangle_m):\frac{\partial\langle\boldsymbol{\beta}\rangle_m}{\partial\boldsymbol{\alpha}} = 2\frac{\eta_{cp}\theta}{\Delta t}(\boldsymbol{\alpha}-\tilde{\boldsymbol{\alpha}}_n) \tag{III .68}$$

with

$$\eta_{cp} = \frac{-3\chi\sigma_m}{3\overline{\overline{\dot{\boldsymbol{\alpha}}}}},\quad \sigma_m = \frac{1}{3}\mathbb{C}^m:(\boldsymbol{\varepsilon}-\boldsymbol{\alpha}-\langle\boldsymbol{\beta}\rangle_m):\boldsymbol{\delta} \tag{III .69}$$

For ease of calculation, we assume that η_{cp} takes its average value in the matrix phase, i.e.,

$$\eta_{cp} = \frac{-3\chi \langle \sigma_m \rangle_m}{3\bar{\bar{\dot{\boldsymbol{\alpha}}}}} \tag{III .70}$$

Substituting Eqs. (III .66) and (III .68) into (III .65) leads to

$$\frac{\partial J_0^m}{\partial \boldsymbol{\alpha}} = -\mathbb{K} : \ \mathbb{C}^m : (\boldsymbol{\varepsilon} - \boldsymbol{\alpha} - \langle \boldsymbol{\beta} \rangle_m) + 2\frac{\eta\theta}{\Delta t}(\boldsymbol{\alpha} - \tilde{\boldsymbol{\alpha}}_n) = 0 \tag{III .71}$$

with

$$\eta = \eta_p + \eta_{cp} = \frac{\langle \sigma_y \rangle_m - 3\chi \langle \sigma_m \rangle_m}{3\bar{\bar{\dot{\boldsymbol{\alpha}}}}} = -\frac{\kappa\left(\langle \sigma_m \rangle_m - c\right)}{\bar{\bar{\dot{\boldsymbol{\alpha}}}}} \tag{III .72}$$

or equivalently, the local deviatoric stress of matrix phase becomes

$$= \mathbb{K} : \mathbb{C}^m : (\ \boldsymbol{\varepsilon} - \boldsymbol{\alpha} - \langle \boldsymbol{\beta} \rangle_m) = 2\frac{\eta}{\Delta t}(\boldsymbol{\alpha} - \boldsymbol{\alpha}_n) = 2\frac{\eta\theta}{\Delta t}(\boldsymbol{\alpha} - \tilde{\boldsymbol{\alpha}}_n) \tag{III .73}$$

Finally, from (III .71), one gets

$$\boldsymbol{\alpha} = \left(\mathbb{C}^m + \frac{2\theta\eta}{\triangle\ t}\mathbb{K}\right)^{-1} : \left[\mathbb{K} : \mathbb{C}^m : \ \boldsymbol{\varepsilon} + \frac{2\theta\eta}{\Delta t}\tilde{\boldsymbol{\alpha}}_n\right] \tag{III .74}$$

Chapter IV

A micromechanics-based plastic damage model for quasi-brittle materials under a large range of compressive stress *

In this chapter, a new micro-mechanics based plastic damage model is proposed for quasi-brittle materials under a large range of compressive stress. The damage is due to initiation and propagation of micro-cracks while the plastic deformation is directly related to frictional sliding along micro-cracks. The two dissipation processes are then physically coupled. With the Mori-Tanaka homogenization procedure and thermodynamics framework, the macroscopic state equations are deduced and the local driving forces of damage and plasticity are defined. New specific criteria are proposed for the description of damage evolution and plastic flow. These criteria take into account the variation of material resistance to damage with confining pressure and the degradation of surface asperity of micro-cracks during the frictional sliding. An analytical analysis of macroscopic peak strength and volumetric compressibility-dilatancy transition is provided. A specific calibration procedure is further proposed for the determination of all model's parameters from conventional triaxial compression tests. The efficiency of the proposed model is verified against experimental data on three different materials and for a very large range of stress. All main features of mechanical behaviors of materials are well captured by the proposed

*Zhao, Lun-Yang, Qi-Zhi Zhu, and Jian-Fu Shao. "A micro-mechanics based plastic damage model for quasi-brittle materials under a large range of compressive stress." International Journal of Plasticity 100 (2018): 156-176.

model.

1 Introduction

Quasi-brittle materials are widely used in various engineering applications. In civil engineering and underground structures, rock-like or cement-based materials are generally subjected to compressive stresses. Damage and plasticity are two main inelastic processes in those materials. The basic physical process of damage is the initiation and propagation of micro-cracks. Under tensile stresses, open micro-cracks mainly propagate in tensile mode and the plastic deformation can be neglected. Under compressive stresses, closed micro-cracks propagate in a complex mode, such as wing cracks. The plastic deformation is directly due to frictional sliding along closed micro-cracks. For instance, during a triaxial compression test with a loading-unloading cycle on a rock-like material, irreversible strains can be obtained and they are enhanced by the increase of confining pressure. Such irreversible strains are considered as a consequence of plastic frictional sliding along closed micro-cracks. Therefore, the physical origin of plastic deformation in this class of materials is clearly different with that in metal materials or soil-like materials and should be described by a physically consistent approach Furthermore, as the propagation of frictional sliding along micro-cracks is driven by the normal and shear stresses locally applied onto micro-cracks, macroscopic mechanical behaviors of quasi-brittle materials are strongly sensitive to compressive mean stress or confining pressure. With the increase of confining pressure, there is a transition from brittle to ductile behavior. Further, the normal aperture of micro-cracks due to frictional sliding induces macroscopic volumetric dilatancy. The occurrence of dilatancy also depends on the level of confining pressure.

During the last decades, a large number of phenomenological models have been developed for modeling damage and plasticity in quasi-brittle materials. Without giving an exhaustive list of all models, only some representative studies are mentioned here. Most models have been developed in the framework of irreversible thermodynamics (Hansen and Schreyer, 1994b) with internal variables for plastic strains and damage. The damage has been either characterized by a scalar variable for isotropic distribution of micro-cracks (Chen et al., 2015; Salari et al., 2004; Shao et al., 2006) or by a tensorial variable for anisotropic distribution of micro-cracks (Chiarelli et al., 2003; Halm and Dragon, 1998).Some studies have been devoted to localization and bifurcation investigation using plastic damage models (He et al., 2015; Xotta et al., 2016). Mechanical behaviors of porous materials have also been described by plastic damage models (Kweon et al.,

2016). In other phenomenological damage models or plastic damage models (Barretta and de Sciarra, 2015; Barretta et al., 2014; De Sciarra, 2008; de Sciarra, 2008), strain softening and size effects have been investigated by using nonlocal or second gradient approaches. Convergence and stability properties in nonlocal models have been discussed. Some studies have been devoted to thermo-mechanical response and large deformation gradient theory for plastic materials (Aldakheel and Miehe, 2017; Anand et al., 2012). In these models, the coupling between damage and plasticity is generally taken into account through the definition of a macroscopic free energy function. Plastic strain tensor and damage variable are not physically connected. The physical origin of plastic deformation, the frictional sliding along micro-cracks, has not been clearly explained.

In order to complete phenomenological models and provide an alternative modeling, a significant progress has been achieved on the development of micro-mechanical models using different homogenization techniques. However, most studies have been devoted to damage modeling considering micro-cracks in elastic solid (Chaboche et al., 2001; Chow and Wang, 1987; Kachanov, 1982; Nemat-Nasser and Obata, 1988; Pensée et al., 2002; Zhu et al., 2008a, 2011). Only few studies have been performed on micro-mechanical modeling of coupled plastic-damage in quasi-brittle materials (Jefferson and Bennett, 2007; Zhu et al., 2008b; Zhu and Shao, 2015; Zhu et al., 2016). In particular, in some recent studies, the coupling between crack propagation and frictional sliding has been properly investigated in micro-mechanics based approaches (Zhu and Shao, 2015; Zhu et al., 2016). A micro-mechanics based thermodynamics formulation has been proposed for isotropic damage with unilateral and friction effects (Zhu et al., 2011). Some analytical and numerical analyses of frictional damage have been performed for specific loading paths (Zhu et al., 2016). Some micro-mechanics based models have been extended to initially anisotropic materials (Qi et al., 2016), and to time-dependent behavior analysis related to sub-critical propagation of micro-cracks (Bikong et al., 2015; Zhao et al., 2016).

In spite of the significant progress made so far, there are still some open issues to be investigated. In most micro-mechanical models recently developed, the effect of confining pressure on propagation kinetics of micro-cracks was neglected. The corresponding macroscopic strength envelop is described by a linear function. These models are not able to properly capture the transition from brittle to ductile behavior with the increase of confining pressure neither the nonlinear strength surface. On the other hand, the progressive degradation of surface asperity of micro-cracks has also not been considered. As a consequence, post-peak behavior and residual strength of materials are not correctly described.

In this chapter, a new micro-mechanics based model is developed for modeling plastic deformation and damage evolution of a wide class of quasi-brittle materials under a very large range of compressive stress. The new model will take into account the effect of confining pressure on material resistance to micro-cracks propagation and the degradation of surface asperity of micro-cracks due to frictional sliding. The efficiency of the proposed model will be verified on three different materials and for a large range of stresses. Compared with existing models, the new model will significantly improve the description of peak and residual strengths, volumetric compressibility - dilatancy transition, brittle to ductility transition and complex post-peak response.

2 Formulation of a micro-mechanics based plastic damage model

One considers a quasi-brittle material constituted of an isotropic elastic solid matrix which is weakened by a randomly distributed set of penny shaped micro-cracks. For the purpose of homogenization, one defines a representative volume element(RVE) occupying a geometric domain $\Omega \subset \mathbb{R}^3$ with its external boundary surface $\partial\Omega \subset \mathbb{R}^2$.

For most quasi-brittle materials, the distribution of micro-cracks is generally anisotropic due to the oriented propagation of micro-cracks in some preferential directions. However, for the sake of computational simplicity but without losing generality, we will assume in the present paper an isotropic distribution of micro-cracks. As mentioned above, several aspects still need to be investigated for a proper modeling of friction-damage coupling even in the isotropic case. Moreover, the general framework developed in the present study can be easily extended to anisotropic cases by considering different kinds of spatial distribution functions of micro-cracks. But the computational algorithm for anisotropic cases becomes significantly more complicated than the isotropic case. Anisotropic cases will be investigated as an extension of the present paper in our ongoing studies. With the isotropic assumption, each penny-shaped micro-crack is characterized by its unit normal vector $\underline{n}$ and the aspect ratio $\epsilon = c/a$ with a and c being the average radius and the half opening, respectively. The volume fraction φ of a family of micro-cracks is then defined as $\varphi = \frac{4}{3}\pi a^2 c\mathcal{N} = \frac{4}{3}\pi\epsilon d$ where $\mathcal{N}$ denotes the micro-crack density (i.e., the number of micro-cracks per unit volume). In the present study, the emphasis is put on the friction-damage coupling in closed micro-cracks under compression-dominated stresses. In such a case, it is reasonable to assume that the aspect ratio of micro-cracks is very small and can mathematically considered as vanished. As a consequence, the volume fraction of

micro-cracks also vanishes and cannot be used as a physical variable to characterize the state of micro-cracks because the effect of closed micro-cracks on mechanical behavior is not cancellated due to possible sliding along crack surfaces. Therefore, a physically pertinent internal variable should be defined. According to (Budiansky and O'connell, 1976), the following damage density variable is here used: $d = \mathcal{N}a^3$. Furthermore, as shown in previous studies (Eshelby, 1957b; Zhu et al., 2011), with a vanished aspect ratio, it is possible to obtain an analytical solution of Eshelby's tensor for a penny-shaped crack in an isotropic elastic solid matrix.

In the present study, one focuses on modeling of plastic deformation and damage evolution under compressive stresses. All micro-cracks are assumed to be closed and elastically glued. There are no elastic displacement discontinuities along crack surfaces. Further, each micro-crack is a rough surface characterized by a local frictional coefficient. Frictional sliding occurs only when local stresses applied on the crack surfaces verify a specific friction criterion. The frictional sliding at the local scale is entirely at the origin of plastic strains at the macroscopic scale. On the other hand, the damage evolution is related to the propagation of micro-cracks (increase of length). Further, the crack propagation is inherently coupled with the frictional sliding. As a consequence, with the assumption of isothermal conditions and small strains, the total strain tensor is decomposed into two parts: an elastic part $\boldsymbol{\varepsilon}^e$ attributed to deformation of the solid matrix and a plastic part $\boldsymbol{\varepsilon}^p$ due to the frictional sliding along closed micro-cracks:

$$\boldsymbol{\varepsilon} = \boldsymbol{\varepsilon}^e + \boldsymbol{\varepsilon}^p. \tag{IV .1}$$

2.1 Free energy and state equations

Due to the decomposition of strain tensor and making use of the results obtained in previous studies (Pensée et al., 2002; Zhu and Shao, 2015), the free energy of cracked material takes the form:

$$W^{close} = \frac{1}{2}\left(\boldsymbol{\varepsilon} - \ \boldsymbol{\varepsilon}^p\right) : \mathbb{C}^m : \left(\boldsymbol{\varepsilon} - \boldsymbol{\varepsilon}^p\right) + \frac{1}{2d}\boldsymbol{\varepsilon}^p : \mathbb{C}^d : \boldsymbol{\varepsilon}^p. \tag{IV .2}$$

The first part of the right-hand side represents the elastic free energy of the solid matrix while the second part is the stored energy due to the frictional sliding along micro-cracks. $\mathbb{C}^m = 2\mu^m\mathbb{K} + 3k^m\mathbb{J}$ is the elastic stiffness tensor of solid matrix, with k^m and μ^m being the bulk and shear moduli of the matrix, respectively. The coupling tensor $\mathbb{C}^d$ can be determined from a homogenization procedure based on Eshelby solution (Eshelby, 1957b) by considering the cracked material as a matrix-inclusion system. As mentioned above,

in order to obtain an analytical expression of $\mathbb{C}^d$, micro-cracks are seen as spheroidal inclusions with a vanished aspect ratio (Zhu et al., 2016). One gets:

$$\mathbb{C}^d = \left(\mathbb{S}^d\right)^{-1}, \ \mathbb{S}^d = (\alpha\mathbb{J} + \beta\mathbb{K}) : \mathbb{S}^m \tag{IV .3}$$

$\mathbb{S}^m = (\mathbb{C}^m)^{-1}$ is the elastic compliance tensor of the solid matrix. Two coefficients α and β are obtained from the Mori-Tanaka homogenization procedure and they are functions of Poisson's ratio of the solid matrix ν^m only (Zhu et al., 2011, 2016). One gets $\alpha = \frac{16}{9}\frac{1-(\nu^m)^2}{1-2\nu^m}$ and $\beta = \frac{32}{45}\frac{(1-\nu^m)(5-\nu^m)}{2-\nu^m}$.

One then derives the macroscopic stress-strain relations from the free energy function as follows:

$$\boldsymbol{\sigma} = \frac{\partial W^{close}}{\partial \varepsilon} = \mathbb{C}^m : (\boldsymbol{\varepsilon} - \boldsymbol{\varepsilon}^p), \tag{IV .4}$$

One can also deduce the thermodynamic forces respectively associated with the plastic strain $\boldsymbol{\varepsilon}^p$ and the damage variable d:

$$\boldsymbol{\sigma}^c = -\frac{\partial W^{close}}{\partial \boldsymbol{\varepsilon}^p} = \boldsymbol{\sigma} - \frac{1}{d}\mathbb{C}^d : \boldsymbol{\varepsilon}^p \tag{IV .5}$$

$$Y_d = -\frac{\partial W^{close}}{\partial d} = \frac{1}{2d^2}\ \boldsymbol{\varepsilon}^p : \mathbb{C}^d : \boldsymbol{\varepsilon}^p, \tag{IV .6}$$

It is interesting to note that $\boldsymbol{\sigma}^c$ is the local stress tensor applied to micro-cracks and it is the driving force of frictional sliding. Further, the local stress tensor is different to the macroscopic one and explicitly depends on the damage variable d. Therefore, the plastic deformation due to frictional sliding is inherently influenced by the damage evolution. Due to this coupling, the local stress and then the macroscopic stress are affected by the damage growth. This can lead to a material softening when the damage density becomes high. On the hand, the damage conjugated thermodynamic force Y_d explicitly depends on the plastic strain tensor $\boldsymbol{\varepsilon}^p$. As a consequence, the damage evolution is directly driven by the plastic deformation due to frictional sliding. It is worth noticing that in the present study, it is assumed that all micro-cracks are elastically glued due to the roughness of asperities on crack surfaces. The plastic frictional sliding is the unique cause of displacement discontinuity along micro-cracks and driving force of crack propagation.

2.2 Damage criterion

The damage evolution is related to the growth of micro-cracks. It is determined by a specific local damage criterion which is a function of the thermodynamic damage force. Inspired by previous studies (Zhu and Shao, 2015), the following general form of damage criterion is here adopted:

$$f_d(Y_d, d) = Y_d - \mathcal{R}(d) \leq 0, \tag{IV .7}$$

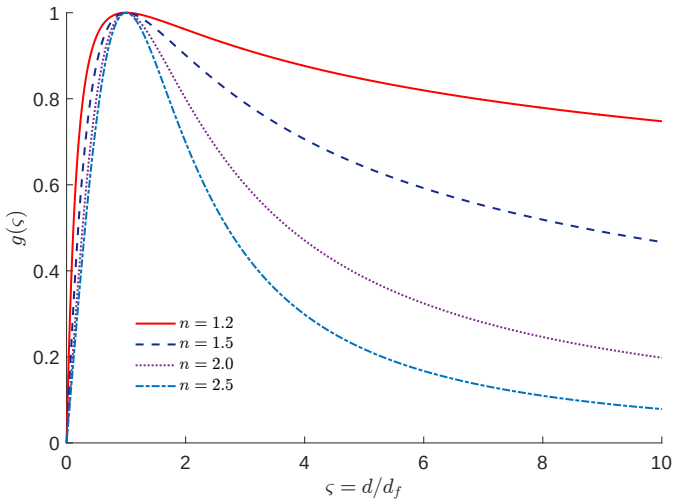

Figure IV .1: Curves of $g(\varsigma)$ for different values of n

In this criterion, the function $\mathcal{R}(d)$ represents the current resistance to damage evolution (micro-crack propagation) of the material. It is physically equivalent to $\mathcal{R}$-curve used in linear fracture mechanics. It is generally observed that when the density of micro-cracks is small, the material resistance $\mathcal{R}(d)$ is an increasing function of damage density variable d, due to material hardening effect, similar to plastic hardening in ductile materials. The propagation of micro-cracks is then stable. When the density of micro-cracks becomes high enough, for instance reaches some critical value, the material resistance starts to decrease due to interactions between micro-cracks. The function $\mathcal{R}(d)$ should then decrease with d. This leads to an unstable propagation of micro-cracks occurs. At the macroscopic scale, the evolution of the function $\mathcal{R}(d)$ should allow the description of the transition from material hardening to softening around peak strength. Based on this physical analysis and inspired by Zhu and Shao (2015), the following specific form is proposed:

$$\mathcal{R}(d) = \tilde{r}_f g(\varsigma), \; g(\varsigma) = \frac{n\varsigma}{\varsigma^n + n - 1}, \; \varsigma = \frac{d}{d_f}, \tag{IV .8}$$

The parameter $n > 1$ controls the damage evolution rate. d_f represents the critical value of damage density variable when the peak strength is obtained; $\tilde{r}_f$ is thus the maximal value of $\mathcal{R}(d)$ when $d = d_f$. In Figure IV .1, one shows the evolution of $g(\varsigma)$ with the relative damage density ς for different values of n. One can notice that $g(\varsigma)_{max} = 1$ when $\varsigma = 1$ for all values of n. The $g(\varsigma)$ curve is significantly influenced by the value of n in the post-peak regime. The impact of the parameter n on the macroscopic response will be discussed in detail later in this paper.

After the damage criterion is defined, the damage evolution rate is determined using

the following normality rule:

$$\triangle d = \lambda^d \frac{\partial f_d}{\partial Y_d} = \lambda^d, \tag{IV .9}$$

where λ^d is the damage multiplier which can be discussed by the consistency conditions discussed later in the paper.

2.3 Friction criterion with an associated plastic flow rule

Like in the macroscopic plastic theory, the plastic deformation due to local frictional sliding is also determined by a yield criterion and flow rule. Due to the fact that the frictional sliding is driven by the local stress tensor $\boldsymbol{\sigma}^c$, the classical Coulomb-type friction criterion is here generalized to the local scale:

$$f_p\left(\boldsymbol{\sigma}^c\right) = \|\boldsymbol{s}^c\| - \eta p^c \leq 0, \tag{IV .10}$$

with $\boldsymbol{s}^c = \mathbb{K} : \boldsymbol{\sigma}^c$ and $p^c = \frac{1}{3}\boldsymbol{\sigma}^c : \boldsymbol{\delta}$ being the local deviatoric stress and mean stress. The parameter η is the local friction coefficient of crack surfaces. From a physical point of view, the friction coefficient is related to the roughness of crack surfaces due to the existence of asperities. With the progress of sliding, asperities of crack surfaces are progressively destroyed. As a consequence, the friction coefficient η should decrease with the accumulated plastic deformation. On the other hand, the damage evolution is also driven by the frictional sliding process. Therefore, it is also possible to establish a relationship between the damage state and degradation of crack surfaces asperities. For convenience, it is assumed that the degradation of crack surface asperity is negligible when the damage density d is less than the critical value d_f. Therefore, the local friction coefficient remains constant when $d \leq d_f$. After this critical state, the degradation of crack surface asperitiy becomes significant and leads to a decrease of the friction coefficient. Based on this analysis, the following relation is proposed to follow the evolution of the local friction coefficient η as a function of damage:

$$\eta = \eta_f - (\eta_f - \eta_r)\tanh\left(b\left\langle\varsigma - 1\right\rangle^2\right), \tag{IV .11}$$

where η_f and η_r are, respectively, the friction coefficient corresponding to the peak strength state ($\varsigma = 1$ or $d = d_f$)and the residual strength state ($\varsigma \to \infty$); b is a parameter controlling the friction coefficient degradation rate in the post-peak region.

By adopting an associated local plastic flow rule, the rate of plastic strain due to frictional sliding is determined by the following normality rule:

$$\triangle \boldsymbol{\varepsilon}^p = \lambda^p \frac{\partial f}{\partial \boldsymbol{\sigma}^c} = \lambda^p \boldsymbol{D}, \tag{IV .12}$$

with λ^p being the the plastic multiplier to be determined from the consistency conditions discussed later. The plastic flow direction $\boldsymbol{D}$ is defined by the following second order tensor:

$$\boldsymbol{D} = \frac{\boldsymbol{s}^c}{\|\boldsymbol{s}^c\|} - \frac{\eta}{3}\boldsymbol{\delta}. \tag{IV .13}$$

3 Strength and deformation analysis at macroscopic scale

Before discussing numerical results given by the proposed micro-mechanics based plastic damage model, it is interesting to perform an analytical analysis of some specific features of mechanical behaviors of quasi-brittle materials. Without losing the generality, this is done on a radial loading path without rotation of principal stress frame. As an example, a triaxial compression test is considered.

3.1 Macroscopic failure strength

The stress state in a conventional triaxial compression test is such that

$$\boldsymbol{\sigma} = \begin{bmatrix} \sigma_1 & 0 & 0 \\ 0 & \sigma_3 & 0 \\ 0 & 0 & \sigma_3 \end{bmatrix} \tag{IV .14}$$

with the algebra sequence $\sigma_1 > \sigma_2 = \sigma_3 \geq 0$. The corresponding deviatoric part $\boldsymbol{s}$ is given by:

$$\boldsymbol{s} = \frac{\sigma_1 - \sigma_3}{3} \begin{bmatrix} 2 & 0 & 0 \\ 0 & -1 & 0 \\ 0 & 0 & -1 \end{bmatrix} \tag{IV .15}$$

According to (IV .13) and after making some mathematical calculations, the direction of plastic flow rate $\boldsymbol{D}$ in this radial loading path can be expressed as follows:

$$\boldsymbol{D} = \frac{1}{\sqrt{6}} \begin{bmatrix} 2 & 0 & 0 \\ 0 & -1 & 0 \\ 0 & 0 & -1 \end{bmatrix} - \frac{\eta}{3}\boldsymbol{\delta} \tag{IV .16}$$

As the friction coefficient η is constant and equal to $\eta = \eta_f$ before the peak strength state, the direction of plastic flow $\boldsymbol{D}$ is also constant until the peak strength. Therefore, the current values of plastic strain and damage in the pre-peak strength region can be measured respectively by their accumulated multipliers such that:

$$\boldsymbol{\varepsilon}^p = \Lambda^p \boldsymbol{D},\ d = \int \lambda^d, \quad \text{with } \Lambda^p = \int \lambda^p. \tag{IV .17}$$

By taking $\eta = \eta_f$ and setting the constant $\chi = \frac{1}{2}\boldsymbol{D} : \mathbb{C}^d : \boldsymbol{D} = \frac{\mu^m}{\alpha} + \frac{k^m \eta_f^2}{2\beta}$, the friction criterion can be rewritten as

$$f_p = \|\boldsymbol{s}\| - \eta_f p - \frac{\Lambda^p}{d}\chi = 0. \tag{IV .18}$$

On the other hand, the damage criterion is cast into the form

$$f_d(Y_d, d) = \left(\frac{\Lambda^p}{d}\right)^2 \chi - \mathcal{R}(d) = 0, \tag{IV .19}$$

from which one can derive the following relation

$$\frac{\Lambda^p}{d} = \sqrt{\frac{\mathcal{R}(d)}{\chi}}. \tag{IV .20}$$

Its insertion into the friction criterion (IV .18) gives

$$f_p = \|\boldsymbol{s}\| - \eta_f p - \sqrt{\mathcal{R}(d)\,\chi} = 0. \tag{IV .21}$$

Under the sign convention of stress adopted here, one has $\|\boldsymbol{s}\| = \sqrt{\frac{2}{3}}(\sigma_1 - \sigma_3)$ and $p = \frac{1}{3}(\sigma_1 + 2\sigma_3)$, the axial stress component σ_1 is finally expressed in terms of σ_3 and d

$$\sigma_1 = \frac{\sqrt{6} + 2\eta_f}{\sqrt{6} - \eta_f}\sigma_3 + \frac{6\sqrt{\mathcal{R}(d)\,\chi}}{\sqrt{6} - \eta_f}. \tag{IV .22}$$

The peak compression strength is attained once the damage variable reaches its critical value $d = d_f$. Combining Eqs. (IV .8) and (IV .22), one can obtain the following analytical expression of failure criterion for a triaxial compression test.

$$\sigma_1^f = \frac{\sqrt{6} + 2\eta_f}{\sqrt{6} - \eta_f}\sigma_3 + \frac{6\sqrt{\tilde{r}_f \chi}}{\sqrt{6} - \eta_f}, \tag{IV .23}$$

where σ_1^f is the axial peak stress which is composed of two terms. The first term on the right side of (IV .23) is related to the frictional effect and then depends on confining pressure σ_3, and the second term represents the uniaxial compression strength for $\sigma_3 = 0$ and is related to the cohesive strength of micro-cracks.

3.2 Volume compressibility/dilatancy (C/D) transition

In quasi-brittle rock-like materials, the transition from volumetric compressibility to dilatancy is a common character and an important feature to be taken into account (Martin, 1994, 1997; Szczepanik et al., 2003). In the present study, we have considered a simplified representative volume element of quasi-brittle materials, which is composed of an elastic solid matrix containing closed micro-cracks with rough surfaces. In this case, the macroscopic dilatancy is directly related to the local normal opening of micro-cracks during the frictional sliding due to the roughness of micro-cracks. The dilatancy is then dependent on the local friction coefficient or the roughness of crack surfaces. Further the frictional sliding and normal opening are controlled by local normal stress level which is related to macroscopic confining pressure. Therefore, at the macroscopic scale, the transition from compressibility to dilatancy is dependent on confining pressure. With the present micro-mechanics based model, the prediction of such a transition stress is here discussed for a conventional triaxial compression path. For this purpose, let denote σ_{cd} as the volume compressibility - dilatancy (C/D) transition stress.

Inspired by the strength prediction, one assumes that there exists a critical damage value d_{cd} corresponds to σ_{cd}. For the sake of convenience, one denotes $g\left(\varsigma_{cd}\right)=\kappa$, with $\varsigma_{cd}=d_{cd}/d_f$. Then one gets the following relation according to Eq. (IV .8)

$$g\left(\varsigma_{cd}\right)=\frac{n\varsigma_{cd}}{{\varsigma_{cd}}^{n}+n-1}=\kappa. \tag{IV .24}$$

Following Eq. (IV .22), the C/D transition σ_{cd} can be expressed as

$$\sigma_{cd}=\frac{\sqrt{6}+2\eta_f}{\sqrt{6}-\eta_f}\sigma_3+\frac{6\sqrt{\tilde{r}_f\kappa\chi}}{\sqrt{6}-\eta_f}. \tag{IV .25}$$

On the other hand, the volume strain ε_v is composed of the elastic volume strain ε_v^e and the plastic volume strain ε_v^p:

$$\varepsilon_v=\varepsilon_v^e+\varepsilon_v^p. \tag{IV .26}$$

By ignoring the inelastic strain caused by the initial crack closure and the volumetric strain generated by confining pressure and by making use of Eqs. (IV .17) and (IV .26), one can rewrite the volume strain generated in the axial loading phase into the following form:

$$\varepsilon_v=\boldsymbol{\delta}:\mathbb{S}^m:\left(\boldsymbol{\sigma}-\sigma_3\boldsymbol{\delta}\right)-\Lambda^p\eta_f. \tag{IV .27}$$

And more precisely, one gets:

$$\varepsilon_v=\frac{1}{3k^m}\left(\left(\frac{2\eta_f+\sqrt{6}}{\sqrt{6}-\eta_f}-1\right)\sigma_3+\frac{6\sqrt{R\left(d\right)\chi}}{\sqrt{6}-\eta_f}\right)-\varsigma d_f\sqrt{\frac{R\left(d\right)}{\chi}}\eta_f. \tag{IV .28}$$

The increment of volume strain can be computed as:

$$\mathrm{d}\varepsilon_v = \frac{\partial \varepsilon_v}{\partial \varsigma}\frac{\partial \varsigma}{\partial d}\mathrm{d}d, \tag{IV .29}$$

where

$$\frac{\partial \varepsilon_v}{\partial \varsigma} = \left(\frac{1}{k^m\left(\sqrt{6}-\eta_f\right)} - \frac{\zeta d_f \eta_f}{2\chi}\right)\frac{\sqrt{\chi \tilde{r}_f}\, g^{'}(\varsigma)}{\sqrt{g(\varsigma)}} - d_f\sqrt{\frac{g(\varsigma)\,\tilde{r}_f}{\chi}}\eta_f, \quad \frac{\partial \varsigma}{\partial d} = \frac{1}{d_f}\ . \tag{IV .30}$$

It is noted that the volume C/D transition point corresponds to $\mathrm{d}\varepsilon_v = 0$. By analyzing Eqs. (IV .29) and (IV .30), it is easily to depict that $\frac{\partial \varepsilon v}{\partial \varsigma} = 0$ and $\varsigma = \varsigma_{cd}$ at this transition point. After a series of mathematical translations, given in Appendix, one can obtain the following characteristic equation:

$$\left(\frac{2d_f}{n-1} - d_f\right){\varsigma_{cd}}^2 + \left(\kappa d_f + 2\vartheta\right)\varsigma_{cd} - 2\kappa\vartheta = 0. \tag{IV .31}$$

The combination of Eqs. (IV .24) and (IV .31) allows the calibration of the parameter n and characteristic damage value ς_{cd} . After the parameter n is determined, the volume C/D transition point can be exactly predicted for different values of confining pressure.

3.3 Strain softening and residual strength

In most macroscopic plastic models, the softening behavior of materials is usually described by some negative hardening law. The physical significance of such a mathematic description is not always clearly explained. In the present micro-mechanics based model, the material softening is explicitly related to two physical processes. The first one is due to the coalescence effect of micro-cracks when the damage density becomes high ($d \geq d_f$). This is described by Eq. (IV .8) as the diminution of material resistance to crack-propagation. The second process is the progressive degradation of crack surface asperity, leading to the decrease of friction coefficient of crack surfaces, as expressed in Eq. (IV .11). However, due to the variation of friction coefficient, it is no more possible to obtain the analytical solution of stress-strain curves as for the pre-peak regime. The numerical analysis of material responses in the post-peak regime will be depicted in Section 6.1.

4 Parameters calibration and influence of confining pressure

The proposed micro-mechanics based model contains 8 parameters. Each parameter has a clear physical meaning can be related to corresponding macroscopic mechanical responses. The calibration method of the parameters from macroscopic conventional triaxial compression tests is here discussed.

4.1 Elastic parameters of solid matrix

The elastic behavior of solid matrix is characterized by Young's modulus E^m and Poisson's ratio ν^m. With the assumption that all micro-cracks are closed and the sliding is possible only when the friction criterion is reached, the elastic parameters of solid matrix can be directly determined from the linear part of stress-strain curves in a conventional compression test. For most rock-like materials, the elastic parameters vary with confining pressure. However, it seems that this variation is not significant for the granite rocks studied in this work. The average values obtained from triaxial compression tests with different values of confining pressure are then adopted. In the case of Kuru granite (Tkalich et al., 2016), one gets $E^m = 78000$MPa and ν^m=0.27.

According to Tkalich et al., 2016, the uniaxial (unconfined) compression strength of Kuru granite is about $\sigma_c = 232$MPa.

4.2 Parameters related to peak strength

In the proposed micro-mechanics base model, three parameters d_f, $\tilde{r}_f$ and η_f are related to the stress and deformation at peak strength state. In Figure V .6, one gives the interpretation of axial strain - deviatoric stress curves obtained on Kuru granite (Tkalich et al., 2016) for different values of confining pressure, in terms of three micro-mechanical parameters. The black vertical arrows in Figure V .6 represent the relationships between each sub-figures. Firstly the peak axial stress σ_1 and the corresponding total axial strain ε_1 for each value of confining pressure are extracted from Figure V .6a. The obtained values are then reported respectively in the diagrams (σ_3 versus σ_1) and (σ_3 versus ε_1^p), as shown in Figures V .6b,c. Note that the total plastic axial strain is given by:

$$\varepsilon_1^p = \varepsilon_1 - \frac{\sigma_1 - \sigma_3}{E^m}. \tag{IV .32}$$

In Figure V .6b, it is found that the failure envelope exhibits a strong nonlinearity at low values of confining pressure but it is defined by a quasi linear line at high values of confining pressure. The following linear function is identified by the optimal fitting of peak stress points in the high confining pressure zone:

$$\sigma_1^f = 6.11\sigma_3 + 391.16 \tag{IV .33}$$

By comparing Eqs. (IV .23) and (IV .33), one can easily calculate the values of parameters η_f and $\tilde{r}_f$ for the range of high confining pressure by assuming a linear strength envelop.

However, as shown in Figure V .6b, the strength envelop cannot be described by a linear function in the range of low confining pressure. By assuming that the value

of η_f is constant, one can still calculate individually the value of $\tilde{r}_f$ for each confining pressure. The obtained values are presented in Figure V .6d. It is found that the peak damage resistance $\tilde{r}_f$ is an increasing function with confining pressure and evolves towards a asymptotic value when the confining pressure becomes high enough. Based on this result, the following function is proposed for the variation of $\tilde{r}_f$ with confining pressure:

$$\tilde{r}_f = r_c + (r_f - r_c)\tanh\left(\frac{\sigma_3}{\sigma_3^{ref}}\right), \tag{IV .34}$$

where r_f and r_c are the value of $\tilde{r}_f$ under high confining pressure and uniaxial compression, respectively, σ_3^{ref} is a reference stress separating the low and high confining zones. It is generally difficult to identify the σ_3^{ref} due to the lack of relevant experimental data. For the sake of simplicity and following previous studies Diederichs (2003); Hoek and Bieniawski (1965), it is proposed to take $\sigma_3^{ref} = \sigma_c/10$, with σ_c being the uniaxial compressive strength. Accordingly, Eq. (IV .34) can be rewritten as:

$$\tilde{r}_f = r_c + (r_f - r_c)\tanh\left(\frac{10\sigma_3}{\sigma_c}\right), \tag{IV .35}$$

The value of σ_c is easily obtained from an uniaxial compression test. Then the values of r_f and r_c can be easily determined by the optimal fitting of $\tilde{r}_f$ versus σ_3. In Figure IV .3, the prediction given by the semi-empirical relation (IV .35) is compared with the calculated values of $\tilde{r}_f$ from experimental data. One can see that a good agreement is obtained.

The parameter d_f is the critical damage value corresponding to the peak strength state. With this in mind and by combining Eqs. (IV .17) and (IV .20), d_f can be expressed as follows:

$$d_f = \varepsilon_{1,f}^p D_{11}\sqrt{\frac{\chi}{\tilde{r}_f}}, \tag{IV .36}$$

where $\varepsilon_{1,f}^p$ is the axial plastic strain at the peak strength state, and $D_{11} = \frac{2}{\sqrt{6}} - \frac{\eta_f}{3}$. With this equation in hand, it is possible to calculate d_f for different values of confining pressure as shown in Figure V .6e. For the sake of clarity, the values of $\tilde{r}_f$ and d_f are also given in Table IV .1. From which one can see that d_f varies from 1.02 to 2.95 and basically increases with confining pressure. This is consistent with previous studies by Lockner (1998). However, for the sake of simplicity and due to the fact that a significant variation of d_f is observed only for very low values of confining pressure, it is taken as constant in this work. In Figure IV .4, one can find a good agreement of peak strength between the numerical prediction and experimental data for Kuru granite.

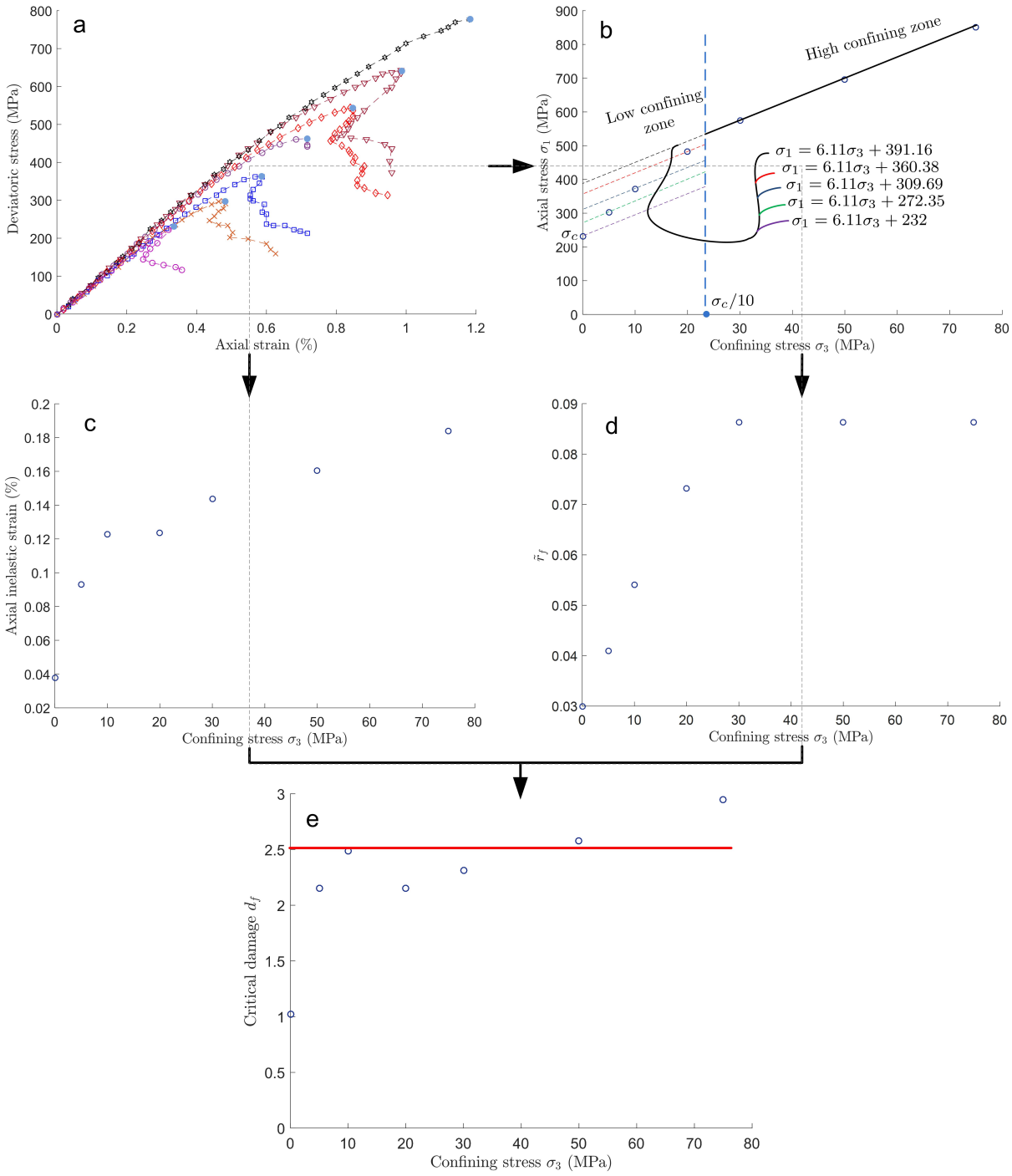

Figure IV .2: Illustration of identification procedure of strength parameters from triaxial compression tests with experimental data extracted from Tkalich et al. (2016): from sub-Figure 2(a), one takes the values of peak stresses and corresponding axial strains for different levels of confining pressure; these values are reported into sub-Figure 2(b) and 2(c); the values of $\tilde{r}_f$ given in sub-Figure 2(d) are obtained by using Eq.(IV .23) and the data given in sub-Figure 2(b); finally the critical damage density d_f given in sub-Figure 2(e) is calculated by using Eq.(IV .36) together with the data given in sub-Figures 2(c) and 2(d)

Table IV .1: Variation of strength parameters with confining pressure

σ_3 (MPa)	0	5	10	20	30	50	75
σ_f (MPa)	232	304	372	483	574	693	852
$\varepsilon^p_{1,f}(\%)$	0.0378	0.0932	0.1229	0.1234	0.1436	0.1604	0.1838
$\tilde{r}_f$	0.03	0.041	0.054	0.073	0.086	0.086	0.086
d_f	1.02	2.15	2.49	2.15	2.31	2.58	2.95

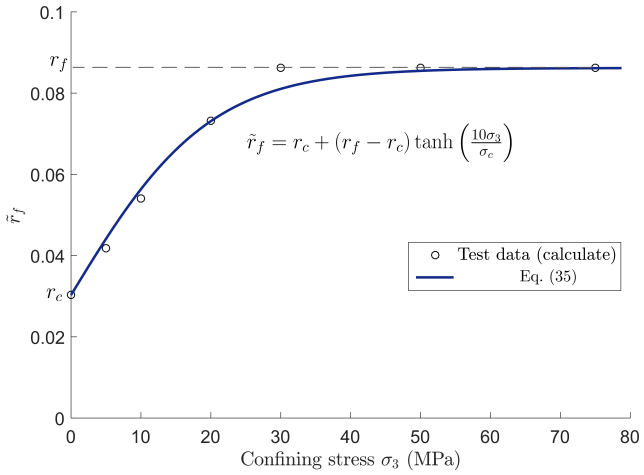

Figure IV .3: Comparison between empirical relation (IV .35) and calculated values of $\tilde{r}_f$

4.3 Parameters related to dilatancy and residual strength

As mentioned above, the parameter n can be determined by solving Eqs. (IV .24) and (IV .31) on the C/D transition points. In this process, the intermediate variable κ must first be identified from experimental tests. For the case of Kuru granite, with the help of linear approximation of C/D transition line in Figure IV .5 and by comparing Eqs (IV .23) and (IV .25), one gets $\kappa = \left(\frac{232}{291.16}\right)^2 = 0.36$. From that, one obtains $n = 1.472$ by making the numerical fitting of data as shown in Figure IV .6. In Figure IV .4, a good agreement is obtained for the C/D transition stress σ_{cd} between the numerical prediction and experimental data for Kuru granite.

The residual friction coefficient η_r can be determined from the slope of residual strength envelope. Using the residual strength data for Kuru granite from Tkalich et al. (2016),

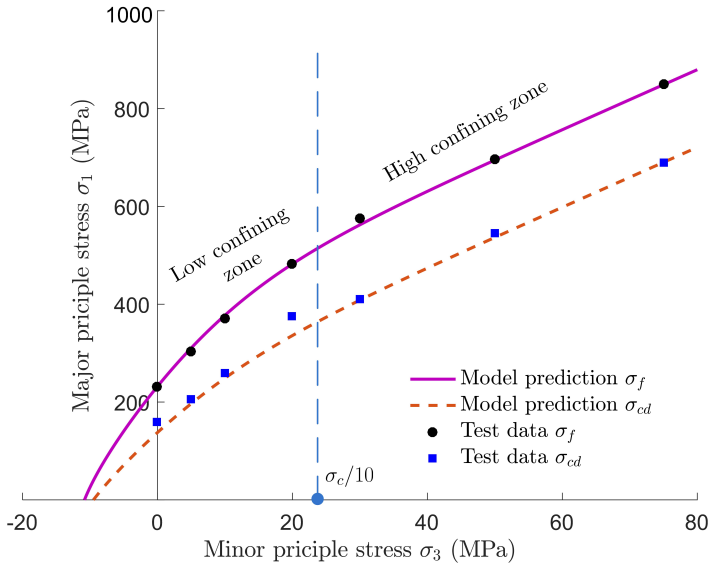

Figure IV .4: Peak strength σ_f and C/D transition stress σ_{cd} predictions of Kuru granite (data extracted from Tkalich et al. (2016))

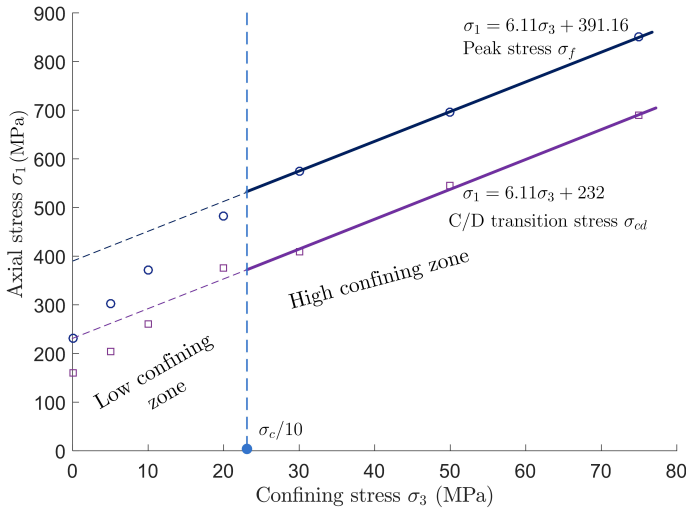

Figure IV .5: Linear fitting of the peak stress and C/D transition stress in high confining zone on (σ_3, σ_1) plane (data extracted from (Tkalich et al., 2016))

one obtains $\eta_r = 1.2$. Finally, the parameter b controls the degradation rate of friction coefficient,$b = 0.2$ is obtained for Kuru granite.

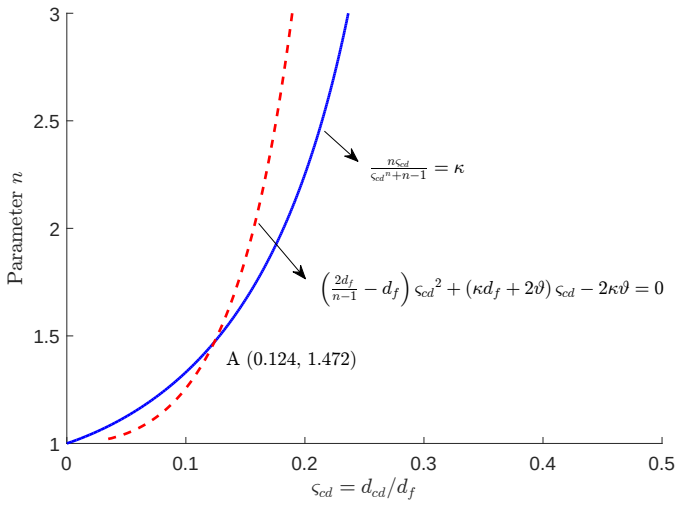

Figure IV .6: Determination of parameter n by using mapping method

5 Computational aspects

In view of engineering applications, the micro-mechanics based plastic damage model is implemented into the standard finite element software *Abaqus* using the provided user subroutine development process $UMAT$. Due to material non-linearities, the loading path is divided into a limit number of increments. For each loading increment, it is convenient to use the rate form of macroscopic stress-strain relations defined by a tangent operator.

5.1 Consistent tangent operator

In the case of time-independent process, the relation between stress increment $\Delta\boldsymbol{\sigma}$ and strain increment $\Delta\boldsymbol{\varepsilon}$ can be obtained by differentiating Eq.(IV .4) and can be written in the form:

$$\Delta\boldsymbol{\sigma} = \mathbb{C}^{\tan} : \Delta\boldsymbol{\varepsilon}. \tag{IV .37}$$

The fourth order tensor $\mathbb{C}^{\tan}$ is the tangent operator which is determined by making use of the damage and friction consistency conditions.

The loading/unloading conditions of plasticity are expressed in the so-called Kuhn-Tucker form, such that

$$\lambda^p \geq 0,\ \ f_p\left(\boldsymbol{\sigma}^c\right) \leq 0,\ \ \lambda^p f_p\left(\boldsymbol{\sigma}^c\right) = 0. \tag{IV .38}$$

It follows the condition in rate form:

$$\lambda^p \Delta f_p = 0. \tag{IV .39}$$

Hence, under plastic loading, one has $\lambda^p \neq 0$ and $\Delta f_p = 0$, leading to:

$$\Delta f_p = \frac{\partial f_p}{\partial \boldsymbol{\varepsilon}} : \Delta \boldsymbol{\varepsilon} + \frac{\partial f_p}{\partial \boldsymbol{\varepsilon}^p} : \Delta \boldsymbol{\varepsilon}^p + \frac{\partial f_p}{\partial d} \Delta d = 0. \tag{IV .40}$$

On the other hand, the damage consistency condition is written as:

$$\Delta f_d = \frac{\partial f_d}{\partial \boldsymbol{\varepsilon}^p} : \Delta \boldsymbol{\varepsilon}^p + \frac{\partial f_d}{\partial d} \Delta d = 0. \tag{IV .41}$$

By combining Eq.(IV .40) and Eq.(IV .41) and recalling that $\triangle \boldsymbol{\varepsilon}^p = \lambda^p \boldsymbol{D}$ and $\Delta d = \lambda^d$, the non-negative multipliers $\left(\lambda^p, \lambda^d\right)$ are given by:

$$\begin{cases} \lambda^p = \frac{1}{H_1} \frac{\partial f_p}{\partial \boldsymbol{\varepsilon}} : \Delta \boldsymbol{\varepsilon} \\ \\ \lambda^d = -\frac{\frac{\partial f_d}{\partial \boldsymbol{\varepsilon}^p} : \boldsymbol{D}}{\frac{\partial f_d}{\partial d} H_1} \frac{\partial f_p}{\partial \boldsymbol{\varepsilon}} : \Delta \boldsymbol{\varepsilon} \end{cases}, \tag{IV .42}$$

where $H_1 = \frac{\partial f_p}{\partial d} \frac{\partial f_d}{\partial \boldsymbol{\varepsilon}^c} : \boldsymbol{D} / \frac{\partial f_d}{\partial d} - \frac{\partial f_p}{\partial \boldsymbol{\varepsilon}^p} : \boldsymbol{D}$ is the hardening modulus.

By substituting Eq.(IV .42) for the differentiated form of Eq.(IV .4), one obtains the following tangent operator $\mathbb{C}^{\tan}$

$$\mathbb{C}^{\tan} = \begin{cases} \mathbb{C}^m, & \text{if } f_p\left(\boldsymbol{\sigma}^c\right) < 0 \\ \\ \mathbb{C}^m - \frac{1}{H_1}\left(\mathbb{C}^m : \boldsymbol{D}\right) \otimes \left(\boldsymbol{D} : \mathbb{C}^m\right), & \text{if } f_p\left(\boldsymbol{\sigma}^c\right) = 0 \end{cases}. \tag{IV .43}$$

Note that the symmetry of the tangent operator $\mathbb{C}^{\tan}$ provides an useful convenience for numerical implementation.

5.2 Local implementation algorithm

The implicit return mapping algorithm (Simo and Taylor, 1985) is widely used for the numerical implementation of elastic-plastic models. However, due to plastic-damage coupling, it was found that an explicit return mapping method was more efficient than the implicit one (Zhu et al., 2016). Therefore, the explicit mapping algorithm proposed in Zhu et al. (2016) is here adopted. For the reason of completeness, the main steps of algorithm are here summarized. At each Gauss integration point, given a strain increment $\Delta \boldsymbol{\varepsilon}_{i+1}$, the current strain tensor is updated as $\boldsymbol{\varepsilon}_{i+1} = \boldsymbol{\varepsilon}_i + \Delta \boldsymbol{\varepsilon}_{i+1}$. The objective is to fund the corresponding stress tensor after updating the plastic strains and damage variable using the proposed constitutive model.

The first step is to calculate an elastic prediction of stress. Considering $d_{i+1} = d_i$ and $\boldsymbol{\varepsilon}^p_{i+1} = \boldsymbol{\varepsilon}^p_i$, the elastic trial stress tensor is calculated by:

$$\boldsymbol{\sigma}^{trial}_{i+1} = \mathbb{C}^m : (\boldsymbol{\varepsilon}_{i+1} - \boldsymbol{\varepsilon}^p_i) \tag{IV .44}$$

Accordingly, the local trial stress tensor is given by:

$$\boldsymbol{\sigma}^{c,trial}_{i+1} = \boldsymbol{\sigma}^{trial}_{i+1} - \frac{1}{d_i}\mathbb{C}^d : \boldsymbol{\varepsilon}^p_i. \tag{IV .45}$$

Next, one checks the plastic and damage criteria. However, in the present model, as the thermodynamic damage force is entirely dependent on plastic strain (see (IV .6)), the check of damage criterion is directly combined with that of plastic criterion $f_p\left(\boldsymbol{\sigma}^{c,trial}_{i+1}\right)$. If $f_p\left(\boldsymbol{\sigma}^{c,trial}_{i+1}\right) \leq 0$, then $\triangle\boldsymbol{\varepsilon}^p_{i+1} = \mathbf{0}$ and $\triangle d_{i+1} = 0$. Otherwise an iterative plasticity-damage correction is performed. In this work, the superscript j ($j = 1, \ldots, m_{iter}$ with $m_{iter} = 100$) is used to denote the inter iterations related to the plastic-damage correction. And for the sake of clarity, the loading subscript $i+1$ will be omitted during the next steps.

One first determines the plastic multiplier with the frozen damage value d_i. For a plastic loading, one gets $f^j_p\left(\boldsymbol{\varepsilon}^{p,j}\right) > 0$ with the elastic prediction and one should have $f^{j+1}_p\left(\boldsymbol{\varepsilon}^{p,j} + \delta\boldsymbol{\varepsilon}^{p,j}\right) = 0$ after the plastic correction. The yield function can then be linearized using the first-order Taylor expansion as follows:

$$f^{j+1}_p = f^j_p + \frac{\partial f^j_p}{\partial \boldsymbol{\varepsilon}^{p,j}} : \delta\boldsymbol{\varepsilon}^{p,j} \approx 0. \tag{IV .46}$$

It follows by using the normality flow rule (IV .12)

$$f^{j+1}_p = f^j_p + \delta\lambda^{p,j}\frac{\partial f^j_p}{\partial \boldsymbol{\varepsilon}^{p,j}} : \boldsymbol{D}^j \approx 0, \tag{IV .47}$$

Thus the change to the plastic multiplier is given by:

$$\delta\lambda^{p,j} = -\frac{f^j_p}{\frac{\partial f^j_p}{\partial \boldsymbol{\varepsilon}^{p,j}} : \boldsymbol{D}^j}. \tag{IV .48}$$

The plastic strain is accordingly updated

$$\boldsymbol{\varepsilon}^{p,j+1} = \boldsymbol{\varepsilon}^{p,j} + \delta\lambda^{p,j}\boldsymbol{D}^j. \tag{IV .49}$$

The damage criterion can be now checked. If $f^j_d\left(\boldsymbol{\varepsilon}^{p,j+1}, d^j\right) \leq 0$, one has $d^{j+1} = d^j$. Otherwise, a damage increment should be calculated so that $f^j_d\left(\boldsymbol{\varepsilon}^{p,j+1}, d^j + \delta d^j\right) = 0$. Similar to the plastic correction, the damage criterion is linearized as follows:

$$f^{j+1}_d = f^j_d + \delta d^j \frac{\partial f^j_d}{\partial d^j} \approx 0 \tag{IV .50}$$

The change to the damage multiplier is given by:

$$\delta\lambda^{d,j} = -\frac{f_d^j}{\frac{\partial f_d^j}{\partial d^j}}. \tag{IV .51}$$

The damage state is then updated

$$d^{j+1} = d^j + \delta\lambda^{d,j}. \tag{IV .52}$$

At the third step, the macroscopic stress tensor is updated:

$$\boldsymbol{\sigma}^{j+1} = \mathbb{C}^m : \left(\boldsymbol{\varepsilon} - \boldsymbol{\varepsilon}^{p,j+1}\right). \tag{IV .53}$$

The inner iteration process is ended if $\left|f_p^{j+1}\right| \leq \epsilon_{\text{local}}$, ϵ_{local} being a chosen convergence tolerance value.

For the sake of clarity, the flowchart for the local numerical integration with explicit return mapping algorithm is arranged in Algorithm 3.

Algorithm 3: Flowchart of the local numerical integration

Input: $\Delta\boldsymbol{\varepsilon}_{i+1}, \boldsymbol{\sigma}_i, \boldsymbol{\varepsilon}_i, d_i, \boldsymbol{\varepsilon}_i^p$
Output: $\boldsymbol{\sigma}_{i+1}, \boldsymbol{\varepsilon}_{i+1}, d_{i+1}, \boldsymbol{\varepsilon}_{i+1}^p, \mathbb{C}^{\tan}$
Elastic prediction $\boldsymbol{\varepsilon}_{i+1} = \boldsymbol{\varepsilon}_i + \Delta\boldsymbol{\varepsilon}_{i+1}$; $\boldsymbol{\sigma}_{i+1}^{trial} = \mathbb{C}^m : (\boldsymbol{\varepsilon}_{i+1} - \boldsymbol{\varepsilon}_i^p)$
if $f_{i+1}(\boldsymbol{\sigma}^c) \leq 0$ **then**
  $\triangle\boldsymbol{\varepsilon}_{i+1}^p = \mathbf{0}$ and $\triangle d_{i+1} = 0$;
  $d_{i+1} = d_i$; $\boldsymbol{\varepsilon}_{i+1}^p = \boldsymbol{\varepsilon}_i^p$; $\mathbb{C}_{i+1}^{\tan} = \mathbb{C}^m$
else
  for $j = 1 \ldots m_{iter}$ **do**
    Calculate the plastic multiplier $\delta\lambda^{p,j} = -\frac{f^j}{\frac{\partial f^j}{\partial \boldsymbol{\varepsilon}^{p,j}} : \boldsymbol{D}^j}$;
    Update $\boldsymbol{\varepsilon}^{p,j+1} = \boldsymbol{\varepsilon}^{p,j} + \delta\lambda^{p,j}\boldsymbol{D}^j$;
    if $g^j\left(\boldsymbol{\varepsilon}^{p,j+1}, d^j\right) \geq 0$ **then**
      The increment of the damage multiplier $\delta\lambda^{d,j} = -g^j / \frac{\partial g^j}{\partial d^j}$
    else
      $\delta\lambda^{d,j} = 0$.
    end
    Update $d^{j+1} = d^j + \delta\lambda^{d,j}$, η^{j+1} and $\boldsymbol{D}^{j+1}$;
    if $\left|f^{j+1}\right| \leq \epsilon_{local}$ **then**
      Return;
    else
      $j = j + 1$
    end
  end
  $\mathbb{C}_{i+1}^{\tan} = \mathbb{C}^m - \frac{1}{H_1}(\mathbb{C}^m : \boldsymbol{D}) \otimes (\boldsymbol{D} : \mathbb{C}^m)$;
  $\boldsymbol{\sigma}^{j+1} = \mathbb{C}^m : \left(\boldsymbol{\varepsilon} - \boldsymbol{\varepsilon}^{p,j+1}\right)$;
end

6 Experimental validation on granites

In this section, the performance of the proposed model is checked against laboratory tests obtained on three granites, respectively from Kuru in Finland, Beishan in China and Lac du Bonnet in Canada.

6.1 Validation on Kuru granite

Using the experimental data found in Tkalich et al. (2016) and the calibration procedure presented above, the model's parameter for Kuru granite is given in Table IV .2.

Table IV .2: Parameter values for Kuru granite

Parameters	E^m(MPa)	ν^m	σ_c(MPa)	d_f	r_f	r_c	n	η_f	η_r	b
Values	78000	0.27	232	2.5	0.086	0.03	1.472	1.54	1.2	0.2

In Figures IV .7 and IV .8, the stress-strain curves of Kuru granite in conventional triaxial compression tests with low (0 to 20MPa) and high (30MPa to 75MPa) confining pressures are shown. One can see a good agreement between model's predictions and experimental data. The basic features of Kuru granite behaviors are reproduced, such as inelastic deformation, pressure sensitivity, volumetric dilatancy, material softening and residual strength.

In Figure IV .9, one shows the numerical prediction of deviatoric stress evolutions versus damage density for a confining pressure of 50MPa, respectively considering friction coefficient degradation ($\eta_r = 1.2$) and without degradation ($\eta_r = \eta_f$). One can clearly see that the material softening is jointly attributed to damage evolution (crack propagation) and degradation of friction coefficient of crack surfaces.

The post-peak behavior of material is further investigated using the proposed model. As mentioned in Section 3.3, the post-peak behavior is mainly controlled by the parameters n, η_r and b. Therefore, a sensitivity study is here performed respectively with respect to these three parameters in a conventional triaxial compression test with a confining pressure of 50MPa.

The value of n varies from 1.2 to 2.5. In Figure IV .10(a), one can see that the parameter n has a significant influence on the post-peak stress-strain curve and on the residual strength. With the increase of n, the residual strength is decreasing. And more interestingly, the post-peak behavior can be transformed from a stable softening (Class

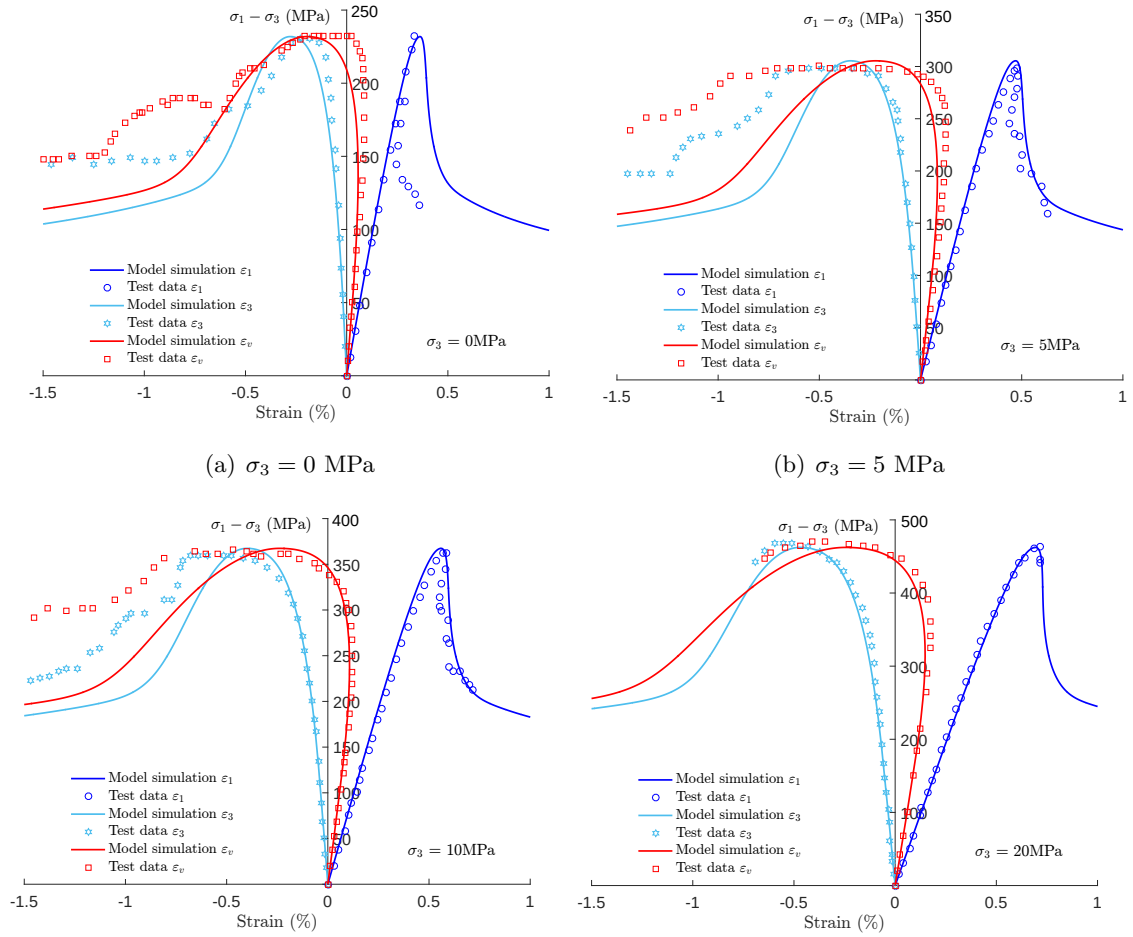

(a) $\sigma_3 = 0$ MPa

(b) $\sigma_3 = 5$ MPa

(c) $\sigma_3 = 10$ MPa

(d) $\sigma_3 = 20$ MPa

Figure IV .7: Comparisons between numerical results and experimental data on Kuru granite for triaxial compression test under low confining pressure (data extracted from Tkalich et al. (2016))

I behavior) to a snap-back softening (Class II behavior). For the Class I behavior, the stress decreases with increasing strain after the peak strength, implying that plastic strain increases faster than elastic strain decreases. For the Class II behavior, on the contrary, both the stress and strain decrease after the peak strength. However, the peak strength remains constant for all values of n. It is worth noting that the parameter n also has a significant influence on volume C/D transition point, ie., the C/D transition stress σ_{cd}. More precisely, σ_{cd} increases with the decrease of n, as shown in Figure IV .10(b).

In Figure IV .11, the evolutions of the crack friction coefficient η are presented by varying η_r from 0.8 to 1.54. The influences of η_r on macroscopic stress-strain curves are

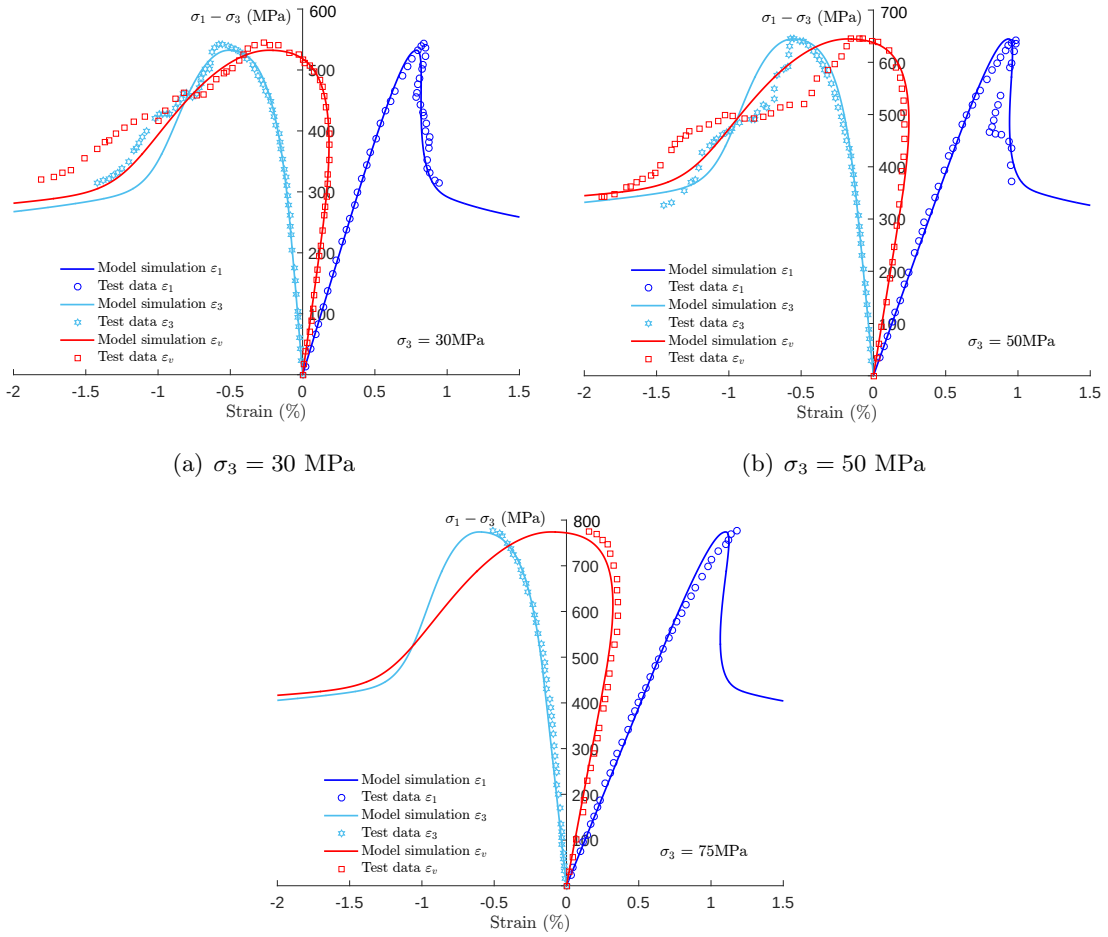

(a) $\sigma_3 = 30$ MPa

(b) $\sigma_3 = 50$ MPa

(c) $\sigma_3 = 75$ MPa

Figure IV .8: Comparisons between numerical results and experimental data on Kuru granite for triaxial compression test under high confining pressure (data extracted from Tkalich et al. (2016))

shown in Figure IV .11(a). One can see that η_r plays a controlling role of the residual strength. Logically, the residual strength decreases as the value of η_r decreases. On the other hand, the snap-back softening can also appear with the gradual decrease of η_r .

As for the parameter b, the sensitivity analysis is performed by varying b from 0.01 to 0.2, as illustrated in Figure IV .12. This parameters mainly influences the strain softening rate (see Figure IV .12(a)) and more precisely the rate of friction coefficient degradation as shown in Figure IV .12(b)). Bigger this parameter is, more rapidly the stress drops and the friction coefficient decreases. The choice of parameter b can also lead to both class I and class II behaviors. However, unlike the parameters n and η_r, the parameter b has no

effect on the residual strength. It only affects the shape of post-peak stress-strain curve.

6.2 Validation on Beishan granite

For a further validation of the model, a series of conventional triaxial compression tests on another brittle rock, Beishan granite are here investigated. By following the parameter determination procedure presented in the section 4, the model's parameters for Beishan granite have been determined and given in Table IV .3. Experimental data used here are extracted from Chen et al. (2014).

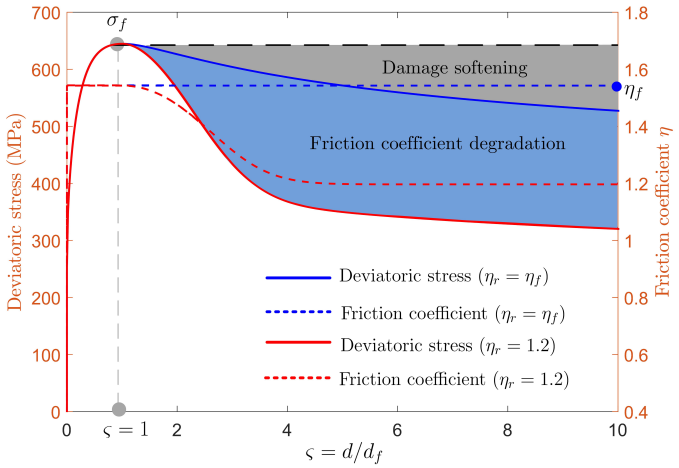

Figure IV .9: Stress-drop due to damage softening and friction coefficient degradation: $\sigma_3 = 50$ MPa

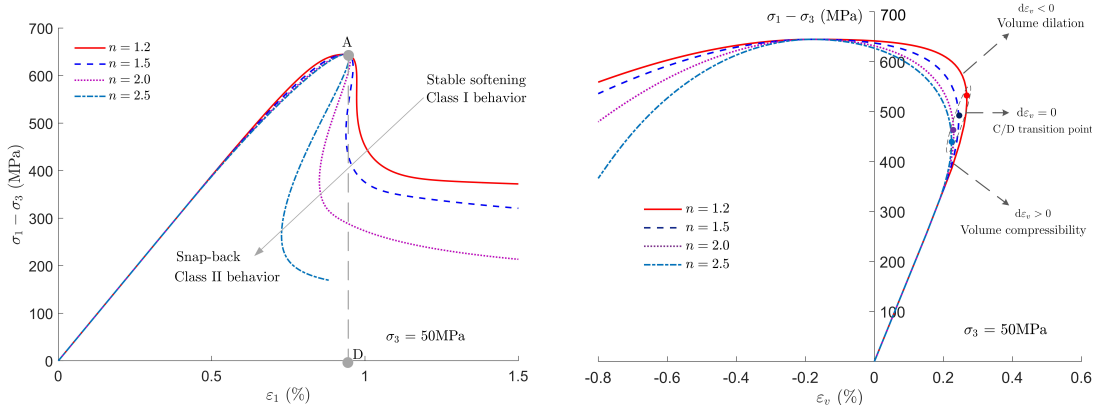

(a) Axial strain versus deviatoric stress (b) Volume strain versus deviatoric stress

Figure IV .10: Sensitivity analyses on the parameter n using triaxial compression tests with $\sigma_3 = 50$MPa

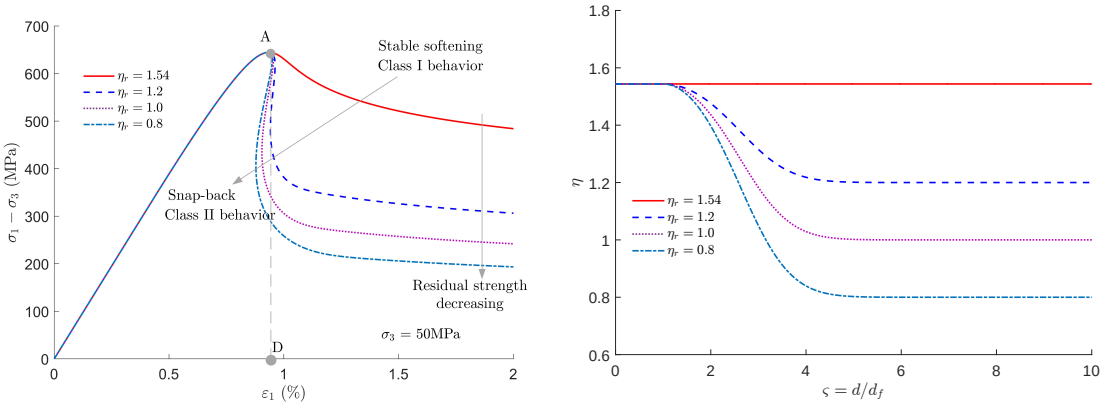

(a) Axial strain versus deviatoric stress (b) η versus ς

Figure IV .11: Sensitivity analyses on the parameter η_r using triaxial compression tests with $\sigma_3 = 50$MPa

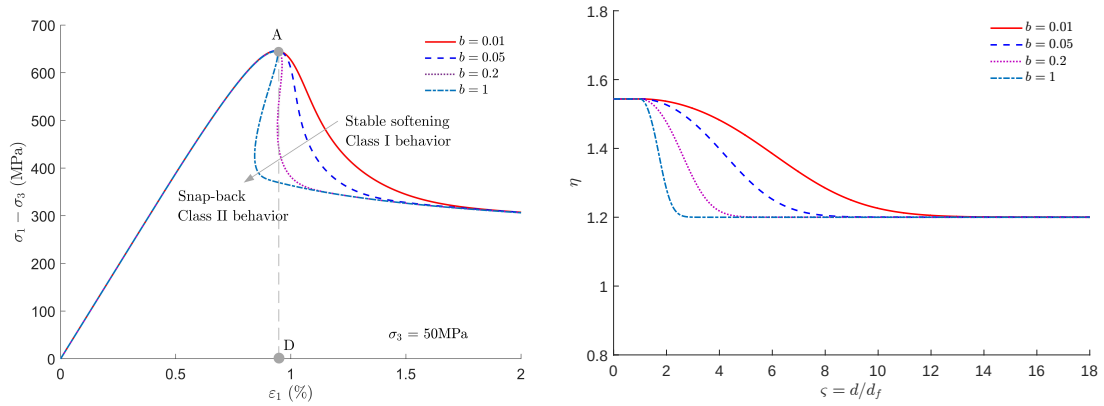

(a) Axial strain versus deviatoric stress (b) η versus ς

Figure IV .12: Sensitivity analyses on the parameter b using triaxial compression tests with $\sigma_3 = 50$MPa

In Figures IV .13, one shown the comparisons of peak strength and volumetric C/D transition threshold between model's predictions and experimental values. A very good agreement is found for all the range of confining pressure. The comparisons of stress-strain curves in triaxial compression tests are presented in Figures IV .14 for five levels of confining pressure, say 0, 5MPa, 10MPa, 20MPa and 30MPa. Again, all features of mechanical responses of material under different confining pressures are well reproduced by the proposed micro-mechanics based model.

In Figure IV .15, one shows the numerical prediction of damage density evolution of

Table IV .3: Parameter values for Beishan granite

Parameters	E^m(MPa)	ν^m	σ_c(MPa)	d_f	r_f	r_c	n	η_f	η_r	b
Values	70000	0.2	167	3.5	0.034	0.016	1.22	1.585	0.8	0.05

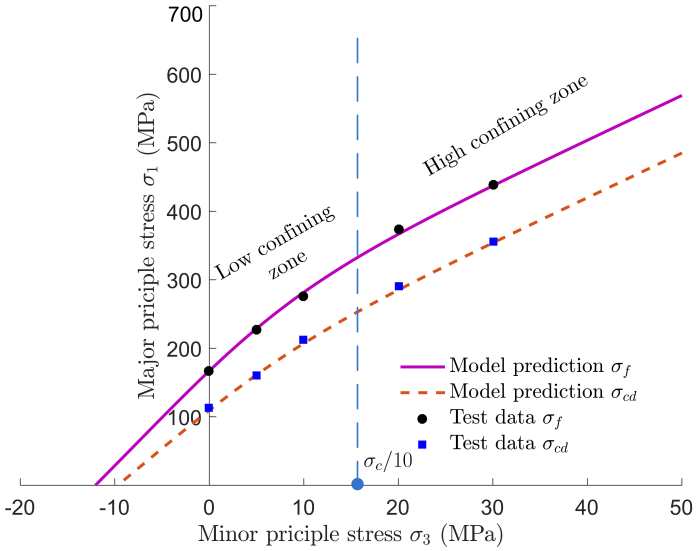

Figure IV .13: Description of peak strength σ_f and C/D transition stress σ_{cd} in Beishan granite (data extracted from Chen et al. (2014))

Beishan granite during the triaxial compression test with a confining pressure of 10MPa, together with the curve of accumulated acoustic emission counts. One can observe a clear correlation between the damage density evolution and the cumulative acoustic emission counts. During the first stage of deviatoric loading (before the point A), the damage evolution is neglected. This stage can be considered as the initial elastic phase and the corresponding stress σ_{ci} acts as the damage initiation threshold. Then, a steady increasing phase of damage (between A and B) is observed with the increase of deviatoric stress, corresponding to the initiation and propagation of micro-cracks. When the deviatoric stress approaches σ_{cd}, the damage density rapidly increases. At the same time, one observes a clear acceleration of acoustic emission counts (see the point C) as a consequence of surface energy generation in micro-cracks. On the other hand, the accelerated frictional sliding along micro-cracks leads to the transition from volumetric compressibility to dilatancy. Thus, the stress at this point σ_{cd}) is defined as the volumetric C/D transition threshold. In the post-peak region, the increasing rate of cumulative AE counts is reduced (after the

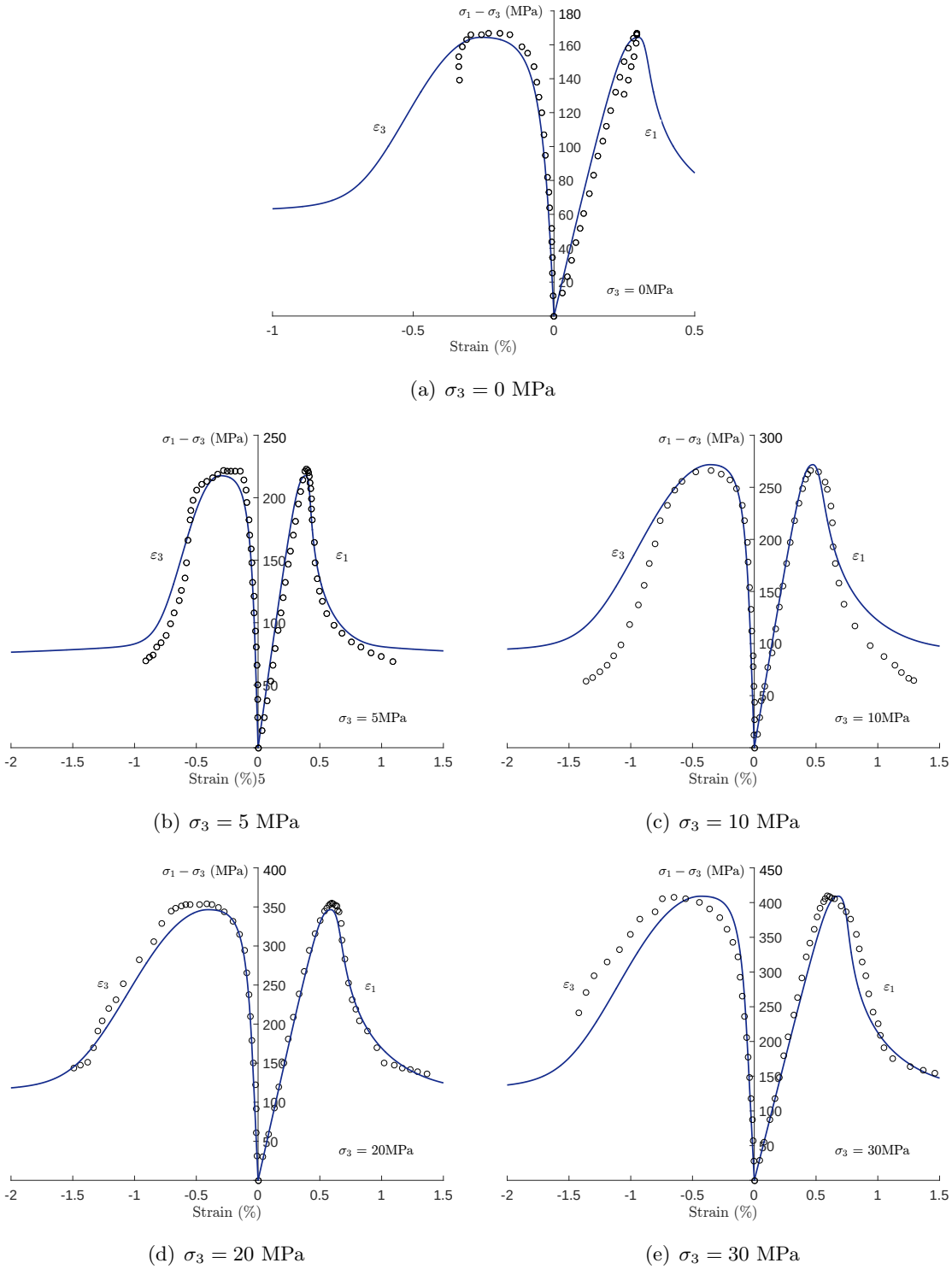

(a) $\sigma_3 = 0$ MPa

(b) $\sigma_3 = 5$ MPa

(c) $\sigma_3 = 10$ MPa

(d) $\sigma_3 = 20$ MPa

(e) $\sigma_3 = 30$ MPa

Figure IV .14: Comparisons between numerical results and experimental data on Beishan granite for triaxial compression tests with different confining pressures (continuous lines are numerical simulations)

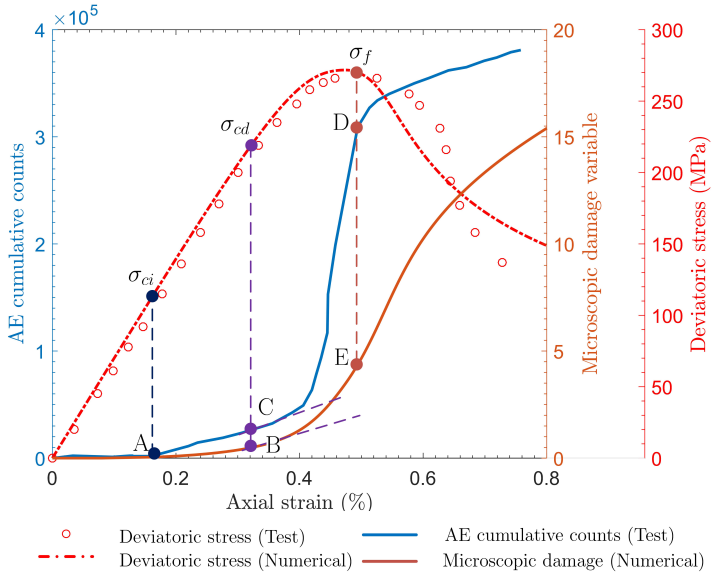

Figure IV .15: Numerical prediction of the microscopic damage evolution during the loading process in Beichan granite ($\sigma_3 = 10$ MPa, data extracted from Chen et al. (2015))

point D) while the damage density continues to rapidly increase after the point E. This difference of evolution can be explained by the fact that the AE events are mainly related to the creation of new surface areas and the new cracks. In another word, the accumulative AE counts are mainly related to the total number of micro-cracks $\mathcal{N}$. On the other hand, the damage density variable $d = \mathcal{N}a^3$ is also dependent on the average crack length a (radius of penny-shaped cracks). According to the results obtained on Beishan granite, it seems that in the post-peak regime, the creation of new cracks is slowed down while the frictional sliding along existing closed cracks is still an active process.

6.3 Validation on Lac du Bonnet granite

The Lac du Bonnet granite has been widely investigated in the framework of geological disposal of radioactive waste in Canada (Aubertin and Li, 2004; Martin and Chandler, 1994; Martin, 1997). The experimental data from Martin (1997) are here used. Unfortunately, no experimental data on lateral or volumetric strains are available. It is then impossible to identify the volumetric C/D transition stress σ_{cd} and to determine the parameter n. Based on the sensitivity study on n in Section 6.1, one takes $n = 1.4$. On the other hand, it seems that the Lac du Bonnet granite exhibits a snap-back behavior in the post-peak regime for a wide range of confining pressure up to 60MPa. In connection

Table IV .4: Model's parameters for Lac du Bonnet granite

Parameters	E^m(MPa)	ν^m	σ_c(MPa)	d_f	r_f	r_c	n	η_f	η_r	b
Values	72000	0.2	184	2.5	0.1	0.031	1.4	1.4	0.6	2

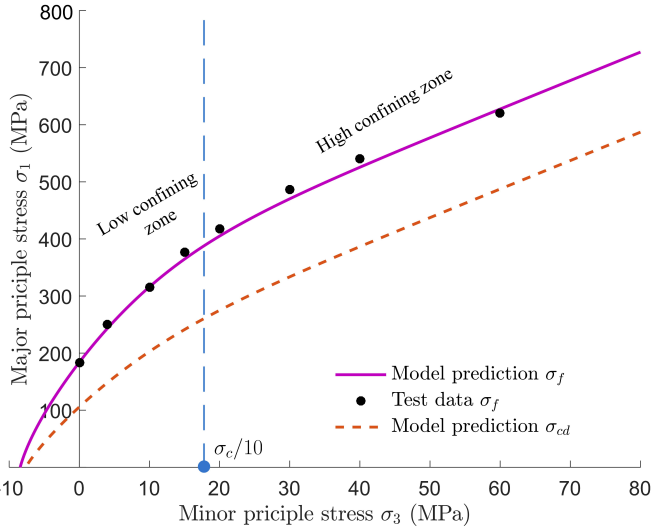

Figure IV .16: Peak strength σ_f and C/D transition stress σ_{cd} predictions of Lac du Bonnet (data extracted from Martin (1997))

with this, $b = 2$ is chosen for this brittle material. The model's parameters for the Lac du Bonnet granite are listed in Table IV .4. In Figure IV .16, one shows the numerical predictions of peak strength σ_f and volumetric C/D transition stress σ_{cd} of the Lac du Bonnet granite. Again, the nonlinear strength envelope is well depicted with respect to the experimental data. In Figure IV .17, stress-strain curves in conventional triaxial compression tests under different confining pressures are shown. Once more, one can see that the proposed model is able to correctly predict the basic features of mechanical behaviors, such as the inelastic axial and lateral strains, the material hardening and softening with snap-back, the peak and residual strength.

7 Concluding remarks

In this work, a micro-mechanics based plastic damage model has been developed for quasi-brittle materials under compressive stresses. The damage evolution of related to the initiation and growth of micro-cracks while the plastic deformation is due to the frictional

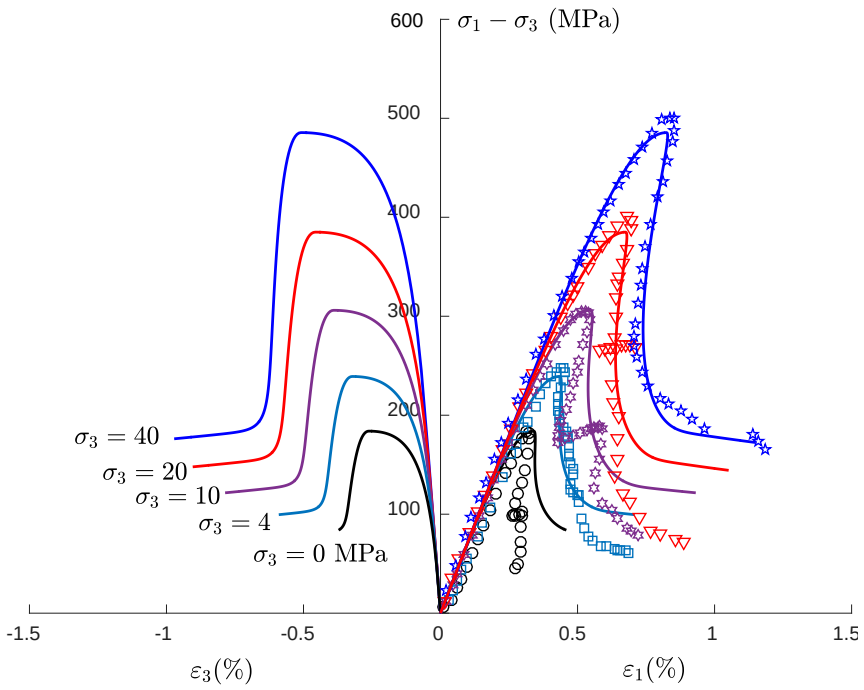

Figure IV .17: Comparisons between numerical results and experimental data on Lac du Bonnet granite for triaxial compression tests with different confining pressure(continuous lines are numerical simulations, data extracted from Martin (1997))

sliding along cracks. In the framework of thermodynamics and a linear homogenization scheme, the macroscopic stress-strain relations and the thermodynamics forces for microscopic frictional sliding and damage evolution have been deduced. The frictional sliding is driven by the local stress tensor applied to micro-cracks, which is affected by the damage state. The damage evolution is controlled by the frictional sliding along micro-cracks. Therefore, two inelastic processes are inherently coupled. In particular, the effect of confining pressure on the material resistance to crack propagation has been taken into account. The proposed model has also considered the progressive degradation of surface asperity of micro-cracks due to frictional sliding.

The proposed model contains a relatively small number of parameters which are physically related to specific features of macroscopic responses. An identification procedure of parameters from macroscopic conventional triaxial compression tests has been proposed.

The performance of the model has been verified through a wide campaign of experimental comparisons on three different materials in triaxial compression tests with a large range of confining pressure. All main features of mechanical responses have been well reproduced such as inelastic strains, volumetric compressibility - dilatancy, peak and residual

strength. The proposed model is able to provide different kinds of post-peak behaviors observed in brittle materials including snap-back softening. Furthermore, the microscopic damage density evolution is consistent with the variation of cumulative acoustic emission counts. It was found that the post-peak behavior was mainly driven by the frictional sliding and propagation along existing micro-cracks.

It is known that the material softening in quasi-brittle and cohesive materials is generally related to the coalescence of micro-cracks and to the transition from diffuse micro-cracks to localized macroscopic cracks. The macroscopic responses of sample after the localization are progressively controlled by those of localized cracks or fractures. This phenomenon is similar to the force chain buckling in granular materials. Different theoretical models and numerical methods have been developed for dealing with the transition from diffuse damage and plasticity to localized cracking and failure. The proposed micromechanics based model can be easily integrated in the analysis of localized cracking and failure through the definition of some critical value of damage density. This interesting aspect is investigated in Chapter V .

Appendix: Derivation of Eq (IV .31)

With the condition of $\frac{\partial \varepsilon_v}{\partial \varsigma} = 0$ at the volumetric C/D transition point and by combining Eq. (IV .30), one can get

$$\left(\frac{\chi}{k^m \left(\sqrt{6} - \eta_f\right) \eta_f} - \frac{\varsigma d_f}{2} \right) \tilde{r}_f g^{'} (\varsigma) - d_f \tilde{r}_f g (\varsigma) = 0 \tag{IV .54}$$

For the sake of simplicity, note that $\vartheta = \frac{\chi}{k^m \left(\sqrt{6} - \eta_f\right) \eta_f}$. Since $\tilde{r}_f \neq 0$, Eq. (IV .54) is equivalent to

$$\left(2\vartheta - \varsigma d_f\right) g^{'} (\varsigma) - 2 d_f g (\varsigma) = 0 \tag{IV .55}$$

Taking ς derivatives of $g(\varsigma)$ in Eq. (IV .8) one can write

$$g^{'} (\zeta) = \frac{\varsigma n}{\varsigma \left(\varsigma^n + n - 1\right)} - \frac{n^2 \varsigma^2 \varsigma^{n-2}}{\left(\varsigma^n + n - 1\right)^2} = \frac{g(\varsigma)}{\varsigma} - g^2 (\varsigma) \varsigma^{n-2} \tag{IV .56}$$

Substituting Eq. (IV .56) for Eq. (IV .55) one arrives at

$$\left(2\vartheta - \varsigma d_f\right) \left(\frac{g(\varsigma)}{\varsigma} - g^2 (\varsigma) \varsigma^{n-2} \right) - 2 d_f g (\varsigma) = 0 \tag{IV .57}$$

It is noted that since $g(\varsigma) \neq 0$, then both sides of Eq. (IV .57) are divided by $g(\varsigma)$ one gets

$$\frac{\left(2\vartheta - \varsigma d_f\right)}{\varsigma} - g(\varsigma) \varsigma^{n-2} \left(2\vartheta - \varsigma d_f\right) - 2 d_f = 0 \tag{IV .58}$$

Considering $\varsigma = \varsigma_{cd}$ and $g(\varsigma_{cd}) = \kappa$, and substituting them for Eq. (IV .58), and after some straightforward computations, one gets the following equation

$$\kappa\varsigma_{cd}^{n-1}(2\vartheta - \varsigma_{cd}d_f) + 3d_f\varsigma_{cd} - 2\vartheta = 0 \tag{IV .59}$$

Obviously, Eq. (IV .24) can be rearranged as follows:

$$\kappa\varsigma_{cd}^{n-1} = n - (n-1)\frac{\kappa}{\varsigma_{cd}} \tag{IV .60}$$

By substituting Eq. (V .69) for Eq. (IV .59), one arrives at

$$(3d_f - d_f n)\varsigma_{cd}^2 + (\kappa(n-1)d_f + 2\vartheta n - 2\vartheta)\varsigma_{cd} - 2\kappa(n-1)\vartheta = 0 \tag{IV .61}$$

and divided by $n-1$, one can obtain

$$\left(\frac{2d_f}{n-1} - d_f\right){\varsigma_{cd}}^2 + (\kappa d_f + 2\vartheta)\varsigma_{cd} - 2\kappa\vartheta = 0 \tag{IV .62}$$

Chapter V

Analysis of localized cracking in quasi-brittle materials with a micro-mechanics based friction-damage approach*

This chapter is devoted to the study of transition from diffuse damage to localized cracking in quasi-brittle materials. A micro-mechanics based friction-damage model is first formulated with a rigorous homogenization procedure. The plastic deformation is related to the frictional sliding along diffuse micro-cracks while the damage is induced by the growth of micro-cracks. The localized cracking is considered as a consequence of coalescence of diffuse micro-cracks. The onset of localized crack is then defined by introducing a critical value of diffuse damage density parameter. The orientation of localized crack is determined from the Mohr's maximization postulate. After the onset of a localized crack, the energy dissipation of material is entirely related to the frictional sliding and propagation of the localized crack. In this context, a localized friction damage model is developed in the framework of thermodynamics to describe the frictional sliding of the localized crack which acts as the driving force for its propagation. As an example, analytical results of localized crack angle are determined for some specific loading paths including plane stress, plane strain and conventional triaxial compression. Moreover, analytical solutions of complete stress-strain curves with the transition from diffuse damage to localized cracking are

*Zhao, Lun-Yang, Jian-Fu Shao, and Qi-Zhi Zhu. "Analysis of localized cracking in quasi-brittle materials with a micro-mechanics based friction-damage approach." Journal of the Mechanics and Physics of Solids 119 (2018): 163-187.

also obtained for conventional triaxial compression tests and compared with experimental data.

1 Introduction

In quasi brittle materials such as concrete, rocks and ceramics, the nucleation, propagation and coalescence of micro-cracks are the main physical process of inelastic deformation and failure. The macroscopic failure is generally induced by the onset of localized cracks which are originated from the coalescence of diffuse micro-cracks. Unlike shear bands in ductile materials like soils, the localized cracks or fractures in rock-like materials are generally surfaces of very small thickness but with strong displacement discontinuities. After the localization, the macroscopic stress-strain relations of cracked material are essentially governed by the behavior of localized cracks. The objective of the present study is to develop a micro-mechanics based approach to describe the plastic damage of quasi-brittle materials before localization, the onset condition of localized cracking, and the mechanical behavior of cracked material after localization.

The concept of localized failure in quasi brittle materials was first introduced in the landmark papers of Ngo and Scordelis (1967) and of Rashid (1968). After that, a great diversity of approaches have been developed to deal with this issue, ranging from continuum mechanics-based models (stress-based models) to fracture mechanics-based models (traction-based models). In the computational context, these approaches have respectively generated smeared crack models (Cervera and Chiumenti, 2006; Ingraffea and Saouma, 1985; Oliver et al., 2002, 2004) and discontinuous crack models (Armero and Garikipati, 1996; Oliver, 2000; Oliver et al., 1999; Wu and Cervera, 2015, 2016). An extended FE strategy for transition from continuum damage to mode I cohesive crack propagation has been proposed in Comi et al. (2007). The material was described by a non-local damage model. An extended finite element approach was used after the localization to follow the propagation path. Jirásek and Zimmermann have developed an embedded crack model (Jirásek and Zimmermann (2001a)) and its combination with smeared cracks (Jirásek and Zimmermann (2001b)). They have proposed a triangular element with an embedded displacement discontinuity that represents a crack.

More specially, in the stress-based models, regularized constitutive relations are generally formulated to study mechanical responses in the post-localization regime. Various regularization techniques have been developed including non-local damage mechanics and higher order plasticity theory. A great number of damage models (Jirásek, 1998; Peerlings

et al., 1998), plastic models (Chambon et al., 2001; Pamin, 1994) and coupled plastic-damage models (Grassl and Jirásek, 2006a; Haddag et al., 2009; Lee and Fenves, 1998; Lubliner et al., 1989) have been employed to investigate the localized failure in different kinds of materials. However, in these models, localized cracks with strong discontinuities are replaced by highly concentrated strain bands or damage zones.

On the other hand, in traction-based models (Bazant and Planas, 1997; Carol et al., 1997; Oliver, 1996), the strain/displacement discontinuities are directly taken into account by embedding discontinuity interfaces inside an elastic continuum along preferred orientations. A crucial step in this kind of models is to determine the onset condition and orientation of localized cracks. The bifurcation theory has been widely adopted for the analysis of strain localization with weak (strain) discontinuities (Rice and Rudnicki, 1980; Rudnicki and Rice, 1975) in soil-like materials. However, this theory is not suitable for the study of localized cracks with strong (displacement) discontinuities (Oliver et al., 1999; Wu and Cervera, 2015).

Therefore, during the last two decades, important efforts have been made on modeling of localized cracks with strong discontinuities. In particular, various criteria for the onset of localized cracking and traction-based models for studying mechanical behaviors of localised cracks have been proposed (Cervera et al., 2012; Cervera and Wu, 2015; Oliver, 1996, 2000; Oliver et al., 2012; Wu and Cervera, 2016). In these models, the authors tried to establish the traction-based model for the localized crack in consistency with the constitutive model used before localization. To the knowledge of the authors, only simple isotropic damage models (Huespe et al., 2006; Oliver et al., 1999) and plastic models (Oliver, 2000) have been so far considered. Moreover, in most previous studies, the emphasis has been put on the study of localized failure after the onset of localization. The crucial issue of the transition from the diffuse damage or plastic deformation to the localized cracking has not been systematically investigated.

In the present chapter, we shall propose a new micro-mechanics based framework for dealing with this crucial issue. The emphasis will be put on closed cracks under compression-dominated stresses. The general methodology is illustrated in Figure 1. Before localization, the material is characterized by a solid matrix weakened by randomly distributed micro-cracks. The diffuse damage evolution is related to the growth of micro-cracks while the frictional sliding along micro-cracks is at the origin of macroscopic plastic strains. The propagation of micro-cracks is driven by the frictional sliding. A micro-mechanics based friction-damage model will be developed for the description of mechanical behavior of micro-cracked material before localization. Based on this model, the onset of

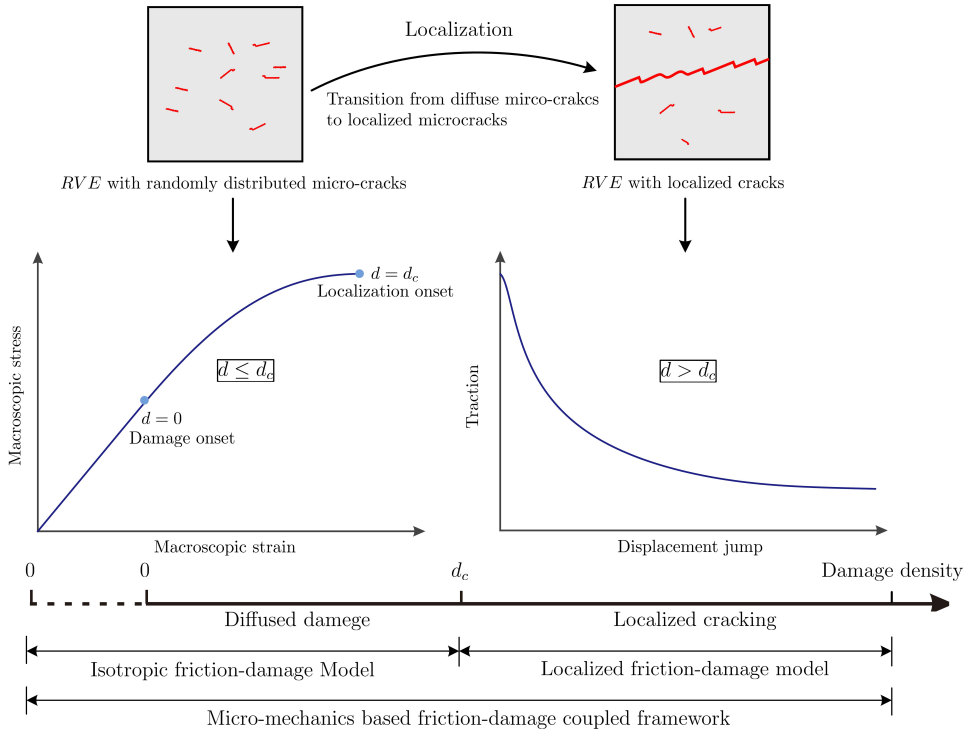

Figure V .1: Schematic representation of the transition from diffuse micro-cracking to localized cracking

localized crack is defined through a critical value of damage (micro-cracks) density parameter, and the orientation of localized crack is determined using the Mohr's maximization postulate. After the localization, the mechanical behavior of cracked material is controlled by the localized crack and a new traction-based friction-damage model will be established for the localized crack. Analytical results in terms of localized crack orientation will be determined for some particular loading paths without rotation of principal stresses including plane stress, plane strain and conventional triaxial compression. Analytical solutions of complete stress-strain curves will also be obtained for conventional triaxial compression tests and compared with experimental data.

2 Micro-mechanics based isotropic friction-damage model

In this section, a micro-mechanics based isotropic friction-damage model is presented to describe the mechanical behavior of material before the onset of localized cracks. This model is used here as the starting point for studying the transition from diffuse damage and localized cracking. The formulation of the model is based on our previous studies

(Zhu and Shao, 2015; Zhu et al., 2016) and only the main features are presented here.

The micro-mechanical frictional damage model is formulated with a linear homogenization procedure and within the irreversible thermodynamics framework. We shall consider quasi-brittle materials as an elastic solid weakened by micro-cracks. To this end, a Representative Volume Element (RVE), as shown in Figure V .2, is selected to represent a macroscopic material point. The RVE occupies the domain $\Omega \subset \mathbb{R}^{n_{\text{dim}}}$ (n_{dim} =1,2,3, being the geometrical dimension of the domain) and it is limited by its external boundary surface $\partial\Omega \subset \mathbb{R}^{n_{\text{dim}}-1}$. Limiting our study to isotropic materials, the RVE is composed of an elastic isotropic solid matrix $\Omega_m \subset \mathbb{R}^{n_{\text{dim}}}$ and randomly distributed micro-cracks $\Omega_c \subset \mathbb{R}^{n_{\text{dim}}}$. Each micro-crack is considered as a spheroidal inclusion embedded in the solid matrix. Before the onset of localization, the size of diffuse micro-cracks is much smaller than that of the RVE. The elastic stiffness tensor of the solid matrix is denoted as $\mathbb{C}^m$, and that of inclusions (micro-cracks) as $\mathbb{C}^c$.

Each micro-crack is characterized by its unit normal vector $\underline{n}$ and the aspect ratio $\epsilon = c/a$ with a and c being the average radius and half opening of the micro-crack respectively (see Figure V .2). The volume fraction of micro-cracks is defined by $\varphi = \frac{4}{3}\pi a^2 c\mathcal{N} = \frac{4}{3}\pi\epsilon d$, with $\mathcal{N}$ denoting the number of micro-cracks per unit volume, and $d = \mathcal{N}a^3$. Due to the fact that the aspect ratio of micro-cracks is generally very small and is equal to zero for closed micro-cracks, the volume fraction φ is not a suitable state variable to characterize the effect of micro-cracks on mechanical properties of materials. Therefore, due to the definition initially given by (Budiansky and O'connell, 1976), the crack density parameter d is here used as the internal variable to characterize the damage state of materials.

The macroscopic strain of cracked materials $\boldsymbol{E}$ is due to the deformation of solid matrix $\boldsymbol{E}^m$ and to the discontinuities of micro-cracks $\boldsymbol{E}^c$. That is:

$$\boldsymbol{E} = \boldsymbol{E}^m + \boldsymbol{E}^c \tag{V .1}$$

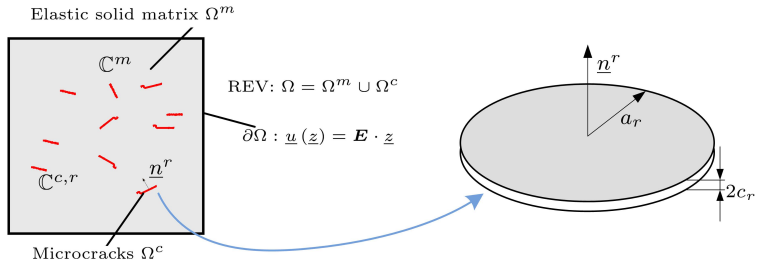

Figure V .2: Representative Volume Element of quasi-brittle materials with diffuse damage

The strain of solid matrix is determined by the elastic compliance tensor of solid matrix: $\boldsymbol{E}^m = \mathbb{S}^m : \boldsymbol{\Sigma}$, with $\mathbb{S}^m = (\mathbb{C}^m)^{-1}$ and $\boldsymbol{\Sigma}$ being the macroscopic stress tensor. The crack-induced strain $\boldsymbol{E}^c$ is related to the displacement discontinuities of micro-cracks. For open micro-cracks, the elastic stiffness $\mathbb{C}^c$ and the local stress field applied onto surfaces of micro-cracks vanish. According to previous studies (Zhu et al., 2008a, 2011), the effective elastic stiffness tensor of the equivalent homogenized medium can be explicitly determined using a linear homogenization procedure based on the Eshelby's solution (Eshelby, 1957b) by considering micro-cracks as inclusions. One gets the following general relation:

$$\boldsymbol{E}^c = (\mathbb{I} - (\mathbb{C}^m)^{-1} : \mathbb{C}^{hom}) : \boldsymbol{E} \tag{V .2}$$

The effective elastic stiffness tensor $\mathbb{C}^{hom}$ is dependent on the homogenization scheme used. As an example, for a matrix-inclusion system, the Mori-Tanaka homogenization scheme (Benveniste, 1987; Mori and Tanaka, 1973c) is generally adopted. For isotropic materials, the effective elastic tensor is given by:

$$\mathbb{C}^{\text{hom}} = 3k^{\text{hom}}\mathbb{J} + 2\mu^{\text{hom}}\mathbb{K} \qquad \text{with} \qquad k^{\text{hom}} = \frac{k^m}{1+\alpha d}, \mu^{\text{hom}} = \frac{\mu^m}{1+\beta d} \tag{V .3}$$

α and β are two constants which are only functions of the Poisson's ratio ν^m of the solid matrix, i.e. $\alpha = \frac{16}{9}\frac{1-(\nu^m)^2}{1-2\nu^m}$ and $\beta = \frac{32}{45}\frac{(1-\nu^m)(5-\nu^m)}{2-\nu^m}$. k^m and μ^m are respectively the bulk and shear moduli of the solid matrix. Moreover, the effective elastic compliance tensor $\mathbb{S}^{\text{hom}}$ can be expressed as the sum of the elastic compliance of the solid matrix $\mathbb{S}^m$ and the additional compliance induced by micro-cracks $\mathbb{S}^d$:

$$\mathbb{S}^{\text{hom}} = \left(\mathbb{C}^{\text{hom}}\right)^{-1} = \mathbb{S}^m + \mathbb{S}^d \quad ; \quad \mathbb{S}^d = \frac{\alpha d}{3k^m}\mathbb{J} + \frac{\beta d}{2\mu^m}\mathbb{K} \tag{V .4}$$

However, in the present study, the emphasis is put on the study of quasi-brittle materials with closed frictional micro-cracks under compressive stresses. In that case, the crack-induced strain $\boldsymbol{E}^c$ cannot be determined from the linear homogenization procedure only. It is related to the frictional sliding along closed micro-cracks. The frictional sliding is at the physical origin at the microscopic scale of the macroscopic plastic strains of quasi-brittle materials. Therefore it is needed to define a specific friction criterion and a flow rule to determine the frictional sliding induced strain $\boldsymbol{E}^c$. This is here achieved by the combination of homogenization procedure and irreversible thermodynamics.

2.1 Free energy and state equations

With the decomposition of strain given in Eq.(V .1), the free energy function of cracked materials can be expressed in the following general form (Zhao et al., 2016; Zhu et al.,

2016):

$$\psi = \frac{1}{2}\left(\boldsymbol{E} - \ \boldsymbol{E}^c\right) : \mathbb{C}^m : \left(\boldsymbol{E} - \boldsymbol{E}^c\right) + \frac{1}{2}\boldsymbol{E}^c : \mathbb{C}^d : \boldsymbol{E}^c \tag{V .5}$$

The first term corresponds to the elastic strain energy of the solid matrix and the second one represents the stored energy related to the frictional sliding related strain. $\mathbb{C}^d$ is a fourth order tensor accounting for the coupling between the frictional sliding and the growth of micro-cracks (damage evolution). The expression of $\mathbb{C}^d$ can be obtained from the continuity condition of free energy between open and closed micro-cracks and by invoking the equivalence between the definition given in (V .5) and the alternative one $\psi = \frac{1}{2}\boldsymbol{E} : \mathbb{C}^{\text{hom}} : \boldsymbol{E}$ and one obtains (Zhu, 2016; Zhu and Shao, 2015):

$$\mathbb{C}^d = \left(\mathbb{S}^d\right)^{-1} = \frac{3k^m}{\alpha d}\mathbb{J} + \frac{2\mu^m}{\beta d}\mathbb{K} \tag{V .6}$$

One can see that the coupling tensor is a function of damage density parameter d. Therefore, $\boldsymbol{E}^c$ and d act as two internal variables to characterize the states of frictional sliding and damage. The positiveness of the intrinsic dissipation leads to:

$$\boldsymbol{\Sigma} = \frac{\partial \psi}{\partial \boldsymbol{E}} = \mathbb{C}^m : \left(\boldsymbol{E} - \boldsymbol{E}^c\right), \quad \boldsymbol{E} = \mathbb{S}^m : \boldsymbol{\Sigma} + \boldsymbol{E}^c \tag{V .7a}$$

$$-\frac{\partial \psi}{\partial \boldsymbol{E}^c} : \dot{\boldsymbol{E}}^c \geq 0 \tag{V .7b}$$

$$-\frac{\partial \psi}{\partial d}\dot{d} \geq 0 \tag{V .7c}$$

where $\dot{x}$ represents the rate with respect to time. Eq.(V .7a) is the state law giving the macroscopic stress-strain relations; Eqs.(V .7b) and (V .7c) denote the energy dissipation due to frictional sliding and that due to damage evolution, respectively. The thermodynamic conjugate force associated with the frictional-sliding induced strain $\boldsymbol{E}^c$ is deduced as follows:

$$\boldsymbol{\Sigma}^c = -\frac{\partial \psi}{\partial \boldsymbol{E}^c} = \boldsymbol{\Sigma} - \mathbb{C}^d : \boldsymbol{E}^c \tag{V .8}$$

$\boldsymbol{\Sigma}^c$ physically represents the local stress field applied onto closed micro-cracks. This local stress field is different to the macroscopic stress $\boldsymbol{\Sigma}$ and explicitly depends on the damage variable d through the coupling tensor $\mathbb{C}^d$. Similarly, the thermodynamic conjugate force associated with damage variable d can also be defined as:

$$\mathcal{Y}^d = -\frac{\partial \psi}{\partial d} = -\frac{1}{2}\boldsymbol{E}^c : \frac{\partial \mathbb{C}^d}{\partial d} : \boldsymbol{E}^c \tag{V .9}$$

2.2 Friction sliding law

The frictional sliding along closed micro-cracks is here described by a generalized Coulomb criterion in terms of the local stress field $\boldsymbol{\Sigma}^c$ applied onto micro-cracks. It is

known that for frictional materials, the sliding is driven by the shear stress vector along the crack surface. The material strength to sliding depends not only on the local friction coefficient of crack surface but also on the normal compressive stress applied onto the crack surface. Therefore, it is convenient to decompose the local stress field $\boldsymbol{\Sigma}^c$ into a spherical part and a deviatoric part (Zhu et al., 2011):

$$\boldsymbol{\Sigma}^c = \mathbb{J} : \boldsymbol{\Sigma}^c + \mathbb{K} : \boldsymbol{\Sigma}^c = \frac{1}{3}\left(\boldsymbol{\Sigma}^c : \boldsymbol{\delta}\right)\boldsymbol{\delta} + \mathbb{K} : \boldsymbol{\Sigma}^c \tag{V .10}$$

The friction criterion is then formulated in terms of the local spherical stress $P^c = \frac{1}{3}\boldsymbol{\Sigma}^c : \boldsymbol{\delta}$ and deviatoric stress $\boldsymbol{S}^c = \mathbb{K} : \boldsymbol{\Sigma}^c$ as follows:

$$\mathcal{F}\left(\boldsymbol{\Sigma}^c\right) = \|\boldsymbol{S}^c\| + c_f P^c \leq 0, \tag{V .11}$$

c_f denotes the local friction coefficient of crack surface. It is noted that the local spherical stress P^c and deviatoric stress $\boldsymbol{S}^c$ are respectively related to the normal stress and shear stress applied onto the crack surface (Zhu et al., 2011). The evolution rate of the frictional sliding related strain $\boldsymbol{E}^c$ can be given by using the normality rule:

$$\dot{\boldsymbol{E}}^c = \lambda^c \frac{\partial \mathcal{F}}{\partial \boldsymbol{\Sigma}} = \lambda^c \frac{\partial \mathcal{F}}{\partial \boldsymbol{\Sigma}^c} = \lambda^c \boldsymbol{D}, \tag{V .12}$$

where λ^c is a non-negative multiplier. The flow direction is defined by:

$$\boldsymbol{D} = \frac{\boldsymbol{S}^c}{\|\boldsymbol{S}^c\|} + \frac{1}{3} c_f \boldsymbol{\delta} \tag{V .13}$$

Accordingly, the friction criterion (V .11) can be rewritten into a compacted form:

$$\mathcal{F}\left(\boldsymbol{\Sigma}, d, \boldsymbol{E}^c\right) = \boldsymbol{\Sigma}^c : \boldsymbol{D} = \boldsymbol{\Sigma} : \boldsymbol{D} - \boldsymbol{D} : \mathbb{C}^d : \boldsymbol{E}^c \tag{V .14}$$

For the sake of simplicity, an associated flow rule is here used to describe the frictional-sliding related strain. However, a non-associated flow rule can be introduced for instance to better evaluate the normal opening of micro-cracks and consequently the macroscopic volumetric strain.

2.3 Damage evolution law

The propagation of micro-cracks occurs when the damage driving force $\mathcal{Y}^d$ reaches the material resistance. Therefore, the damage criterion can be written in the following general form:

$$\mathcal{G}\left(\mathcal{Y}^d, d\right) = \mathcal{Y}^d - \mathcal{R}\left(d\right) \leq 0, \tag{V .15}$$

The function $\mathcal{R}\left(d\right)$ defines the current material resistance (toughness) to micro-crack growth. It plays a similar role as the critical stress intensity factor in linear fracture

mechanics for propagation of macroscopic fracture. The material toughness may evolve with the crack density due to material hardening and interactions between micro-cracks. In general, the material resistance first increases when the crack density is small and then decreases when the crack density becomes high enough. It is then convenient to express the material toughness as a function of the damage density parameter d. Based on experimental data for different kinds of rock-like materials, the following form has been proposed in Zhao et al. (2018):

$$\mathcal{R}(d) = \mathcal{R}(d_c)\,\frac{b\xi}{b-1+\xi^b},$$

$\xi = d/d_c$ is a dimensionless variable defining the damage level. The parameter d_c defines a critical value of damage so that when $d = d_c$, $\mathcal{R}(d)$ reaches its maximal value $\mathcal{R}(d_c)$. The material parameter $b > 1$ controls the material resistance evolution rate. It shall take different values for different materials. In the present study, the proposed model is applied to granite for which the specific value of $b = 2$ is retained. Therefore, one gets the following simplified form:

$$\mathcal{R}(d) = \mathcal{R}(d_c)\,\frac{2\xi}{1+\xi^2}, \tag{V .16}$$

For the sake of simplicity, the evolution rate of damage is also given by the normality rule:

$$\dot{d} = \lambda^d \frac{\partial \mathcal{G}}{\partial \mathcal{Y}^d} = \lambda^d, \tag{V .17}$$

where λ^d is a non-negative multiplier.

The rate form of the effective stress-stress relations of the homogenized medium can be obtained as follows:

$$\dot{\boldsymbol{\Sigma}} = \mathbb{C}^{\tan} : \dot{\boldsymbol{E}}\ , \qquad \dot{\boldsymbol{E}} = \mathbb{S}^{\tan} : \dot{\boldsymbol{\Sigma}} \tag{V .18}$$

$\mathbb{C}^{\tan}$ and $\mathbb{S}^{\tan}$ are the consistent tangent operators with $\mathbb{C}^{\tan} : \mathbb{S}^{\tan} = \mathbb{I}$. $\dot{\boldsymbol{\Sigma}}$ and $\dot{\boldsymbol{E}}$ respectively denote the macroscopic stress and strain increments. The expressions of tangent operators can be determined by making use of the damage and friction consistency conditions. By using the flow rules for frictional sliding and damage and after making some

mathematical operations (Zhu et al., 2016), one obtains:

$$\mathbb{C}^{\tan} = \begin{cases} \mathbb{C}^m, & \text{if } \mathcal{F}(\boldsymbol{\Sigma}^c) < 0 \\ \mathbb{C}^m - \frac{1}{H_1}\mathbb{C}^m : (\boldsymbol{D} \otimes \boldsymbol{D}) : \mathbb{C}^m, & \text{if } \mathcal{F}(\boldsymbol{\Sigma}^c) = 0 \end{cases} \tag{V .19a}$$

$$\mathbb{S}^{\tan} = \begin{cases} \mathbb{S}^m, & \text{if } \mathcal{F}(\boldsymbol{\Sigma}^c) < 0 \\ \mathbb{S}^m + \frac{1}{H_1}\boldsymbol{D} \otimes \boldsymbol{D}, & \text{if } \mathcal{F}(\boldsymbol{\Sigma}^c) = 0 \end{cases} \tag{V .19b}$$

where $H_1 = \frac{\partial \mathcal{F}}{\partial d}\frac{\partial \mathcal{G}}{\partial \boldsymbol{E}^c} : \boldsymbol{D} / \frac{\partial \mathcal{G}}{\partial d} - \frac{\partial \mathcal{F}}{\partial \boldsymbol{E}^c} : \boldsymbol{D}$ is the hardening modulus. Note that thanks to the associated frictional and damage evolution laws considered here, the consistent tangent operators $\mathbb{C}^{\tan}$ and $\mathbb{S}^{\tan}$ are symmetric, providing a sound convenience for numerical implementation.

2.4 Analytical stress-based yield criterion

With the micro-mechanics based friction-damage model proposed here, the frictional sliding criterion is defined in terms of the local stress field applied onto micro-cracks. For general loading paths, the macroscopic stresses at the frictional sliding state should be calculated by the integration of the micro-mechanics model along the corresponding loading history. However, for loading paths without the rotation of principal stress directions, it is possible to obtain an analytical plastic yield criterion in terms of macroscopic stresses, and moreover to get analytical stress-strain relations for these simple loading paths (Zhu et al., 2016). Indeed, for those loading paths, the frictional flow direction given in Eq.(V .13) is simplified to:

$$\boldsymbol{D} = \frac{\boldsymbol{S}}{\|\boldsymbol{S}\|} + \frac{1}{3}c_f\boldsymbol{\delta}. \tag{V .20}$$

with $\boldsymbol{S} = \mathbb{K} : \boldsymbol{\Sigma}$ being the deviatoric part of macroscopic stress tensor.

Accordingly, the yield criterion (V .14) can be rewritten into a form similar to the classical Drucker-Prager criterion as follows:

$$\mathcal{F}(\boldsymbol{\Sigma}, \boldsymbol{E}^c, d) = \boldsymbol{\Sigma} : \boldsymbol{D} - \boldsymbol{D} : \mathbb{C}^d : \boldsymbol{E}^c = \|\boldsymbol{S}\| + c_f P - \boldsymbol{D} : \mathbb{C}^d : \boldsymbol{E}^c \leq 0. \tag{V .21}$$

where $P = \frac{1}{3}\boldsymbol{\delta} : \boldsymbol{\Sigma}$ is the spherical part of macroscopic stress tensor. Furthermore, due to the fixed principal stress directions, the frictional flow direction does not change. Therefore, the frictional sliding induced strains can be given by:

$$\boldsymbol{E}^c = \int \dot{\boldsymbol{E}}^c = \Lambda \boldsymbol{D}, \quad \text{with } \Lambda = \int \lambda^c \tag{V .22}$$

Substituting (V .22) for (V .21), one gets:

$$\mathcal{F}\left(\boldsymbol{\Sigma},\Lambda,d\right)=\|\boldsymbol{S}\|+c_{f}P-\Lambda\boldsymbol{D}:\mathbb{C}^{d}:\boldsymbol{D}\leq 0. \tag{V .23}$$

On the other hand, in the proposed micro-mechanics based model, the frictional sliding is inherently coupled with the damage evolution. Accordingly, by substituting (V .22) for (V .9), the damage criterion (V .15) becomes:

$$\mathcal{G}\left(\mathcal{Y}^{d},d\right)=\frac{1}{2}\left(\frac{\Lambda}{d}\right)^{2}\chi-\mathcal{R}\left(d\right)=0, \tag{V .24}$$

with $\chi/d=\boldsymbol{D}:\mathbb{C}^{d}:\boldsymbol{D}$. One can notice that from (V .24)

$$\Lambda=d\sqrt{\frac{2\mathcal{R}\left(d\right)}{\chi}} \tag{V .25}$$

Combining (V .23) and (V .24), we finally obtain the macroscopic yield criterion as a function of macroscopic stresses and damage density parameter:

$$\mathcal{F}\left(\boldsymbol{\Sigma},d\right)=\|\boldsymbol{S}\|+c_{f}P-\sqrt{2\mathcal{R}\left(d\right)\chi}\leq 0. \tag{V .26}$$

From Eqs.(V .22), (V .24) and (V .26), one can see that given any damage value, the corresponding frictional sliding strain $\boldsymbol{E}^{c}$ and macroscopic stress $\boldsymbol{\Sigma}$ can be analytically calculated for some stress paths (e.g, plane stress, conventional triaxial compression, proportional compression, lateral extension, etc.), and then the macroscopic total strain $\boldsymbol{E}$ can also be calculated using Eq.(V .7a). More details on the analytical calculation process can be found in (Zhu et al., 2016).

3 Analysis for localized cracks

The mechanical behavior of material before localization is described by the micro-mechanics based friction damage model presented above. With the growth of micro-cracks and when the crack density reaches some critical value, there is the coalescence of micro-cracks leading to the onset of localized cracks in some preferential orientations. As a fundamental difference with shear bands in soil-like materials, the localized cracks or fractures in rock-like materials are characterized by strong displacement discontinuities. Further, the thickness of localized cracks is generally very small so that each crack can be seen an a discontinuity interface. Based on some previous studies (Oliver et al., 2012; Wu and Cervera, 2015, 2016), a traction-based strong discontinuity method is here adopted.

To this end, we consider the representative volume element (RVE) of localized cracked material shown in Figure V .3. The RVE ($\Omega \subset \mathbb{R}^{n_{\dim}}$) exhibits a displacement discontinuity jump $\underline{g}$ on the interface $\mathcal{S} \to \mathbb{R}^{n_{\dim}-1}$. The interface $\mathcal{S}$ denotes the localized crack with the unit normal $\underline{n}$ pointing to Ω^+.

3.1 Kinematic description of localized cracked material

Based on the representation given in Figure V .3 and introducing the Heaviside function $\mathcal{H}_{\mathcal{S}}(\underline{x})$ so that $\mathcal{H}_{\mathcal{S}}(\underline{x}) = 1$ if $\underline{x} \in \Omega^+$ and $\mathcal{H}_{\mathcal{S}}(\underline{x}) = 0$ otherwise, the displacement field $\underline{u}(\underline{x})$ in the localized RVE can be expressed as follows:

$$\underline{u}(\underline{x}) = \underbrace{\underline{u}^-(\underline{x})}_{\text{regular (continuous)}} + \underbrace{\mathcal{H}_{\mathcal{S}}(\underline{x})\,[\![\underline{u}]\!](\underline{x})}_{\text{singular (discontinuous)}}, \qquad [\![\underline{u}]\!](\underline{x}) = \underline{u}^+(\underline{x}) - \underline{u}^-(\underline{x}) \tag{V .27}$$

The symbol $[\![\cdot]\!] = (\cdot)^+_{\mathcal{S}} - (\cdot)^-_{\mathcal{S}}$ denotes the jump of the specific variable $(\cdot)$ across $\mathcal{S}$. $\underline{u}^-(\underline{x})$ and $\underline{u}^+(\underline{x})$ are the displacement fields respectively in the sub-domains Ω^- and Ω^+, and the former also represents the continuous displacement field in Ω. $[\![\underline{u}]\!](\underline{x}) : \Omega \to \mathbb{R}^{n_{\dim}}$, satisfying the property $[\![\underline{u}]\!](\underline{x} \in \mathcal{S}) = \underline{g}$, stands for the relative displacement field of the part Ω^+ with respect to the other one Ω^-.

The strain field $\boldsymbol{\varepsilon}(\underline{x})$ can be obtained by calculating the symmetric part of the dis-

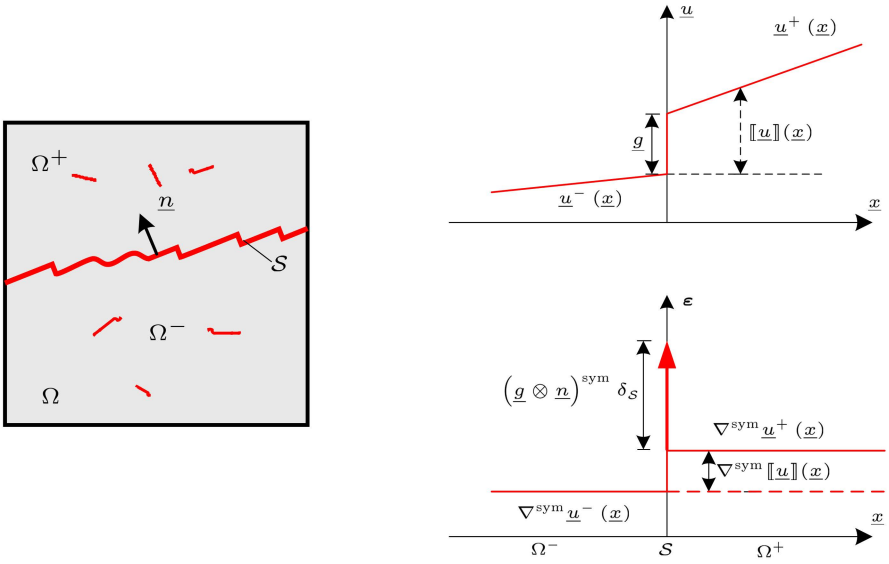

Figure V .3: Kinematics of strong discontinuity in RVE with localized cracks

placement gradient, i.e.

$$\begin{aligned} \boldsymbol{\varepsilon}(\underline{x}) &= \nabla^{\mathrm{sym}}\underline{u}(\underline{x}) = \nabla^{\mathrm{sym}}\left[\underline{u}^{-}(\underline{x}) + \mathcal{H}_{\mathcal{S}}(\underline{x})[\![\underline{u}]\!](\underline{x})\right] \\ &= \underbrace{\nabla^{\mathrm{sym}}\underline{u}^{-}(\underline{x}) + \nabla^{\mathrm{sym}}[\![\underline{u}]\!](\underline{x})\mathcal{H}_{\mathcal{S}}(\underline{x})}_{\text{bounded part}} + \underbrace{\delta_{\mathcal{S}}(\underline{x})(\underline{g}\otimes\underline{n})^{\mathrm{sym}}}_{\text{unbounded part}} \end{aligned} \tag{V .28}$$

The bounded part $\nabla^{\mathrm{sym}}\underline{u}^{-}(\underline{x}) + \nabla^{\mathrm{sym}}[\![\underline{u}]\!](\underline{x})\mathcal{H}_{\mathcal{S}}(\underline{x})$ represents the strain field in the intact part of RVE. As shown in Figure V .3, $\delta_{\mathcal{S}}(\underline{x})(\underline{g}\otimes\underline{n})^{\mathrm{sym}}$ denotes the unbounded part of strain discontinuity, which is associated with the localized deformation along the interface, emerging from the gradient of the Heaviside function $\mathcal{H}_{\mathcal{S}}(\underline{x})$ appearing in Eq. (V .27), $\delta_{\mathcal{S}}(\underline{x})$ being the Dirac-Delta function.

In the approach pursued here the discontinuity is embedded in the constitutive law by averaging the localized deformation over the considered RVE. Accordingly, by making the volume average of Eq.(V .28) (Haghighat and Pietruszczak, 2015; Moallemi and Pietruszczak, 2017), one can obtain the macroscopic strain:

$$\boldsymbol{E} = \frac{1}{V}\int_{V}\boldsymbol{\varepsilon}(\underline{x})\,\mathrm{d}\Omega = \frac{1}{V}\int_{V}\nabla^{\mathrm{sym}}\underline{u}^{-}(\underline{x}) + \nabla^{\mathrm{sym}}[\![\underline{u}]\!](\underline{x})\mathcal{H}_{\mathcal{S}}(\underline{x})\,\mathrm{d}\Omega + \frac{1}{V}\int_{A_{\mathcal{S}}}(\underline{g}\otimes\underline{n})^{\mathrm{sym}}\,\mathrm{d}\mathcal{S} \tag{V .29}$$

where $A_{\mathcal{S}}$ represents the surface area of the localized crack within the considered reference volume V. Ignoring the variation of $(\underline{g}\otimes\underline{n})^{\mathrm{sym}}$ within a small enough V, by defining $l = V/A_{\mathcal{S}}$, and $\zeta = V_{\Omega^{+}}/V$, Eq. (V .29) approximately satisfies

$$\boldsymbol{E} \simeq \underbrace{\nabla^{\mathrm{sym}}\left(\underline{u}^{-}(\underline{x}) + \zeta[\![\underline{u}]\!](\underline{x})\right)}_{\boldsymbol{E}^{m}+\boldsymbol{E}^{c}} + \underbrace{(\underline{e}\otimes\underline{n})^{\mathrm{sym}}}_{\tilde{\boldsymbol{E}}^{c}}, \quad \text{with} \quad \underline{e} = \underline{g}/l \tag{V .30}$$

where ζ denotes the volume fraction. l represents a characteristic length, which will play an essential role in the numerical analysis of localized problems. It is known that the boundary values problem becomes ill-posed due to localization and suffers the inherent mesh sensitivity. The use of such a characteristic length will allow to regularize the localized problem and avoid the mesh sensitivity (Haghighat and Pietruszczak, 2015; Moallemi and Pietruszczak, 2017; Nguyen et al., 2017). For instance, in the context of finite element method, the characteristic length l can be calculated as the ratio between the volume of cracked element and the surface area of crack. With the homogenization method followed here, the total macroscopic strain of RVE is calculated as the sum of two parts. The first part is the strain $\boldsymbol{E}^{m}+\boldsymbol{E}^{c} = \nabla^{\mathrm{sym}}\left(\underline{u}^{-}(\underline{x}) + \zeta[\![\underline{u}]\!](\underline{x})\right)$, where $\boldsymbol{E}^{m}$ is the intact solid matrix strain and $\boldsymbol{E}^{c}$ stems from diffuse micro-cracks before localization, and the second one is $\tilde{\boldsymbol{E}}^{c} = (\underline{e}\otimes\underline{n})^{\mathrm{sym}}$ that results from the discontinuous motion along the localized crack averaged over the RVE. Finally, Eq. (V .30) can be rewritten as

$$\boldsymbol{E} \simeq \boldsymbol{E}^{m} + \boldsymbol{E}^{c} + \tilde{\boldsymbol{E}}^{c} \tag{V .31}$$

It is noted that, the last term $\tilde{\boldsymbol{E}}^c$ vanishes before the localized crack appears, and the inelastic strain $\boldsymbol{E}^c$ can be calculated by the micro-mechanical model presented in Section 2.

3.2 Onset criterion of localized crack

After the onset of a localized crack, the frictional sliding may occur along the localized crack and the damage process is related to the propagation of the localized crack. All the energy dissipation is then attributed to the frictional sliding and the propagation of localized crack. We discuss here the onset criterion for the localized crack in relation with the micro-mechanics based friction-damage model proposed above.

In most previous studies (Wu and Cervera, 2015, 2016), the onset of localized cracking was defined in terms of macroscopic stresses by neglecting the transition from diffuse damage (micro-cracking) to localized cracking (failure). In this study, the diffuse damage of material is described by a micro-mechanics based friction-damage model with a damage density coefficient d physically representing the density of micro-cracks. We consider that the onset of localized cracking is a consequence of coalescence of micro-cracks when the micro-cracks density is high enough. As shown above, when the damage density parameter reaches the critical value d_c, the material toughness to micro-crack propagation reaches its maximal value $\mathcal{R}(d_c)$ leading to a material softening. Therefore, it seems physically sound to assume that the onset of a localized crack occurs when the damage density coefficient d reaches a critical value d_c. At the macroscopic scale, for brittle rock-like materials, experimental data in laboratory tests have shown that the onset of localized cracking generally occurs around the peak stress point (Fredrich et al., 1989; Wong, 1982). Therefore, the value of d_c can be identified from the peak stress in a triaxial compression test. The onset criterion of localized crack is thus simply defined as:

$$d = d_c \tag{V .32}$$

At the same time, the thermodynamics conjugate force associated with the damage evolution $\mathcal{Y}^d$ is directly dependent on the frictional sliding induced strain $\boldsymbol{E}^c$ as shown in Eq. (V .9). Therefore, it is also convenient to define the localization onset criterion by the fact that the frictional sliding induced strain reaches its critical value $\boldsymbol{E}^{cl}$. One can obtain in the following integral form:

$$\boldsymbol{E}^{cl} = \int_0^{d_c} \lambda^c \boldsymbol{D} \tag{V .33}$$

After the onset of the localized crack, the inelastic strain $\boldsymbol{E}^c$ keeps constant, i.e., $\boldsymbol{E}^c = \boldsymbol{E}^{cl}$ for $d \geq d_c$.

Remark 4

For loading paths without the rotation of principal stresses, the critical strain for the onset of localized cracks $\boldsymbol{E}^{cl}$ *can be explicitly obtained by substituting* $d = d_c$ *for Eq.*(V .24) *and together using Eqs.* (V .22) *and* (V .16)*:*

$$\boldsymbol{E}^{cl} = \Lambda^{cl}\boldsymbol{D} = d_c\sqrt{\frac{2\mathcal{R}(d_c)}{\chi}}\boldsymbol{D} \tag{V .34}$$

It is useful to point out that the validity of the onset criterion of localized cracking proposed in this paper should be verified by further experimental investigations. Furthermore, the ont onset of localization has been largely been investigated in various engineering materials by different approaches such as the bifurcation theory and second order work criterion. It will be also interesting to compare the proposed criterion with other approaches.

3.3 Identification of the localized crack orientation

Another crucial step is to determine the orientation of the localized crack. This is studied in this section. Let us consider the spectral decomposition of the macroscopic stress tensor

$$\boldsymbol{\Sigma} = \sum_{i=1}^{3} \Sigma_i \underline{v}_i \otimes \underline{v}_i \tag{V .35}$$

Σ_i denote the three principal stresses with the corresponding principal vectors $\underline{v}_i$ satisfying the orthogonal property $\underline{v}_i \cdot \underline{v}_j = \delta_{ij}$ for $i, j = 1, 2, 3,$, as shown in Figure V .4(a).

For a localized penny-shaped crack in a general 3D configuration (see Figure V .4(a)), a

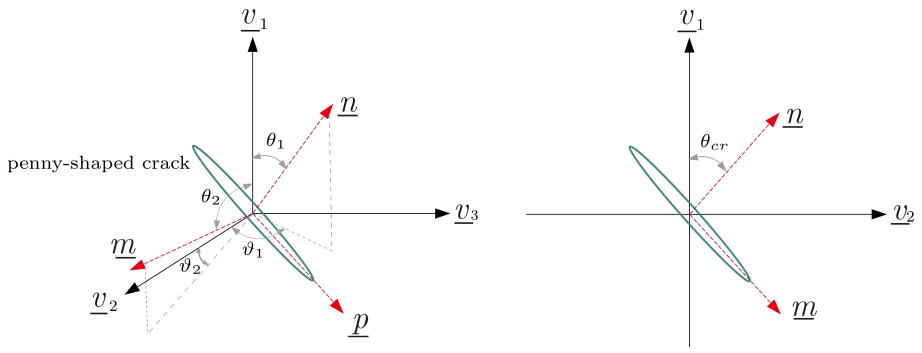

(a) 3D cases (b) 2D cases

Figure V .4: Illustration of a localized penny-shaped crack (discontinuity) in 3D and 2D cases

local orthogonal frame $(\underline{n}, \underline{m}, \underline{p})$ is introduced, with $\underline{n}$ being the normal vector of the localized crack. The vectors $\underline{m}$ and $\underline{p}$ are perpendicular to $\underline{n}$ and tangent to the localized crack surface. In the coordinate system of principal stresses, for the convenience of calculation of localized crack orientation in three dimensional situation, the base vectors $(\underline{n}, \underline{m}, \underline{p})$ are here expressed in terms of a set of four characteristic angles $\boldsymbol{\theta} = [\theta_1, \theta_2, \vartheta_1, \vartheta_2]$, as shown in Figure V .4(a):

$$\underline{n}(\boldsymbol{\theta}) = [\cos\theta_1, \sin\theta_1\cos\vartheta_1, \sin\theta_1\sin\vartheta_1] \tag{V .36a}$$

$$\underline{m}(\boldsymbol{\theta}) = [\cos\theta_2, \sin\theta_2\cos\vartheta_2, \sin\theta_2\sin\vartheta_2] \tag{V .36b}$$

$$\underline{p}(\boldsymbol{\theta}) = \underline{n}(\boldsymbol{\theta}) \times \underline{m}(\boldsymbol{\theta}) \tag{V .36c}$$

The traction $\underline{t}$ acting on the localized crack can be expressed in the local coordinate system:

$$\underline{t} := \boldsymbol{\Sigma} \cdot \underline{n} = t_n \underline{n} + t_m \underline{m} + t_p \underline{p} \tag{V .37}$$

Three components t_n, t_m and t_p respectively along the base vectors $\underline{n}, \underline{m}, \underline{p}$ can be related to the macroscopic stress tensor:

$$t_n = \Sigma_{nn} = \underline{n} \cdot \boldsymbol{\Sigma} \cdot \underline{n} \tag{V .38a}$$

$$t_m = \Sigma_{nm} = \underline{n} \cdot \boldsymbol{\Sigma} \cdot \underline{m} \tag{V .38b}$$

$$t_p = \Sigma_{np} = \underline{n} \cdot \boldsymbol{\Sigma} \cdot \underline{p} \tag{V .38c}$$

3.3.1 Mohr's maximization postulate

In the framework of bifurcation theory for weak discontinuities, the orientation of strain localization band is determined from the characteristic equation of acoustic tensor (Mosler, 2005; Oliver et al., 1999; Ottosen and Runesson, 1991; Rice and Rudnicki, 1980; Rudnicki and Rice, 1975; Runesson et al., 1991). Recently, for the approach of strong discontinuities, Wu and Cervera (2015, 2016) have proposed a novel method for the determination of localized cracks by using the Mohr's maximization postulate in the case of a macroscopic plastic damage model. In this study, the Mohr's maximization postulate is also adopted.

Within the context of the Mohr's maximization framework, at the onset of a localized crack, the traction-based failure friction criterion $\mathcal{F}(\underline{t}) \leqslant 0$ can be deduced by projecting the corresponding macroscopic stress-based failure friction criterion $\mathcal{F}(\boldsymbol{\Sigma}) \leqslant 0$ (Eq.(V .14) with the condition of $d = d_c$) onto the orientation of localized crack

$$\mathcal{F}(\underline{t}(\boldsymbol{\theta})) = \underline{t} \cdot \underline{\gamma} - \boldsymbol{D} : \mathbb{C}_c^d : \boldsymbol{E}^{cl} \leq 0. \tag{V .39}$$

where the dissipative flow vector $\underline{\gamma}$ satisfying $\left(\underline{\gamma} \otimes \underline{n}\right)^{\text{sym}} = \boldsymbol{D}$, $\mathbb{C}_c^d$ is the value of $\mathbb{C}_c$ at $d = d_c$. Note that, without rotation of principal stresses, (V .39) can be further rewritten as

$$\mathcal{F}\left(\underline{t}\left(\boldsymbol{\theta}\right)\right) = \underline{t} \cdot \underline{\gamma} - \sqrt{2\mathcal{R}\left(d_c\right)\chi} \leq 0. \tag{V .40}$$

Mohr's maximization postulate assumes that cracks are localized on the orientation $\underline{n}(\boldsymbol{\theta}_{cr})$ upon which the traction maximizes the failure friction criterion $\mathcal{F}\left(\underline{t}\left(\boldsymbol{\theta}\right)\right)$ (Eq.(V .39)). The characteristic angle $\boldsymbol{\theta}_{cr}$ is then given by:

$$\boldsymbol{\theta}_{cr} = \arg\max \mathcal{F}\left(\underline{t}\left(\boldsymbol{\theta}\right)\right) \tag{V .41}$$

Mathematically, the following stationarity conditions holds

$$\left.\frac{\partial \mathcal{F}}{\partial \boldsymbol{\theta}}\right|_{\boldsymbol{\theta}_{cr}} = \left(\frac{\partial \mathcal{F}}{\partial \underline{t}} \cdot \frac{\partial \underline{t}}{\partial \boldsymbol{\theta}}\right)_{\boldsymbol{\theta}_{cr}} = \left(\underline{\gamma} \cdot \frac{\partial \underline{t}}{\partial \boldsymbol{\theta}}\right)_{\boldsymbol{\theta}_{cr}} = \left(\gamma_n \frac{\partial t_n}{\partial \boldsymbol{\theta}} + \gamma_m \frac{\partial t_m}{\partial \boldsymbol{\theta}} + \gamma_p \frac{\partial t_p}{\partial \boldsymbol{\theta}}\right)_{\boldsymbol{\theta}_{cr}} = \boldsymbol{0} \tag{V .42}$$

with the following negative definite Hessian matrix:

$$\hat{\boldsymbol{\theta}} \cdot \left.\frac{\partial^2 \mathcal{F}}{\partial \boldsymbol{\theta}^2}\right|_{\boldsymbol{\theta}_{cr}} \cdot \hat{\boldsymbol{\theta}} < 0, \forall \hat{\boldsymbol{\theta}} \tag{V .43}$$

The dissipative flow vector $\underline{\gamma}$ satisfies (Oliver, 2000)

$$\underline{\gamma} = 2\underline{n} \cdot \boldsymbol{D} - \underline{n} D_{nn} = \gamma_n \underline{n} + \gamma_m \underline{m} + \gamma_p \underline{p} \tag{V .44}$$

The components γ_n, γ_m and γ_p of the dissipative flow vector in the local orthogonal system $\left(\underline{n}, \underline{m}, \underline{p}\right)$ are expressed as

$$\gamma_n := \underline{\gamma} \cdot \underline{n} = D_{nn},\ \gamma_m := \underline{\gamma} \cdot \underline{m} = 2D_{nm},\ \gamma_p := \underline{\gamma} \cdot \underline{p} = 2D_{np} \tag{V .45}$$

The stationary condition (V .42) results in a set of nonlinear equations in terms of the traction components given in (V .38), from which the characteristic angles $\boldsymbol{\theta}_{cr}$ can be determined. Note that, if the solution exists, the crack localization can occur.

Remark 5

Under general 3D conditions, the numerical results of the characteristic angles $\boldsymbol{\theta}_{cr}$ of the localized crack can be obtained by using any known optimization technique, such as the augmented Lagrangian method. Although, the analytical solutions of $\boldsymbol{\theta}_{cr}$ for general cases are hardly obtained, some analytical solutions for special cases can be obtained and examples will be given in Section 5.

4 Formulation of localized friction-damage model

In this section, a new traction-based friction-damage model is established to describe the mechanical behavior of material after the onset of localized crack in the framework of irreversible thermodynamics. As mentioned above, the localization corresponds to the coalescence of micro-cracks and to the formation of localized macroscopic cracks in the RVE. According to experimental investigations on rock-like materials (Labuz et al., 1996; Lockner et al., 1992), the macroscopic failure is a progressive fracturing process. Several localized cracks may be created in a fracture process zone. In order to formulate a frictional-damage model for the post-localization behavior in the same esprit of the micro-mechanical model before localization. We shall use the same damage density parameter $d \geq d_c$ to represent the overall density evolution of cracks in the RVE after localization.

4.1 Free energy and thermodynamic forces

Inspired by the previous study in Zhu and Shao (2015), after the onset of localized crack, the free energy function of the RVE in Figure V .3 can be expressed in the following form:

$$\psi = \frac{1}{2}\boldsymbol{\Sigma} : \mathbb{S}^m : \boldsymbol{\Sigma} + \boldsymbol{\Sigma} : \left(\tilde{\boldsymbol{E}}^c + \boldsymbol{E}^{cl}\right) - \frac{1}{2}\tilde{\boldsymbol{E}}^c : \mathbb{C}^n : \tilde{\boldsymbol{E}}^c + \psi^b \tag{V .46}$$

where $\mathbb{C}^n = \frac{1}{d-d_c}(c_n\mathbb{N}+c_t\mathbb{T})$, $d-d_c$ represents the damage evolution caused by the growth of the localized crack, the constants c_n and c_t are related to the elastic modulus E^m and Poisson's ratio ν^m of the intact solid matrix, i.e., $c_n = \frac{3E^m}{16(1-(\nu^m)^2)}$ and $c_t = c_n\,(2-\nu^m)$ (Kachanov, 1992) . Fourth order tensors $\mathbb{N}$ and $\mathbb{T}$ are both functions of the unit normal vector $\underline{n}$ determined in Section

$$\mathbb{N} = \boldsymbol{N} \otimes \boldsymbol{N}, \quad \mathbb{T} = \boldsymbol{N}\underline{\otimes}\boldsymbol{T} + \boldsymbol{T}\underline{\otimes}\boldsymbol{N} \tag{V .47}$$

with $\boldsymbol{N} = \underline{n} \otimes \underline{n}$ and $\boldsymbol{T} = \boldsymbol{\delta} - \boldsymbol{N}$. For an arbitrary second-order tensor $\boldsymbol{A}$, the operations $\mathbb{N} : \boldsymbol{A}$ and $\mathbb{T} : \boldsymbol{A}$, respectively lead to the normal and tangential part of the tensor $\boldsymbol{A}$. Further, the following conditions are verified:

$$\mathbb{N} : \boldsymbol{N} = \boldsymbol{N}, \quad \mathbb{N} : \boldsymbol{T} = \boldsymbol{0}, \quad \mathbb{T} : \boldsymbol{T} = \boldsymbol{T}, \quad \mathbb{T} : \boldsymbol{N} = \boldsymbol{0}$$

It is noted that the free energy Eq.(V .5) should be equivalent to Eq.(V .46) at the onset of localized crack, thus one can obtain the explicit expression of ψ^b

$$\psi^b = -\frac{1}{2}\boldsymbol{E}^{cl} : \mathbb{C}_c^d : \boldsymbol{E}^{cl} \tag{V .48}$$

The thermodynamic force $\tilde{\boldsymbol{\Sigma}}^c$ and $\mathcal{Y}^d$ respectively associated with the inelastic strain $\tilde{\boldsymbol{E}}^c$ and damage variable d are given by

$$\tilde{\boldsymbol{\Sigma}}^c = \frac{\partial \psi}{\partial \tilde{\boldsymbol{E}}^c} = \boldsymbol{\Sigma} - \mathbb{C}^n : \tilde{\boldsymbol{E}}^c \tag{V .49a}$$

$$\tilde{\mathcal{Y}}^d = \frac{\partial \psi}{\partial d} = -\frac{1}{2}\tilde{\boldsymbol{E}}^c : \frac{\partial \mathbb{C}^n}{\partial d} : \tilde{\boldsymbol{E}}^c \tag{V .49b}$$

4.2 Frictional-sliding criterion and damage criterion of localized crack

Given the local stress $\tilde{\boldsymbol{\Sigma}}^c$ acting on the localized crack, a simple linear Coulomb-type criterion is formulated to describe the frictional sliding along the localized crack

$$\tilde{\mathcal{F}}\left(\tilde{\boldsymbol{\Sigma}}^c\right) = \|\underline{\tau}^c\| + \tilde{c}_f \Sigma_n^c \leq 0 \tag{V .50}$$

where $\tilde{c}_f$ is the friction coefficient of the localized crack. $\underline{\tau}^c$ and Σ_n^c are respectively the shear and normal components of $\tilde{\boldsymbol{\Sigma}}^c$, which can be obtained by projecting the stress vector $\tilde{\boldsymbol{\Sigma}}^c \cdot \underline{n}$ into the normal direction and localized crack plane. With the help of (V .49a), one obtains:

$$\underline{\tau}^c = \tilde{\boldsymbol{\Sigma}}^c \cdot \underline{n} \cdot \boldsymbol{T} = \underline{\tau} - \underline{n} \cdot \boldsymbol{T} \cdot \mathbb{C}^n : \tilde{\boldsymbol{E}}^c \tag{V .51}$$

$$\Sigma_n^c = \underline{n} \cdot \tilde{\boldsymbol{\Sigma}}^c \cdot \underline{n} = t_n - \boldsymbol{N} : \mathbb{C}^n : \tilde{\boldsymbol{E}}^c \tag{V .52}$$

where the vector $\underline{\tau}$ is the shear component of macroscopic stress $\boldsymbol{\Sigma}$, i.e., $\underline{\tau} = \boldsymbol{\Sigma} \cdot \underline{n} \cdot \boldsymbol{T}$.

Taking the advantage of results of Zhu (2017), the flow direction inside the localized crack plane located in the plane $(\underline{v}_1, \underline{v}_2)$, denoted by $\underline{\varrho}$, is defined as

$$\underline{\varrho} = \operatorname{sign}\left(\Sigma_1 - \Sigma_2\right) \frac{\underline{v}_1 - \left(\underline{v}_1 \cdot \underline{n}\right)\underline{n}}{\sqrt{1 - \underline{v}_1 \cdot \underline{n}}} \tag{V .53}$$

Then the norm $\|\underline{\tau}^c\|$ can be reformulated in terms of norm $\|\underline{\tau}\|$

$$\|\underline{\tau}^c\| = \underline{\tau}^c \cdot \underline{\varrho} = \underline{\tau} \cdot \underline{\varrho} - \underline{n} \cdot \boldsymbol{T} \cdot \mathbb{C}^n : \tilde{\boldsymbol{E}}^c \cdot \underline{\varrho} = \|\underline{\tau}\| - \left(\underline{\varrho} \otimes \underline{n}\right)^{\mathrm{sym}} \cdot \boldsymbol{T} \cdot \mathbb{C}^n : \tilde{\boldsymbol{E}}^c \tag{V .54}$$

Combining Eqs. (V .52) and (V .54), the frictional sliding criterion of localized crack (Eq.(V .50)) can be reformulated as

$$\tilde{\mathcal{F}}\left(\boldsymbol{\Sigma}, \tilde{\boldsymbol{E}}^c, d\right) = \|\underline{\tau}\| + \tilde{c}_f t_n - \boldsymbol{V} : \mathbb{C}^n : \tilde{\boldsymbol{E}}^c \leq 0. \tag{V .55}$$

where $\boldsymbol{V}$ is the second order flow direction tensor, defined as

$$\boldsymbol{V} = \left(\underline{\varrho} \otimes \underline{n}\right)^{\mathrm{sym}} + \tilde{c}_f \boldsymbol{N} \tag{V .56}$$

this expression thanks to the properity $\left(\underline{\varrho}\otimes\underline{n}\right)^{\mathrm{sym}}\cdot\boldsymbol{T}=\left(\underline{\varrho}\otimes\underline{n}\right)^{\mathrm{sym}}$.

Similarly, the strain energy release rate-based damage criterion for describing the localized damage evolution is adopted here

$$\tilde{\mathcal{G}}\left(d,\tilde{\boldsymbol{E}}^{c}\right)=\tilde{\mathcal{Y}}^{d}-\tilde{\mathcal{R}}\left(d\right)=-\frac{1}{2}\tilde{\boldsymbol{E}}^{c}:\frac{\partial\mathbb{C}^{n}}{\partial d}:\tilde{\boldsymbol{E}}^{c}-\tilde{\mathcal{R}}\left(d\right)=0,\quad d>d_{c} \tag{V .57}$$

It is noted that after localization, the frictional sliding along localized cracks becomes a dominating dissipation process. This generally leads to a material softening at the macroscopic scale. This mechanism is here described by the progressive decrease of the material resistance $\tilde{\mathcal{R}}$ with the increase of overall crack density d. For the sake of simplicity, the same function as that given in Eq.(V .16) in the model for the diffused damage is here adopted:

$$\tilde{\mathcal{R}}\left(d\right)=\tilde{\mathcal{R}}\left(d_{c}\right)\frac{2\xi}{1+\xi^{2}},\qquad d>d_{c}, \tag{V .58}$$

with $\tilde{\mathcal{R}}\left(d_{c}\right)$ being the maximum value of $\tilde{\mathcal{R}}\left(d\right)$.

For a given admissible state $\left(\boldsymbol{\Sigma},\tilde{\boldsymbol{E}}^{c},d\right)$, constrained by the friction and damage criteria (V .50) and (V .57), the real friction and damage evolution rates $\left(\dot{\tilde{\boldsymbol{E}}}^{c},\dot{d}\right)$ are given by the following normality rules:

$$\dot{\tilde{\boldsymbol{E}}}^{c}=\tilde{\lambda}_{c}\frac{\partial\tilde{\mathcal{F}}}{\partial\tilde{\boldsymbol{\Sigma}}^{c}}=\tilde{\lambda}_{c}\boldsymbol{V} \tag{V .59a}$$

$$\dot{d}=\tilde{\lambda}^{d}\frac{\partial\tilde{\mathcal{G}}}{\partial\tilde{\mathcal{Y}}^{d}}=\tilde{\lambda}^{d}, \tag{V .59b}$$

where the $\tilde{\lambda}_{c}$ and $\tilde{\lambda}^{d}$ are respectively the plastic and damage multipliers of the localized crack. Moreover, $\tilde{\lambda}_{c}$ satisfies the following Kuhn-Tucker loading/unloading conditions:

$$\tilde{\lambda}_{c}\geq0,\tilde{\mathcal{F}}\left(\boldsymbol{\Sigma},\tilde{\boldsymbol{E}}^{c},d\right)\leq0,\ \tilde{\lambda}_{c}\tilde{\mathcal{F}}\left(\boldsymbol{\Sigma},\tilde{\boldsymbol{E}}^{c},d\right)=0. \tag{V .60}$$

When the frictional sliding of localized crack is inactive, i.e., $\tilde{\mathcal{F}}\left(\boldsymbol{\Sigma},\tilde{\boldsymbol{E}}^{c},d\right)\leq0$, one has $\tilde{\lambda}_{c}=\tilde{\lambda}^{d}=0$. On the other hand, when the frictional sliding occurs, i.e., $\tilde{\lambda}_{c}>0$ and $\tilde{\lambda}^{d}>0$, it follows that $\tilde{\mathcal{F}}\left(\boldsymbol{\Sigma},\tilde{\boldsymbol{E}}^{c},d\right)=0$ and $\tilde{\mathcal{G}}\left(d,\tilde{\boldsymbol{E}}^{c}\right)=0$, and the consistency conditions of Eqs.(V .50) and (V .57) are written as

$$\dot{\tilde{\mathcal{F}}}\left(\boldsymbol{\Sigma},\tilde{\boldsymbol{E}}^{c},d\right)=\frac{\partial\tilde{\mathcal{F}}}{\partial\boldsymbol{\Sigma}}:\dot{\boldsymbol{\Sigma}}+\frac{\partial\tilde{\mathcal{F}}}{\partial d}\dot{d}+\frac{\partial\tilde{\mathcal{F}}}{\partial\tilde{\boldsymbol{E}}^{c}}:\dot{\tilde{\boldsymbol{E}}}^{c}=0 \tag{V .61a}$$

$$\dot{\tilde{\mathcal{G}}}\left(d,\underline{e}\right)=\frac{\partial\tilde{\mathcal{G}}}{\partial d}\dot{d}+\frac{\partial\tilde{\mathcal{G}}}{\partial\tilde{\boldsymbol{E}}^{c}}:\dot{\tilde{\boldsymbol{E}}}^{c}=0 \tag{V .61b}$$

The non-negative multipliers $\left(\tilde{\lambda}^c, \tilde{\lambda}^d\right)$ are determined by solving the set of equations (V .61) and by using Eq.(V .59):

$$\begin{cases} \tilde{\lambda}^c = \frac{1}{H_e}\dot{\boldsymbol{\Sigma}} : \boldsymbol{V} \\ \tilde{\lambda}^d = -\tilde{\lambda}^c \frac{\partial \tilde{\mathcal{G}}/\partial \tilde{\boldsymbol{E}}^c}{\partial \tilde{\mathcal{G}}/\partial d} : \boldsymbol{V} \end{cases} \tag{V .62}$$

where $H_e = \frac{\partial \tilde{\mathcal{F}}}{\partial d}\frac{\partial \tilde{\mathcal{G}}}{\partial \tilde{\boldsymbol{E}}^c} : \boldsymbol{V} / \frac{\partial \tilde{\mathcal{G}}}{\partial d} - \frac{\partial \tilde{\mathcal{F}}}{\partial \tilde{\boldsymbol{E}}^c} : \boldsymbol{V}$ is the hardening modulus.

4.3 Analytical traction-based yield criterion for localized crack

In the case of loading paths without the rotation of principal stresses, the flow direction tensor $\boldsymbol{V}$ is independent on the stress level, the inelastic strain of localized crack $\tilde{\boldsymbol{E}}^c$ can be directly calculated as $\tilde{\boldsymbol{E}}^c = \tilde{\Lambda}^c \boldsymbol{V}$ with the cumulation $\tilde{\Lambda}^c = \int \tilde{\lambda}^c$ operated after the onset of localized crack. In this case, the localized friction criterion (V .55) can be rewritten as

$$\tilde{\mathcal{F}}\left(\boldsymbol{\Sigma}, \tilde{\Lambda}^c, d\right) = \|\underline{\tau}\| + \tilde{c}_f t_n - \frac{\tilde{\Lambda}^c}{d - d_c}\kappa \leq 0. \tag{V .63}$$

$$\tilde{\mathcal{G}}\left(d, \tilde{\boldsymbol{E}}^c\right) = \frac{1}{2}\left(\frac{\tilde{\Lambda}^c}{d - d_c}\right)^2 \kappa - \tilde{\mathcal{R}}(d) \leq 0, \quad d > d_c \tag{V .64}$$

with $\kappa = \boldsymbol{V} : (d - d_c)\,\mathbb{C}^n : \boldsymbol{V}$, one obtains from Eq.(V .64)

$$\tilde{\Lambda}^c = (d - d_c)\sqrt{\frac{2\tilde{\mathcal{R}}(d)}{\kappa}} \tag{V .65}$$

Substituting Eq.(V .65) for (V .63), we finally obtain the analytical macroscopic traction-based friction criterion for the localized crack

$$\tilde{\mathcal{F}}(\underline{t}, d) = \|\underline{\tau}\| + \tilde{c}_f t_n - \sqrt{2\tilde{\mathcal{R}}(d)\,\kappa} \leq 0, \qquad d > d_c \tag{V .66}$$

Remark 6

According to Eq.(V .31), the rate form of localized inelastic strain becomes:

$$\dot{\tilde{\boldsymbol{E}}}^c = (\dot{\underline{e}} \otimes \underline{n})^{sym} \tag{V .67}$$

Combining Eqs.(V .56) and (V .59a), one obtains

$$\dot{\underline{e}} = \tilde{\lambda}^c\left(\underline{\varrho} + \tilde{c}_f \underline{n}\right) \tag{V .68}$$

In the case of without rotation of the principal stresses, one gets

$$\underline{e} = \tilde{\Lambda}^c\left(\underline{\varrho} + \tilde{c}_f \underline{n}\right) \tag{V .69}$$

5 Analytical analysis of some specific cases

In this section, we first consider the crack localization in a 2D cracked solid $\Omega \subset \mathbb{R}^2$ in the plane stress and strain conditions, and then we extend it to the conventional triaxial loading condition ($\Sigma_1 = \Sigma_3 < 0$). The in-plane principal stresses are denoted by Σ_1 and Σ_2 ($\Sigma_1 > \Sigma_2$) respectively, with the principal vectors v_1 and v_2. Σ_3 is orthogonal to the plane defined by v_1 and v_2. In these cases the crack orientation can be characterized by the inclination angle $\theta \in \left[-\frac{\pi}{2}, \frac{\pi}{2}\right]$ between the normal vector $\underline{n}$ of the localized crack and the the principal vector $\underline{v}_1$ (see in Figure V .4(b)). Accordingly, the base vectors of local coordinate system $(\underline{n}, \underline{m}, \underline{p})$ are given by:

$$\underline{n} = [\cos\theta, \sin\theta, 0],\ \underline{m} = [\sin\theta, -\cos\theta, 0],\ \underline{p} = [0, 0, -1] \tag{V .70}$$

The traction components (t_n, t_m) in the plane are obtained from Eq. (V .38)

$$t_n = \Sigma_{nn} = \frac{\Sigma_1 + \Sigma_2}{2} + \frac{\Sigma_1 - \Sigma_2}{2}\cos(2\theta) \tag{V .71a}$$

$$t_m = \Sigma_{nm} = \frac{\Sigma_1 - \Sigma_2}{2}\sin(2\theta) \tag{V .71b}$$

As the dissipative flow tensor $\boldsymbol{D}$ is coaxial to the stress (Itskov, 2007), the dissipative flow vector components (γ_n, γ_m) in the plane can be given by considering Eq.(V .45):

$$\gamma_n = D_{nn} = \frac{D_1 + D_2}{2} + \frac{D_1 - D_2}{2}\cos(2\theta) \tag{V .72a}$$

$$\gamma_m = 2D_{nm} = (D_1 - D_2)\sin(2\theta) \tag{V .72b}$$

where D_1, D_2 are the in-plane principal values of $\boldsymbol{D}$**.** Applying the Mohr's maximization postulate to the 2D conditions, the localized crack angle θ_{cr} is identified (Cervera and Wu, 2015) as follows:

$$\sin^2\theta_{cr} = -\frac{D_2}{D_1 - D_2}, \quad \cos^2\theta_{cr} = \frac{D_1}{D_1 - D_2} \qquad D_1 \geq 0\ ,\ D_2 \leq 0 \tag{V .73a}$$

$$\theta_{cr} = 0 \qquad D_1 > D_2 > 0 \tag{V .73b}$$

$$\theta_{cr} = \frac{\pi}{2} \qquad D_2 < D_1 < 0 \tag{V .73c}$$

For the loading paths without rotation of principal stresses, the dissipative flow tensor $\boldsymbol{D}$ has been expressed in terms of macroscopic stresses in Eq.(V .20). Accordingly, for the case of $D_1 \geq 0$ and $D_2 \leq 0$ given in Eq.(V .73a), the crack angle θ_{cr} is explicitly computed as follows:

$$\sin^2\theta_{cr} = -\frac{S_2 + 1/3c_f\,\|\boldsymbol{S}\|}{S_1 - S_2}, \qquad \cos^2\theta_{cr} = \frac{S_1 + 1/3c_f\,\|\boldsymbol{S}\|}{S_1 - S_2} \tag{V .74}$$

where S_1 and S_2 denote the two principal values of macroscopic deviatoric stress tensor $\boldsymbol{S}$ in the plane. Note that in this case, the analytical macroscopic stress-based yield criterion (V .26) and the traction-based yield criterion (V .40) are both satisfied. Therefore, the following analytical studies for plane stress, plane strain and conventional triaxial compression conditions will be performed in terms of both macroscopic stresses and local traction. Moreover, the analytical results of complete stress-strain curves with the transition from diffuse damage to localized cracking in conventional triaxial compression loading are presented and compared with the experimental results.

5.1 Analytical analysis for plane stress

In the case of plane stress ($\Sigma_3 = 0$), the results (V .74) become

$$\sin^2\theta_{cr} = -\frac{(2\Sigma_2 - \Sigma_1) + c_f\sqrt{\frac{2}{3}\left(\Sigma_1^2 + \Sigma_2^2 - \Sigma_1\Sigma_2\right)}}{3\left(\Sigma_1 - \Sigma_2\right)} \tag{V .75a}$$

$$\cos^2\theta_{cr} = \frac{(2\Sigma_1 - \Sigma_2) + c_f\sqrt{\frac{2}{3}\left(\Sigma_1^2 + \Sigma_2^2 - \Sigma_1\Sigma_2\right)}}{3\left(\Sigma_1 - \Sigma_2\right)} \tag{V .75b}$$

The conditions $D_1 \geq 0$ and $D_2 \leq 0$ result in $\Sigma_1 \geq \Sigma_2/\eta_1$ and $\Sigma_1 \geq \eta_2\Sigma_2$ where the parameters η_1 and η_2 are given by

$$\eta_1 = \frac{1}{2}\left[1 - c_f\sqrt{3/\left(6 - c_f^2\right)}\right], \eta_2 = \frac{1}{2}\left[1 + c_f\sqrt{3/\left(6 - c_f^2\right)}\right] \tag{V .75c}$$

Together with Eq.(V .73), the macroscopic principal stress-based failure criterion defined in (V .26) when $d = d_c$ becomes:

$$f\left(\boldsymbol{\Sigma}\right) = \tfrac{1}{3}\sqrt{6\left(\Sigma_1^2 + \Sigma_2^2 - \Sigma_1\Sigma_2\right)} + \tfrac{1}{3}c_f\left(\Sigma_1 + \Sigma_2\right) - \sqrt{2\mathcal{R}\left(d_c\right)\chi} \leq 0 \quad D_1 \geq 0\ ,\ D_2 \leq 0 \tag{V .76}$$

With the crack angle given in (V .73a), the traction-based failure criterion consistent with (V .76) is given by (see Appendix A.1):

$$\mathcal{F}\left(\underline{t}\right) = t_m^2 + \frac{3 - 2c_f^2}{2\left(6 - c_f^2\right)}t_n^2 + \frac{c_f\sqrt{2\mathcal{R}\left(d_c\right)\chi}}{2\left(6 - c_f^2\right)}t_n - \frac{6\mathcal{R}\left(d_c\right)\chi}{\left(6 - c_f^2\right)} \leq 0 \tag{V .77}$$

It is noted that although it is not easy to identify the geometrical type of the macroscopic stress-based failure criterion given in (V .76), the traction-based criterion given in (V .77) indicates a standard conic section. Therefore the following three cases can be depicted regrading the value of friction coefficient $c_f \in \left[0, \sqrt{6}\right)$

- $c_f \geq 0$ and $3 - 2c_f^2 > 0 \Leftrightarrow 0 \leq c_f < \sqrt{\frac{3}{2}}$: The traction based criterion (V .77) gives an ellipse on the (t_n, t_m) plane, the macroscopic stress-based counterpart also gives an ellipse on the (Σ_1, Σ_3) plane, as shown in Figure V .5, in which we take $c_f = 0.8$ as an example.

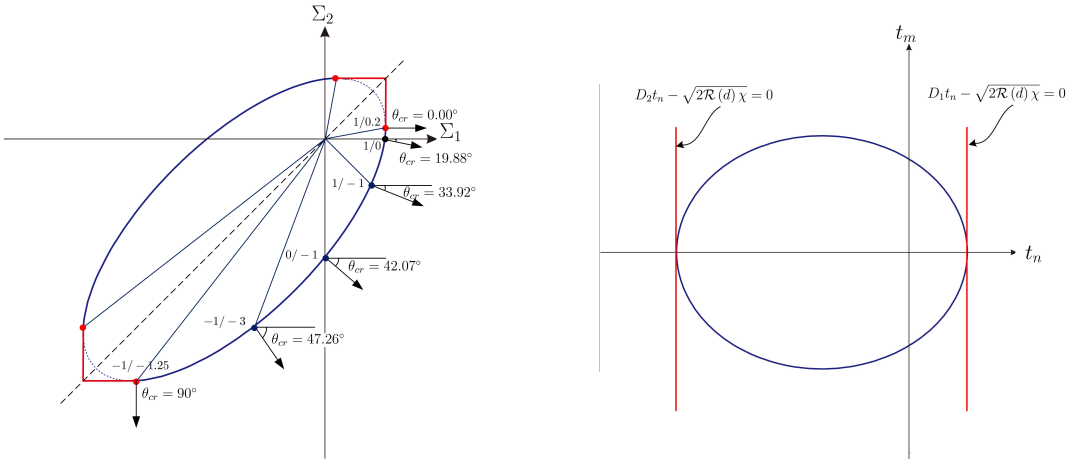

(a) Marcostress-based (b) Traction-based

Figure V .5: Deduced failure criterion in plane stress condition:elliptic type ($c_f = 0.8$)

- $3 - 2c_f^2 = 0 \Leftrightarrow c_f = \sqrt{\frac{3}{2}}$: The traction based criterion (V .77) is a parabolic form on the (t_n, t_m) plane (see Figure V .6(b)), while the macroscopic stress-based one is also a parabolic form on the (Σ_1, Σ_3) plane (see Figure V .6(a)).
- $c_f < \sqrt{6}$ and $3 - 2c_f^2 < 0 \Leftrightarrow \sqrt{\frac{3}{2}} < c_f < \sqrt{6}$: The traction based criterion (V .77) is a hyperbolic form on the (t_n, t_m) plane, and the macroscopic stress-based criterion is also a hyperbolic form on the (Σ_1, Σ_3) plane, as shown in Figure V .5 with $c_f = 2$ as an example.

For completeness, the forms of both the macroscopic stress-based and traction based criteria for the particular cases of $D_1 > D_2 > 0$ and $D_2 < D_1 < 0$ are also studied and indicated by the red solid lines in Figures V .5-V .7. The detailed calculations are given in Appendix B.

The angles of localized cracks θ_{cr} in the plane stress conditions are summarized in Table V .1 and illustrated in Figure V .8 with the different values of friction coefficient c_f and macroscopic stress ratio.

Remark 7

As shown in Figures V .6 and V .7, for the fictional coefficient $c_f \in \left[\sqrt{\frac{3}{2}}, \sqrt{6}\right)$ *the*

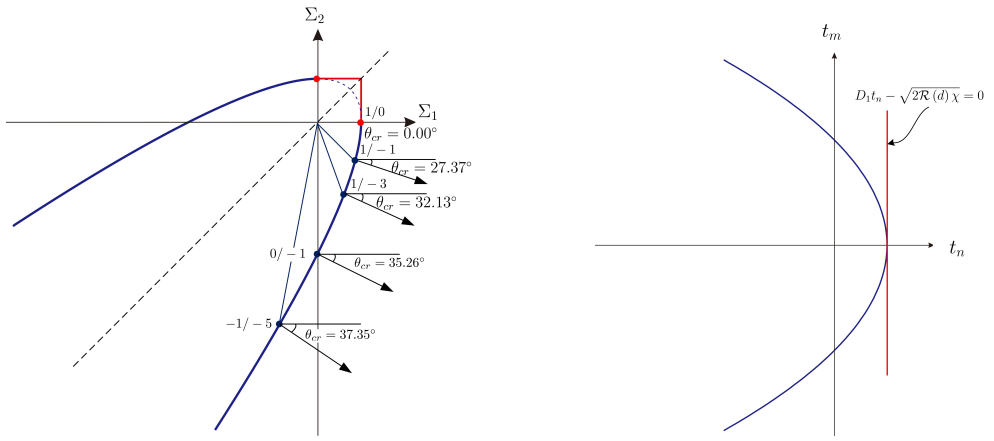

(a) Marcostress-based (b) Traction-based

Figure V .6: Deduced failure criterion in plane stress condition:parabolic type ($c_f = \sqrt{\frac{3}{2}}$)

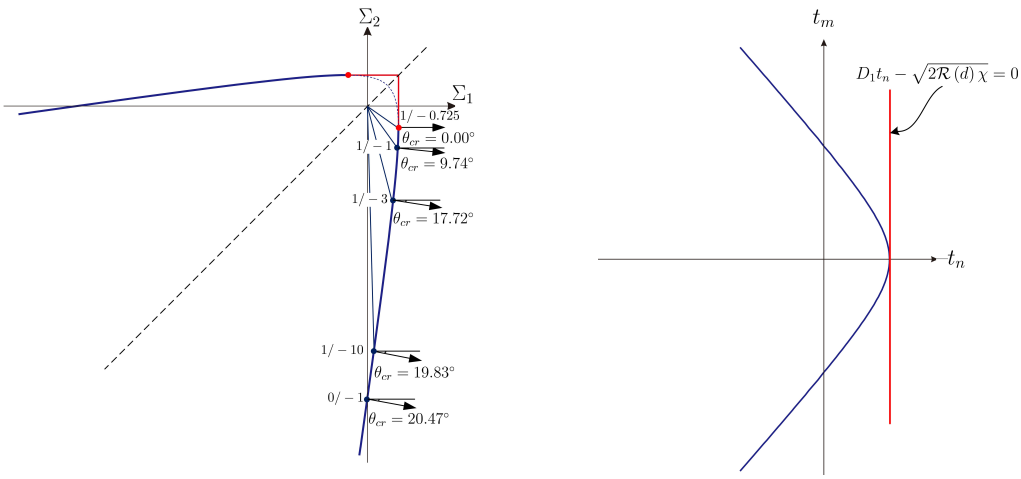

(a) Marcostress-based (b) Traction-based

Figure V .7: Deduced failure criterion in plane stress condition:hyperbolic type ($c_f = 2$)

deduced criterion (V .26) has an open locus in the principal stress plane (Σ_1, Σ_2). As a consequence, there must exist a limit value of θ_{cr}. In order to determine θ_{cr}, it is first needed to know the slant asymptotic functions of the yield surface, or at least the slope of asymptotic function in compression-compression region (i.e., $\Sigma_1 < 0$ and

Table V .1: Localized crack angle θ_{cr} in plane stress condition

c_f	Macroscopic stress ratio Σ_1/Σ_2										
	$-1:-1$	$-1:-1.25$	$-1:-3$	$-1:-5$	$0:-1$	$1:-10$	$1:-3$	$1:-1$	$1:-0.725$	$1:0$	$1:0.2$
0.8	90°	90°	47.26°	45.66	42.07°	40.85°	38.47°	33.92°	32.21°	19.88°	0.00°
$\sqrt{3/2}$	45°	43.42°	38.78°	37.35°	35.26°	34.27°	32.13°	27.37°	25.37°	0.00°	0.00°
2	-	-	-	-	20.47°	19.83°	17.72°	9.74°	0.00°	0.00°	0.00°

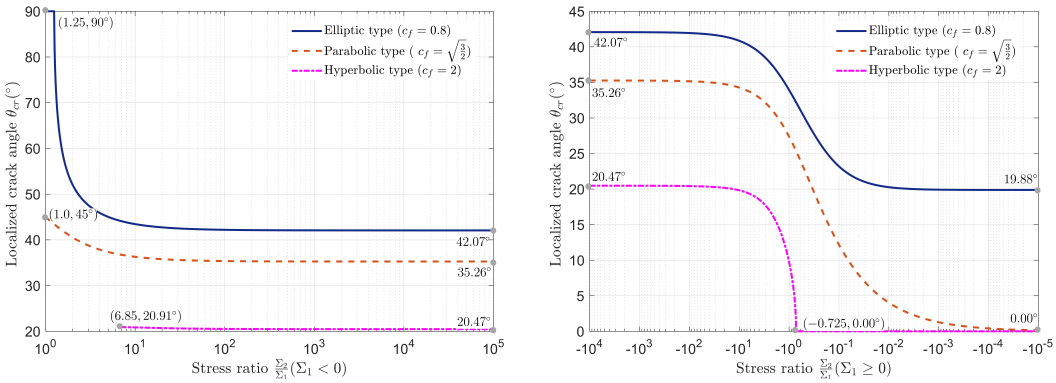

(a) Compression-compression quadrant (b) Tension-compression quadrant

Figure V .8: Localized crack angle θ_{cr} in plane stress condition

$\Sigma_2 < 0$). *Here by solving*

$$\lim_{\Sigma_1 \to -\infty} \frac{1}{3}\sqrt{6\left(1+\left(\frac{\Sigma_2}{\Sigma_1}\right)^2 - \frac{\Sigma_2}{\Sigma_1}\right)} + \frac{1}{3}c_f\left(1+\frac{\Sigma_2}{\Sigma_1}\right) - \frac{\sqrt{2\mathcal{R}\left(d_c\right)\chi}}{\Sigma_1} = 0 \qquad \text{(V .78)}$$

one obtains the slope of the asymptotic function:

$$k = \frac{\Sigma_2}{\Sigma_1} = \frac{c_f^2 + 3 + 3\sqrt{2c_f^2 - 3}}{6 - c_f^2} \qquad \text{(V .79)}$$

Then the limit crack angle satisfies

$$\lim_{\Sigma_2 \to k\Sigma_1 < 0} \sin\theta_{cr}^2 = \lim_{\Sigma_2 \to k\Sigma_1 < 0} -\frac{(2\Sigma_2 - \Sigma_1) + c_f\sqrt{\frac{2}{3}\left(\Sigma_1^2 + \Sigma_2^2 - \Sigma_1\Sigma_2\right)}}{3\left(\Sigma_1 - \Sigma_2\right)} \qquad \text{(V .80)}$$

- *For the parabolic criterion* ($c_f = \sqrt{\frac{3}{2}}$), *one can obtain* $k = 1$. *Accordingly, the limit crack angle is* $\lim_{\Sigma_2 \to \Sigma_1 < 0} \theta_{cr} = 45°$.

- *For the hyperbolic criterion* ($c_f \in (\sqrt{\frac{3}{2}}, \sqrt{6})$)*, as an example, for the friction coefficient* $c_f = 2, k = \frac{7+3\sqrt{5}}{2} \approx 6.85$*, one obtains* $\lim_{\Sigma_2 \to k\Sigma_1 < 0} \theta_{cr} = 20.91°$.

5.2 Analytical analysis for plane strain

In the case of plane strain, the classical discontinuous bifurcation analysis gives (Runesson et al., 1991):

$$\sin^2 \theta_{cr} = -\frac{D_2 + \nu^m D_3}{D_1 - D_2}, \qquad \cos^2 \theta_{cr} = \frac{D_1 + \nu^m D_3}{D_1 - D_2} \tag{V .81}$$

which coincidence with Maxwell's compatibility condition (V .72a), requiring that

$$D_3 = 0 \Rightarrow \frac{S_3}{\|\boldsymbol{S}\|} + \frac{1}{3} c_f = 0 \tag{V .82}$$

As it is noted in Wu and Cervera (2016), this extra condition (Eq.(V .82)) is not taken into account in the classical discontinuous bifurcation analysis. Accordingly, the results in the case of plane strain derived from Maxwell's compatibility condition are not only consistent with, but more demanding than, the classical ones.

For completeness, the extra condition (Eq.(V .82)) is equivalent to

$$\Sigma_3 = \frac{3 + c_f^2}{6 - c_f^2} (\Sigma_1 + \Sigma_2) - \frac{3 c_f \sqrt{2\mathcal{R}(d_c)\chi}}{6 - c_f^2} \tag{V .83}$$

As $\mathrm{tr}\boldsymbol{S} = 0$, one obtains

$$S_1 + S_2 = -S_3 = \frac{1}{3} c_f \|\boldsymbol{S}\| \geq 0 \tag{V .84}$$

or equivalently

$$S_1^2 + \frac{18 - 2c_f^2}{9 - 2c_f^2} S_1 S_2 + S_2^2 = 0 \tag{V .85}$$

Accordingly, the crack angle defined in (V .74) is determined by

$$\sin^2 \theta_{cr} = -\frac{S_2 + 1/3 c_f \|\boldsymbol{S}\|}{S_1 - S_2} = -\frac{2S_2 + S_1}{S_1 - S_2} = -\frac{2 + \varsigma}{\varsigma - 1} \tag{V .86a}$$

$$\cos^2 \theta_{cr} = \frac{S_1 + 1/3 c_f \|\boldsymbol{S}\|}{S_1 - S_2} = \frac{2S_1 + S_2}{S_1 - S_2} = \frac{2\varsigma + 1}{\varsigma - 1} \tag{V .86b}$$

The ratio $\varsigma := S_1/S_2$ is given from the relation (V .85)

$$\varsigma = \frac{c_f^2 - 9 - c_f \sqrt{18 - 3c_f^2}}{9 - 2c_f^2} \tag{V .87}$$

Table V .2: Localized crack angle θ_{cr} in plane strain condition

Frictional coefficient c_f	0	0.2	0.4	0.6	0.8	1.0	$\sqrt{\frac{3}{2}}$
Crack angle θ_{cr}	45°	40.92°	36.67°	32.02°	26.62°	19.62°	0°

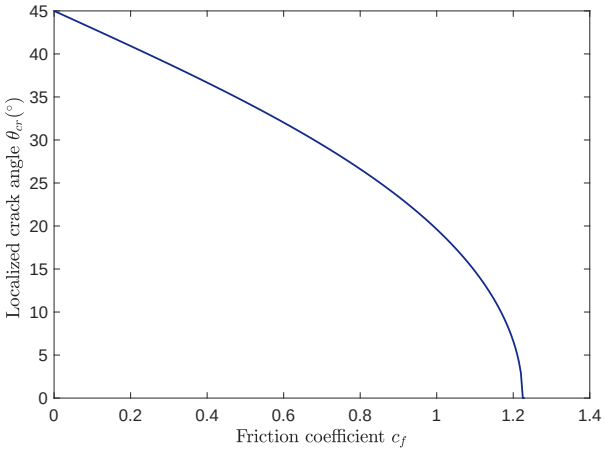

Figure V .9: Localized crack angle θ_{cr} in plane strain condition

Since the following condition must be satisfied

$$2S_2 + S_1 \leq 0,\ 2S_1 + S_2 \geq 0,\ S_1 + S_2 \geq 0 \tag{V .88}$$

One obtains:

$$\varsigma \in [-2, -1] \Leftrightarrow c_f \in \left[0, \sqrt{\frac{3}{2}}\right] \tag{V .89}$$

One can notice from Eqs.(V .86) and (V .87) that the crack angle θ_{cr} only depends on the frictional coefficient $c_f \in \left[0, \sqrt{\frac{3}{2}}\right]$. For instance, the values of crack angle are presented in Table V .2 and Figure V .9 for some values of frictional coefficient.

Using the crack angle given in (V .86), the traction-based failure criterion in the condition of plane strain can be derived as follows (see Appendix A.2):

$$\mathcal{F}(\underline{t}) = t_m^2 - \frac{3}{6 - 4c_f^2}\left(c_f t_n - \sqrt{2\mathcal{R}(d_c)\chi}\right)^2 \leq 0 \tag{V .90}$$

The left branch of interest can be expressed as

$$|t_m| + \tan\varphi \cdot t_n - c \leq 0 \tag{V .91}$$

where the frictional angle φ and cohesion c are given by:

$$\tan\varphi = \sqrt{\frac{3c_f^2}{6 - 4c_f^2}},\quad c = \sqrt{\frac{6\mathcal{R}(d_c)\chi}{6 - 4c_f^2}} \tag{V .92}$$

Table V .3: Localized crack angle θ_{cr} in conventional triaxial compression condition

Frictional coefficient c_f	0	0.3	0.6	0.9	1.2	1.5	1.8
Crack angle θ_{cr}	54.73°	48.83°	43.09°	37.27°	31.10°	24.10°	14.96°

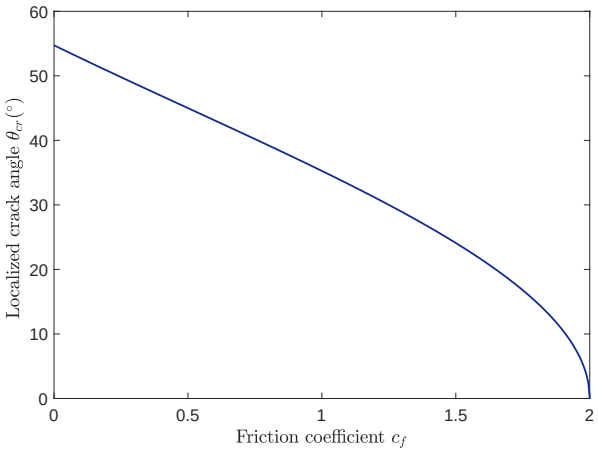

Figure V .10: Localized crack angle θ_{cr} in conventional triaxial compression condition

One can see that in the case of plane strain, the deduced criterion (V .40) turns into a Mohr-Coulomb type. The macroscopic parameters involved can de directly calibrated from microscopic parameters c_f and $\mathcal{R}(d_c)$.

5.3 Analytical analysis of conventional triaxial compression

5.3.1 Analytical results of localized crack angle

In the case of conventioal triaxial compression ($0 > \Sigma_1 = \Sigma_3 > \Sigma_2$), $\|\boldsymbol{S}\| = \Sigma_1 - \Sigma_2$, $P = \frac{1}{3}(2\Sigma_1 + \Sigma_2)$, here $\Sigma_1 = \Sigma_3$ denotes the confining pressure, while Σ_2 represents the axial stress. With this loading condition, the results (V .74) become

$$\begin{cases} \sin^2\theta_{cr} = \frac{2}{3} - \frac{c_f}{3} \\ \cos^2\theta_{cr} = \frac{1}{3} + \frac{c_f}{3} \end{cases} \qquad c_f \in [0,2] \tag{V .93}$$

One can also notice from Eqs.(V .93) that the crack angle θ_{cr} in this loading condition only depends on the frictional coefficient $c_f \in [0,2]$. The values of localized crack angles are presented in Table V .3 and Figure V .10 for some values of frictional coefficient.

5.3.2 Analytical results of complete stress-strain curves

As indicated in the previous sections, the deformation process involves two stages, one deals with a homogeneous deformation that is governed by the micro-mechanics based diffuse friction-damage model before the onset of localized cracks in Section 2 and the other one is associated with the localized deformation controlled by the localized friction-damage model. It is worth noting that, both the diffuse and localized friction-damage models can provide the analytical yield criteria (Eqs.(V .26) and (V .66)) without the rotation of principal stresses. In this context, once the localized crack angle is determined, it is easy to obtain the analytical complete stress-strain curves considering the damage from diffused to localized state.

The macroscopic stress-based yield criterion defined in (V .26) in the conventional triaxial compression becomes:

$$\mathcal{F}(\boldsymbol{\Sigma}, d) = \Sigma_2 - \frac{2c_f + \sqrt{6}}{\sqrt{6} - c_f}\Sigma_1 + 3\sqrt{2\mathcal{R}(d)\,\chi} \leq 0 \qquad d \leq d_c \tag{V .94}$$

One the other hand, the analytical traction-based yield criterion (V .66) for localized crack can be rewritten in the principal stresses form in the conventional triaxial compression loading condition (Zhu, 2017)

$$\tilde{\mathcal{F}}(\boldsymbol{\Sigma}, d) = \Sigma_2 - \frac{\sin\theta_{cr}\cos\theta_{cr} + \tilde{c}_f \sin^2\theta_{cr}}{\sin\theta_{cr}\cos\theta_{cr} - \tilde{c}_f\cos^2\theta_{cr}}\Sigma_1 + \frac{1}{\sin\theta_{cr}\cos\theta_{cr} - \tilde{c}_f\cos^2\theta_{cr}}\sqrt{2\tilde{\mathcal{R}}(d)\,\kappa} \leq 0 \qquad d > d_c \tag{V .95}$$

At the onset of localization, one has:

$$\begin{cases} \mathcal{F}(\boldsymbol{\Sigma}, d_c) = \lim_{d \to d_c^+} \tilde{\mathcal{F}}(\boldsymbol{\Sigma}, d) = 0 \\ \Sigma_2 \Big|_{d \to d_c^+} \geq \Sigma_2 (d = d_c) \end{cases} \tag{V .96}$$

In a monotonic conventional triaxial compression test, $\Sigma_1 = \Sigma_3$ is constant and equals to the prescribed confining pressure. In addition, the damage variable will monotonically increase. Therefore, the analytical complete stress-strain relations can be obtained by the following procedure:

1. Given a damage variable d, if $d \leq d_c$, calculate $\mathcal{R}(d)$ and Λ with Eqs. (V .16) and (V .25), else calculate $\tilde{\mathcal{R}}(d)$ and $\tilde{\Lambda}$ with Eqs. (V .58) and (V .65).

2. Calculate Σ_2 by using (V .94) and (V .95) with the prescribed confining pressure Σ_1 and damage variable d.

Table V .4: Values of parameters used in the diffuse friction-damage model for Lac du Bonnet granite

Parameters	E^m(MPa)	ν^m	d_c	c_f	$\mathcal{R}(d_c)$
Values	72000	0.2	2.8	1.45	0.1

3. Calculate the macroscopic strain by using

$$\boldsymbol{E} = \mathbb{S}^m : \boldsymbol{\Sigma} + \ \Lambda \boldsymbol{D} + \tilde{\Lambda} \boldsymbol{V}, \tag{V .97}$$

In order to show the efficiency of the proposed model, the analytical solutions are now compared with the experimental data on the Lac du Bonnet granite in conventional triaxial compression tests. It is important to point out that due to localization, the tested specimen cannot be seen as a material point but as a small structure submitted to boundary conditions. Therefore, a suitable boundary values problem should be solved by using for instance the finite element method. The proposed frictional-damage model should be implemented in a computer code and used inside each element which is seen as a representative volume element. The characteristic length for the cracked element is the ratio between the element volume and the localized crack surface. However, as a first approximation and in order to use the analytical solution, a simplified approach is here proposed. The tested sample is seen as a single element with the onset of an oriented localized crack according to the criteria proposed above. Then the macroscopic strains and stresses are determined by the analytical solutions and compared with experimental data. The presented model contains 7 parameters that can be determined from a series of conventional triaxial compression tests. Here as an example, the experimental data with three confining pressures of Σ_1 = -30, -40 and -60MPa extracted from Martin (1997) are used for the determination of parameters and the comparisons with the analytical results. The calibration procedure of the diffuse friction damage model parameters (5 parameters) has been introduced in detail in Zhao et al. (2018); Zhu et al. (2016). By using that procedure, we have obtained the parameters listed in Table V .4. The localized crack angle $\theta_{cr} = 25.29°$ can be obtained by using Eq.(V .93). The two parameters involved in the localized friction-damage model are easy to be determined with Eq.(V .96) ($\tilde{c}_f \leq 0.37$ and $\tilde{\mathcal{R}}(d_c) \leq 0.032$). Here we take $\tilde{c}_f = 0.37$ and $\tilde{\mathcal{R}}(d_c) = 0.032$ for study the mechanical behavior of the Lac du Bonnet granite.

In Figure V .11, one shows the analytical relations between applied traction $\|\underline{\tau}\|$ and

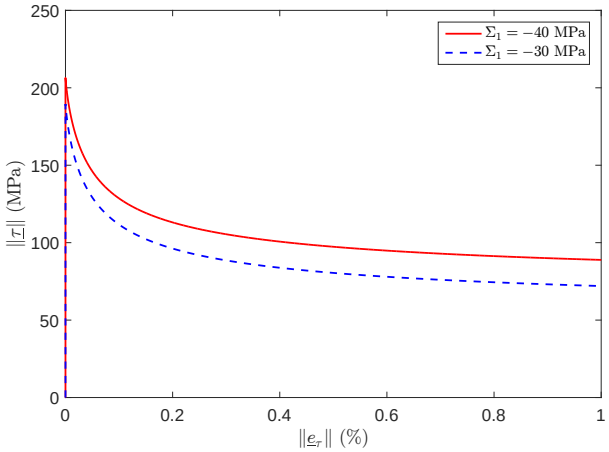

Figure V .11: Analytical traction-sliding curves for Lac du Bonnet granite under two conventional triaxial compression with different confining pressures

frictional sliding $\|\underline{e}_\tau\|$ under two different confining pressures. Here $\|\underline{e}_\tau\| = \|\underline{e} \cdot \boldsymbol{T}\|$, with $\underline{e}$ can be calculated by using Eq.(V .69).

Furthermore, the analytical stress-strain curves with and without considering the onset of localization for the conventional triaxial compression tests with two confining pressures of $\Sigma_1 = -30$ and -40MPa are presented and compared with experimental data in Figure V .12. The critical value of damage density parameter d_c corresponds to the peak deviatoric stress. It is seen that both the analytical results with and without considering the localized crack can correctly capture the general features of mechanical behavior of Lac du Bonnet granite, such as the non-linear strain, confining pressure effect and volumetric dilatation, strain hardening and softening. However, in a quantitative way, there is a large discrepancy between the solutions provided by the model without considering localized crack and experimental data in the post-peak regime. This is due to the fact that the mechanical response of the granite in the post-peak regime is essentially governed by the localized crack and not by the diffuse micro-cracks. The diffuse friction-damage model is not able to capture this physical mechanism. As a comparison, the friction-damage model with considering the localized crack is in a very good agreement with experimental data. Furthermore, the mechanical response in the post-localization regime is controlled by the mechanical properties and orientation of the localized crack.

In Figure V .13, we present the analytical stress-strain curves with different values of the parameters $\tilde{c}_f$ (Figure V .13(a)) and $\tilde{\mathcal{R}}(d_c)$ (Figure V .13(b)) in the conventional triaxial compression test with a confining pressure of $\Sigma_1 = -40$MPa. It is found that when $\tilde{c}_f < 0.37$ or $\tilde{\mathcal{R}}(d_c) < 0.032$, there exists a sharp stress drop just after the onset of localized

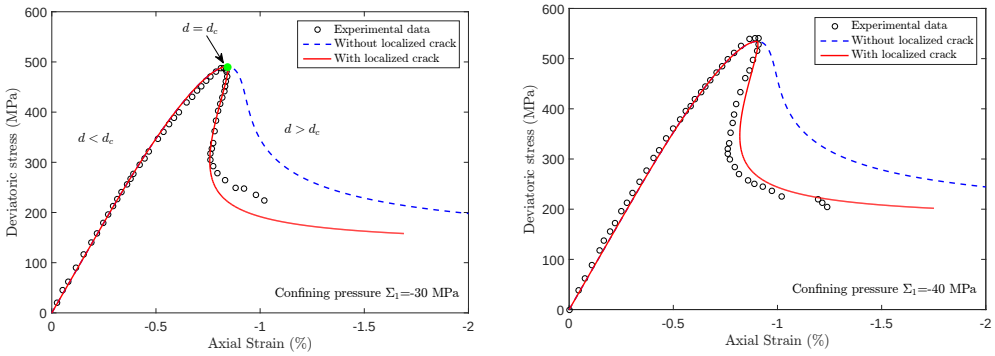

(a) Confining pressure $\Sigma_1 = -30$ MPa (b) Confining pressure $\Sigma_1 = -40$ MPa

Figure V .12: Analytical stress-strain curves of triaxial compression test on Lac du Bonnet granite with and without considering localized crack (experimental data extracted from Martin (1997))

crack. The magnitude of stress drop increases with the decrease of $\tilde{c}_f$ and $\tilde{\mathcal{R}}(d_c)$. From the end of the stress drop, the cracked material will exhibit the strain softening behavior controlled by the yield function of the localized crack (V .95).

In Figure V .14, the stress-strain curves with the different values of the localized crack angle θ_{cr} in the range from $\frac{\pi}{6}$ to $\frac{\pi}{3}$ are presented and compared with the curve provided by the diffuse model without considering the localized crack. One can see that the localized crack angle θ_{cr} has a significant influence on the post-peak stress-strain curve and on the residual strength. More interestingly, the post-peak behavior can be transformed from a snap-back softening (Class II behavior) to a stable softening (Class I behavior). For the Class II behavior, both the stress and strain decrease after the peak strength. For the Class I behavior, on the contrary, the stress decreases with the increasing strain after the peak strength, implying that plastic strain increases faster than the elastic strain decreases.

6 Concluding remarks

In this chapter, we have developed a micro-mechanics based approach for studying the transition from diffuse damage to localized cracking in quasi-brittle materials. The emphasis was put on closed cracks under compressive stresses. For the description of mechanical behavior of material with randomly distributed micro-cracks before localization, a coupled friction-damage model has been formulated using a rigorous homogenization scheme. The damage is related to the growth of micro-cracks while the frictional sliding induces the macroscopic plastic strain. The damage evolution is driven by the frictional sliding while

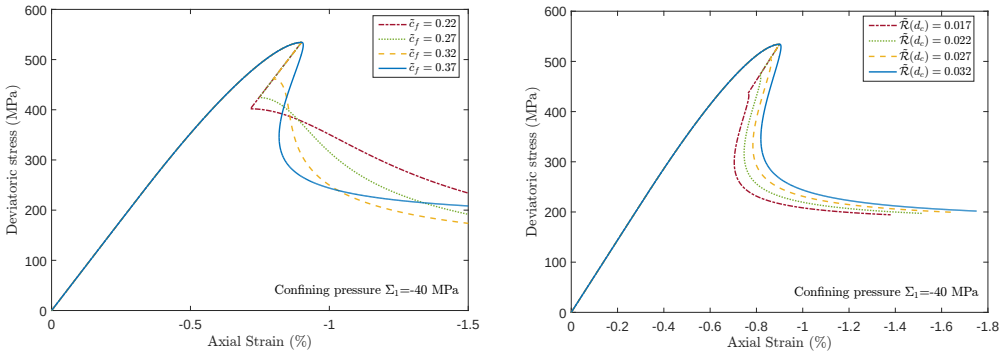

(a) Sensitivity analyses on $\tilde{c}_f$ (b) Sensitivity analyses on $\tilde{\mathcal{R}}(d_c)$

Figure V .13: Sensitivity analyses on the localized friction damage model parameters ($\tilde{c}_f$ and $\tilde{\mathcal{R}}(d_c)$) using triaxial compression tests with Σ_1 = -40MPa

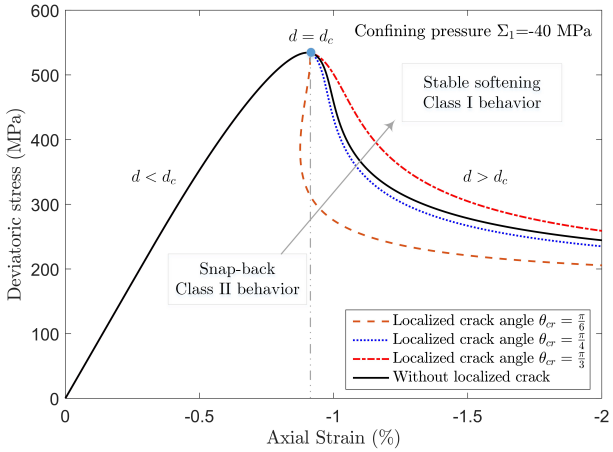

Figure V .14: Sensitivity analyses on the localized angle θ_{cr} using triaxial compression tests with Σ_1 = -40MPa

the latter is enhanced by the damage growth. The onset of a localized crack occurs when the damage density parameter (density of micro-cracks) reaches a critical value which corresponds to the maximal value of material resistance to the propagation of micro-cracks. After the onset of a localized crack, the energy dissipation of material is entirely related to the frictional sliding and propagation of the localized crack. A traction-based model has been developed to describe the frictional sliding of the localized crack which acts as the driving force for its propagation. The overall deformation of material is then attributed to the frictional sliding induced displacement discontinuity in the localized crack and the elastic deformation of matrix. The continuity conditions and kinematic constraints on the localized crack have been discussed. The orientation of localized crack has been in-

vestigated using the Mohr's maximization postulate. Analytical results of the localized crack angle have been obtained for plane stress, plane strain and conventional triaxial compression conditions. It is found that the crack orientation is essentially controlled by the local frictional coefficient along micro-cracks. For loading paths without rotation of principal stresses, the proposed approach has allowed to obtain an analytical stress-based and traction-based criterion for both the frictional sliding of diffuse micro-cracks and that of the localized crack. Moreover, the analytical solutions of complete stress-strain curves with and without considering localized crack have been obtained for conventional triaxial compression tests, and compared with experimental results. It is found that the friction-damage model with localized crack is able to well capture the mechanical response of material in the post-peak regime. However, in the present study, only a single localized crack has been considered in the cracked material volume. In future studies, the proposed friction-damage model with localization will be implemented into a finite element code and applied to investigate the whole failure process with progressive growth of localized cracks in both sample and structure scales.

Appendix A: Traction-based failure criterion for some cases

A.1: Case of plane stress

In the case of plane stress, by the substitution (V .75) for (V .71), we arrive at

$$t_n = \frac{2}{3}\left(1 - \frac{c_f^2}{6}\right)(\Sigma_1 + \Sigma_2) + \frac{c_f}{3}\sqrt{2\mathcal{R}(d_c)\chi} \tag{V .98a}$$

$$t_m^2 = -(S_1 + 1/3c_f\|\boldsymbol{S}\|)(S_2 + 1/3c_f\|\boldsymbol{S}\|) \tag{V .98b}$$

Similarly, substituting (V .75) for (V .72), one obtains

$$\gamma_n = \frac{1}{\|\boldsymbol{S}\|}\left(\frac{-2c_f^2 t_n + 3t_n + 3c_f\sqrt{2\mathcal{R}(d_c)\chi}}{6 - c_f^2}\right) \tag{V .99a}$$

$$\gamma_m = \frac{2t_m}{\|\boldsymbol{S}\|} \tag{V .99b}$$

The norm $\|\boldsymbol{S}\|$ can be evaluated from (V .26) and (V .98a)

$$\|\boldsymbol{S}\| = -\frac{1}{3}c_f(\Sigma_1 + \Sigma_2) + \sqrt{2\mathcal{R}(d_c)\chi} = -\frac{3c_f t_n - c_f^2\sqrt{2\mathcal{R}(d_c)\chi}}{6 - c_f^2} + \sqrt{2\mathcal{R}(d_c)\chi} \geq 0 \tag{V .100}$$

The substitution of (V .98) and (V .99) for (V .40) leads to the following traction-based failure criterion:

$$\mathcal{F}\left(\underline{t}\right)=\frac{2}{\|\boldsymbol{S}\|}\left[t_m^2+\frac{3-2c_f^2}{2\left(6-c_f^2\right)}t_n^2+\frac{c_f\sqrt{2\mathcal{R}\left(d_c\right)\chi}}{2\left(6-c_f^2\right)}t_n-\frac{6\mathcal{R}\left(d_c\right)\chi}{\left(6-c_f^2\right)}\right]\leq 0 \tag{V .101}$$

A.2: Case of plane strain

For the plane strain condition, using the crack angle given in (V .86) and recalling (V .83), the normal traction can be given by

$$t_n=\Sigma_1+\Sigma_2-\Sigma_3=\frac{3-2c_f^2}{6-c_f^2}\left(\Sigma_1+\Sigma_2\right)+\frac{3c_f\sqrt{2\mathcal{R}\left(d_c\right)\chi}}{6-c_f^2} \tag{V .102}$$

This yields the following relations

$$\Sigma_1+\Sigma_2=\frac{\left(6-c_f^2\right)t_n-3c_f\sqrt{2\mathcal{R}\left(d_c\right)\chi}}{3-2c_f^2} \tag{V .103a}$$

$$\Sigma_3=\frac{\left(3+c_f^2\right)t_n-3c_f\sqrt{2\mathcal{R}\left(d_c\right)\chi}}{3-2c_f^2} \tag{V .103b}$$

The square of the tangential traction t_m^2 is also obtained

$$t_m^2=\Sigma_{nm}^2=-\left(2S_1+S_2\right)\left(S_1+2S_2\right) \tag{V .104}$$

By substituting (V .86) for (V .72) and recalling (V .84), one gets

$$\gamma_n=D_1+D_2=\frac{S_1+S_2}{\|\boldsymbol{S}\|}+\frac{2}{3}c_f=c_f \tag{V .105a}$$

$$\gamma_m=2\left(D_1-D_2\right)\sin\theta_{cr}\cos\theta_{cr}=\frac{2t_m}{\|\boldsymbol{S}\|}=\frac{2c_ft_m}{3\left(S_1+S_2\right)} \tag{V .105b}$$

with the following relation

$$S_1+S_2=\frac{\Sigma_1+\Sigma_2-2\Sigma_3}{3}=\frac{\sqrt{2\mathcal{R}\left(d_c\right)\chi}c_f-c_f^2t_n}{3-2c_f^2} \tag{V .106}$$

Further by the substitution of (V .106) for (V .105b), one obtains

$$\gamma_m=\frac{2\left(-3+2c_f^2\right)t_m}{3c_ft_n-3\sqrt{2\mathcal{R}\left(d_c\right)\chi}} \tag{V .107}$$

Finally, by substituting (V .105a) and (V .107) for (V .40), the traction-based failure criterion is written as follows:

$$\mathcal{F}\left(\underline{t}\right)=t_m^2-\frac{3}{6-4c_f^2}\left(c_ft_n-\sqrt{2\mathcal{R}\left(d_c\right)\chi}\right)^2\leq 0 \tag{V .108}$$

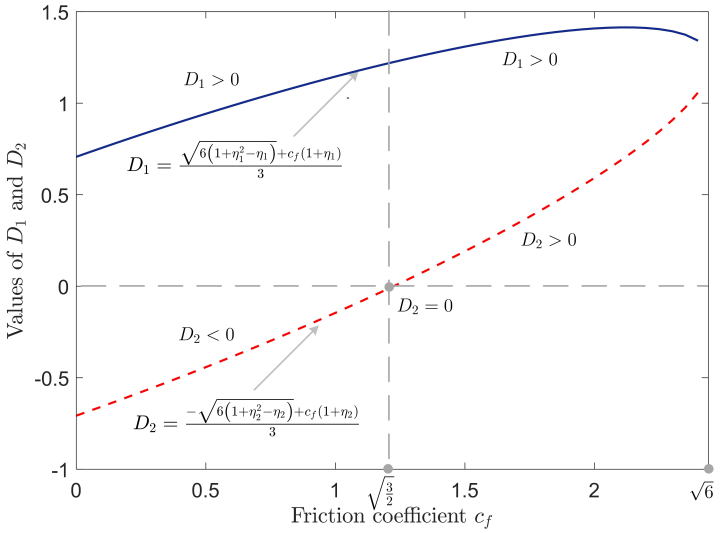

Figure V .15: Values of D_1 and D_2 versus frictional coefficient c_f

Appendix B: Particular 2D cases

It is noted that the crack angles given in (V .73b) and (V .73c) correspond to the particular values of $D_2 = 0$ and $D_1 = 0$ in (V .73a). As a consequence, the macroscopic stress-based criterion given in Eq.(V .26) can be rewritten as

$$\mathcal{F}(\boldsymbol{\Sigma}) = \begin{cases} D_1\Sigma_1 - \sqrt{2\mathcal{R}(d_c)\,\chi} \leq 0 \quad D_1 > D_2 > 0 \\ D_2\Sigma_2 - \sqrt{2\mathcal{R}(d_c)\,\chi} \leq 0 \quad D_2 < D_1 < 0 \end{cases} \tag{V .109}$$

Similarly, the corresponding traction-based failure criterion $\mathcal{F}(\underline{t})$ is expressed by

$$\mathcal{F}(\underline{t}) = \begin{cases} D_1 t_n - \sqrt{2\mathcal{R}(d_c)\,\chi} \leq 0 \quad D_1 > D_2 > 0 \\ D_2 t_n - \sqrt{2\mathcal{R}(d_c)\,\chi} \leq 0 \quad D_2 < D_1 < 0 \end{cases} \tag{V .110}$$

The aim here is the determination of D_1 and D_2 in (V .109) and (V .110). Note that the two particular cases respectively correspond to the conditions $\Sigma_1 < \Sigma_2/\eta_1$ and $\Sigma_1 < \eta_2\Sigma_2$, with η_1 and η_2 given in (V .75c). By respectively taking $\Sigma_2 \to \eta_1\Sigma_1$ and $\Sigma_1 \to \eta_2\Sigma_2$ in (V .76), one obtains D_1 and D_2 as follows:

$$D_1 = \frac{\sqrt{6\left(1+\eta_1^2-\eta_1\right)} + c_f\left(1+\eta_1\right)}{3} > 0 \tag{V .111a}$$

$$D_2 = \frac{-\sqrt{6\left(1+\eta_2^2-\eta_2\right)} + c_f\left(1+\eta_2\right)}{3} < 0 \tag{V .111b}$$

As depicted in (V .111) and (V .75c), the values of D_1 and D_2 only depend on the friction coefficient $c_f \in [0, \sqrt{6})$. It is worth noticing that if the inequality condition in (V .111) is not satisfied, the corresponding particular case does not exist. In Figure V .15, we show the values of D_1 and D_2 in all range of friction coefficient c_f. One can see that, for $c_f \in [\sqrt{\frac{3}{2}}, \sqrt{6})$, $D_2 \geq 0$. This implies that only one particular case exists in this region, as also shown in Figures V .6 and V .7.

Chapter VI

Conclusions and perspectives

1 Conclusions

This thesis aims to propose a series of homogenization methods for modeling the effective (overall) behaviors of ductile and brittle rock-like materials via incremental variational and micro-mechanics based friction-damage approaches. For this purpose, we consider that the ductile and brittle rock-like materials have different micro-structures. The ductile rock-like materials are composed of plastic solid matrix and in which mineral inclusions and (or) pores are embedded, while the brittle ones are composed of elastic solid matrix weakened by micro-cracks. In this context, different homogenization approaches have been introduced. The main conclusions of this thesis are following

- An incremental variational homogenization model have been proposed for describing the elastic-plastic behavior of ductile rock-like material with an associated Drucker-Prager plastic matrix. The non-uniform local plastic strain field is taken into account in the model. The approach have been validated from comparison with direct finite element simulations for inclusion-reinforced and porous materials, together with comparison with experimental tests carried out on a cement mortar and a typical porous sandstone.

- A new bi-potential based incremental variational (BIV) homogenization approach for ductile rock-like materials with a non-associated Drucker-Prager plastic matrix have been established. The bi-potential theory and the incremental variational principle was well combined. The accuracy of the proposed model have been assessed by a series of comparisons with reference solutions obtained from full-field finite element simulations respectively for inclusion-reinforced materials and porous materials. The

model have been also used to simulate the mechanical behavior of claystone and sandstone under different loading paths.

- For describing the effective behavior of brittle rock-like materials under a larger range of compressive stress, a micro-mechanics friction damage coupled model have been proposed in the frame-work of thermodynamics combined with Mori-Tanaka homogenization scheme. An analytical analysis of macroscopic peak strength and volumetric compressibility-dilatancy transition have been provided. The efficiency of the proposed model have been verified against experimental data on three typical brittle granites and for a very large range of stress.
- The transition from diffuse damage to localized cracking in brittle materials have been envisaged with a micro-mechanics based friction-damage. The localized cracking is considered as a consequence of coalescence of diffuse micro-cracks approach. The orientation of localized crack is determined from the Mohr's maximization postulate and the frictional sliding of the localized crack was described by a localized friction damage model. Analytical solutions have been derived for some specific loading paths.

2 Perspectives

This thesis opened up new dictions for the development of homogenization approaches for rock-like materials. However, there still a lot of work to do to capture the complex mechanical behaviors of these materials with complex microstructure. In the future, we may improve the presented models in the following directions:

- All these models focused on the short-term mechanical behavior of dry rock-like materials, we will extended the models to describe the time-dependent behaviors and to consider saturated and unsaturated conditions as well as thermo-mechanical coupling.
- Considering the plastic matrix obeys to a nonlinear yield criterion in the incremental variational homogenization model, for instances, Mises–Schleicher yield criterion, and other analytical nonlinear yield criterion derived for porous Drucker-Prager matrix (Guo et al., 2008b; Maghous et al., 2009a). This could be useful for instance to capture influence of intra-particle pores.
- Proposing a more sophisticated definition of the LCC, such as second-order procedure (Castañeda, 2002a), to consider the fluctuations in the variational framework.

- Proposing a unified homogenization approach to consider the inclusions, pores and cracks in same scale and describing ductile-brittle transition phenomenon.

To conclude, developing homogenization approaches for complex behavior of rock-like materials, such as elastoplasticity and plastic damage, requires a compromise between accuracy, theoretical rigor, and numerical cost. The final goal, not achieved yet, is to propose a model which has the virtue of the three.

Bibliography

Abu-Lebdeh, T. M. and Voyiadjis, G. Z. (1993). Plasticity-damage model for concrete under cyclic multiaxial loading. *Journal of Engineering mechanics*, 119(7):1465–1484.

Agoras, M., Avazmohammadi, R., and Castañeda, P. P. (2016). Incremental variational procedure for elasto-viscoplastic composites and application to polymer-and metal-matrix composites reinforced by spheroidal elastic particles. *International Journal of Solids and Structures*, 97:668–686.

Aldakheel, F. and Miehe, C. (2017). Coupled thermomechanical response of gradient plasticity. *International Journal of Plasticity*, 91:1–24.

Anand, L., Aslan, O., and Chester, S. A. (2012). A large-deformation gradient theory for elastic–plastic materials: strain softening and regularization of shear bands. *International Journal of Plasticity*, 30:116–143.

Armand, G., Conil, N., Talandier, J., and Seyedi, D. M. (2016). Fundamental aspects of the hydromechanical behaviour of callovo-oxfordian claystone: From experimental studies to model calibration and validation. *Computers & Geotechnics*.

Armero, F. and Garikipati, K. (1996). An analysis of strong discontinuities in multiplicative finite strain plasticity and their relation with the numerical simulation of strain localization in solids. *International Journal of Solids and Structures*, 33(20-22):2863–2885.

Aubertin, M. and Li, L. (2004). A porosity-dependent inelastic criterion for engineering materials. *International Journal of Plasticity*, 20(12):2179–2208.

Barretta, R. and de Sciarra, F. M. (2015). Analogies between nonlocal and local bernoulli–euler nanobeams. *Archive of Applied Mechanics*, 85(1):89–99.

Barretta, R., De Sciarra, F. M., and Diaco, M. (2014). Small-scale effects in nanorods. *Acta Mechanica*, 225(7):1945–1953.

Bazant, Z. P. and Planas, J. (1997). *Fracture and size effect in concrete and other quasibrittle materials*, volume 16. CRC press.

Benveniste, Y. (1986). On the mori-tanaka method in cracked bodies. *Mech.Res. Commun.*, 13(4):193–210.

Benveniste, Y. (1987). A new approach to the application of mori-tanaka's theory in composite materials. *Mechanics of materials*, 6(2):147–157.

Bésuelle, P., Desrues, J., and Raynaud, S. (2000). Experimental characterisation of the localisation phenomenon inside a vosges sandstone in a triaxial cell. *International Journal of Rock Mechanics and Mining Sciences*, 37(8):1223–1237.

Bikong, C., Hoxha, D., and Shao, J. F. (2015). A micro-macro model for time-dependent behavior of clayey rocks due to anisotropic propagation of microcracks. *International Journal of Plasticity*, 69:73–88.

Bodovillé, G. (2001a). The implicit standard material theory for modelling the nonassociative behaviour of metals. *Archive of Applied Mechanics*, 71(6-7):426–435.

Bodovillé, G. (2001b). On generalised and implicit normality hypotheses. *Meccanica*, 36(3):273–290.

Bodovillé, G. and De Saxcé, G. (2001). Plasticity with non-linear kinematic hardening: modelling and shakedown analysis by the bipotential approach. *European Journal of Mechanics-A/Solids*, 20(1):99–112.

Boudet, J., Auslender, F., Bornert, M., and Lapusta, Y. (2016). An incremental variational formulation for the prediction of the effective work-hardening behavior and field statistics of elasto-(visco)plastic composites. *International Journal of Solids & Structures*, 83:90–113.

Bousshine, L., Chaaba, A., and De Saxce, G. (2002). Plastic limit load of plane frames with frictional contact supports. *International Journal of Mechanical Sciences*, 44(11):2189–2216.

Bousshine, L., Chaaba, A., and De Saxce, G. (2003). A new approach to shakedown analysis for non-standard elastoplastic material by the bipotential. *International Journal of Plasticity*, 19(5):583–598.

Brassart, L., Stainier, L., Doghri, I., and Delannay, L. (2011). A variational formulation for the incremental homogenization of elasto-plastic composites. *Journal of the Mechanics and Physics of Solids*, 59(12):2455–2475.

Brassart, L., Stainier, L., Doghri, I., and Delannay, L. (2012). Homogenization of elasto-(visco) plastic composites based on an incremental variational principle. *International Journal of Plasticity*, 36:86–112.

Budiansky, B. and O'connell, R. J. (1976). Elastic moduli of a cracked solid. *International journal of Solids and structures*, 12(2):81–97.

Carol, I. and Bazant, Z. P. (1997). Damage and plasticity in microplane theory. *International journal of solids and structures*, 34(29):3807–3835.

Carol, I., Prat, P. C., and Lopez, C. M. (1997). Normal/shear cracking model: application to discrete crack analysis. *Journal of engineering mechanics*, 123(8):765–773.

Castañeda, P. P. (1991). The effective mechanical properties of nonlinear isotropic composites. *Journal of the Mechanics and Physics of Solids*, 39(1):45–71.

Castañeda, P. P. (1992). New variational principles in plasticity and their application to composite materials. *Journal of the Mechanics and Physics of Solids*, 40(8):1757–1788.

Castañeda, P. P. (1996). Exact second-order estimates for the effective mechanical properties of nonlinear composite materials. *Journal of the Mechanics and Physics of Solids*, 44(6):827–862.

Castañeda, P. P. (2002a). *Heterogeneous materials. Lecture Notes.* Department of Mechanics, Ecole Polytechnique.

Castañeda, P. P. (2002b). Second-order homogenization estimates for nonlinear composites incorporating field fluctuations: I theory. *Journal of the Mechanics and Physics of Solids*, 50(4):737–757.

Castañeda, P. P. and Suquet, P. (1997). Nonlinear composites. In *Advances in applied mechanics*, volume 34, pages 171–302. Elsevier.

Cervera, M. and Chiumenti, M. (2006). Smeared crack approach: back to the original track. *International journal for numerical and analytical methods in geomechanics*, 30(12):1173–1199.

Cervera, M., Chiumenti, M., and Di Capua, D. (2012). Benchmarking on bifurcation and localization in j 2 plasticity for plane stress and plane strain conditions. *Computer Methods in Applied Mechanics and Engineering*, 241:206–224.

Cervera, M. and Wu, J.-Y. (2015). On the conformity of strong, regularized, embedded and smeared discontinuity approaches for the modeling of localized failure in solids. *International Journal of Solids and Structures*, 71:19–38.

Chaboche, J., Kanouté, P., and Roos, A. (2005). On the capabilities of mean-field approaches for the description of plasticity in metal matrix composites. *International journal of Plasticity*, 21(7):1409–1434.

Chaboche, J. L., Kruch, S., Maire, J. F., and Pottier, T. (2001). Towards a micromechanics based inelastic and damage modeling of composites. *International Journal of Plasticity*, 17(4):411–439.

Chambon, R., Caillerie, D., and Matsuchima, T. (2001). Plastic continuum with microstructure, local second gradient theories for geomaterials: localization studies. *International Journal of Solids and Structures*, 38(46):8503–8527.

Chen, L., Liu, J. F., Wang, C. P., Liu, J., Su, R., Wang, J., Chen, L., Liu, J. F., Wang, C. P., and Liu, J. (2014). Characterization of damage evolution in granite under compressive stress condition and its effect on permeability. *International Journal of Rock Mechanics & Mining Sciences*, 71(287-290):340–349.

Chen, L., Wang, C. P., Liu, J. F., Liu, J., Wang, J., Jia, Y., and Shao, J. F. (2015). Damage and plastic deformation modeling of beishan granite under compressive stress conditions. *Rock Mechanics and Rock Engineering*, 48(4):1623–1633.

Cheng, L., Jia, Y., Oueslati, A., De Saxcé, G., and Kondo, D. (2015). A bipotential-based limit analysis and homogenization of ductile porous materials with non-associated drucker–prager matrix. *Journal of the Mechanics and Physics of Solids*, 77:1–26.

Chiarelli, A.-S. (2000). Etude expérimentale et modélisation du comportement mécanique de l'argilité de l'est: influence de la profondeur et de la teneur en eau.

Chiarelli, A. S., Shao, J. F., and Hoteit, N. (2003). Modeling of elastoplastic damage behavior of a claystone. *International Journal of Plasticity*, 19(1):23–45.

Chow, C. L. and Wang, J. (1987). An anisotropic theory of elasticity for continuum damage mechanics. *International Journal of Fracture*, 33(1):3–16.

Cicekli, U., Voyiadjis, G. Z., and Al-Rub, R. K. A. (2007). A plasticity and anisotropic damage model for plain concrete. *International Journal of plasticity*, 23(10-11):1874–1900.

Comi, C., Mariani, S., and Perego, U. (2007). An extended fe strategy for transition from continuum damage to mode i cohesive crack propagation. *Int. J. for Numerical and Analytical Methods in Geomechanics*, 31:213–238.

Conil, N., Djeran-Maigre, I., Cabrillac, R., and Su, K. (2004). Poroplastic damage model for claystones. *Applied Clay Science*, 26(1-4):473–487.

Danas, K. and Castañeda, P. P. (2012). Influence of the lode parameter and the stress triaxiality on the failure of elasto-plastic porous materials. *International Journal of Solids and Structures*, 49(11-12):1325–1342.

De Saxcé, G. (1995). The bipotential method, a new variational and numerical treatment of the dissipative laws of materials. In *Proc. 10th Int. Conf. on Mathematical and Computer Modelling and Scientific Computing,(Boston, 1995)*.

De Saxcé, G. and Bousshine, L. (1998). Limit analysis theorems for implicit standard materials: application to the unilateral contact with dry friction and the non-associated flow rules in soils and rocks. *International Journal of Mechanical Sciences*, 40(4):387–398.

De Saxcé, G. and Bousshine, L. (2002). Implicit standard materials. In *Inelastic behaviour of structures under variable repeated loads*, pages 59–76. Springer.

De Saxcé, G. and Feng, Z.-Q. (1991). New inequality and functional for contact with friction: The implicit standard material approach. *Journal of Structural Mechanics*, 19(3):301–325.

De Sciarra, F. M. (2008). A general theory for nonlocal softening plasticity of integral-type. *International Journal of Plasticity*, 24(8):1411–1439.

de Sciarra, F. M. (2008). Variational formulations, convergence and stability properties in nonlocal elastoplasticity. *International Journal of Solids and Structures*, 45(7):2322–2354.

Deude, V., Dormieux, L., Kondo, D., and Pensee, V. (2002). Conewise linear elastic materials. *C.R. Mécanique*, 330:587–592.

Diederichs, M. (2003). Manuel rocha medal recipient rock fracture and collapse under low confinement conditions. *Rock Mechanics and Rock Engineering*, 36(5):339–381.

Doghri, I., Brassart, L., Adam, L., and Gérard, J.-S. (2011). A second-moment incremental formulation for the mean-field homogenization of elasto-plastic composites. *International Journal of Plasticity*, 27(3):352–371.

Doghri, I. and Ouaar, A. (2003). Homogenization of two-phase elasto-plastic composite materials and structures: Study of tangent operators, cyclic plasticity and numerical algorithms. *International Journal of Solids & Structures*, 40(7):1681–1712.

Doghri, I. and Tinel, L. (2005). Micromechanical modeling and computation of elasto-plastic materials reinforced with distributed-orientation fibers. *International Journal of Plasticity*, 21(10):1919–1940.

Dragon, A., Halm, D., and Désoyer, T. (2000). Anisotropic damage in quasi-brittle solids: modelling, computational issues and applications. *Computer methods in applied mechanics and engineering*, 183(3-4):331–352.

Dragon, A. and Mroz, Z. (1979). A continuum model for plastic-brittle behaviour of rock and concrete. *International Journal of Engineering Science*, 17(2):121–137.

Dvorak, G. J. and Benveniste, Y. (1992). On transformation strains and uniform fields in multiphase elastic media. *Proc. R. Soc. Lond. A*, 437(1900):291–310.

Eshelby, J. (1961). Elastic inclusions and inhomogeneities. *In: Sneddon, I.N., Hill, R.(Eds), Progress in solid Mechanics 2.*, 241:89–140.

Eshelby, J. D. (1957a). The determination of the elastic field of an ellipsoidal inclusion, and related problems. *Proceedings of the Royal Society of London*, 241(1226):376–396.

Eshelby, J. D. (1957b). The determination of the elastic field of an ellipsoidal inclusion, and related problems. In *Proceedings of the Royal Society of London A: Mathematical, Physical and Engineering Sciences*, volume 241, pages 376–396. The Royal Society.

Frantziskonis, G. and Desai, C. (1987). Elastoplastic model with damage for strain softening geomaterials. *Acta Mechanica*, 68(3-4):151–170.

Fredrich, J., Evans, B., and Wong, T. (1989). Micromechanics of the brittle to plastic transition in carrara marbe. *J. of Geophys. Res.*, 94:4129–4145.

Gambarotta, L. and Lagomarsino, S. (1993). A microcrak damage model for brittle materials. *Int. J. Solids Structures*, 30(2):177–198.

Grassl, P. and Jirásek, M. (2006a). Damage-plastic model for concrete failure. *International journal of solids and structures*, 43(22):7166–7196.

Grassl, P. and Jirásek, M. (2006b). Plastic model with non-local damage applied to concrete. *International Journal for Numerical and Analytical Methods in Geomechanics*, 30(1):71–90.

Guéry, A. C., Cormery, F., Shao, J. F., and Kondo, D. (2008). A micromechanical model of elastoplastic and damage behavior of a cohesive geomaterial. *International Journal of Solids & Structures*, 45(5):1406–1429.

Guéry, A. C., Cormery, F., Shao, J. F., and Kondo, D. (2010). A multiscale modeling of damage and time-dependent behavior of cohesive rocks. *International Journal for Numerical & Analytical Methods in Geomechanics*, 33(5):567–589.

Guo, T., Faleskog, J., and Shih, C. (2008a). Continuum modeling of a porous solid with pressure sensitive dilatant matrix. *J. Mech. Phys. Solids*, 56:2188–2212.

Guo, T., Faleskog, J., and Shih, C. (2008b). Continuum modeling of a porous solid with pressure-sensitive dilatant matrix. *Journal of the Mechanics and Physics of Solids*, 56(6):2188–2212.

Haddag, B., Abed-Meraim, F., and Balan, T. (2009). Strain localization analysis using a large deformation anisotropic elastic–plastic model coupled with damage. *International Journal of Plasticity*, 25(10):1970–1996.

Haghighat, E. and Pietruszczak, S. (2015). On modeling of discrete propagation of localized damage in cohesive-frictional materials. *International Journal for Numerical & Analytical Methods in Geomechanics*, 39(16):1774–1790.

Halm, D. and Dragon, A. (1998). An anisotropic model of damage and frictional sliding for brittle materials. *European Journal of Mechanics - A/Solids*, 17(3):439–460.

Halphen, B. and Nguyen, Q. S. (1975). Sur les matériaux standard généeralisés.

Hansen, N. and Schreyer, H. (1994a). A thermodynamically consistent framework for theories of elastoplasticity coupled with damage. *International Journal of Solids and Structures*, 31(3):359–389.

Hansen, N. R. and Schreyer, H. L. (1994b). A thermodynamically consistent framework for theories of elastoplasticity coupled with damage. *International Journal of Solids & Structures*, 31(3):359–389.

Hashin, Z. (1962). The elastic moduli of heterogeneous materials. *Journal of Applied Mechanics*, 29(1):2938–2945.

He, W., Wu, Y. F., Xu, Y., and Fu, T. T. (2015). A thermodynamically consistent nonlocal damage model for concrete materials with unilateral effects. *Computer Methods in Applied Mechanics and Engineering*, 297:371–391.

Hill, R. (1965a). Continuum micro-mechanics of elastoplastic polycristals. *Journ. of Mech. Phys. Solids*, 13:89–101.

Hill, R. (1965b). Continuum micro-mechanics of elastoplastic polycrystals. *Journal of the Mechanics and Physics of Solids*, 13(2):89–101.

Hill, R. (1967). The essential structure of constitutive laws for metal composites and polycrystals. *Journal of the Mechanics & Physics of Solids*, 15(2):79–95.

Hjiaj, M., Fortin, J., and De Saxcé, G. (2003). A complete stress update algorithm for the non-associated drucker–prager model including treatment of the apex. *International Journal of Engineering Science*, 41(10):1109–1143.

Hoek, E. and Bieniawski, Z. (1965). Brittle fracture propagation in rock under compression. *International Journal of Fracture Mechanics*, 1(3):137–155.

Huang, Y., Guéry, A. C., and Shao, J. F. (2015). Incremental variational approach for time dependent deformation in clayey rock. *International Journal of Plasticity*, 64:88–103.

Huespe, A., Oliver, J., Pulido, M., Blanco, S., and Linero, D. (2006). On the fracture models determined by the continuum-strong discontinuity approach. *International journal of fracture*, 137(1-4):211–229.

Idiart, M. I. and Castañeda, P. P. (2007). Field statistics in nonlinear composites. i. theory. In *Proceedings of the Royal Society of London A: Mathematical, Physical and Engineering Sciences*, volume 463, pages 183–202. The Royal Society.

Ingraffea, A. and Saouma, V. (1985). Numerical modelling of discrete crack propagation in reinforced and plain concrete. *Fracture Mechanics of concrete*, pages 171–225.

Itskov, M. (2007). *Tensor algebra and tensor analysis for engineers*. Springer.

Jason, L., Huerta, A., Pijaudier-Cabot, G., and Ghavamian, S. (2006). An elastic plastic damage formulation for concrete: Application to elementary tests and comparison with

an isotropic damage model. *Computer methods in applied mechanics and engineering*, 195(52):7077–7092.

Jefferson, A. D. and Bennett, T. (2007). Micro-mechanical damage and rough crack closure in cementitious composite materials. *International journal for numerical and analytical methods in geomechanics*, 31(2):133–146.

Jiang, T., Guéry, A. A.-C., Kondo, D., and Shao, J.-F. (2009). Multi-scale modeling for inelastic behavior of a cohesive geomaterial. *Mechanics Research Communications*, 36(6):673–681.

Jiang, T. and Shao, J.-F. (2009). On the incremental approach for nonlinear homogenization of composite and influence of isotropization. *Computational Materials Science*, 46(2):447–451.

Jiang, T., Shao, J.-F., and Xu, W. (2013). A non-uniform transformation field analysis for frictional cohesive geomaterials. *European Journal of Mechanics-A/Solids*, 42:97–111.

Jirásek, M. (1998). Nonlocal models for damage and fracture: comparison of approaches. *International Journal of Solids and Structures*, 35(31-32):4133–4145.

Jirásek, M. and Zimmermann, T. (2001a). Embedded crack model: I. basic formulation. *Int. J. for Numerical Methods in Engineering*, 50:1269–1290.

Jirásek, M. and Zimmermann, T. (2001b). Embedded crack model. part ii: Combination with smeared cracks. *Int. J. for Numerical Methods in Engineering*, 50:1291–1305.

Joli, P. and Feng, Z.-Q. (2008). Uzawa and newton algorithms to solve frictional contact problems within the bi-potential framework. *International journal for numerical methods in engineering*, 73(3):317–330.

Kachanov, M. (1992). Effective elastic properties of cracked solids: Critical review of some basic concepts. *Applied Mechanics Reviews*, 45(8):304–335.

Kachanov, M. L. (1982). A microcrack model of rock inelasticity part i: Frictional sliding on microcracks. *Mechanics of Materials*, 1(1):19–27.

Khan, A. S., Xiang, Y., and Huang, S. (1991). Behavior of berea sandstone under confining pressure part i: yield and failure surfaces, and nonlinear elastic response. *International journal of plasticity*, 7(6):607–624.

Khazraei, R. (1996). *Experimental Study and Modeling of Damage in Brittle Rocks*. PhD thesis, University of Lille, Lille,France.

Kweon, S., Sagsoy, B., and Benzerga, A. A. (2016). Constitutive relations and their time integration for anisotropic elasto-plastic porous materials. *Computer Methods in Applied Mechanics and Engineering*, 310:495–534.

Labuz, J. F., Dai, S. T., and Papamichos, E. (1996). Plane-strain compression of rock-like materials. *International Journal of Rock Mechanics & Mining Sciences & Geomechanics Abstracts*, 33(6):573–584.

Lahellec, N. and Suquet, P. (2007a). Effective behavior of linear viscoelastic composites: a time-integration approach. *International Journal of Solids and Structures*, 44(2):507–529.

Lahellec, N. and Suquet, P. (2007b). On the effective behavior of nonlinear inelastic composites: I. incremental variational principles. *Journal of the Mechanics and Physics of Solids*, 55(9):1932–1963.

Lahellec, N. and Suquet, P. (2007c). On the effective behavior of nonlinear inelastic composites: Ii: A second-order procedure. *Journal of the Mechanics and Physics of Solids*, 55(9):1964–1992.

Lahellec, N. and Suquet, P. (2013). Effective response and field statistics in elasto-plastic and elasto-viscoplastic composites under radial and non-radial loadings. *International Journal of Plasticity*, 42:1–30.

Lee, J. and Fenves, G. L. (1998). Plastic-damage model for cyclic loading of concrete structures. *Journal of engineering mechanics*, 124(8):892–900.

Lemaitre, J., Author, Chaboche, J. L., Author, and Maji, A. K. (1993). Mechanics of solid materials. *Journal of Engineering Mechanics*, 119(3):642–643.

Lockner, D., Byerlee, J., Kuksenko, V., Ponomarev, A., and Sidorin, A. (1992). Observations of quasistatic fault growth from acoustic emissions. In *International Geophysics*, volume 51, pages 3–31. Elsevier.

Lockner, D. A. (1998). A generalized law for brittle deformation of westerly granite. *Journal of Geophysical Research*, 103:5107–5123.

Lubarda, V. and Krajcinovic, D. (1995). Some fundamental issues in rate theory of damage-elastoplasticity. *International Journal of Plasticity*, 11(7):763–797.

Lubliner, J., Oliver, J., Oller, S., and Onate, E. (1989). A plastic-damage model for concrete. *International Journal of solids and structures*, 25(3):299–326.

Luccioni, B. and Rougier, V. (2005). A plastic damage approach for confined concrete. *Computers & structures*, 83(27):2238–2256.

Maghous, S., Dormieux, L., and Barthélémy, J. (2009a). Micromechanical approach to the strength properties of frictional geomaterials. *European Journal of Mechanics-A/Solids*, 28(1):179–188.

Maghous, S., Dormieux, L., and Barthélémy, J. (2009b). Micromechanical approach to the strength properties of frictional geomaterials. *European Journal of Mechanics A/Solid*, 28:179–188.

Mareau, C., Favier, V., and Berveiller, M. (2009). Micromechanical modeling coupling time-independent and time-dependent behaviors for heterogeneous materials. *International Journal of Solids & Structures*, 46(2):223–237.

Martin, C. and Chandler, N. (1994). The progressive fracture of lac du bonnet granite. In *International Journal of Rock Mechanics and Mining Sciences & Geomechanics Abstracts*, volume 31, pages 643–659. Elsevier.

Martin, C. D. (1994). *The strength of massive Lac du Bonnet granite around underground openings*. University of Manitoba.

Martin, C. D. (1997). Seventeenth canadian geotechnical colloquium: the effect of cohesion loss and stress path on brittle rock strength. *Canadian Geotechnical Journal*, 34(5):698–725.

Masson, R., Bornert, M., Suquet, P., and Zaoui, A. (2000). An affine formulation for the prediction of the effective properties of nonlinear composites and polycrystals. *Journ. Mech. Phys. Solids*, 48:1203–1227.

Masson, R. and Zaoui, A. (1999). Self-consistent estimates for the rate-dependentelastoplastic behaviour of polycrystalline materials. *Journal of the Mechanics & Physics of Solids*, 47(7):1543–1568.

Maugin, G. A. (1992). *The thermomechanics of plasticity and fracture*, volume 7. Cambridge University Press.

Michel, J.-C. and Suquet, P. (2003). Nonuniform transformation field analysis. *International journal of solids and structures*, 40(25):6937–6955.

Michel, J.-C. and Suquet, P. (2004). Computational analysis of nonlinear composite structures using the nonuniform transformation field analysis. *Computer methods in applied mechanics and engineering*, 193(48-51):5477–5502.

Moallemi, S. and Pietruszczak, S. (2017). Analysis of localized fracture in 3d reinforced concrete structures using volume averaging technique. *Finite Elements in Analysis and Design*, 125:41–52.

Mori, T. and Tanaka, K. (1973a). Average stress in a matrix and average elastic energy of materials with misfitting inclusions. *Acta Metall. Mater.*, 42(7):597–629.

Mori, T. and Tanaka, K. (1973b). Average stress in matrix and average elastic energy of materials with misfitting inclusions. *Acta Metallurgica*, 21:571–574.

Mori, T. and Tanaka, K. (1973c). Average stress in matrix and average elastic energy of materials with misfitting inclusions. *Acta Metallurgica*, 21(5):571–574.

Mosler, J. (2005). Numerical analyses of discontinuous material bifurcation: Strong and weak discontinuities. *Computer Methods in Applied Mechanics and Engineering*, 194(9):979–1000.

Nemat-Nasser, S. and Obata, M. (1988). A microcrack model of dilatancy in brittle materials. *Journal of applied mechanics*, 55(1):24–35.

Ngo, D. and Scordelis, A. (1967). Finite element analysis of reinforced concrete beams. In *Journal Proceedings*, volume 64, pages 152–163.

Nguyen, C. T., Nguyen, G. D., Das, A., and Bui, H. H. (2017). Constitutive modelling of progressive localised failure in porous sandstones under shearing at high confining pressures. *International Journal of Rock Mechanics and Mining Sciences*, 93:179–195.

Oliver, J. (1996). Modelling strong discontinuities in solid mechanics via strain softening constitutive equations. part 1: Fundamentals. *International journal for numerical methods in engineering*, 39(21):3575–3600.

Oliver, J. (2000). On the discrete constitutive models induced by strong discontinuity kinematics and continuum constitutive equations. *International journal of solids and structures*, 37(48):7207–7229.

Oliver, J., Cervera, M., and Manzoli, O. (1999). Strong discontinuities and continuum plasticity models: the strong discontinuity approach. *International journal of plasticity*, 15(3):319–351.

Oliver, J., Huespe, A., and Dias, I. (2012). Strain localization, strong discontinuities and material fracture: Matches and mismatches. *Computer Methods in Applied Mechanics and Engineering*, 241:323–336.

Oliver, J., Huespe, A., Pulido, M., and Chaves, E. (2002). From continuum mechanics to fracture mechanics: the strong discontinuity approach. *Engineering fracture mechanics*, 69(2):113–136.

Oliver, J., Huespe, A., Samaniego, E., and Chaves, E. (2004). Continuum approach to the numerical simulation of material failure in concrete. *International Journal for Numerical and Analytical Methods in Geomechanics*, 28(7-8):609–632.

Ortiz, M. and Stainier, L. (1999). The variational formulation of viscoplastic constitutive updates. *Computer Methods in Applied Mechanics & Engineering*, 171(3):419–444.

Ottosen, N. S. and Runesson, K. (1991). Discontinuous bifurcations in a nonassociated mohr material. *Mechanics of materials*, 12(3-4):255–265.

Pamin, J. (1994). Gradient-dependent plasticity in numerical simulation of localization phenomena.

Peerlings, R., De Borst, R., Brekelmans, W., and Geers, M. (1998). Gradient-enhanced damage modelling of concrete fracture. *Mechanics of Cohesive-frictional Materials*, 3(4):323–342.

Pensee, V., Kondo, D., and Dormieux, L. (2002). Micromechanical analysis of anisotropic damage in brittle materials. *J. Engng. Mech., ASCE*, 128(8):889–897.

Pensée, V., Kondo, D., and Dormieux, L. (2002). Micromechanical analysis of anisotropic damage in brittle materials. *Journal of Engineering Mechanics*, 128(8):889–897.

Pensée, V., Kondo, D., and Dormieux, L. (2002). Micromechanical analysis of anisotropic damage in brittle materials. *Journal of Engineering Mechanics*, 128(8):889–897.

Ponte-Castañeda, P. and Suquet, P. (1998). Nonlinear composites. *Adv. Appl. Mech.*, 34:171–302.

Ponte-Castañeda, P. and Willis, P. (1995). The effect of spatial distribution on the behaviour of composite materials and cracked media. *J. Mech. Phys. Solids*, 43:1919–1951.

Ponte Castaneda, P. (2002). Second-order homogenization estimates for nonlinear composites incorporating field fluctuations: I-theory. *Journal of the Mechanics & Physics of Solids*, 50(4):737–757.

Ponte Castañeda, P. and Suquet, P. (1997). Nonlinear composites. *Advances in Applied Mechanics*, 34:171–302.

Ponte Castaneda, P. and Willis, J. (1999). Variational second-order estimates for nonlinear composites. In *Proceedings of the Royal Society of London A: Mathematical, Physical and Engineering Sciences*, volume 455, pages 1799–1811. The Royal Society.

Ponte-Castaneda, P. and Willis, J.-R. (1995). The effect of spatial distribution of effective behavior of composite materials and cracked media. *Journ. Mech. Phys. Solids*, 43:1919–1951.

Qi, M., Shao, J. F., Giraud, A., Zhu, Q. Z., and Colliat, J. B. (2016). Damage and plastic friction in initially anisotropic quasi brittle materials. *International Journal of Plasticity*, 82:260–282.

Rashid, Y. (1968). Ultimate strength analysis of prestressed concrete pressure vessels. *Nuclear engineering and design*, 7(4):334–344.

Rice, J. R. and Rudnicki, J. W. (1980). A note on some features of the theory of localization of deformation. *International Journal of solids and structures*, 16(7):597–605.

Robinet, J., Sardini, P., Coelho, D., Parneix, J., Pret, D., Sammartino, S., Boller, E., and Altmann, S. (2012). Effects of mineral distribution at mesoscopic scale on solute diffusion in a clay-rich rock: Example of the callovo-oxfordian mudstone(bure, france). *Water Resources Research*, 48:05554.

Robinet, J. C. (2008). Minéralogie, porosité et diffusion des solutés dans l'argilite du callovo-oxfordien de bure (meuse, haute-marne, france) de l'échelle centimétrique à micrométrique. *Bibliogr.*

Rudnicki, J. W. and Rice, J. (1975). Conditions for the localization of deformation in pressure-sensitive dilatant materials. *Journal of the Mechanics and Physics of Solids*, 23(6):371–394.

Runesson, K., Ottosen, N. S., and Dunja, P. (1991). Discontinuous bifurcations of elastic-plastic solutions at plane stress and plane strain. *International Journal of Plasticity*, 7(1-2):99–121.

Salari, M. R., Saeb, S., Willam, K. J., Patchet, S. J., and Carrasco, R. C. (2004). A coupled elastoplastic damage model for geomaterials. *Computer Methods in Applied Mechanics & Engineering*, 193(27-29):2625–2643.

Saxcé, G. D. and Bousshine, L. (1998). Limit analysis theorems for implicit standard materials: Application to the unilateral contact with dry friction and the non-associated flow rules in soils and rocks. *International Journal of Mechanical Sciences*, 40(4):387–398.

Shao, J. and Henry, J. (1991). Development of an elastoplastic model for porous rock. *International Journal of plasticity*, 7(1-2):1–13.

Shao, J. F., Jia, Y., Kondo, D., and Chiarelli, A. S. (2006). A coupled elastoplastic damage model for semi-brittle materials and extension to unsaturated conditions. *Mechanics of Materials*, 38(3):218–232.

Shen, W., Kondo, D., Dormieux, L., and Shao, J. (2013). A closed-form three scale model for ductile rocks with a plastically compressible porous matrix. *Mechanics of Materials*, 59:73 – 86.

Shen, W., Shao, J.-F., Kondo, D., and Gatmiri, B. (2012). A micro–macro model for clayey rocks with a plastic compressible porous matrix. *International journal of plasticity*, 36:64–85.

Shen, W., Zhang, J., Shao, J., and Kondo, D. (2017). Approximate macroscopic yield criteria for drucker-prager type solids with spheroidal voids. *International Journal of Plasticity*, 99:221–247.

Shen, W. Q., Oueslati, A., and De Saxce, G. (2015). Macroscopic criterion for ductile porous materials based on a statically admissible microscopic stress field. *International Journal of Plasticity*, 70:60–76.

Shojaei, A., Taleghani, A. D., and Li, G. (2014). A continuum damage failure model for hydraulic fracturing of porous rocks. *International Journal of Plasticity*, 59:199–212.

Simo, J. C. and Taylor, R. L. (1985). Consistent tangent operators for rate-independent elastoplasticity. *Computer Methods in Applied Mechanics & Engineering*, 48(1):101–118.

Sun, C. T. and Vaidya, R. S. (1996). Prediction of composite properties from a representative volume element. *Composites Science & Technology*, 56(2):171–179.

Suquet, P. (1995). Overall properties of nonlinear composites: a modified secant moduli theory and its link with ponte castañeda's nonlinear variational procedure.

Suquet, P. (1996). Overall properties of nonlinear composites. In *IUTAM Symposium on Micromechanics of Plasticity and Damage of Multiphase Materials*, pages 149–156. Springer.

Szczepanik, Z., Milne, D., Kostakis, K., Eberhardt, E., et al. (2003). Long term laboratory strength tests in hard rock. In *10th ISRM Congress*. International Society for Rock Mechanics.

Tkalich, D., Fourmeau, M., Kane, A., Li, C. C., and Cailletaud, G. (2016). Experimental and numerical study of kuru granite under confined compression and indentation. *International Journal of Rock Mechanics & Mining Sciences*, 87:55–68.

Voyiadjis, G. Z., Taqieddin, Z. N., and Kattan, P. I. (2008). Anisotropic damage–plasticity model for concrete. *International journal of plasticity*, 24(10):1946–1965.

Walsh, J. B. (1980). Static deformation of rock. *Journal Of The Engineering Mechanics Division*, 106:1005–1019.

Wang, L., Bornert, M., Heripre, E., Chanchole, S., Pouya, A., and Halphen, B. (2015). The mechanisms of deformation and damage of mudstones: a micro-scale study combining esem and dic. *Rock Mechanics and Rock Engineering*, 48:1913–1926.

Wang, L., Bornert, M., Heripre, E., Chanchole, S., and Tanguy, A. (2014). Full-field measurements on low-strained geomaterials using environmental scanning electron microscopy and digital image correlation: Improved imaging conditions. *Strain*, 50:370–380.

Willis, J. R. (1981). Variational and related methods for the overall properties of composites. *Advances in Applied Mechanics*, 21:1–78.

Willis, J. R. (1989). The structure of overall constitutive relations for a class of nonlinear composites. *Journal of Applied Mathematics*, 43:231–242.

Wong, T. (1982). Micromechanics of faulting in westerly granite. *Int. J. Rock Mech. Min. Sci.*, 19:49–62.

Wu, J. Y. and Cervera, M. (2015). On the equivalence between traction-and stress-based approaches for the modeling of localized failure in solids. *Journal of the Mechanics and Physics of Solids*, 82:137–163.

Wu, J.-Y. and Cervera, M. (2016). A thermodynamically consistent plastic-damage framework for localized failure in quasi-brittle solids: Material model and strain localization analysis. *International Journal of Solids and Structures*, 88:227–247.

Xie, S. and Shao, J.-F. (2006). Elastoplastic deformation of a porous rock and water interaction. *International Journal of Plasticity*, 22(12):2195–2225.

Xotta, G., Beizaee, S., and Willam, K. J. (2016). Bifurcation investigations of coupled damage-plasticity models for concrete materials. *Computer Methods in Applied Mechanics and Engineering*, 298:428–452.

Yan, Y., Geng, L., and Li, A. (2007). Experimental and numerical studies of the effect of particle size on the deformation behavior of the metal matrix composites. *Materials Science and Engineering: A*, 448(1-2):315–325.

Yazdani, S. and Schreyer, H. (1990). Combined plasticity and damage mechanics model for plain concrete. *Journal of engineering mechanics*, 116(7):1435–1450.

Yuan, X., Liu, H., and Wang, Z. (2013). An interacting crack-mechanics based model for elastoplastic damage model of rock-like materials under compression. *International Journal of Rock Mechanics and Mining Sciences*, 58:92–102.

Yurtdas, I., Burlion, N., and Skoczylas, F. (2004). Experimental characterisation of the drying effect on uniaxial mechanical behaviour of mortar. *Materials and Structures*, 37(3):170–176.

Zhang, K., Zhou, H., and Shao, J. (2013). An experimental investigation and an elastoplastic constitutive model for a porous rock. *Rock mechanics and rock engineering*, 46(6):1499–1511.

Zhao, L.-Y., Zhu, Q.-Z., and Shao, J.-F. (2018). A micro-mechanics based plastic damage model for quasi-brittle materials under a large range of compressive stress. *International Journal of Plasticity*, 100:156–176.

Zhao, L. Y., Zhu, Q. Z., Xu, W. Y., Dai, F., and Shao, J. F. (2016). A unified micromechanics-based damage model for instantaneous and time-dependent behaviors of brittle rocks. *International Journal of Rock Mechanics & Mining Sciences*, 87:187–196.

Zhou, H., Bian, H., Jia, Y., and Shao, J.-F. (2013). Elastoplastic damage modeling the mechanical behavior of rock-like materials considering confining pressure dependency. *Mechanics Research Communications*, 53:1–8.

Zhu, Q. (2006). Applications des approches d'homogénéisation à la modélisation tridimensionnel de l'endommagement des matériaux quasi fragile: Formulations, validations et implémentations numérique. *Ph.D Thesis University of Lille 1 (In French)*.

Zhu, Q., Kondo, D., and Shao, J. (2008a). Micromechanical analysis of coupling between anisotropic damage and friction in quasi brittle materials: role of the homogenization scheme. *International Journal of Solids and Structures*, 45(5):1385–1405.

Zhu, Q., Kondo, D., Shao, J., and Pensee, V. (2008b). Micromechanical modelling of anisotropic damage in brittle rocks and application. *International Journal of Rock Mechanics & Mining Sciences*, 45(4):467–477.

Zhu, Q., Zhou, C., Shao, J.-F., and Kondo, D. (2010). A discrete thermodynamic approach for anisotropic plastic–damage modeling of cohesive-frictional geomaterials. *International journal for numerical and analytical methods in geomechanics*, 34(12):1250–1270.

Zhu, Q. Z. (2016). Strength prediction of dry and saturated brittle rocks by unilateral damage-friction coupling analyses. *Computers and Geotechnics*, 73:16–23.

Zhu, Q. Z. (2017). A new rock strength criterion from microcracking mechanisms which provides theoretical evidence of hybrid failure. *Rock Mechanics & Rock Engineering*, 50(2):1–12.

Zhu, Q. Z. and Shao, J. F. (2015). A refined micromechanical damage–friction model with strength prediction for rock-like materials under compression. *International Journal of Solids and Structures*, 60:75–83.

Zhu, Q. Z., Shao, J. F., and Kondo, D. (2011). A micromechanics-based thermodynamic formulation of isotropic damage with unilateral and friction effects. *European Journal of Mechanics - A/Solids*, 30(3):316–325.

Zhu, Q. Z., Zhao, L. Y., and Shao, J. F. (2016). Analytical and numerical analysis of frictional damage in quasi brittle materials. *Journal of the Mechanics & Physics of Solids*, 92:137–163.

Zouain, N., Pontes Filho, I., Borges, L., and da Costa, L. M. (2007). Plastic collapse in non-associated hardening materials with application to cam-clay. *International journal of solids and structures*, 44(13):4382–4398.